Detection of Stress Concentration Zones in Ferrous Material using Stand-off Magnetometry

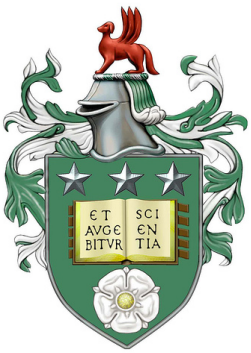

Chau Ky Vo

School of Electronic and Electrical Engineering

University of Leeds

Submitted in accordance with the requirements for the degree of

Doctor of Philosophy

October 2015

The candidate confirms that the work submitted is his own and that appropriate credit has been given where reference has been made to the work of others.

This thesis is dedicated to my family.

Acknowledgements

I want to thank my PhD. supervisors Dr. Steven Freear and Prof. Ben Varcoe for their guidance during my PhD., especially for Steve who gave so generously of his time and support for both of my academic and personal life.

I want to thank Dr. David M. J. Cowell, Stephen G. H. Staples and Dr. Sevan Harput for their great contribution and valuable support during this work.

I acknowledge the financial support from the Vietnam International Education Development (VIED) and Speir Hunter Ltd., and personally would like to thank Paul Jaram for his kindly support and communication during my PhD.

I thank Anna de Jong for her secretarial assistance. I would also like to thank Hanh H. Vu, Huong T. Nguyen, Hai X. Nguyen from VIED for their communication and administrative support.

I would like to thank my friends, in particular, Khoa D. Nguyen, Tuan Q. Nguyen, Quang B. Vu for their personal support.

I want to thank again all the people of the Ultrasound Group and the Magnetic group, in particular, Dr. Steven Freear, Dr. David M. J. Cowell, Dr. Sevan Harput, Dr. James R. McLaughlan, Stephen G.H. Staples, Benjamin Raiton, Dr. Peter R. Smith, Gael Leaute, Christopher Cookson, David Charutz.

I also want to thank the people from the industrial companies for their support during my work, in particular, Paul Jaram, Peter J. Norlan, Peter B. Martin, Mark A. Saunders, and Phil Keogh.

Finally, I have not enough words to express the love for my parents, my wife and sons and my big family for their love and endless support.

Abstract

Detection of stress concentration zones using stand-off magnetometry based on the magnetomechanical effect has recently been applied to pipeline inspection. This study addresses the lack of scientific evidence encountered in the development of the technology by using a combination of laboratory experiments, field observations, and computer simulations to study the magnetic indication of local stress concentrations in the bulk material. It then offers new techniques to determine features of underground pipelines, and evaluates their performance using field survey data and standard inspection reports.

The models proposed in this study are capable of simulating the effects of stress cycles on magnetisation of steel bars and pipes placed in the earth's magnetic field. The experimental and simulation results have shown that the magnetic indication of a local stress concentration zone (SCZ) is due to the distribution of magnetisation between the local SCZ and the surrounding area or the bulk material, which has explained the reverse in the polarity of the magnetic indication when varying the applied stress. It also implies the possibility to monitor stress conditions in ferrous material.

It is proposed that the gradient magnetic field should be used in order to extract the magnetic indication from the measured magnetic field, together with a parameter K as the criteria for detection and characterisation of local SCZ using the remote magnetic field. It has found that K is linear with the initial magnetic condition induced in low field at a given stress. Inversely, at a given initial condition, variation of K with stress follows the stress-magnetisation relationship of

the material. K is more sensitive with stress at stronger initial conditions. The study has also established the quantitative exponential relationship between K and the measurement distance, which implies a technique to solve for stress condition from the remote magnetic field.

A study on circumferential welded joints of pipelines has found magnetic features of the welds, which implies the possibility to locate them using above-ground surveys. A technique is proposed and is capable of locating 70% of the actual welds with an offset of 3 meters and the probability of false call of 20% for the pipelines of 17 meters constructed length buried with more than 2 meters depth of cover.

A new practical technique to estimate the depth of cover of underground pipelines from the remote passive magnetic field, which has the tolerance of 8% of the measurement depth, is also proposed.

Importantly, this study proposes a preliminary technique to detect SCZs in underground pipelines using the remote magnetic field, which can detect side bends and sag bends, and shows promises for detection of SCZs caused by mechanical defects. The development of these techniques are important milestones in non-invasive remote pipeline condition monitoring.

Contents

List of Figures

LIST OF FIGURES

List of Tables

Abbreviations

CNC	Computer Numerical Control
DWT	Discrete Wavelet Transform
FEA	Finite Element Analysis
FEM	Finite Element Method
GNSS	Global Navigation Satellite System
ILI	In-Line Inspection
LSM	Large Stand-Off Magnetometry
MFL	Magnetic Flux Leakage
MMM	Metal Magnetic Memory
MTM	Metal Tomography Method
NDT	Non-destructive Testing
ODE	Ordinary Differential Equation
PDE	Partial Differential Equation
PoD	Probability of Detection
PoF	Probability of False Detection
PoM	Probability of Missed Detection
RTK	Real Time Kinematic
SMFL	Self-Magnetic Leakage Field
SCT	Stress Concentration Tomography
SCZ	Stress Concentration Zone
SNR	Signal to Noise Ratio

List of Symbols

B	magnetic flux density
B_{bkg}	background magnetic flux density
B_σ	stress-induced magnetic field
d	measurement height
E	Young's modulus
F	applied force
H	magnetic field
H_e	effective magnetic field
K	strength of magnetic indication
L	length of stress concentration
M	magnetisation
M_s	saturation magnetisation
M_σ	stress-induced magnetisation
M_{an}	anhysteretic magnetisation
M_{irr}	irreversible component of magnetisation
M_{rev}	reversible component of magnetisation
P	applied pressure
σ	stress

Chapter 1

Introduction

In recent years, a new magnetic non-destructive testing (NDT) technology for pipeline inspection, which has the generic term Stand-Off Magnetometry, has attracted both research and industrial interest. One of its advantages compared to the traditional magnetic NDT methods is the remote assessment of stress condition of a pipeline, therefore, allowing the early detection of stress concentration zone (SCZ) without interrupting pipeline service.

This magnetic inspection method is based on an effect of magnetostriction in which applying external stress to a ferromagnetic substance changes its magnetisation and vice versa, by that magnetic field can be seen as a projection of stress.

In practice, as presented by Kolesnikov et al. [1], Transkor-K, a Russian company, has developed Magnetic Tomography Method (MTM) including both survey instrument and analysis software for inspecting underground pipeline since 2002. MTM can identify stress concentration zones caused by defects, characterise their features and predict the degree of danger using the remote magnetic field at a distance of up to 20 pipe diameters [1].

Although MTM has been used for pipeline inspection services in Russia and other countries for decades, almost no peer review publications can be found in literature. Since 2011, the University of Leeds has collaborated with Speir Hunter, DNV/GL and National Grid to develop Stress Concentration Tomography (SCT) as a remote inspection method for underground pipelines.

1.1 Introduction to Stress Concentration Tomography method for pipeline inspection

Today, oil and gas pipelines are a vital part of the energy infrastructure. Pipeline inspection techniques including magnetic methods have been developed for many years to maintain the integrity of the pipeline network.

A typical magnetic inspection of underground pipelines relies on In-Line Inspection (ILI) technology, in which an inspection tool called a pig (Pipeline Inspection Gauge) is pushed through the pipeline using launching and receiving stations [2]. It carries strong magnets to magnetically saturate the pipe wall.

Leakage of the magnetic flux caused by defects on the wall will be detected using magnetometers around the pig. This technique, called Magnetic Flux Leakage (MFL), is well-known for underground pipeline inspection [3, 4].

However, in practice, due to the physical width and length of the ILI inspection instrument, bends and width restrictions make certain pipelines impossible to inspect. These are known as unpiggable pipelines [5].

A non-invasive inspection method called Stress Concentration Tomography (SCT) has been developed at the University of Leeds in collaboration with the research sponsor Speir Hunter [6, 7]. It is a method of inferring localised stress of underground pipelines from the magnetic field remotely measured from above ground using an array of magnetometers.

Theoretically, SCT is based on the magnetomechanical effect by which magnetisation of ferrous materials is changed under stress. A stress concentration zone (SCZ) in underground pipelines, which could be caused by defects such as material loss, cracks, dents, or excessive mechanical stress areas caused by ground movements or bends, can produce a magnetic anomaly which is detectable from the ground.

It is proposed that SCT is used as a screening technique for underground pipeline inspection. It also plays a complementary role in providing more inspection data. Based on the above-ground surveys, localisation can be improved, for example by using satellite navigation systems such as Global Positioning System (GPS). Importantly, the technique works with both piggable and unpiggable pipelines without interrupting pipeline services. Because it aims to assess the pipe based on its stress condition, dangerous stress concentration zones can be early detected.

1.2 Literature Review

Magnetostriction is a phenomenon involving the interaction between mechanical stress and magnetisation. Many effects of magnetostriction have been found since the 19th century, however, the two main effects found by Joule and Villari usually appear in literature.

1. INTRODUCTION

The magnetostriction effect was first found by Joule [8]. In the experiment, an iron rod changed its length along the direction of magnetisation with a transverse contraction in small fields. The ratio $\Delta l/l$, where l and Δl are the length and the change in length, respectively, is called the magnetostrictive strain. Its saturation value, called the magnetostriction constant, is usually small and varies in both sign and magnitude with materials.

The inverse effect, known as the Villari effect, in which magnetisation of a material is changed under mechanical stress, was found by Villari [9]. The relationship is hysteretic and non-linear.

The physical origin of magnetostriction can be explained in terms of the domain theory, which was originally proposed by Weiss [10]. The theory suggests that magnetic material is divided into regions called magnetic domains. Within a domain, magnetic moments are aligned in parallel so that magnetisation of that domain is almost saturated. Magnetisation of material is determined by the net magnetisation of all domains whose direction varies between domains. By applying magnetic field or stress, the direction of individual magnetic domains are re-aligned in parallel which results in a change in length or in magnetisation of material respectively. Reviews of magnetostriction and other effects of stress can be found in the following texts: [11, 12, 13].

Stoner and Wohlfarth presented the fundamental aspects of ferromagnetism for intrinsic magnetisation and magnetisation curves [14, 15]. The process of reversible and irreversible boundary movements was also discussed. The authors explained the importance of energy formulas in the magnetostriction theory and concluded the complication of a general theory of the joint effect of stress and magnetic field. The relation between the magnetic energy expressions was presented and the thermodynamic relation was derived [16].

The theory of magnetostriction has been quantitatively developed since the 1930s. Brown Jr [17], based on the thermodynamic relation [16], extended the statistical domain theory of ferromagnetism [18, 19]. General formulas were derived to compute strain and magnetisation from stresses in low magnetisation.

The residual magnetisation resulting from application and subsequent removal of tension was discussed by Brown Jr [20]. The authors presented the irreversible magnetic effect of stress and developed a Rayleigh's law-based theoretical model

to account for this effect. In this work, magnetic field and stress were equivalent to a hydrostatic pressure on the domain walls.

Bozorth [11] showed that within the elastic limit, the first application of stress produces a larger change of magnetisation than successive cycles of stress. Stress causes the irreversible component of magnetisation as after stress cycles, the magnetisation approaches a limit that is different from the original value induced from the applied field only.

In addition to the irreversible magnetisation, a relation between stress and magnetisation was shown for small and reversible changes of stress and magnetostriction. It implied a reversible relation between the magnetostrictive and magnetomechanical effects.

Based on the domain theory and energies associated with field and stress, the authors suggested that changes of magnetisation can be predicted on the basis of the magnetoelastic anisotropy energy.

Magnetoelastic and magnetocrystalline anisotropy energies were also discussed by Cullity and Graham [21]. In this work the authors show that the sign of the product of saturation magnetostriction and direction of stress determines how the magnetisation responds to the stress. The authors concluded the dominated mechanism of magnetostriction is domain rotation by which the easy axis of magnetisation due to stress is formed.

Craik and Wood [22] performed a series of experiments investigating changes of magnetisation induced by stress on nickel, mild steel and both isotropic and cube-textured silicon-iron in a small constant applied field. Both tensile and compressive stresses were considered in the experiments.

Birss et al. [23] performed experiments investigating the variation of magnetisation with magnetic fields under either compressive or tensile stresses for iron and iron-carbon alloys. The authors concluded that the current theory could not explain the observations and later proposed an additional mechanism related to domain wall pressure to account for that [24].

Jiles and Atherton [25] initially developed a theory of magnetisation process based on the ideas of domain rotation and domain wall movement, and used it to explain effects of stress on magnetisation. The authors concluded that the

magnetomechanical effect can not be predicted simply on the basis of the magnetostriction constant. In fact, changes of magnetisation depend on the initial and the anhysteretic magnetisation. Generally speaking, under stress, magnetisation tends to approach the anhysteretic curve.

Based on the process of domain wall movements, Jiles and Atherton [26] developed the theory of ferromagnetic hysteresis. Although it didn't take into account the process of domain rotation, all of main features of hysteresis such as the initial magnetisation curve, magnetisation saturation, and remanence were included. This theory of hysteresis was validated by Pitman [27]. Importantly, Sablik et al. [28] extended the theory to include the effect of uniaxial stress on hysteresis.

The most recent theory of the magnetomechanical effect was discussed by Jiles [29]. The authors reviewed the inconsistency between the experiments [22, 24] with the existing theories [11, 20]. It was concluded that the domain theory is not sufficient to explain the magnetomechanical effect. This theory, called the law of approach, suggested three factors determining the magnitude and sign of magnetomechanical coefficient. They are the displacement between the magnetisation and the anhysteretic curve, the sensitivity of this displacement to stress, and the response of the anhysteretic curve to stress. There were also modifications of the Jiles-Atherton model [30, 31, 32].

Recently, many laboratory experiments have investigated the stress-magnetic field relationship in case of uni-axial stress such as steel bars or complex stress such as bars with defects or pipelines. Variation with stress of the surface magnetic field of ferromagnetic steel was explored [33, 34, 35, 36, 37]. Effects of applying many stress cycles were also studied [38, 39]. Role of the initial residual magnetisation was discussed by Leng et al. [40].

In practice, there were efforts to apply the magnetomechanical effect as a pipeline inspection method. However, although there are theoretical models of the stress-magnetisation relationship, a practical technique of detecting and characterising stress concentration zones (SCZs) for underground pipelines has not yet been established.

A series of experiments on steel pipes was performed to investigate the induced magnetisation of bending stress and applying multiple stress cycles [41, 42].

Using the effects of stress on magnetisation for monitoring bending stress was discussed [43, 44]. Importantly, the authors suggested that anomalous stresses can be detected and characterised using magnetic surveys. A simple model of underground pipelines which is as a series of magnetic dipoles was also introduced.

Viana et al. [45] presented the induced magnetic field of cylinders under stress and derived an analytical model which is extended from the Jiles-Atherton model [46]. The inverse solution for thin shell cylinder where distribution of magnetisation was solved from the measured magnetic field was presented [47].

Using the self-magnetic leakage field (SMFL) measured close on the surface of steel structures, Dubov [48] introduced the term Metal Magnetic Memory (MMM) and has applied it for Non-Destructive Testing (NDT) since then [49]. There is an ISO standard specifying requirements for applying MMM as a magnetic NDT method [50]. In fact, the experiments with ferromagnetic steel presented above employed the surface magnetic field as in MMM.

As presented by Kolesnikov et al. [1], Transkor-K has developed Magnetic Tomography Method (MTM) which is mainly used to inspect underground pipelines. While MMM utilises the surface magnetic field, the MTM method has been claimed to be able to detect and characterise SCZs in underground gas pipelines using above-ground magnetic surveys.

1.3 Motivation

Recently, driven by industrial needs, a new magnetic method called Stress Concentration Tomography (SCT) has been developed at Leeds for pipeline inspection, in which stress condition in the pipe wall is inferred through the magnetic field remotely measured by above-ground surveys using an array of magnetometers. The technique has an advantage of being usable for unpiggable pipelines. It is also being used as a screening method for defects or a complementary method for other inspection techniques such as ILI.

The principle of the SCT technology is very similar to Magnetic Tomography Method (MTM). However, although MTM has already been used for decades, there is very little background on how it works. Therefore, the main motivation

of this study is to provide scientific evidence in order to support the development of SCT.

It is known in the research literature that magnetic anomaly of a stress concentration zone (SCZ) is recognisable when measured on the surface of the ferrous material. However, an issue with SCT is the need for detection at a distance of at least 2 m, as this is the typical depth of cover of underground pipelines. Thus, strength of the magnetic anomaly is much smaller when compared to that of the surface field, so the magnetic field induced by the bulk material needs to be taken into account. For this reason, the question raised is not only whether this magnetic indication is recognisable and what is its criteria when measured at a distance, but also how it varies with the stress level and the measurement distance in the effect of the bulk field, and how it is affected by other features of the pipeline, for example bends or welded joints.

Another issue is, because of the survey method in which the surveyor holds the magnetometer array and walks along the pipeline route, the detected magnetic field of the pipe is distorted by the array movement. Additionally, there are unknown survey parameters including the depth of cover and magnetic condition of individual pipe sections which may also affect the magnetic indication of SCZ. For this reason, SCT will be questioned about its reliability as well as the confidence of its report unless it is supported by scientific evidence.

Although the development of SCT at Leeds has gone through a number of field trials, including blind trials on 40 km of pipelines in collaboration with National Grid (NG), DNV/GL and Speir Hunter services since 2012, it is noted that SCT is still at the early research stage when compared to the ILI technology.

1.4 Objectives

The development of SCT is related to many aspects including the theoretical background, small-scale laboratory experiments, large-scale field observations, field trials, modelling and signal processing techniques. The first objective is to be able to simulate the magnetomechanical effect. Based on this, the effects of stress and cycling stress to the magnetic field can be studied using finite element models.

In this study, a series of experiments was performed scaling up in size. Firstly, steel bars were used as specimens. The reason for this is the distribution of stress is in the axial direction only, so it simplifies the stress-magnetisation relationship. Defects were introduced to the bars, so that, the magnetic indication of a local SCZ can be studied with variation of the measurement distance and the effect of the bulk field. Secondly, experiments were performed with steel pipes, in which the induced magnetic field was measured while pressure was applied to the pipe. Additionally, a pipe manufactured by cutting into two halves and welding them together was useful to study the effect of welded joints in pipeline.

In addition to the laboratory experiments, field observations on above-ground live pipelines were also performed. The advantage here is that it is possible to visually check features of the pipeline such as bends or welded joints and control the measurement distance while providing the condition close to that of field surveys on underground pipelines.

For computer simulations, based on the model of the magnetomechanical effect, multi-physics models were developed for both steel bars and pipes using the finite element method. This is to simulate the effect of stress to magnetisation, which allows the study of magnetic indication of stress concentration zone as well as its variation with the measurement distance and the bulk field. The models can be verified using the experimental and observation results.

From understanding the magnetic field of underground pipelines, techniques to process the field survey data were proposed. The aim is to characterise a number of stress-induced features of the underground pipeline from the magnetic field measured using above-ground surveys.

1.5 Contribution

Modelling of the magnetomechanical effect based on the Jiles-Atherton model will be presented in Chapter 2. It presents a system of differential equations to numerically solve for the anhysteretic magnetisation, its stress dependence, and the reversible and irreversible components of the stress-induced magnetisation. Rather than assuming the magnetisation is not changed during the stress

relaxation, an additional term representing the direction of the applied stress is proposed, so that, magnetisation can be solved while cycling stress.

Chapter 3 describes the methodology for the development of SCT. It establishes the path of SCT development and relates the five aspects mentioned above. The chapter serves as an explanation for the methods of the laboratory experiments, field observations and field surveys, together with the description of three corresponding measurement systems used in this study.

Chapter 4 presents the stress-induced magnetic field of steel bars. Using the finite element model, this study has contributed to the understanding of the distribution of magnetisation of steel bars in the earth's field with stress, and based on that it explains the appearance of magnetic indication of a local stress concentration zone in the bulk field. The study has also explained the reverse in polarity of the magnetic indication with stress, as well as analysed the effects of measurement distance and the initial magnetic condition. It provides evidence to support solving the inverse problem, in which stress condition is estimated from the remote-sensing magnetic field, and also suggests practical techniques.

Chapter 5 studies the remote-sensing stress-induced magnetic field of steel pipes. The study has extended the understanding of magnetic field of pipelines when measured at a distance. A hypothesis of magnetic features of welding pipe sections together is presented and verified using the experimental, simulation and field observation results. The study proposes a technique to locate the welds, so that it may help to improve the probability of detection of local SCZs.

Based on the understanding of the remote-sensing stress-induced magnetic field, practical techniques to estimate the depth of cover, locate welded joints, and importantly, detect stress concentration zones of underground pipelines using above-ground magnetic surveys have been presented in this study, see Chapter 6. The performance of the techniques has been evaluated using the current standard methods and has shown very promising results that are now being exploited by our commercial sponsor, Speir Hunter.

In terms of scientific publication, this study has contributed to the following publications:

- US/UK Patent Publication No PCT/GB2013/050524, "Fault detection for pipelines"

- US/UK Patent Publication No PCT/GB2013/050526, "Fault detection for pipelines"
- S. Staples, C. Vo, D.M.J Cowell, S. Freear, C. Ives, B. Varcoe, "Solving the inverse problem of magnetisationstress resolution", *Journal of Applied Physics*, 113.13 (1013), 133905.

The following papers are currently undergoing submission and peer review:

- Magnetic indication of stress concentration in ferrous material.
- A preliminary technique to detect stress concentration zones in underground pipelines using above-ground magnetic surveys.
- A new technique to estimate the depth of cover of underground pipelines using the passive magnetic field measured by above-ground surveys.
- A new technique to locate circumferential welded joints of underground pipelines using above-ground magnetic surveys.

Chapter 2

Solving the Model of the Magnetomechanical Effect

This section presents a methodology for solving the magnetomechanical effect. The model of the stress-magnetisation relationship solved is based on the original theories shown by Jiles and Atherton [26], Jiles [29]. This study proposes an additional term similarly derived as in the ferromagnetic hysteresis model to solve for both tension and stress relaxation as it was usually assumed that changes of magnetisation due to unloading stress is negligible [51].

2.1 Solving the model of the ferromagnetic hysteresis

A model of the ferromagnetic hysteresis is needed as it allows determining the initial magnetic condition of the material in an external magnetic field. The theory presented by Jiles and Atherton [26] is used in this study for modelling the hysteresis.

Under the applied field H, the effective field H_e that causes the induced magnetisation in the material is

$$H_e = H + \alpha M, \tag{2.1}$$

where α is a parameter representing coupling between adjacent domains.

2. SOLVING THE MODEL OF THE MAGNETOMECHANICAL EFFECT

The anhysteretic magnetisation M_{an} is given by

$$M_{an} = M_s(\coth\frac{H_e}{a} - \frac{a}{H_e}), \tag{2.2}$$

in which M_s is saturation magnetisation; a is an experimentally determined parameter which characterises the shape of the anhysteretic curve.

When applying the magnetic field, the irreversible magnetisation M_{irr} due to pinning is

$$M_{irr} = M_{an} - \delta k\frac{dM_{irr}}{dH_e}, \tag{2.3}$$

in which the parameter δ takes the value of +1 when $dH/dt > 0$ and -1 when $dH/dt < 0$; and k is a coefficient modifying the shape of the curve.

The reversible magnetisation M_{rev} is a fraction, represented by the coefficient c, of the difference between M_{an} and M_{irr}

$$M_{rev} = c(M_{an} - M_{irr}). \tag{2.4}$$

The magnetisation M is then given by

$$\begin{aligned} M &= M_{rev} + M_{irr} \\ &= (1-c)M_{irr} + cM_{an}. \end{aligned} \tag{2.5}$$

In order to numerically solve for the magnetisation with respect to the applied field H, ordinary differential equations are written as

$$\begin{aligned} \tfrac{dM_{an}}{dH} &= \tfrac{dM_{an}}{dH_e}\tfrac{d(H+\alpha M)}{dH} \\ &= \tfrac{M_s}{a}[1-(\coth\tfrac{H_e}{a})^2 + (\tfrac{a}{H_e})^2](1+\alpha\tfrac{dM}{dH}) \\ &= D(1+\alpha\tfrac{dM}{dH}), \end{aligned} \tag{2.6a}$$

in which D represents $\frac{M_s}{a}[1-(\coth\frac{H_e}{a})^2 + (\frac{a}{H_e})^2]$, and

$$\begin{aligned} \tfrac{dM_{irr}}{dH} &= \tfrac{dM_{irr}}{dH_e}\tfrac{dH_e}{dH} \\ &= \tfrac{M_{an}-M_{irr}}{\delta k}(1+\alpha\tfrac{dM_{irr}}{dH}) \\ &= \tfrac{M_{an}-M}{\delta k(1-c)}(1+\alpha\tfrac{dM_{irr}}{dH}) \\ &= \tfrac{M_{an}-M}{\delta k(1-c)-\alpha(M_{an}-M)}, \end{aligned} \tag{2.6b}$$

therefore, Equ. 2.5 can be rewritten as

$$\begin{aligned} \tfrac{dM}{dH} &= (1-c)\tfrac{dM_{irr}}{dH} + c\tfrac{dM_{an}}{dH} \\ &= (1-c)\tfrac{M_{an}-M}{\delta k(1-c)-\alpha(M_{an}-M)} + cD(1+\alpha\tfrac{dM}{dH}) \\ &= [(1-c)\tfrac{M_{an}-M}{\delta k(1-c)-\alpha(M_{an}-M)} + cD]/\,[1-\alpha cD]. \end{aligned} \tag{2.6c}$$

Fig. 2.1 shows a solution of the induced magnetisation when the applied magnetic field was increased from 0 to 10 kA/m and then changed back and forth between 10 kA/m and -10 kA/m.

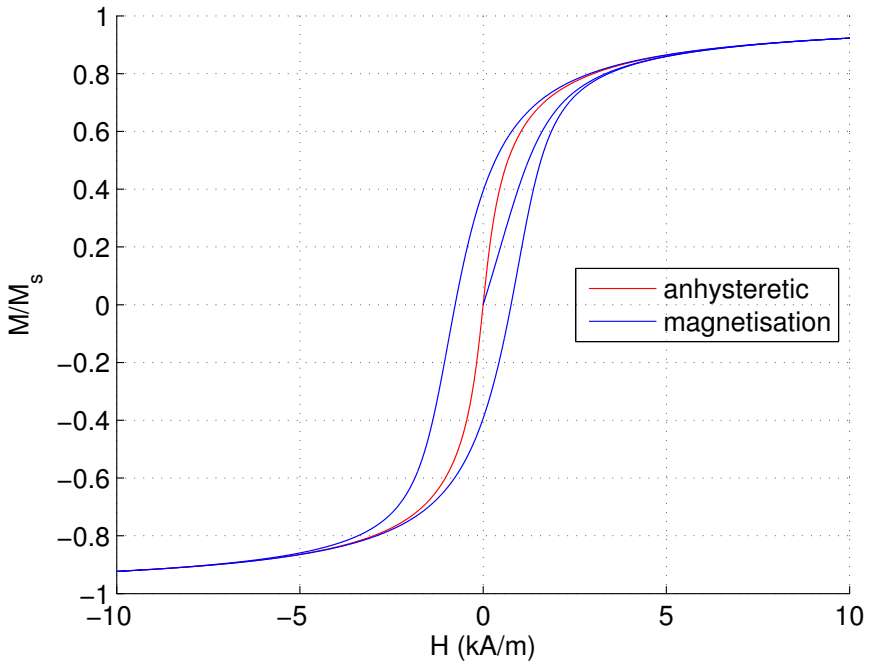

Figure 2.1: The hysteresis loop where $\alpha = 0.001$, $a = 900$ A/m, $c = 0.1$, $k = 2000$ A/m, and $M_s = 1.71 \times 10^6$ A/m.

2.2 Solving the model of the magnetomechanical effect

As presented in the law of approach [29], stress σ can be considered as an additional field H_σ, therefore, the effective field H_e can be written as

$$H_e = H + \alpha M + H_\sigma, \tag{2.7a}$$

in which

$$\begin{aligned} H_\sigma(M,\sigma) &= \tfrac{3}{2}\tfrac{\sigma}{\mu_0}\left(\tfrac{\partial\lambda}{\partial M}\right) \\ &\approx \tfrac{3\sigma}{\mu_0}[(\gamma_{11}+\gamma_{12}\sigma)M + 2(\gamma_{21}+\gamma_{22}\sigma)M^3], \end{aligned} \tag{2.7b}$$

where the magnetostriction λ was approximated using a Taylor series expansion with coefficients γ_{ij} [29].

Derivatives with respect to stress are

$$\frac{\partial H_\sigma}{\partial \sigma} = \frac{3}{\mu_0}(A + B\frac{\partial M}{\partial \sigma}), \tag{2.8a}$$

where

$$\begin{aligned} A &= (\gamma_{11} + 2\gamma_{12}\sigma)M + 2(\gamma_{21} + 2\gamma_{22}\sigma)M^3, \\ B &= \sigma[(\gamma_{11} + \gamma_{12}\sigma) + 6(\gamma_{21} + \gamma_{22}\sigma)M^2], \end{aligned}$$

and therefore,

$$\begin{aligned} \tfrac{\partial H_e}{\partial \sigma} &= \alpha\tfrac{\partial M}{\partial \sigma} + \tfrac{\partial H_\sigma}{\partial \sigma} \\ &= \tfrac{3A}{\mu_0} + (\alpha + \tfrac{3B}{\mu_0})\tfrac{\partial M}{\partial \sigma}. \end{aligned} \tag{2.8b}$$

Under stress, the induced magnetisation M approaches the anhysteretic magnetisation M_{an}, which is also stress dependent and is represented as

$$M_{an} = M_s(\coth\frac{H_e}{a} - \frac{a}{H_e}). \tag{2.9}$$

The irreversible magnetisation M_{irr} is

$$M_{irr} = M_{an} - \frac{\xi E}{\sigma}\frac{\partial M_{irr}}{\partial \sigma}, \tag{2.10}$$

where E is the Young's modulus and ξ is a coefficient with dimensions of energy per unit volume. And the reversible magnetisation is written as

$$M_{rev} = c(M_{an} - M_{irr}). \tag{2.11}$$

Similarly, derivatives of magnetisation can be expressed as

$$\begin{aligned} \tfrac{\partial M_{an}}{\partial \sigma} &= D[\tfrac{3A}{\mu_0} + (\alpha + \tfrac{3B}{\mu_0})\tfrac{\partial M}{\partial \sigma}] \\ &= \tfrac{3AD}{\mu_0} + D(\alpha + \tfrac{3B}{\mu_0})\tfrac{\partial M}{\partial \sigma}, \end{aligned} \tag{2.12a}$$

$$\begin{aligned} \tfrac{\partial M_{irr}}{\partial \sigma} &= \tfrac{\sigma}{\xi E}(M_{an} - M_{irr}) \\ &= \tfrac{\sigma}{\xi E}\tfrac{M_{an} - M}{1-c}, \end{aligned} \tag{2.12b}$$

and from Equ. 2.5,

$$\begin{aligned} \tfrac{\partial M}{\partial \sigma} &= (1-c)\tfrac{\partial M_{irr}}{\partial \sigma} + c\tfrac{\partial M_{an}}{\partial \sigma} \\ &= \tfrac{\sigma}{\xi E}(M_{an} - M) + c(\tfrac{3AD}{\mu_0} + D(\alpha + \tfrac{3B}{\mu_0})\tfrac{\partial M}{\partial \sigma}) \\ &= [\tfrac{\sigma}{\xi E}(M_{an} - M) + c\tfrac{3AD}{\mu_0}]/\,[1 - cD(\alpha + \tfrac{3B}{\mu_0})]. \end{aligned} \tag{2.12c}$$

The above ordinary differential equations can be solved to model changes of magnetisation while stress is increased. However, for stress relaxation, the solution shows no hysteresis for small stress levels while producing negative stress-induced magnetisation for large stress levels, see Fig. 2.2.

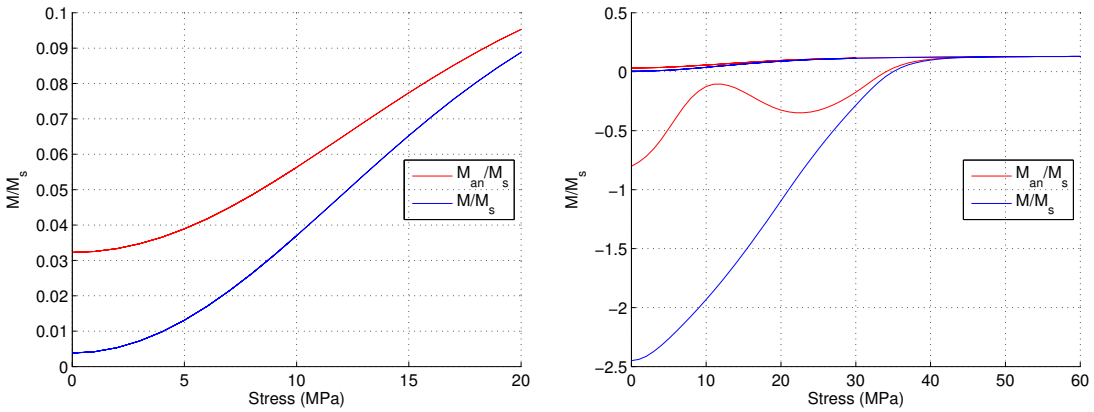

(a) No hysteresis for two cycles of 10 MPa and 20 MPa.

(b) Negative magnetisation for two cycles of 30 MPa and 50 MPa.

Figure 2.2: The stress-induced magnetisation curve where $H = 80\text{A/m}$, $\alpha = 0.001$, $a = 900$ A/m, $c = 0.1$, $k = 2000$ A/m, $M_s = 1.71 \times 10^6$ A/m, $\xi = 605\text{Pa}$, $E = 205 \times 10^9$ Pa, $\gamma_{11} = 2 \times 10^{-18}$ A^{-2}m^2, $\gamma_{12} = -1.5 \times 10^{-26}$ $\text{A}^{-2}\text{m}^2\text{Pa}^{-1}$, $\gamma_{21} = -2 \times 10^{-30}$ A^{-4}m^4, $\gamma_{22} = 5 \times 10^{-39}$ $\text{A}^{-4}\text{m}^4\text{Pa}^{-1}$. The solution of stress relaxation wasn't correct as it showed no hysteresis for small stresses and negative magnetisation for large stresses.

2.2.1 Solving the induced magnetisation for stress relaxation

It can be seen when compared Equ. 2.10 with Equ. 2.3 that the term δ can also be used to reflect stress relaxation. Therefore, Equ. 2.10 can be modified as

$$M_{irr} = M_{an} - \delta \frac{\xi E}{\sigma} \frac{dM_{irr}}{d\sigma}, \tag{2.13}$$

where δ takes the value of +1 when $d\sigma/dt > 0$ and -1 when $d\sigma/dt < 0$. And the derivative of the stress-induced magnetisation can be rewritten as

$$\frac{\partial M}{\partial \sigma} = [\delta \frac{\sigma}{\xi E}(M_{an} - M) + c\frac{3AD}{\mu_0}] / [1 - cD(\alpha + \frac{3B}{\mu_0})] \tag{2.14}$$

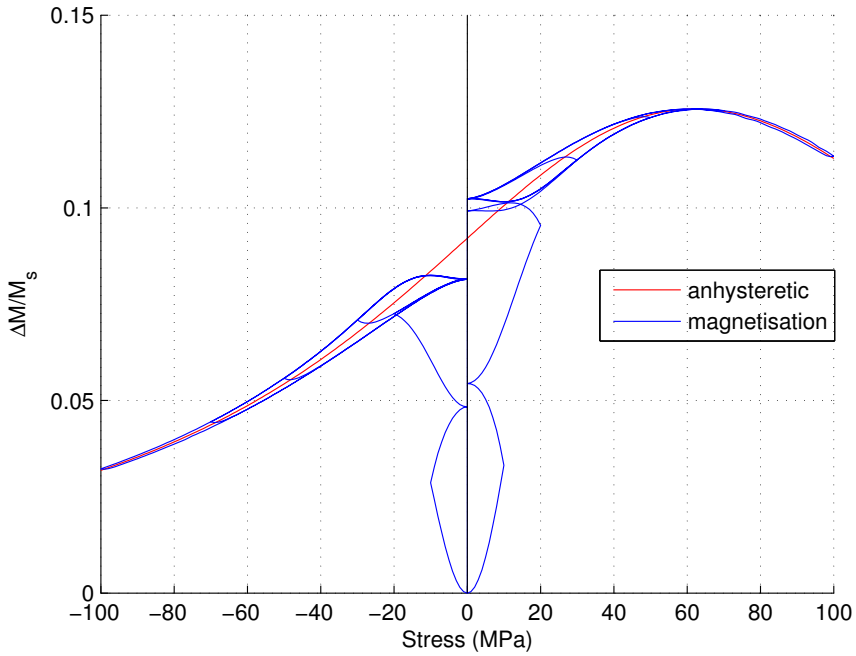

Figure 2.3: Changes of magnetisation with respect to stress using the modified equations of the irreversible magnetisation. Tensile and compressive stress cycles of 10 MPa to 100 MPa were applied. The equations used the same set of parameters shown in Fig. 2.2.

Fig. 2.3 shows the induced magnetisation with cycles of tensile and compressive stress of 10 MPa to 100 MPa solved by using the modified equations with the same values of the model parameters used in Fig. 2.2. The magnetisation was changed with stress and stress cycles. Largest irreversible changes of magnetisation occurred with the first one or two cycles, i.e. 10 MPa or 20 MPa. Successive cycles, i.e. 30 MPa to 100 MPa, added smaller irreversible magnetisation. Besides, the magnetisation tends to approach the stress-dependent anhysteretic magnetisation as suggested by the Jiles-Atherton model.

2.3 Conclusions

This chapter presented the differential equations based on the original theory proposed by Jiles and Atherton [26], Jiles [29] to model the magnetomechanical effect.

The model of the ferromagnetic hysteresis was solved first. It has been used to determined the initial magnetic condition of a ferrous material placed in an external field, for example the earth's field, before applying stress.

Solving the original differential equations of the Jiles-Atherton model resulted in no irreversible magnetisation at small stresses and negative magnetisation at large stresses for stress relaxation. Therefore, an additional term has been introduced so that the induced magnetisation can be solved for both of loading and unloading stress. These underlying equations have been employed to simulate the effect of stress to magnetic field of steel structures.

This model has a limitation as it didn't take into account the effect of magnetocrystalline anisotropy in a material or the minor loops.

Chapter 3

Methodology of the Development of Stress Concentration Tomography

3.1 Introduction

This chapter presents the methodology used to study the remote-sensing stress-induced magnetic field of ferrous material. The chapter also serves as a description of the experimental, field observation, and field survey methods.

Generally, this study is comprised of:

1. Small-scale laboratory experiments on steel bars and 6-inch steel pipes.
2. Large-scale field observations of 18-inch to 30-inch live above-ground high-pressure gas pipelines.
3. Theoretical background and model development.
4. Signal processing techniques.
5. Field trials on live underground gas pipelines.

Three different measurement systems built and used in this study were:

1. A stationary Computer Numerical Control (CNC)-based measurement system for laboratory experiments on steel bars.

2. A mobile CNC-based measurement system for laboratory experiments on steel pipes and large-scaled field observations.

3. A portable UNISCAN instrument for field surveys.

3.2 Methodology

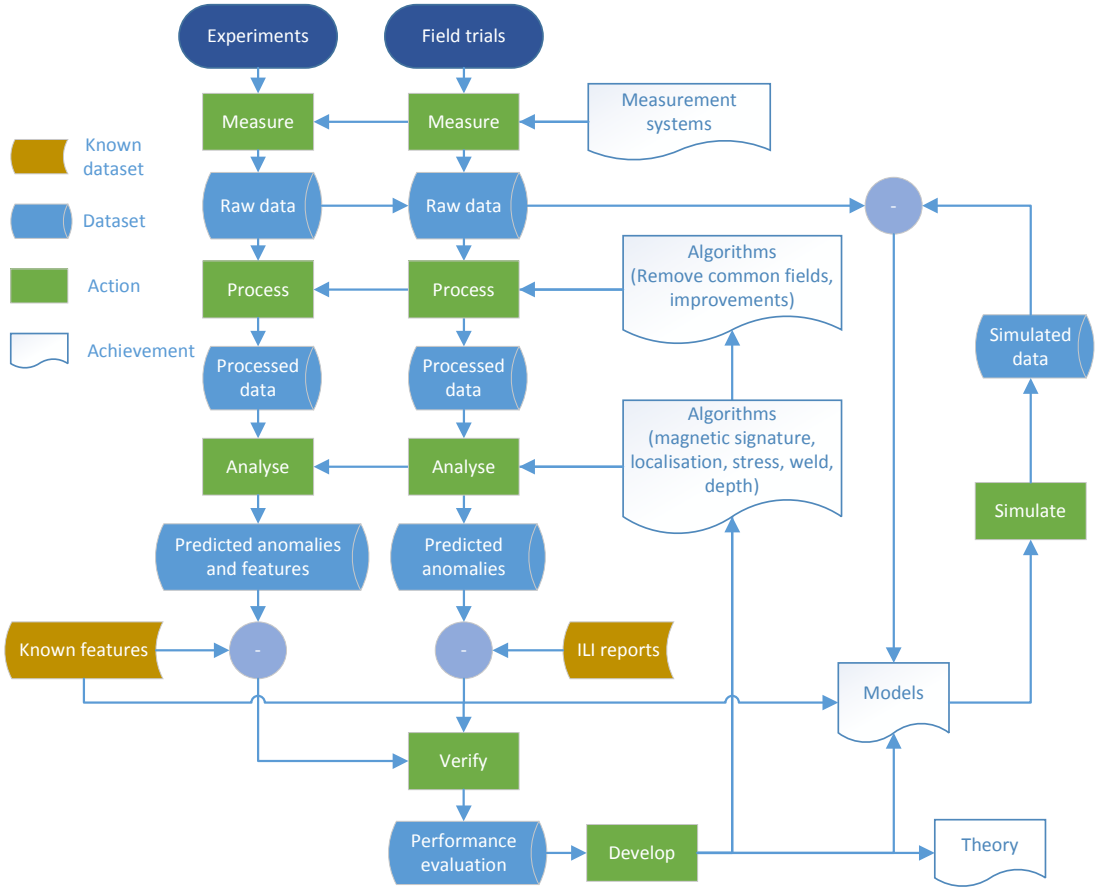

Figure 3.1: The path of SCT development.

Fig. 3.1 shows the methodology to develop the Stress Concentration Tomography technology (SCT). First, experiments, field observations and field surveys were performed to collect magnetic field in both controlled and uncontrolled environments.

For the laboratory experiments, the stress-induced magnetic field was studied not only on steel bars, in which stress was in the axial direction, but also on 6-inch steel pipes which had complex stress distribution, see Section 3.4 and 3.5.

For the field observations, magnetic field was measured on live above-ground high pressure gas pipelines at an unmanned site at Pannal (North Yorkshire, England). These live field measurements allowed a level of control not obtainable for underground pipelines. Features of the pipelines, for example bends or welds, were known and measurable; measurement planes were in control, for example the measurement distance, see Section 3.6. However, information concerning the background field, which should have been measured without the pipe, and the pipe magnetic history before pressurisation, or variation of the magnetic field with the pressure could not be obtained.

Further field surveys were conducted on live underground high pressure gas pipelines around Pannal. Predicted features were reported and verified against standard reports, such as ILI or through excavation if possible. It should be noted that because different positioning techniques were used by ILI and SCT to locate the pipeline and its features, there was an uncertainty when directly comparing their predicted features, see Section 3.7.

In addition to the experiments and field surveys, simulation models were also developed to predict features of the stress-induced magnetic field, see chapters 4 and 5. The experimental and field observation results were used to verify the models. However, because of its limitations, the models can only be used to qualitatively compare to the measurements.

Finally, techniques to process and analyse the data, and predict pipeline features were developed and verified by the field survey data. It provided a feedback loop to verify the hypotheses and improve the models, see Chapter 6.

3.2.1 Summary of the experiments, field observations and field surveys

Table 3.1 shows a summary of the experiments, field observations and field surveys. It also shows the sample and the measurement system used in each case.

Description	Sample	Measurement system
Small-scale laboratory experiments, see Sec. 3.4	Steel bars	Stationary, see Sec. 3.3.1
Small-scale laboratory experiments, see Sec. 3.5	6-inch steel pipes	Mobile, see Sec. 3.3.2
Large-scale field observations, see Sec. 3.6	30-inch above-ground gas pipeline	Mobile, see Sec. 3.3.2
Field surveys, see Sec. 3.7	Live underground gas pipelines	UNISCAN instrument, see Sec. 3.3.3

Table 3.1: Summary of experiments and field trials

In small-scale laboratory experiments, samples, i.e. steel bars and 6-inch steel pipes, were subjected to stress and stress cycles. The measurements were performed at a high resolution using a CNC-based measurement system which offered a high-accuracy positioning. It allowed building a 3D map of magnetic field surrounding the samples. Measurements of magnetic field included the background field, the initial magnetic field, which was measured before applying stress, and the stress-induced magnetic field, which was measured after the sample had been stressed.

In large-scale field observations, the surveyed pipelines included 18-inch to 30-inch above-ground live pipelines at Pannal. Magnetic field data was measured using a mobile CNC-based system. By integrating a high accuracy Global Navigation Satellite System (GNSS), up to 15 mm accuracy, this system allowed mapping the magnetic field of the pipelines on horizontal planes at different heights. It was impossible to alter the applied pressure because the pipeline was in operation. Furthermore, measurements of the background field and the initial magnetic field could not be performed.

Field surveys were conducted on underground gas pipelines using a portable UNISCAN instrument developed at Leeds for research and for industrial use. The integrated GNSS system allowed accurately recording the pipeline route, which

had been tracked and marked by an industrial pipe locator (RD8000). The depth of cover of the underground pipelines is usually unknown, however, during these field surveys, the depth was measured using the RD8000. This data was used to verify the depth estimation technique, see Chapter 6.

3.3 The measurement systems

This section describes three following measurement systems:

1. A stationary CNC-based measurement system used in the laboratory.
2. A mobile CNC-based measurement system used for both laboratory experiments and field observations.
3. A portable UNISCAN instrument developed for field surveys.

3.3.1 The stationary CNC-based measurement system

In order to accurately control measurement points, a CNC-based measurement system was built in the laboratory, see Fig. 3.2. The system included a 3-axis CNC machine on which two 3-axis magnetometers were mounted. The rig was built using aluminium profiles so that it did not interfere with the measured magnetic field.

The CNC machine included 24 V, 2.8 A Nanotec stepper motors for x and y axes, and a 24 V, 4.8 A Nanotec stepper motor for z axis. Motors were driven by Parker ViX250IM and ViX500IM microsteppers, see Fig. 3.3a. Axes were built from Igus linear bearings and rail system. The resolution of the CNC machine was 0.033 mm.

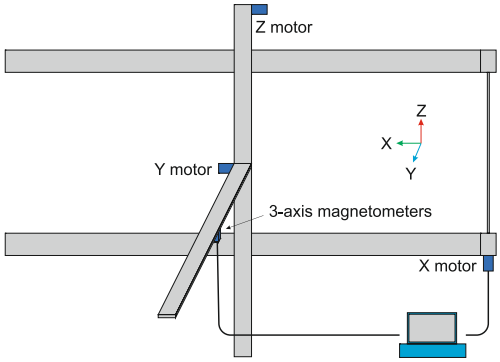

(a) Diagram of the system

(b) The stationary system

Figure 3.2: The measurement system included a 3-axis CNC machine, two 3-axis magnetometers and a software developed in Matlab to control the machine and measure the magnetic field.

(a) Motors and drives

(b) Bartington magnetometer

Figure 3.3: Parts used in the measurement system.

Two fluxgate magnetometers were used to measure the magnetic field, see Fig. 3.3b. The first one was a Freescale Mag3110 magnetometer, which had a full range of ± 1000 μT and a resolution of 1 μT. It was used to measure in near field region, which was close to the surface of the samples. The second one, a Bartington low power three-axis magnetic field sensor Mag649 [52], which had a resolution of 0.1 μT and a full range of ± 100 μT was used to measure the magnetic field in far field region.

A program to control the mechanical system and record the measurement data was developed in Matlab (MathWorks Inc., Natick, MA, USA), see Fig. 3.4. The coordinate of measurement positions, including x, y, and z, can be loaded into the program as a text file.

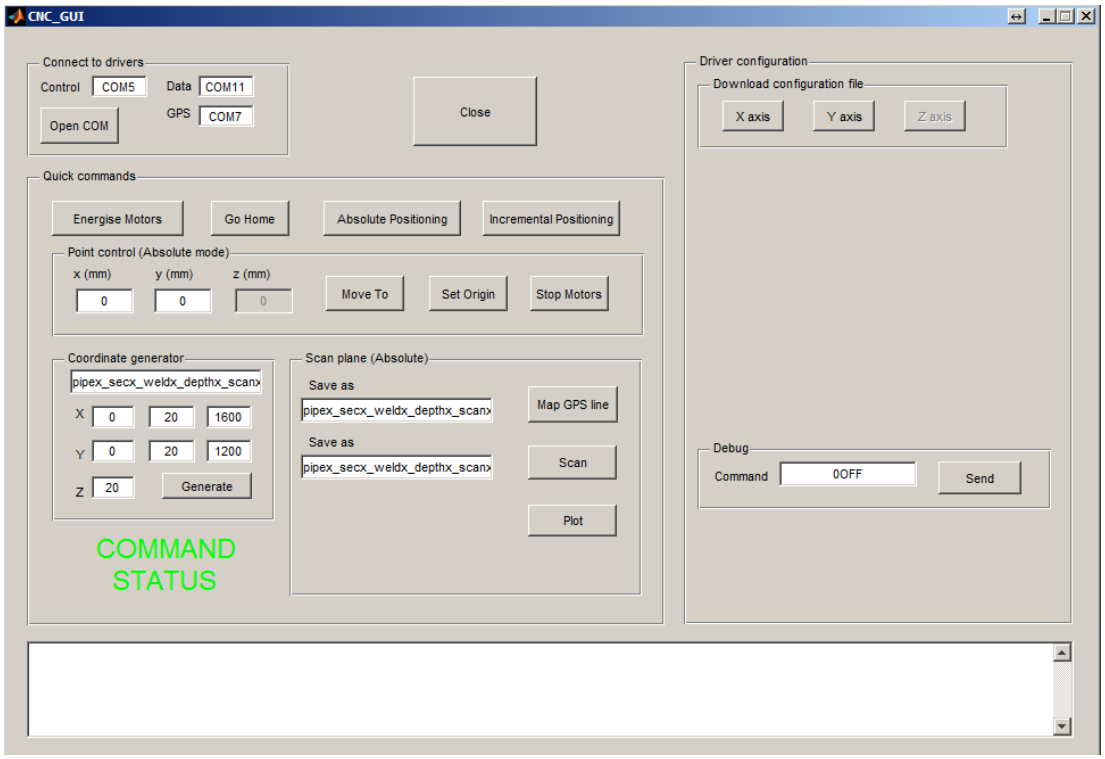

Figure 3.4: The program to control the measurement system.

3.3.2 The mobile CNC-based measurement system

Another CNC-based measurement system was built for the laboratory experiments on steel pipes and field observations on above-ground live pipelines. Because the site was unmanned and the pipelines were in operational conditions, a permanent and fixed CNC system as the one used in the laboratory was not suitable. For this reason, a mobile CNC-based measurement system was developed.

The system was custom built to be able to load onto a van, carry to the site, quickly assemble and measure magnetic field in three dimensions, and then disassemble at the end of the working day. It was designed to be able to work outdoor.

Fig. 3.5 shows the design of the mobile system and Fig. 3.6 shows the deployment of the system at the Pannal site. Instead of a 3-axis CNC machine as it was in the laboratory, the mobile system included an XY table and a lift, ST-25 Genie Super Tower, to manually control the measurement height above the pipes, which was similar to the z axis in the laboratory.

A Bartington magnetometer Mag649 was mounted on the Y arm, away from the lift to reduce magnetic interference. The controller of this system also used Nanotec stepper motors and Parker drivers.

One of the issues of the field observations was that it required a technique to manage measurement points relative to the pipeline because it was impossible to set up this mobile system at the exact location everyday in the field observations. So, in order to resolve the issue, position of the measurement plane were managed by using a high accuracy positioning system from Topcon. The system used two GR-5 receivers, which was set as a base station and a rover in Real Time Kinematic mode (RTK). When the base station was deployed at a fix location, position of the rover could be localised at an accuracy of up to 15 mm. This function was used to build a map of the pipeline and its measurement planes. Use of the GNSS system will be described in Section 3.6.2.2.

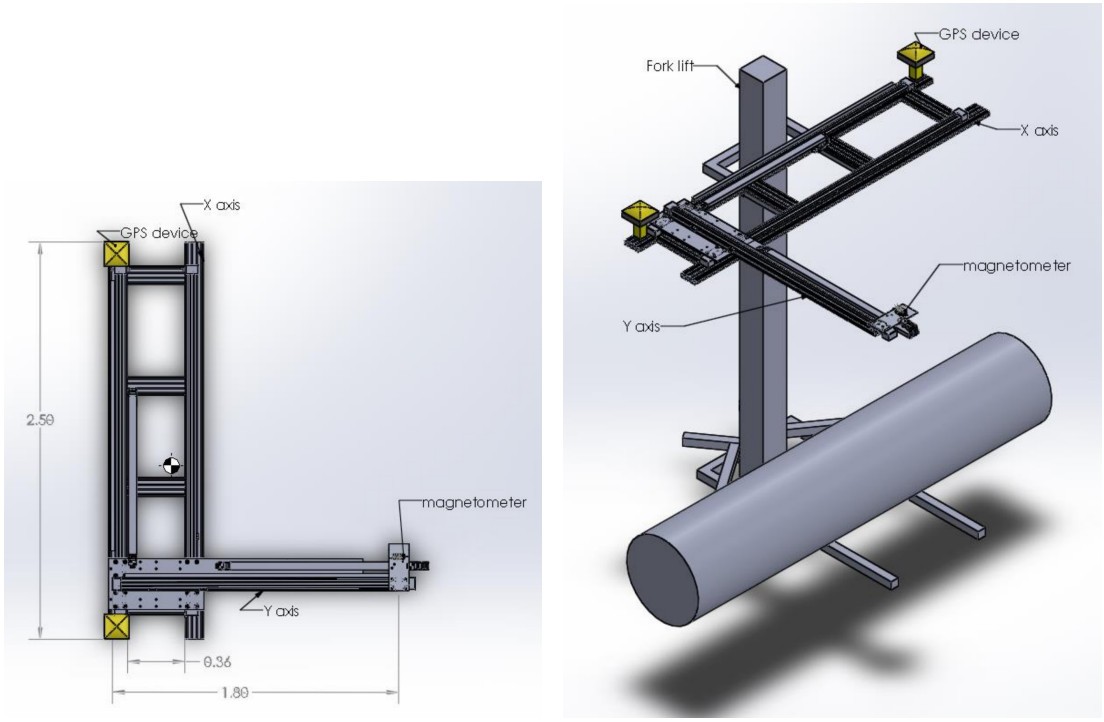

(a) Design of the XY table.

(b) The XY table on the lift.

Figure 3.5: Design of the mobile system.

Figure 3.6: The mobile CNC measurement system deployed at the Pannal site.

Although the controller and data recorder of the mobile CNC system was similar to the system used in the laboratory, measurements performed by the mobile system had limitations including:

- Accuracy of positioning depends on the GNSS receivers.
- The measured magnetic field could be affected by the lift and other constructed objects on site.

In order to resolve these limitations, spatial resolution of the measurement plane was reduced when compared to that in the laboratory. This was still acceptable because dimensions of the pipe on site were much larger compared to the samples in the laboratory. Additionally, measurements of the background field with and without the lift were performed. This allowed considering magnetic effect of the lift and the array.

3.3.3 The portable UNISCAN instrument

This portable instrument constitutes the UNISCAN Tools, which has been developed at Leeds for non-invasive magnetic inspection of underground pipelines. The UNISCAN Tools included a patented portable UNISCAN instrument and patented UNISCAN software, in which the UNISCAN instrument was used for field surveys. Since 2012, this system has been used by our commercial research sponsor Speir Hunter to record and analyse magnetic field of underground gas pipelines all over the world including UK, France, Germany, Canada, Oman, and China, see Fig. 3.7.

Figure 3.7: The UNISCAN instrument in use.

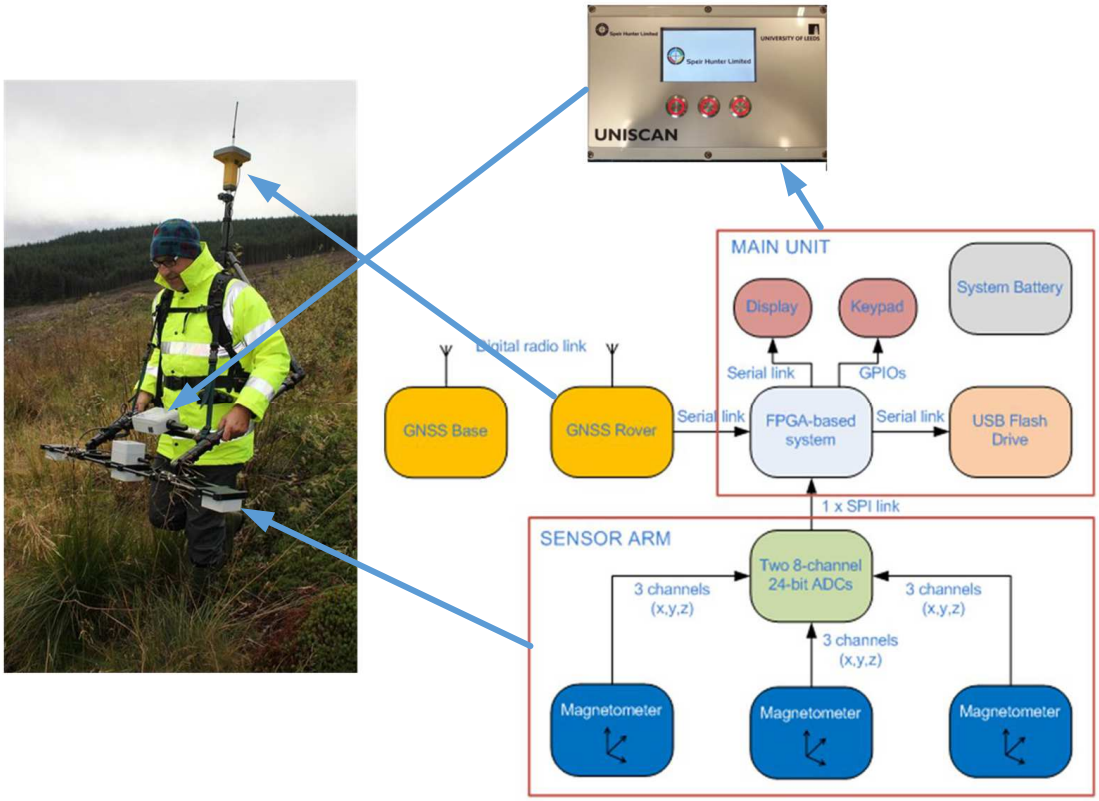

Figure 3.8: Design of the UNISCAN instrument.

Fig. 3.8 shows the diagram of the UNISCAN instrument. It includes a FPGA-based main unit, an array of three 3-axis magnetometers and a high accuracy GNSS system of two RG-5 receivers configuring in RTK mode [53]. The main unit consists of the display and the keypad, which allows the surveyor to operate the instrument. The embedded system in the FPGA chip receives the magnetic data from the magnetometer array and writes the data to a Flash drive attached to the main unit, together with the GNSS coordinates received from the rover.

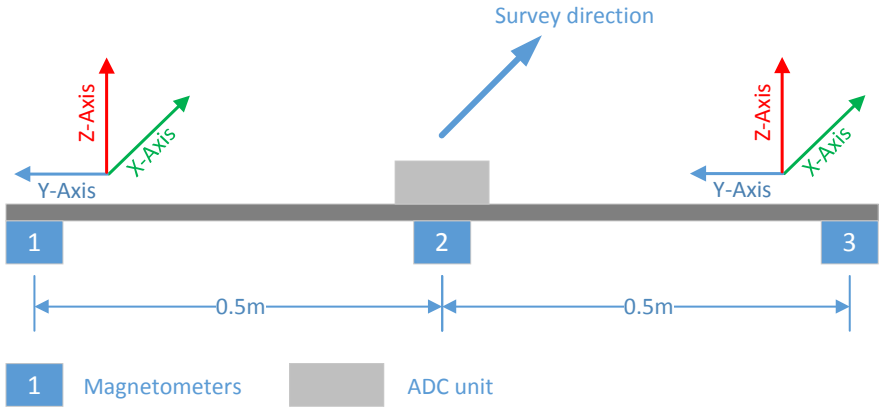

Figure 3.9: The magnetometer array.

Fig. 3.9 shows the design of the magnetometer array. Three magnetometers are arranged on a horizontal line at 0.5 m separation. Each of them is a 3-axis flux gate magnetometer similar to the one used in the laboratory experiments and field observations. When walking along the pipeline route, it would be ideal if the surveyor could keep magnetometer No. 2 on the centre line, and magnetometers 1 and 3 are on the left and right side of the pipe. However, this is impossible in practice because of the accuracy of the pipe locator and human factors. For example, for the field surveys in this study, the centre of the pipe located using the RD8000 instrument (made by SPX) could have the offset of 20 cm for the 48-inch pipeline. The coordinate system is also shown in the figure. The x axis is the walking direction, y is towards magnetometer 1 and z is vertical to the pipeline.

Data recorded by the instrument was then imported and analysed by the UNISCAN software implementing SCT techniques. The software reports location

and features of magnetic anomalies, which were then ready to issue to pipeline operators. Based on the reports and use of the high accuracy GNSS system, features predicted by the UNISCAN software could be quickly located within a small spatial error if required.

3.4 Small-scale laboratory experiment on steel bars

3.4.1 Introduction

This section describes a series of laboratory experiments on steel bars. This was to study the relationship between stress and the stress-induced magnetic field in both near-field and far-field regions.

The bars were chosen in order to simplify the stress distribution as it was directed along the length of the bar. For this reason, it was possible to study the stress-induced magnetic field caused by only one component of stress instead of a stress tensor.

The section presents the experimental method including geometry and material of the steel bars, applying stress cycles, measurement planes and measurement procedure in order to have the stress-induced magnetic field of the bars. It then shows some measurement results mainly to provide an idea of what being measured while the main results will be discussed in Chapter 4.

3.4.2 Experimental method

3.4.2.1 Steel bars

Samples of 1045 grade carbon steel, a typical grade of pipeline steel, used in the experiment are shown in Fig. 3.10, see Table 3.2 and Table 3.3 for chemical and mechanical properties of the material.

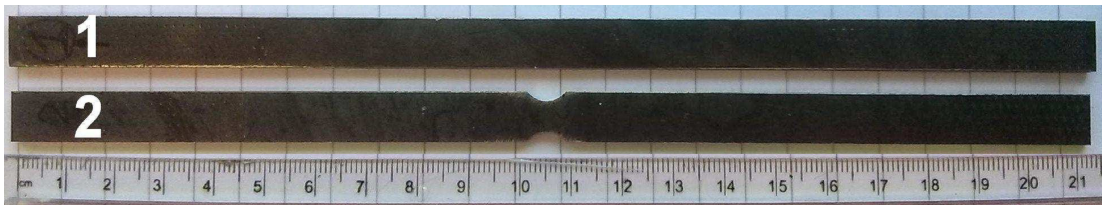

Figure 3.10: Steel samples used in the experiment. The stressed section was from 45 mm to 165 mm.

Element	Carbon (C)	Iron (Fe)	Manganese (Mn)	Phosphorous (P)	Sulphur (S)
Content (%)	0.420 - 0.50	98.51 - 98.98	0.60 - 0.90	≤ 0.040	≤ 0.050

Table 3.2: Chemical properties of steel specimens

Tensile strength (MPa)	Yield point (MPa)
570	295

Table 3.3: Mechanical properties of steel specimens

The respective dimensions of the samples were L200 mm × W10 mm × H3 mm. Sample 1 was a plain bar while sample 2 had a defect causing stress concentration zones (SCZ). The geometry of this defect is shown in Fig. 3.11. An issue of using this shape was that the area where stress applied required to priorly mark on the sample.

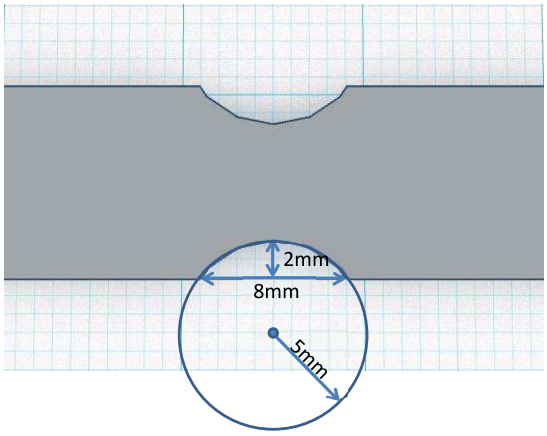

Figure 3.11: Dimensions of the defect.

3.4.2.2 Applying stress

The samples were subjected to stress using a RDP Howden tensile stress testing machine and were always kept in the elastic stage, see Fig. 3.12.

Fig. 3.13 shows the applied force and its equivalent stress cycle. During a cycle, the force was increased to maximum level, held for 10 s and then relaxed, see Table B.1 in Appendix B for a summary of stress cycles and measurements performed in the laboratory. Stress was estimated from the force using the cross-sectional area of the sample. It was also simulated using the finite element model.

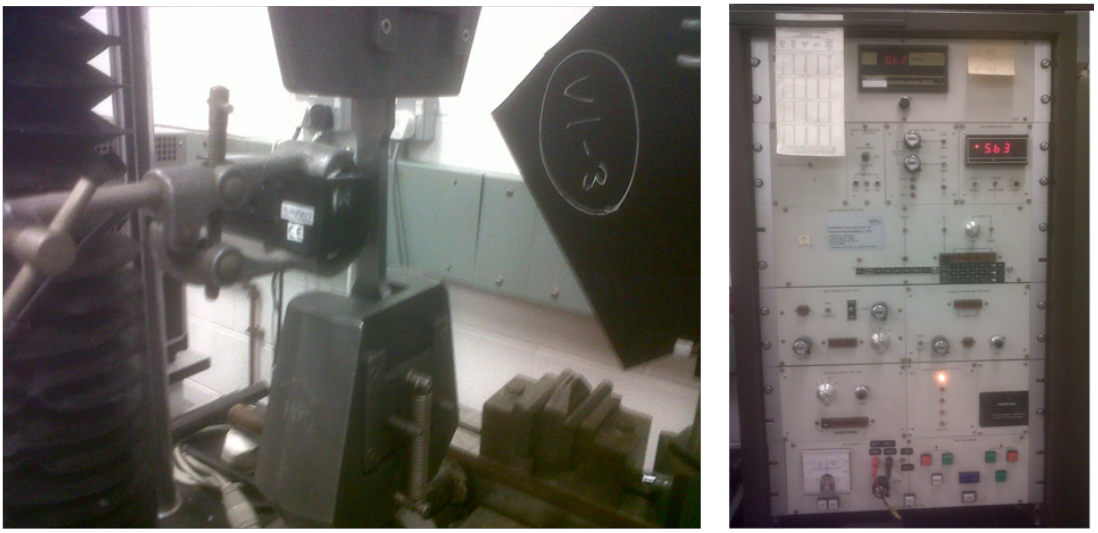

Figure 3.12: The Howden stress testing machine.

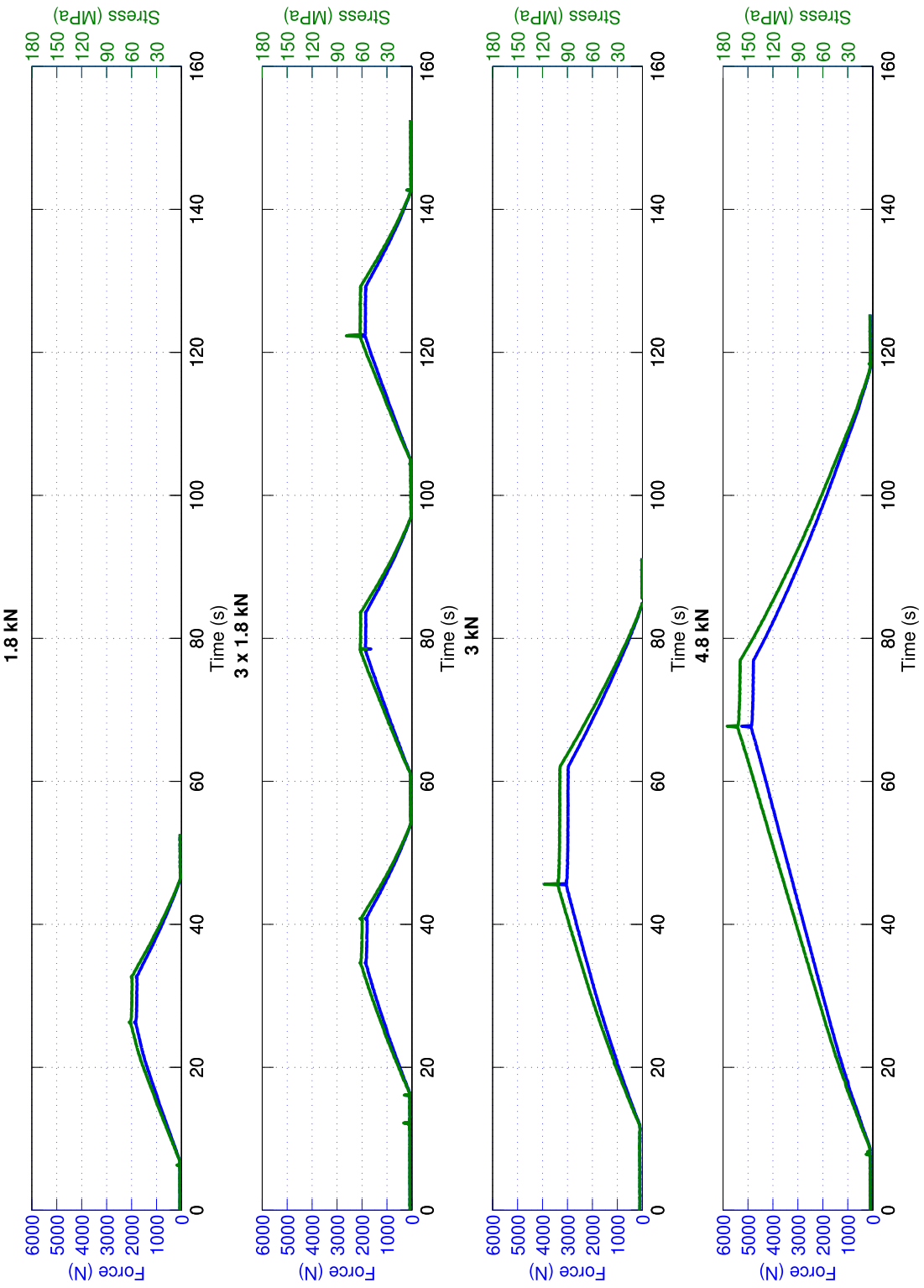

Figure 3.13: Typical force cycles applied to the samples in the experiment.

3.4.2.3 Measurement planes

Fig. 3.14 outlines a sample, measurement planes and a corresponding coordinate system. Magnetic field was measured on horizontal xy planes above the sample, denoted P_d or PF_d when focused on the defect area.

The sample was placed at the centre of the xy plane P_d of L250 mm × W40 mm. When viewing along the x axis, the sample was from 25 mm to 225 mm, the two clamping positions for applying stress were at 65 mm and 185 mm. Finer-spatial resolution planes PF_d, which focused on the defect area, were from 100 mm to 150 mm in x axis and from 10 mm to 30 mm in y axis. Distance d between the measurement plane P_d or PF_d and the top surface of the sample was between 3 mm and 30 mm in z axis.

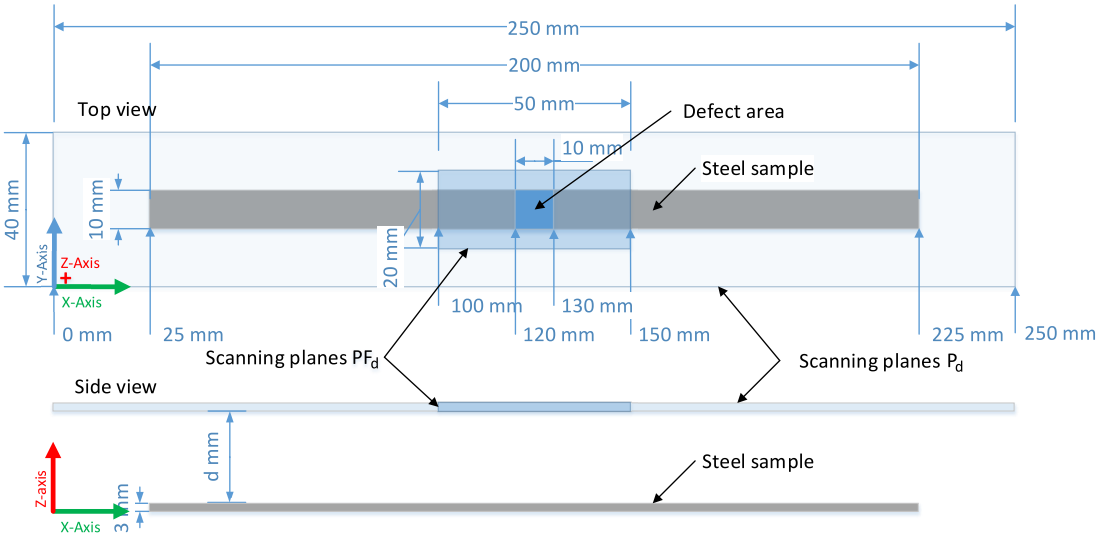

Figure 3.14: The steel sample was placed at the centre of L250 mm × W40 mm measurement planes P_d. Finer-resolution measurement planes PF_d focusing on the defect area was from 100 mm to 150 mm in x axis.

3.4.2.4 Measurement procedure

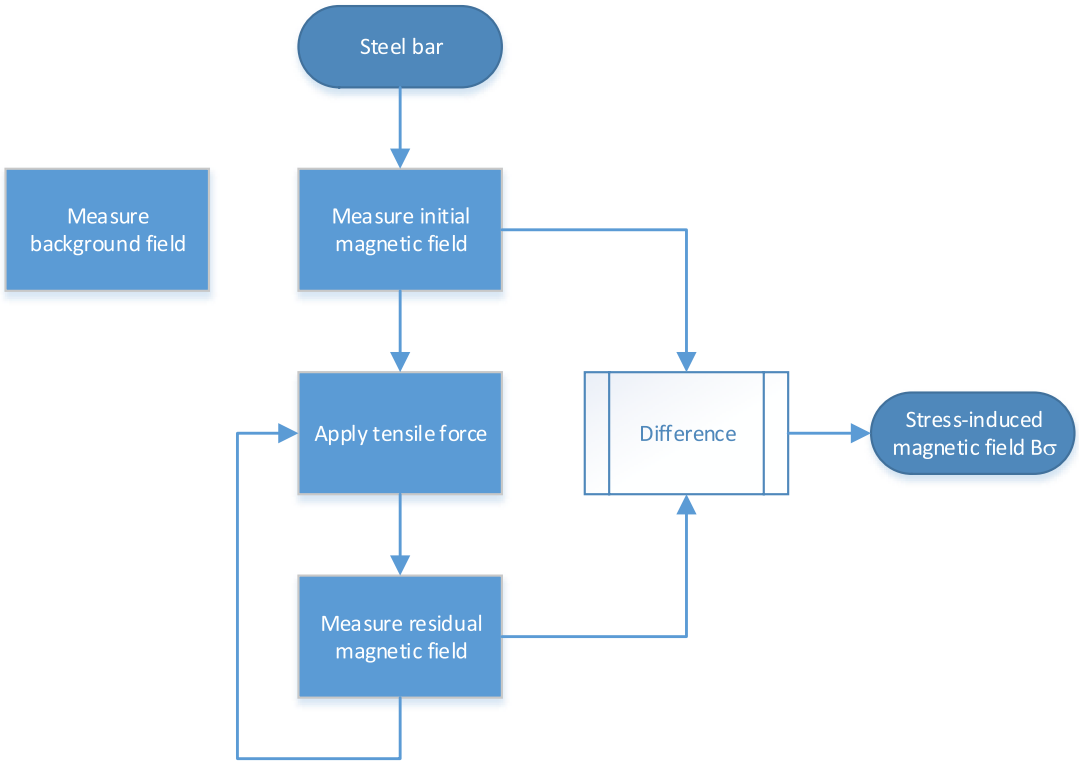

Figure 3.15: Measurement procedure for each steel bar.

First, the background field $\mathbf{B}_{bkg}$ without the steel bars was measured. It was repeated after a few days to update variations. The reason of doing this was because subtracting this from the field measured with the sample would give the magnetic field induced from the sample itself.

As shown in Fig. 3.15, in order to measure the stress-induced magnetic field of the samples, $\mathbf{B}_{\sigma}$, the following steps were performed for each sample:

Step 1 Measure the initial magnetic field $\mathbf{B}_i$. This is the magnetic field of the sample before being subjected to stress.

Step 2 Apply the tensile force to the sample using the tensile stress machine, held for 10 seconds and removed the force. The sample was then taken from the stress machine.

Step 3 Measure the residual magnetic field $\mathbf{B}_r$. This is the magnetic field after the sample was taken from the stress machine, placed on a wooden platform and measured using the measurement system.

Step 4 Repeat step 2 and 3 for different maximum force levels.

The magnetic field induced by the sample would be calculated as

$$\mathbf{B}_{sample} = \mathbf{B}_r - \mathbf{B}_{bkg}, \tag{3.1}$$

and the stress-induced magnetic field would be

$$\mathbf{B}_\sigma = \mathbf{B}_r|_\sigma - \mathbf{B}_i. \tag{3.2}$$

Measurements of the stress-induced magnetic field were also performed at different heights, in z axis, starting from 3 mm. This was to collect magnetic field in both near-field and far-field regions.

3.4.3 Demonstration of the measured magnetic field

In this section, magnetic field in the x and y axes, respectively denoted B_x and B_y, were two horizontal components, in which B_x is pointing along the length of the sample; B_z is the vertical component, see Fig. 3.14 or Fig. 3.16b.

3.4.3.1 The background magnetic field $\mathbf{B}_{bkg}$

A measurement was conducted to record the magnetic field of the working environment, called the background field $\mathbf{B}_{bkg}$. This field was measured without the sample. Subtracting it from the field measured with the sample would give the magnetic field induced from the sample itself.

The average value of the background field was $(-8, -7, -51)$ μT in the working environment, see Fig. 3.16a. It was mainly due to the earth's magnetic field. Variation of components of the background field was less than 1 μT on the working planes.

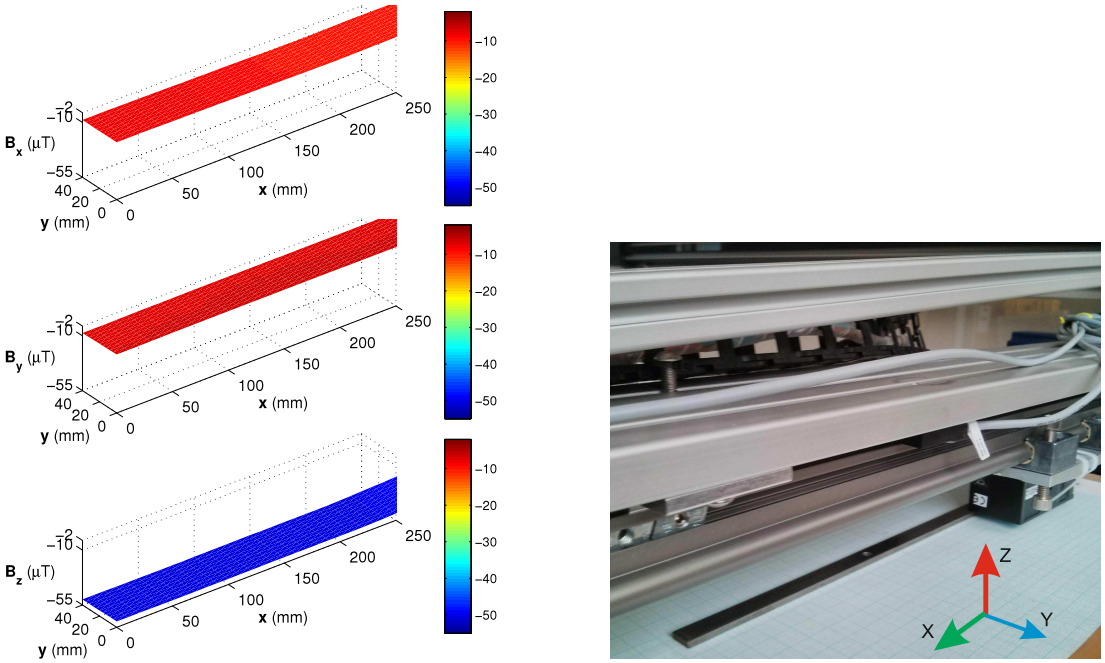

(a) The background magnetic field

(b) The associated coordinate system

Figure 3.16: The background magnetic field $\mathbf{B}_{bkg}$ in the laboratory and the associated coordinate system.

3.4.3.2 The initial magnetic field $\mathbf{B}_i$

The initial magnetic field of a sample $\mathbf{B}_i$ is measured before the sample was subjected to stress. It was useful because a comparison of the magnetic field measured before and after subjecting the sample to stress would allow the study on the effect of stress to the magnetic field of that sample.

Fig. 3.17a and Fig. 3.18a show the initial magnetic field of the samples used in the experiment. It was measured on P_{17mm}, which was the horizontal plane measured at 17 mm from the top surface of the sample.

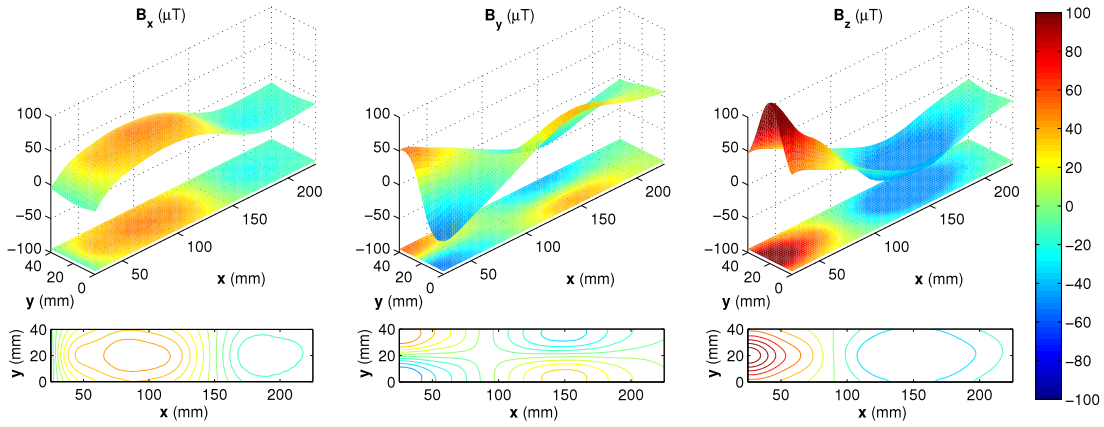

(a) The initial field.

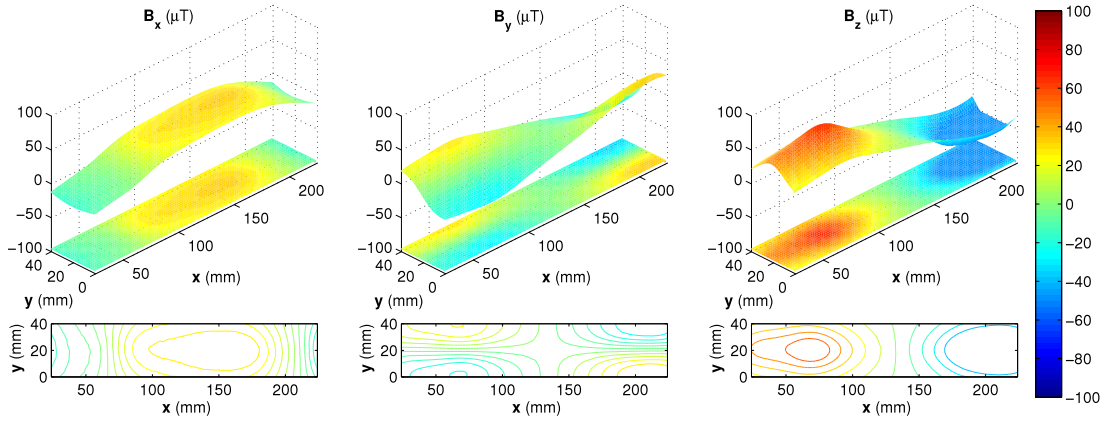

(b) The field after 3 kN.

Figure 3.17: The magnetic field of sample 1 before and after applying stress when measured on the horizontal plane P_{17mm}.

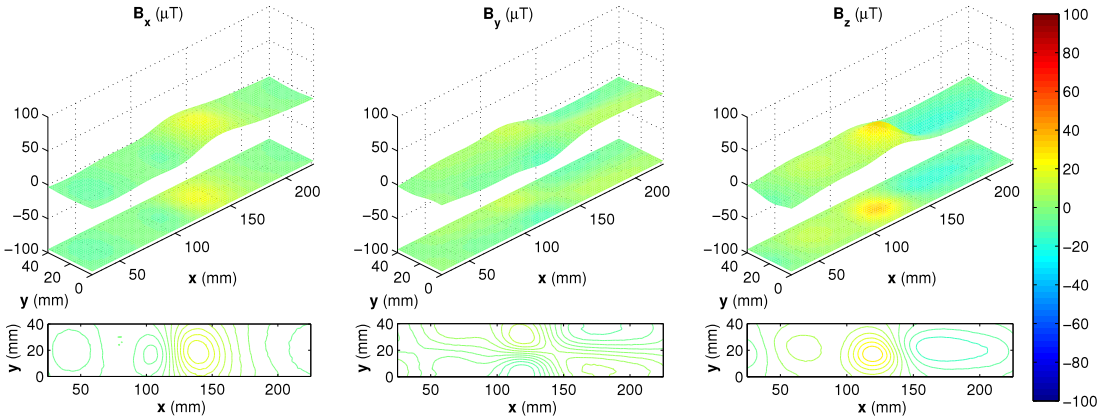

(a) The initial field.

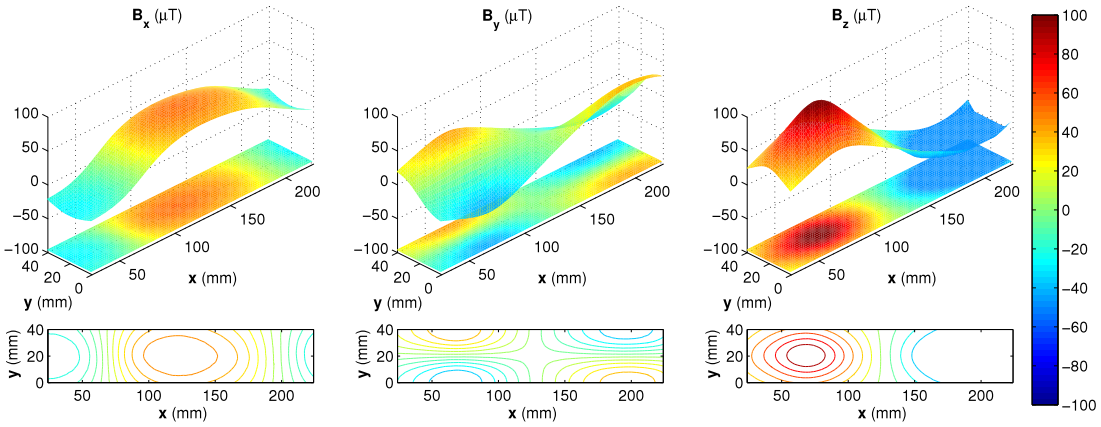

(b) The field after 3 kN.

Figure 3.18: The magnetic field of sample 2 before and after applying stress when measured on the horizontal plane P_{17mm}.

In can be seen that although cut from the same steel plate in the same direction, the initial magnetic field of the samples had an arbitrary distribution.

3.4.3.3 The residual stress-induced magnetic field $\mathbf{B}_r$

The residual stress-induced magnetic field $\mathbf{B}_r$ is measured after the sample was subjected to stress, see Fig. 3.17b and Fig. 3.18b. Although the initial magnetic field of the samples was different, in the figure, the magnetic field of the samples measured after the sample had been stressed showed similar shapes with different magnitudes. It should be noted that the background field was already removed.

The results shown here are for demonstration purpose only. The main results will be discussed in Chapter 4 to support model development and verification.

3.5 Small-scale laboratory experiment on steel pipes

3.5.1 Introduction

This section presents the experiments in the laboratory to study the stress-induced magnetic field of 6-inch steel pipes while the pipe was being pressurised. In addition to plain pipes, pipes with a circumferential welded joint were also used to study the effect of welding on the stress-induced field.

In the experiment, the pipe was filled with water and then pressurised up to 60 bar using a pressure tester and valves. This pressure was chosen as it is similar to those found on the National Grid high pressure gas distribution network. Magnetic field was measured on horizontal planes, from 100 mm to 1500 mm above the pipe to study its variation with the measurement distance.

Using the mobile CNC-based measurement system, while the magnetometer was controlled by the CNC machine on horizontal planes, xy planes, the height, z axis, was manually controlled by the lift, see Section 3.3.2.

This section presents the experimental method including dimensions and material of the pipes, then it describes measurement planes as well as measurement procedure. Finally, some example results are presented in order to give an idea

of the measured magnetic field. Detailed results and analysis will be discussed in Chapter 5.

3.5.2 Experimental method

3.5.2.1 Steel pipes

(a) Four 6-inch test pipes.

(b) Pipe with a welded joint.

Figure 3.19: 6-inch test pipes with and without welds.

Four 6-feet (1.83 m) pipes of X42 material, 6-inch (168.3 mm) nominal diameter, 0.213-inch (5.4 mm) wall thickness, had been manufactured and tested by our collaborator DNV/GL to be safely pressurised up to 60 bar, see Fig. 3.19. Two pipes were plain pipes while the other two pipes had a circumferential weld added offsetting from the centre of the pipe length, which was to avoid the end effect of the pipe. Each pipe had two welded-dome ends and two vents at one end for pressurising and draining arrangements. Chemical and mechanical properties of the material are shown in Table. 3.4 and Table. 3.5.

Element	C	Si	Mn	P	S
Content (%)	≤ 0.17	≤ 0.40	≤ 1.2	≤ 0.025	≤ 0.02

Table 3.4: Chemical properties of steel pipes

Tensile strength (MPa)	Yield point (MPa)
466	293

Table 3.5: Mechanical properties of steel pipes

3.5.2.2 Applying stress

In order to apply stress onto the pipe wall, the pipe was filled with water and pressurised using a pressure tester, see Fig. 3.20. The pressure was held at a constant level during a measurement of magnetic field.

Figure 3.20: Pipe with valves and the pressure tester.

Hoop stress can be estimated from the internal pressure using the equation of thin-wall pressure vessel:

$$\sigma = \frac{Pr}{t}, \tag{3.3}$$

where P is the internal pressure, r is pipe's mean radius and t is its wall thickness.

Table 3.6 shows pressures and the equivalent hoop stress calculated for 6-inch pipes in the experiment.

Pressure (bar)	10	20	30	40	50	60
Hoop stress (MPa)	15.6	31.2	46.8	62.3	77.9	93.5

Table 3.6: Pressure and its equivalent hoop stress for 6-inch pipes.

3.5.2.3 Measurement planes

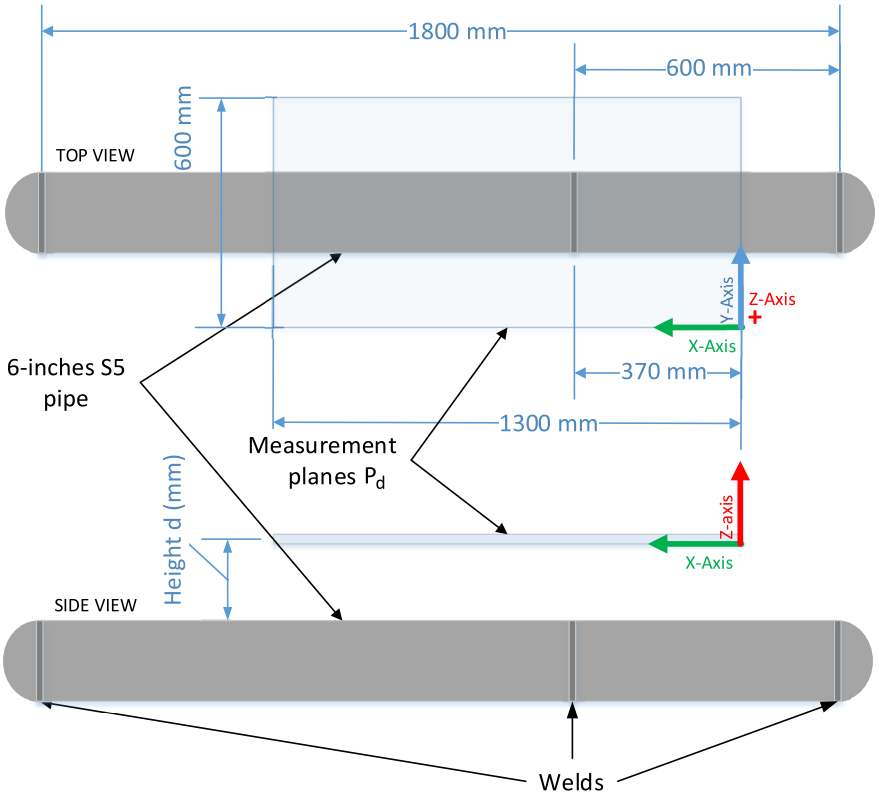

Figure 3.21: 6-inch pipe and its measurement planes.

Fig. 3.21 outlines a welded pipe, its measurement planes and a corresponding coordinate system. A measurement plane P_d was horizontal and above the pipe at the height d. Its dimensions were L1300 mm × W600 mm covering the weld area. The weld was at 370 mm in the x axis. In the experiment, distance d between the pipe's top and the measurement plane, which was manually controlled by the lift, was from 100 mm to 1500 mm.

3.5.2.4 Measurement procedure

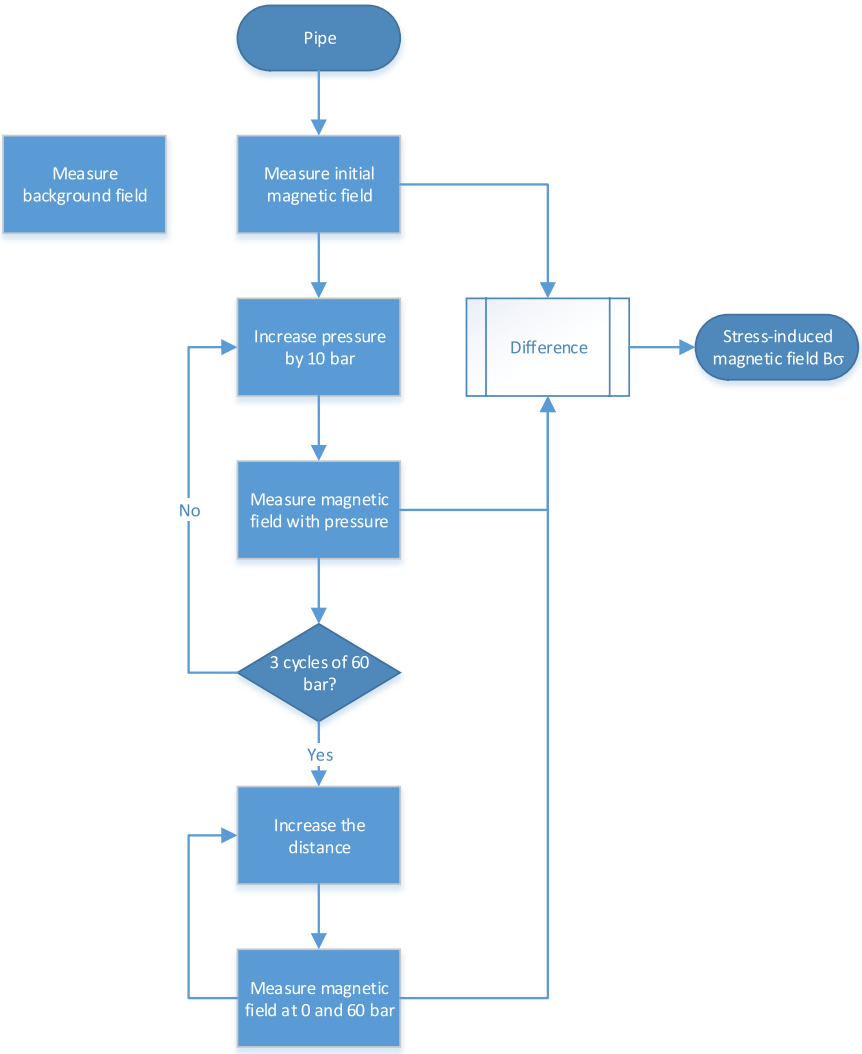

Figure 3.22: Measurement procedure for each pipe.

Fig. 3.22 shows steps to measure the stress-induced magnetic field of the pipe when pressurised. First, the background field $\mathbf{B}_{bkg}$ was measured when there was no pipe in place. It was used to remove the effect of other steel structures in the laboratory to the magnetic field induced by the pipe. After that, following steps were performed:

Step 1 Measure the initial magnetic field $\mathbf{B}_i$, which is magnetic field of the pipe

before applied the pressure, at different heights.

Step 2 Increase the pressure by 10 bar.

Step 3 Measure the magnetic field while pressurising.

Step 4 Repeat steps 2 and 3 until the pressure was at 60 bar for at least 3 cycles. This was to investigate change of magnetic field with the applied pressure.

Step 5 Increase the measurement height d between the pipe and the measurement plane.

Step 6 Measure the magnetic field when the pressure was at 0 bar and 60 bar.

Step 7 Repeat step 5 and 6 up to the distance $d = 1500$ mm. This was to study effects of the measurement height to the stress-induced magnetic field.

Similar to the experiment with steel bars, the magnetic field due to the pipe, $\mathbf{B}_{pipe}$, was calculated by removing the background field. And the stress-induced magnetic field would be calculated by taking the difference of magnetic field measured at different pressure levels, or with the initial magnetic field, $\mathbf{B}_i$.

$$\mathbf{B}_{pipe} = \mathbf{B} - \mathbf{B}_{bkg}, \tag{3.4}$$

and

$$\mathbf{B}_{\sigma} = \mathbf{B}|_{\sigma} - \mathbf{B}_i. \tag{3.5}$$

3.5.3 Demonstration of the measured magnetic field

In order to illustrate what had been measured in the experiment, Fig. 3.23 shows magnetic field measured at 200 mm above the pipe at pressures of 0 bar and 60 bar. And Fig. 3.24 show the difference of the magnetic field measured at these two pressures.

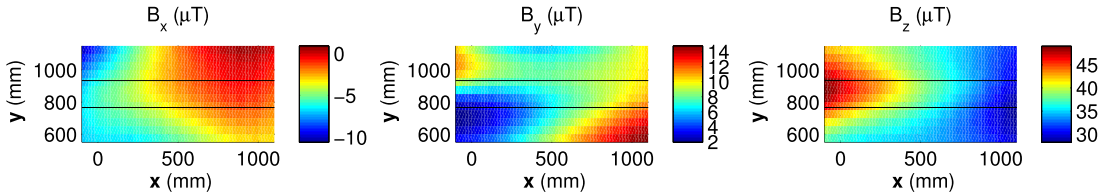

(a) 0 bar

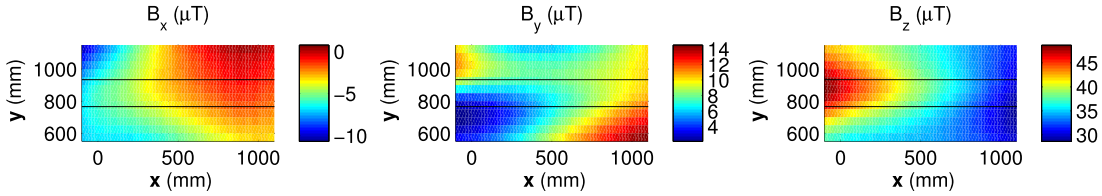

(b) 60 bar

Figure 3.23: Magnetic field of a 6-inch pipe at 0 bar and 60 bar measured at 200 mm above the pipe. The black outline is the underlying pipe.

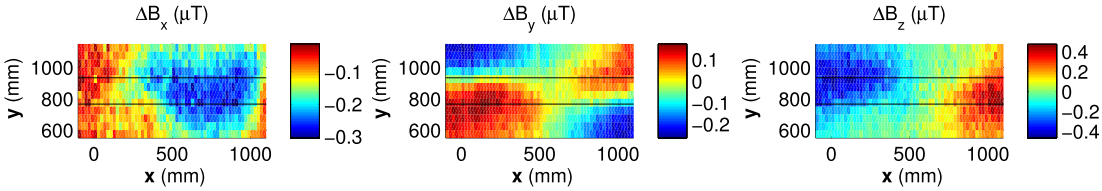

Figure 3.24: Difference of the magnetic field of a 6-inch pipe between 60 bar and 0 bar measured at 200 mm height. The black outline is the underlying pipe.

The delta field in Fig. 3.24 was calculated by the following steps:

Step 1 Measure magnetic field B_0 at 0 bar

Step 2 Measure magnetic field B_{60} at 60 bar

Step 3 Calculate $\Delta B = B_{60} - B_0$

As shown in Fig. 3.23, the magnetic field measured at 0 bar and 60 bar was very similar. However, there was actually a small difference which is shown in Fig. 3.24. Interestingly, this delta field was similar to that of the bar and had a shape of the magnetic field of a magnetic dipole. Details about magnetic indication of the stress-induced magnetic field of the pipes will be discussed in Chapter 5.

3.6 Large-scale field observations on above-ground gas pipelines

3.6.1 Introduction

In addition to the laboratory experiments, field observations were also performed on 18-inch to 30-inch above-ground live National Grid gas pipelines at Pannal. This was to study the magnetic field of the operational pipelines with actual features such as circumferential welds, seam welds, or welded bends. In the observations, it was able to control the measurement height between the horizontal measurement plane and the pipe, which allowed the study on the effect of the depth of cover of underground pipelines to the measured magnetic field. In practice, this depth is usually unknown.

These observations provided an extensive view compared to the laboratory experiments. The results will be discussed in Chapter 5 together with the laboratory experimental results.

3.6.2 Observation method

3.6.2.1 Selected above-ground pipe sections

There were two pipe sections selected for the observation. One was a section of a 30-inch pipeline including circumferential welds and a 90° side bend. This was a big pipeline, therefore, there were pipe supports and flanges close to the welds. Another one was a straight section of an 18-inch pipeline containing one circumferential weld. There was no pipe support or flange within 2 m from the weld. Fig. 3.25 shows the sections selected to perform magnetic surveys.

(a) 30-inch pipe section

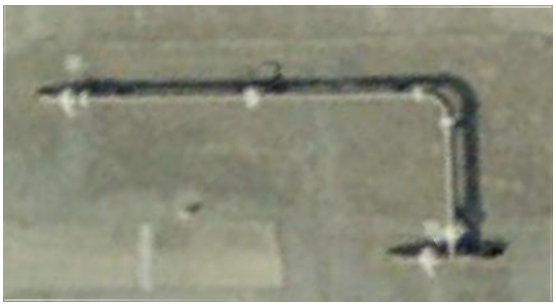

(b) 30-inch pipe section view on Google Earth

(c) 18-inch pipe section

Figure 3.25: 30-inch and 18-inch pipe sections selected for observation.

For the 30-inch pipe section, it was 600 mm from the ground. Its diameter was 760 mm and wall thickness was 16.75 mm. The top of the section was about 1360 mm from the ground. The operating pressure was varied between 30 bar to 60 bar. The 18-inch pipe section was 457 mm diameter and 7.925 mm wall thickness. Its operating pressure during the observations was between 40 bar to 50 bar.

3.6.2.2 Localisation of pipe sections and measurement planes

Because it could not set up a fixed measurement system, the mobile CNC-based system was used for the field observations. And because it was impossible to deploy the measurement system at the exact location everyday, pipe sections and measurement planes had been localised using two high accuracy GNSS receivers in Real Time Kinematic mode (RTK), in which, one was configured as a base station and the other one was as a rover. The system could provide an accuracy of up to 15 mm.

For the localisation of pipe sections, while the base station was deployed on a tripod at a fixed location, the rover was placed on top of the pipe at several positions so that the GNSS coordinates were recorded, see Fig. 3.26.

For the localisation of measurement planes, the rover was fixed on the XY table of the mobile CNC-based system. It was then controlled to move along the x axis by the CNC machine. The GNSS coordinates of this movement were recorded by the controller, see Fig. 3.27a. It formed a base line, which was parallel with x axis and at $y = -480$ mm to the edge of the measurement plane, see Fig. 3.27b.

(a) Base station setup.

(b) Locate a weld by the rover.

Figure 3.26: Use of the GNSS receivers to localise pipe sections on site.

(a) Use of the rover on the Y arm to position the measurement plane.

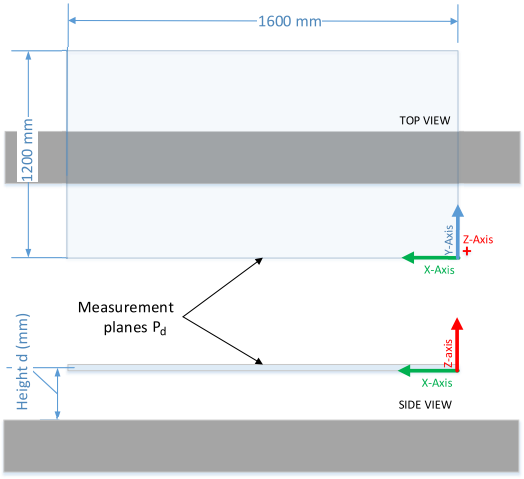

(b) Above-ground pipeline and its measurement planes.

Figure 3.27: The measurement rig and its measurement plane.

With knowledge of the GNSS coordinates of the pipe and the base line, position of the pipe section relative to the measurement plane could be derived using the following steps:

1. From the GNSS coordinates of the pipe and the base line, calculate the distance between the pipe and the base line.

2. From the distance and knowing that the base line was 480 mm to the edge of the measurement plane, calculate position of the pipe in relative to the measurement plane.

Although using the mobile system did not offer an accuracy as high as the fixed system used in the laboratory, the performance of the localisation was still acceptable considering dimensions of the pipelines on site. Moreover, the spatial resolution in measurements was set as 20 mm, met with 15 mm accuracy of the GNSS receivers.

3.6.2.3 Measurement procedure

Fig. 3.28 shows the measurement procedure and use of the measurement system on the 30-inch pipe. In the field observation, measurements of the background field $\mathbf{B}_{bkg}$ and the initial field $\mathbf{B}_i$ could not be performed. As the pipelines are live distribution lines, it was impossible to control the internal pressure. For this reason, there was no measurement of variation of the magnetic field with stress. In fact, a measurement of the background was actually performed, however, it was not at the same location but at about 7 m away from the pipe. This could only be used when considering effects of the rig to the measured magnetic field.

As shown in Fig. 3.28a, the magnetic field was only measured with variation of the measurement height, or depth. It was manually controlled by the lift and was from 200 mm up to 4 m above the pipe.

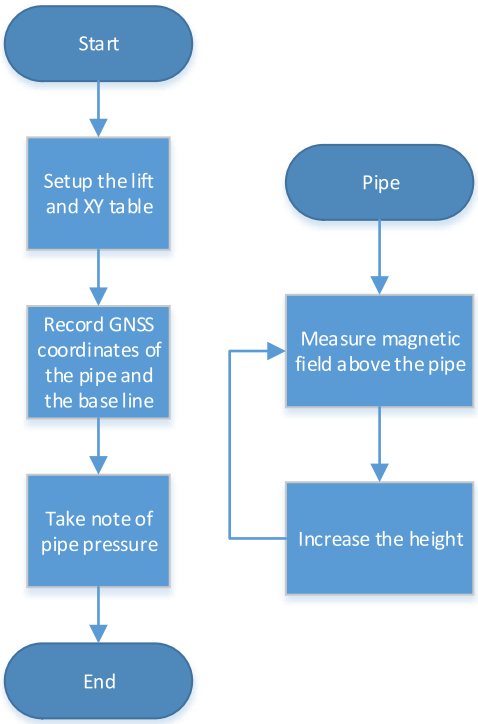

(a) Measurement procedure

(b) Use of the mobile CNC-based measurement system on the 30-inch pipeline.

Figure 3.28: Measurement procedure in field experiment.

3.6.3 Demonstration of the measured magnetic field

Fig. 3.29a shows the magnetic field measured when the XY table was not placed on the lift but on an aluminium platform. This was to measure the background field at the Pannal site. A similar measurement was performed when the XY table was placed on the lift, see Fig. 3.29b.

Fig. 3.30 shows the magnetic field measured at 200 mm above the 18-inch pipe before and after removing the background field with the lift. There was not much difference between the measurements because the variation of the background field was less than 1 μT compared to at least 10 μT of the field induced by the pipe. In the figure, location of the pipe and the weld were overlaid on the field map using the technique shown in Section 3.6.2.2. The main results will be discussed in Chapter 5 together with the laboratory experimental results.

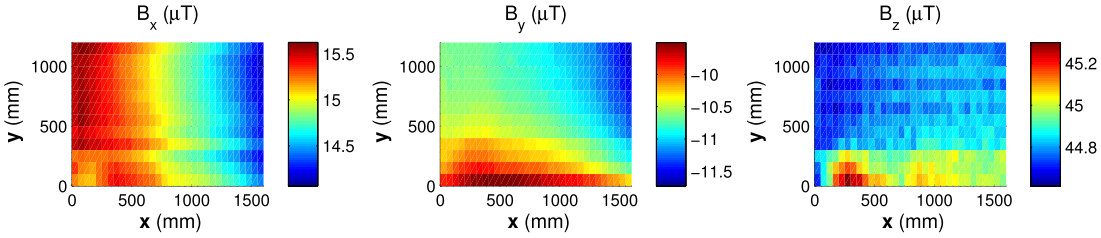

(a) Background field without the lift.

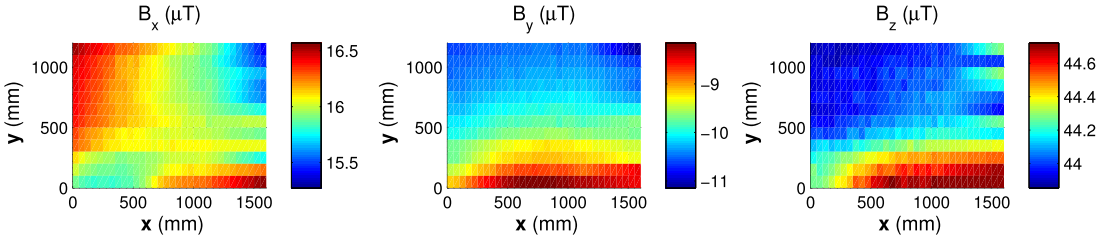

(b) Background field when the XY table was placed on the lift.

Figure 3.29: Background field 7 m away from the 18-inch pipe.

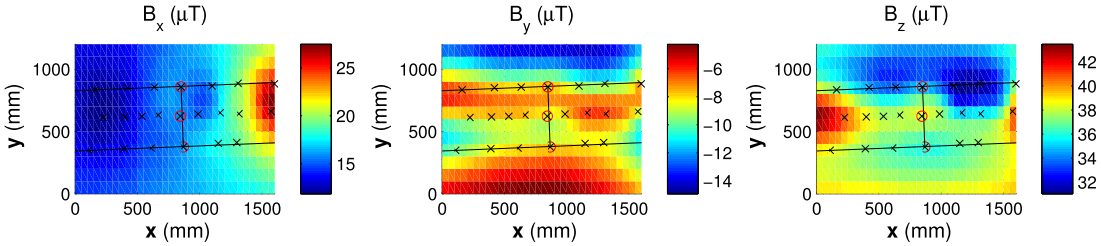

(a) Before removing background field.

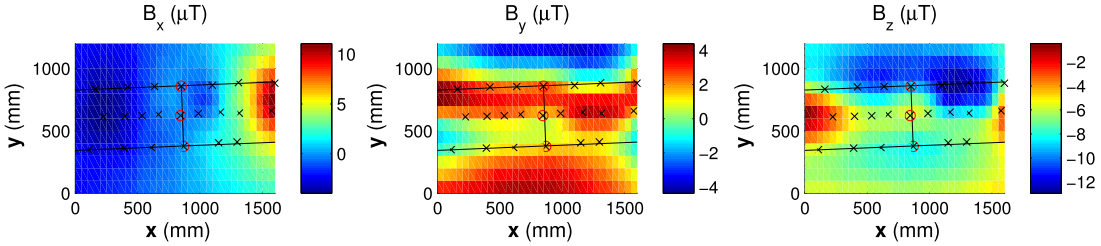

(b) After removing the background field.

Figure 3.30: Magnetic field measured at 200 mm above the pipe before and after removing the background field. The black layout is the underlying pipe and the weld. Its coordinates were calculated using the GNSS coordinates.

3.7 Field surveys on underground gas pipelines

3.7.1 Introduction

In addition to the above experiments and observations, field surveys were conducted on National Grid underground gas pipelines. The aim was to collect real data, so that the SCT techniques could be tested and verified. During this research, more than 20 km of pipelines were surveyed across the UK. Several kilometres of the survey routes had the verification data obtained from National Grid.

The portable UNISCAN instrument was used for field surveys, see Section 3.3.3. This is the instrument that aims to be used for industrial pipeline inspection. By using the Topcon GR-5 receivers in RTK mode, the instrument allows indexing magnetic samples using GNSS coordinates. Therefore, any magnetic anomaly could be easily tracked back on the field.

As discussed in Section 3.3.3, the instrument was designed so that it could be simply used. First, the two GNSS receivers were set up, one as a base station and one as a rover. The rover was mounted on the back of the UNISCAN instrument. Then, the surveyor only needs to hold the array of magnetometers and walk along the survey route, which was marked before.

Because of this survey method, there were uncontrollable factors which affected the measured magnetic field when compared to the experiments. For example, it was impossible for the operator to keep walking on the centre line of the pipeline. This means the instrument might be moved from one side to the other side of the pipeline. Moreover, because of motion, the magnetometers could be at a slight angle and any depth to the pipe axis. It added un-wanted variations to the magnetic field of the pipe. Another factor was that because only three magnetometers were used in the UNISCAN instrument, the spatial resolution in the field surveys was much lower than that of the experiments. And the depth information was usually not obtained.

Field survey data was used to verify the hypotheses and provided a feedback to the development of SCT as shown in Fig. 3.1. Based on that, signal processing techniques were developed. Details about this will be discussed in Chapter 6.

3.7.2 Demonstration of measurement results

Fig. 3.31a shows the mapping of 1.8 km survey route on Google Maps. The magnetic field recorded by the UNISCAN instrument is shown in Fig. 3.31b. In the figure, three components of the magnetic field, (B_x,B_y,B_z), of three magnetometers are shown, in which, x axis is along the pipeline axis, y is in the horizontal direction, and z is the upward direction.

From the measured magnetic field, it can be seen that there were strong fluctuations along the pipeline. If any of these fluctuations was actually due to anomaly on the pipeline, it can be easily located using the GNSS coordinates. This study was to understand the measured magnetic field, then to localise and characterise pipeline features.

3.8 Conclusions

This chapter explained the methodology to develop the SCT technology. It was a combination of the experiments, field observations and blind trials on underground live pipelines, modelling and developing signal processing techniques. It explained the method to conduct the laboratory experiments, field observations and field surveys. Three different measurement systems custom built at Leeds for this study were also described. The measured magnetic field was shown in this chapter in order to illustrate the results. The main results will be discussed altogether in the following chapters.

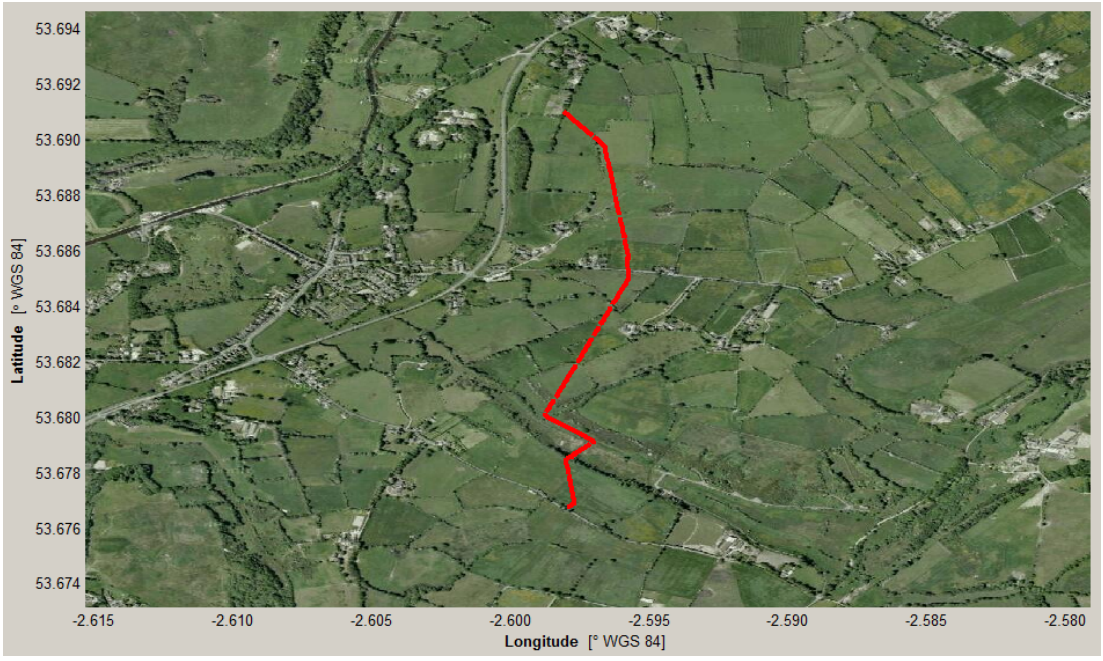

(a) Re-creating the survey route using the GNSS coordinates.

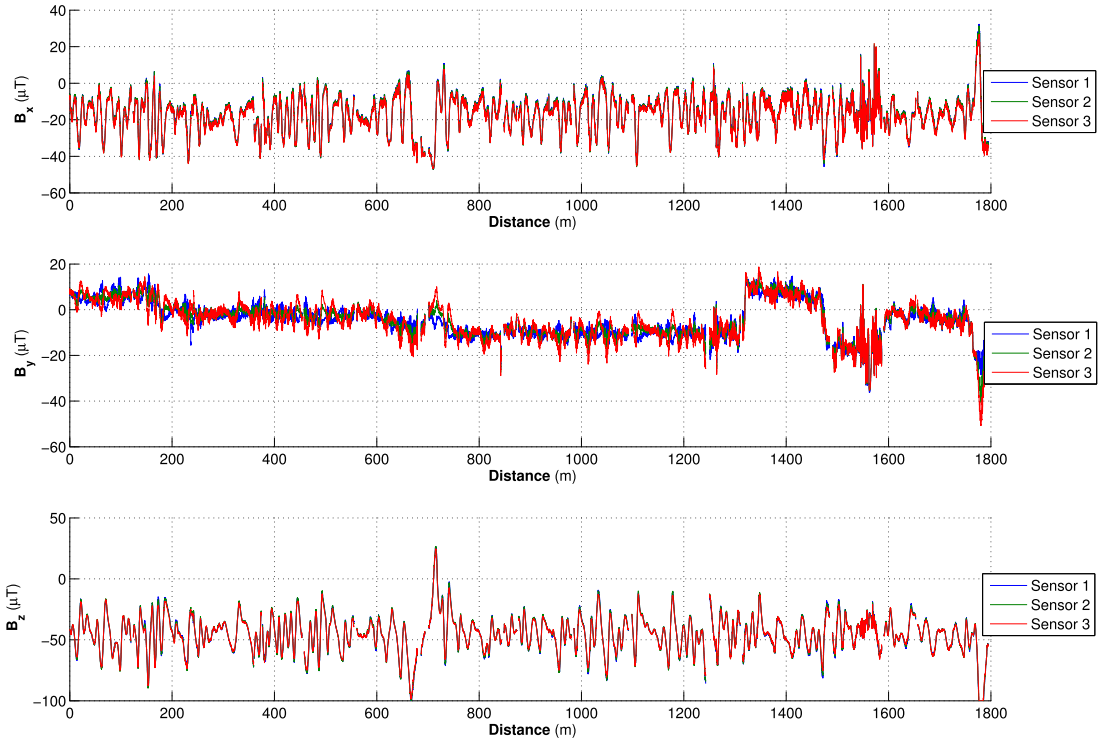

(b) Magnetic field of three magnetometers measured along the survey route.

Figure 3.31: Demonstration of 1.8 km field survey.

3. METHODOLOGY OF THE DEVELOPMENT OF STRESS CONCENTRATION TOMOGRAPHY

Chapter 4

Stress-Induced Magnetic Field of Steel Bars in the Earth's Field

4.1 Introduction

This chapter studies the stress-induced magnetic field of steel bars in the earth's field. A finite element model has been developed to support the analysis. Results from the laboratory experiments described in Section 3.4 have been used to verify the model.

Simulation of magnetic flux leakage (MFL) and the stress-induced magnetic field have appeared in literature before. Dutta et al. [54] used the dipole model to simulate MFL signal of a defect in a ferromagnetic specimen. Zhong et al. [55] utilised the Jiles-Atherton model to simulate the magnetic field of a bar having a defect with increasing stress. Yao et al. [56] performed the analysis of the residual magnetic field of stress concentration zone with changing of the geometry. However, these studies used the surface magnetic field, where local stress concentration dominates the bulk of the material. Also, no cycling stress or magnetic history was studied.

Analysis of the remote-sensing stress-induced magnetic field plays an important role as there is still a gap in understanding the magnetic indication of a stress concentration zone observed at a distance. Varying model parameters including stress level, geometrical dimensions, material properties, and measurement distance allows analysing the effect of stress to the remote-sensing magnetic field.

Importantly, it supports solving the inverse problem, where the stress condition in the material can be characterised from the remote-sensing magnetic field.

For the simulation model presented in this chapter, the COMSOL multiphysics modelling software is employed. The model requires three COMSOL modules including the structural mechanics module which is often used to analyse mechanical structures under load, the AC/DC module to analyse magnetic field using constitutive relations, and the material module to define material properties.

In this chapter, Section 4.2 summaries the experimental method, while the details were presented in Section 3.4. The development of the bar model including implementation of the stress-magnetisation relationship is described in Section 4.3. Section 4.4.2 studies the effect of stress and cycling stress on the induced magnetisation. The distribution of the induced magnetisation due to anomalous stresses is also discussed. Section 4.4.3 analyses variation of the remote-sensing magnetic field with stress and the measurement distance. Magnetic indication of stress concentration zone is presented in Section 4.4.4. Factors affecting the strength of the magnetic indication which includes the stress level, the initial magnetic condition, and the measurement distance are also studied in this section. Finally, a schema of the bulk effect will be proposed in Section 4.4.5.

4.2 Experimental method

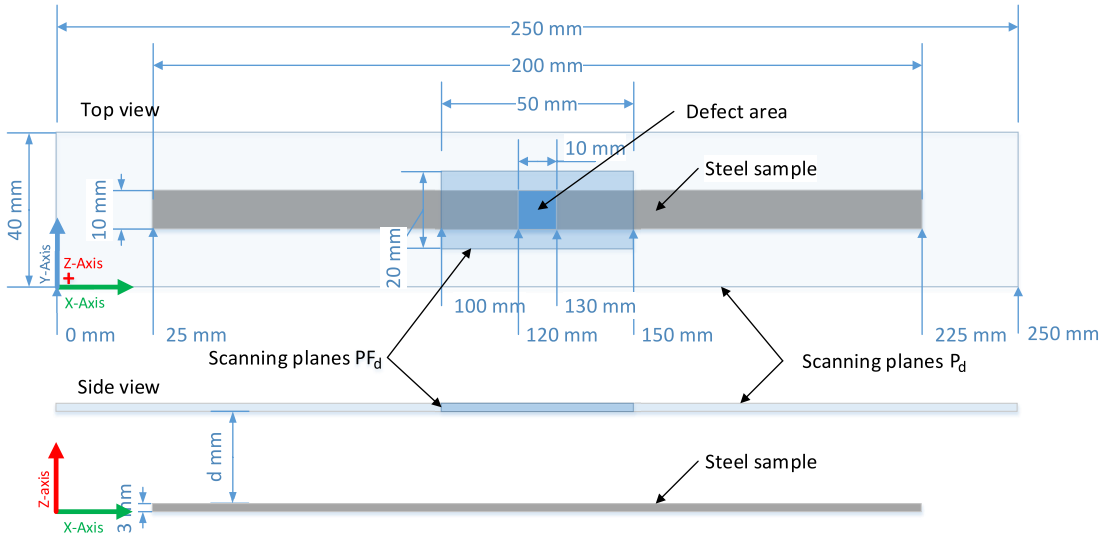

Figure 4.1: The steel sample was placed at the centre of L250 mm × W40 mm measurement planes P_d. Finer-resolution measurement planes PF_d focusing on the defect area was from 100 mm to 150 mm in x axis.

The method of the laboratory experiments on steel bars was described in details in Section 3.4 and will be summarised here.

Steel bars of L200 mm × W10 mm × D3 mm, with and without a defect, were subjected to cycles of stress in the axial direction. Magnetic field was then measured on horizontal planes P_d above the bar at different heights d before and after every stress cycle, see Fig. 4.1 for dimensions of a measurement plane.

4.3 Model development

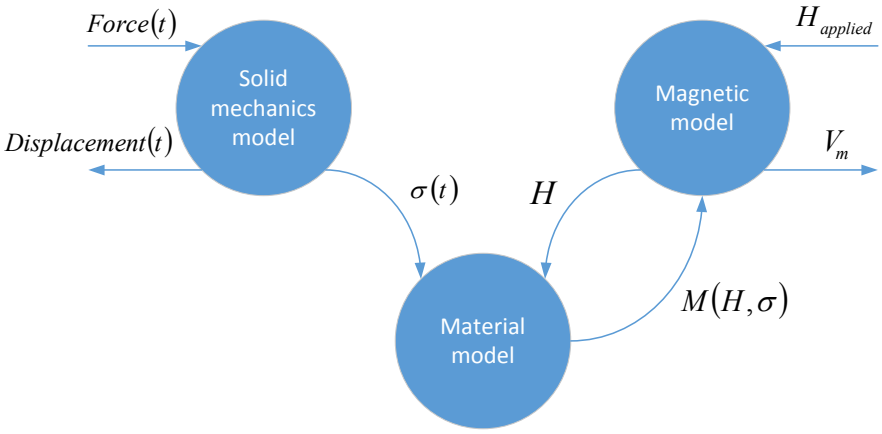

Figure 4.2: Method of coupling constitutive relations.

A finite element model implementing the stress-magnetisation relationship presented in Chapter 2 was developed in order to simulate the stress-induced magnetic field of steel bars.

Modelling of the stress-induced magnetic field was related to solving three coupled models shown in Fig. 4.2. The solid mechanics model solved for the displacement **u** and the stress state $\sigma(t)$ from the applied force $F(t)$. The material model, which included the differential equations presented in Chapter 2, took $\sigma(t)$ as an input and then solved for the magnetisation M using the resultant magnetic field H from the magnetic model. The stress-induced magnetisation M was provided back to the magnetic model to solve for the induced magnetic field **B** through the magnetic scalar potential V_m.

4.3.1 Geometry

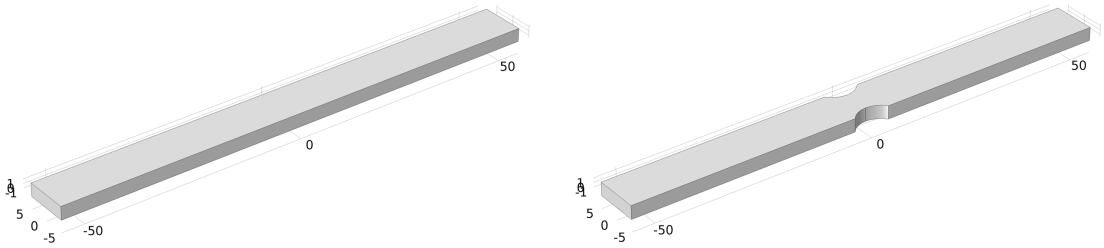

(a) **Sample 1**: the plain bar. (b) **Sample 2**: the defective bar.

Figure 4.3: Geometry of the steel bars.

Two models of steel bars were created in COMSOL. Fig. 4.3 shows the geometry of these two samples. Sample 1 was a plain bar, and sample 2 had a defect.

The geometry representing the sample was then placed in the middle of a block representing the surrounding air. In terms of domains in COMSOL, the air was domain 1, and domain 2 was the steel sample, see Fig. 4.5.

4.3.2 Boundary conditions

For the solid mechanics interface, in order to simulate the applied force, the boundary at the end of the bar was constrained as a fixed boundary while a load was applied to the other end, see Fig. 4.4a.

In the simulation, three force cycles of 1 kN, 2 kN and 3 kN were applied to the boundary as shown in Fig. 4.4b. The force was increased from 0 to a maximum level and then relaxed. The period of each stage was 10 s simulation time. A time-dependent solver was employed to calculate magnetisation of the material while the material was being loaded using the differential equations derived in Chapter 2, so that the variation of the magnetisation with stress through the time variable could be established.

For the magnetic fields interface, the sample was placed in the earth's field only, which was in the same orientation with the background field in the laboratory $\mathbf{B_{bkg}} = (8, -7, -46)$ μT. This was set in the model by forcing the total

field to be the earth's field on the six outer boundaries of the air domain using the External Magnetic Field Interface:

$$\mathbf{n} \cdot \mathbf{B} = \mathbf{n} \cdot \mathbf{B}_{bkg}, \tag{4.1}$$

where $\mathbf{n}$ is the normal unit vector, $\mathbf{B}$ is magnetic flux density and $\mathbf{B}_{bkg}$ is the background magnetic flux density.

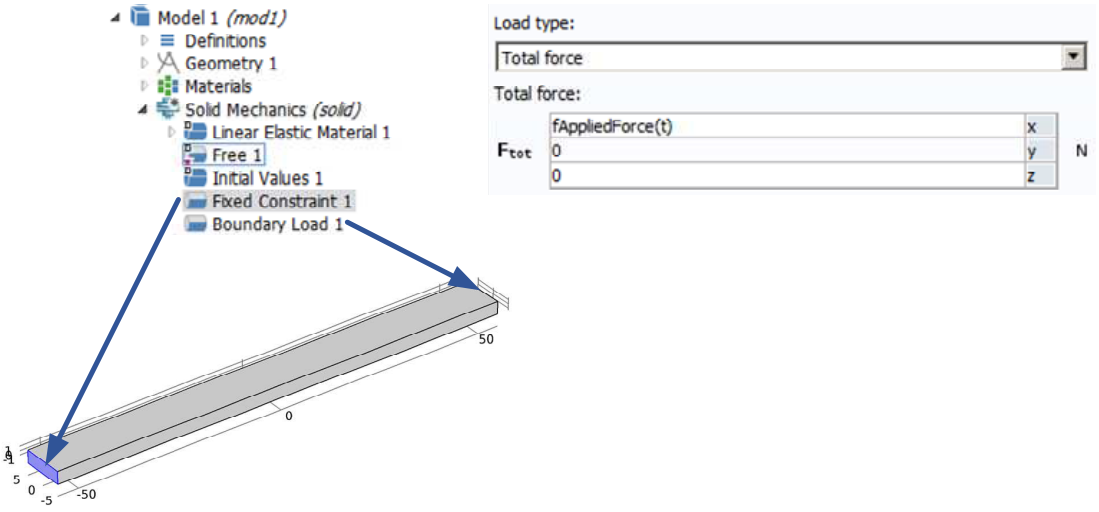

(a) Applying constraints in COMSOL.

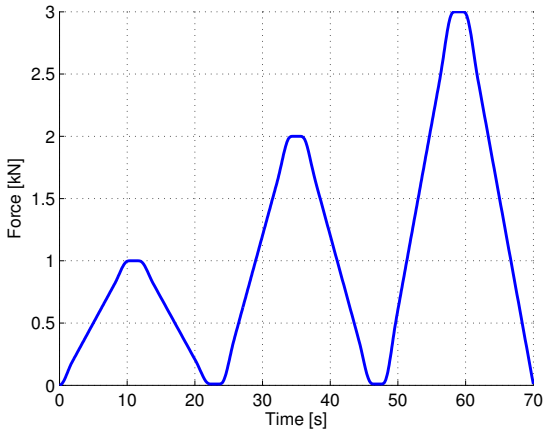

(b) Force cycles applied to the sample.

Figure 4.4: Boundary conditions of the solid mechanics interface.

4.3.3 Materials

COMSOL Multiphysics integrates a material library which provides access to over 2,500 materials including non-linear magnetic materials.

As shown in Fig. 4.5, air was chosen for the block surrounding the sample, i.e. domain 1, meanwhile low carbon steel was assigned to the steel sample, i.e. domain 2. Table. 4.1 shows the mechanical properties of the steel used in the simulation.

It is worth to note that although the mechanical properties of the material definitely plays a role in the stress-magnetisation relationship, studying material properties is out of scope of this thesis.

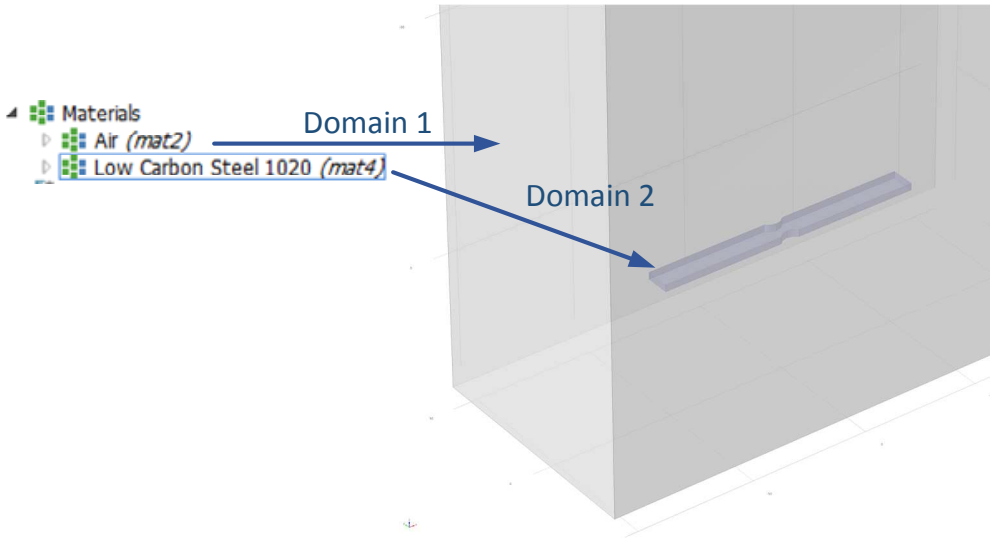

Figure 4.5: Materials used in the model.

Material	Elastic modulus (Pa)	Poisson's ratio	Density (kg/m^3)
Low Carbon Steel	205×10^9	0.28	7850

Table 4.1: Mechanical properties of steel used in the model

4.3.4 Implementation of the constitutive relations

As presented in Fig. 4.2, three models were required to be solved. The first was the solid mechanics model, whose dependent variable solved for was the displacement in x, y, and z axis, $\mathbf{u}(u, v, w)$. The second was the magnetic model, whose dependent variable solved for was the magnetic scalar potential V_m. And the third was the material model which solved for the stress-magnetisation relationship. This relationship was implemented by a series of coefficient form partial differential equations (PDEs) combined with a domain ordinary differential equation (ODE) in order to solve for changes of magnetisation with stress, $M(\sigma)$.

4.3.4.1 The solid mechanics model

Stress analysis has already been supported in COMSOL Multiphysics, see [57]. In the Solid Mechanics Interface, the total strain tensor was represented in terms of the displacement gradient:

$$\varepsilon = \frac{1}{2}(\nabla \mathbf{u} + \nabla \mathbf{u}^T), \tag{4.2}$$

where $\mathbf{u}(u, v, w)$ is the displacement, and ε is the strain tensor, which can be written as follows:

$$\begin{pmatrix} \varepsilon_x & \varepsilon_{xy} & \varepsilon_{xz} \\ \varepsilon_{yx} & \varepsilon_y & \varepsilon_{yz} \\ \varepsilon_{zx} & \varepsilon_{zy} & \varepsilon_z \end{pmatrix}$$

The time-dependent equation that solved for the displacement was written as:

$$\rho \frac{\partial^2 \mathbf{u}}{\partial^2 t} = \mathbf{f}_V - \nabla \cdot \sigma, \tag{4.3}$$

where σ is the Cauchy stress tensor:

$$\begin{pmatrix} \sigma_x & \tau_{xy} & \tau_{xz} \\ \tau_{yx} & \sigma_y & \tau_{yz} \\ \tau_{zx} & \tau_{zy} & \sigma_z \end{pmatrix},$$

which includes three normal stresses $(\sigma_x, \sigma_y, \sigma_z)$ and six shear stresses (τ_{ij}); $\mathbf{f}_V$ is the volume force vector, and ρ is the material density.

4.3.4.2 The magnetic model

In order to calculate the stress-induced magnetic field, the Magnetic Fields, No Currents Interface was used [58]. This was to solve for the scalar magnetic potential V_m.

The equations required to solve for were:

$$\nabla \cdot \mathbf{B} = \nabla \cdot (\mu_0 \mu_r \mathbf{H}) = 0, \tag{4.4}$$

and

$$\mathbf{H} = -\nabla V_m + \mathbf{H}_b, \tag{4.5}$$

in which $\mathbf{H}$ is the magnetic field, $\mathbf{H}_b$ is the background field, μ_r is the relative permeability of the material, and $\mathbf{B} = \mu_0(\mathbf{H} + \mathbf{M})$ is the magnetic flux density, where $\mathbf{M}$ was actually stress-dependent and was solved by the material model of the steel sample.

4.3.4.3 Stress-magnetic field relationship

This section shows the equations used to solve for the dependent variable $M(\sigma)$ that coupled the solid mechanics model with the magnetic field model.

In order to simulate the effect of stress on magnetisation, the Jiles-Atherton model was used as presented in Section 2.2. In the model, stress was considered as an additional magnetic field H_σ. And the effective magnetic field was written as

$$H_e = H + \alpha M + \frac{3}{2}\frac{\sigma}{\mu_0}\left(\frac{d\lambda}{dM}\right)_\sigma, \tag{4.6}$$

in which, magnetostriction λ can be represented by

$$\lambda(\sigma, M) \quad = \gamma_1 M^2 \quad + \quad \gamma_2 M^4 \ .$$

The equation solved for the induced magnetisation M was

$$\frac{dM}{d\sigma} = \frac{1}{\epsilon^2}\sigma(M_{an} - M) + c\frac{dM_{an}}{d\sigma}, \tag{4.7}$$

in which the anhysteretic magnetisation $M_{an} = M_s(\coth\frac{H_e}{a} - \frac{a}{H_e})$.

Value of the parameters chosen for this model was represented in Table C.1. These values were actually established by Jiles [29]. It should be noted that the

aim of this study was not to find the actual stress-magnetisation relationship of the material.

Dependent variables, σ, H_e, and M_{an} were defined using the coefficient-form partial differential equations (PDEs). Meanwhile, the equation to solve for M, Equ. 4.7, was implemented using an ordinary differential equation (ODE).

By defining the dependent variables for each element of the steel sample, the stress-magnetisation relationship could be separately solved for each element, which then contributed towards the total effect.

It is noted that the model only considered the effect of the principal stress component to the corresponding magnetisation component. In this case, it was the axial stress, which is along the length of the bar.

4.3.5 Mesh

No special requirement was needed for meshing. Domain 2 was meshed as extra fine compared to the mesh of domain 1, which was the surrounding air. This was to resolve the material property of domain 2, see Fig. 4.6.

The solving model consisted of over 45 thousands domain elements with the size from 0.45 mm to 10.5 mm, in which over two thousands domain elements were of the steel sample.

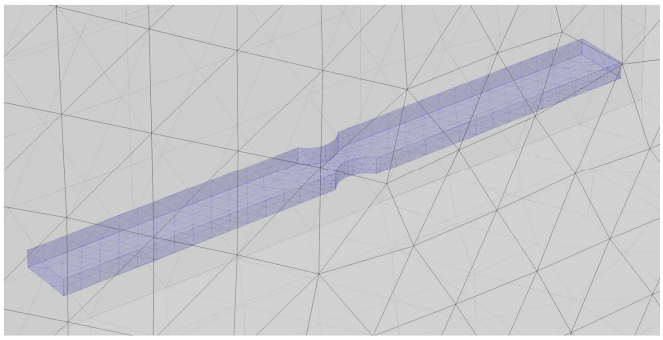

Figure 4.6: Mesh of domain 2 compared to domain 1.

4.3.6 Parameters

Model parameters including dimensions of the sample, the maximum stress level and parameters of the stress-dependent magnetisation curve can be found in Appendix C, Table. C.1.

4.3.7 State of the sample before applying stress

In order to determine the initial distribution of magnetisation M_i of the steel sample, i.e. the state before subjecting the sample to stress, the hysteresis curve of the material presented in Section 2.1 was separately solved in Matlab and imported into COMSOL, see Fig. 4.7. The curve was then used as a magnetic property of the steel sample.

M_i plays an active role in determining magnitude of the stress-induced magnetic field. It should be noted that, in practice, M_i may include the residual magnetisation resulted from manufacturing.

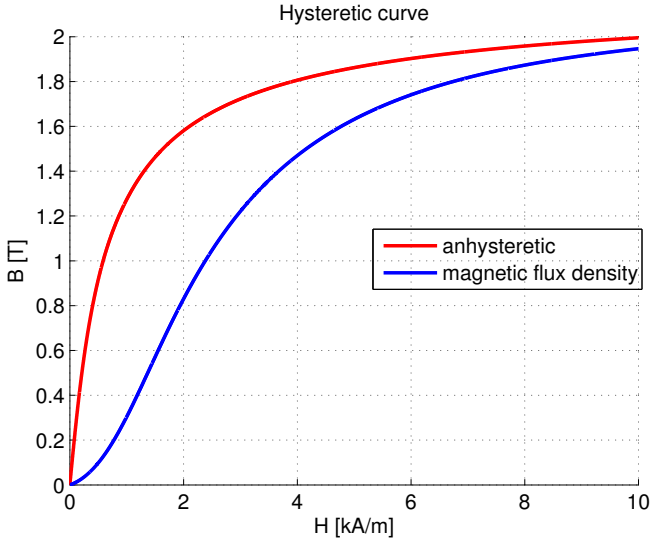

Figure 4.7: The hysteresis curve used to solve for the initial condition.

4.3.8 Model studies

The solver of the model consisted of two study steps, stationary and time dependent. The stationary step was employed to solve for the initial state of the sample as presented above in Section 4.3.7. The solution of this stationary step was used as the initial condition for the first time-dependent step, $t = 0$.

The time-dependent study was employed to solve for the effect of stress to the induced magnetisation by the material model. In this study, the applied force was increased with time up to a maximum stress level and then relaxed, i.e. loaded and unloaded, and the dependent variables were calculated for all elements of the model.

4.4 Results and discussions

4.4.1 Initial magnetisation before applying stress

As explained in Section 4.3.7 and Section 4.3.8, it was assumed that the initial distribution of magnetisation was due to the earth's field only, and was solved by the stationary step using the hysteresis curve of the material, see Fig. 4.7.

Fig. 4.8 shows the simulation of the initial distribution of magnetisation M while the sample was placed in the earth's field $\mathbf{B_{bkg}} = (8, -7, -46)$ μT. For sample 1, i.e. the plain bar, M was gradually changed from 0.5 to 1 kA/m. For sample 2, because there was a defect, or geometric discontinuity, M at this area was rapidly changed and caused a magnetic anomaly. In fact, no measurement of magnetisation was performed in the experiment, therefore this simulation result was not verified by the experimental result.

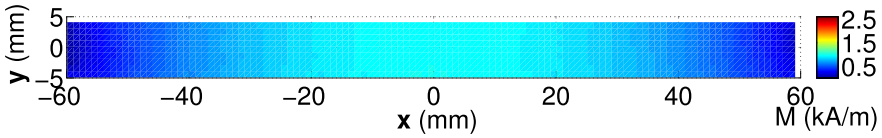

(a) Sample 1

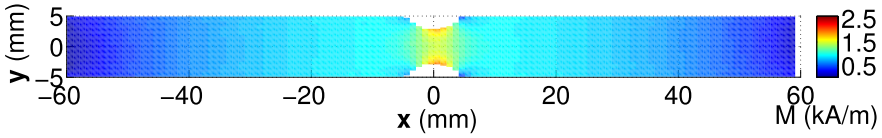

(b) Sample 2

Figure 4.8: Simulation of the initial magnetisation M_i of the samples due to the earth's magnetic field before it was subjected to stress. There was a magnetic anomaly in sample 2.

4.4.2 Effects of stress on magnetisation

Fig. 4.9b simulates variation of the magnetisation M with the applied force F at area A and B of the plain bar, while the sample was being subjected to three consecutive force cycles of 1, 2 and 3 kN as shown in Section 4.3.2.

For the plain bar, the initial magnetisation at A and B was $M_{i_A} = 0.98$ kA/m and $M_{i_B} = 0.90$ kA/m, respectively. Stress enhanced the magnetisation M from its initial state. In the simulation, M was increased about 80% and reached the maximum value at the force between 1.5 kN to 2.5 kN, i.e. approximately 50 MPa to 80 MPa. Importantly, although M at A and B had different values, its variation with F was very similar because these two areas were under similar stress conditions.

Cycling stress added the irreversible and reversible magnetisation to the sample. In the simulation, M at A was initially 0.98 kA/m. After two force cycles of 1 and 2 kN, M raised 50% to 1.5 kA/m when the force was released. When obtained this level, M became reversible with F and almost followed the same curve with successive force cycles.

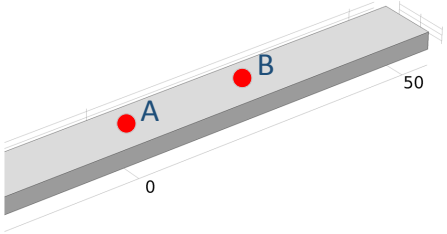

(a) Area A and B where magnetisation M was investigated.

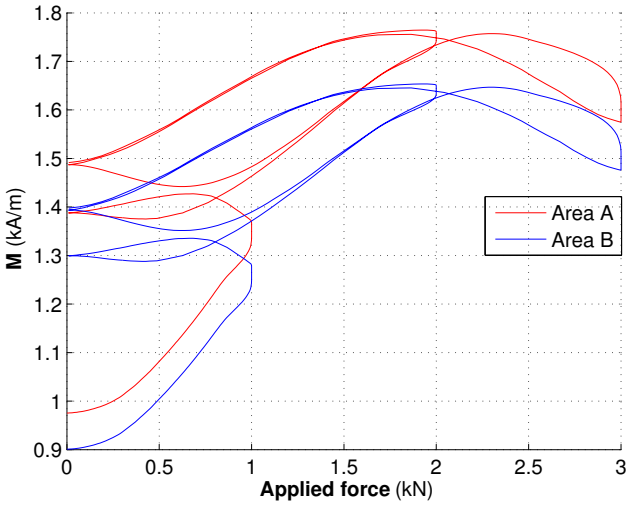

(b) Variation of magnetisation M with the applied force.

Figure 4.9: Simulation of variation of the magnetisation M with the applied force F at two areas A and B on the plain bar.

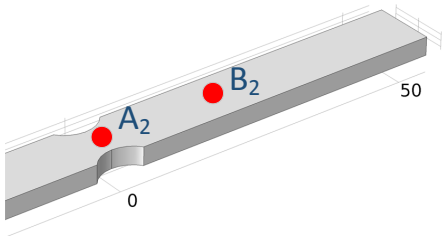

(a) Area A_2 and B_2 where magnetisation M was investigated.

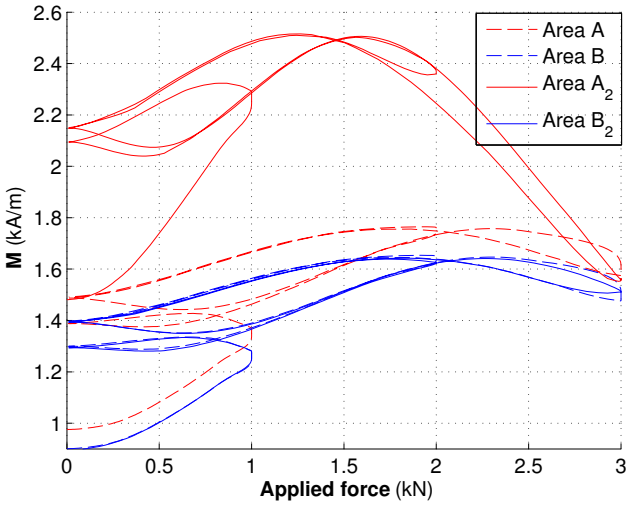

(b) Dissimilar variation of magnetisation M at A_2 could change the distribution of magnetisation.

Figure 4.10: Comparison of variations of the magnetisation M of two samples with the applied force F.

Unlike the plain bar, sample 2 had a defect which caused a stress concentration zone, see Fig. 4.10a. A comparison of variation of the magnetisation M between two samples is shown in Fig. 4.10b. With the variation of the force F, while M at the normal stressed areas A, B and B_2 similarly varied at the same rate, M at the stress concentration zone (SCZ) A_2 was varied differently. The reason for this is A_2 was under a higher stress condition, therefore, M was quickly increased, soon reached the level of 2.5 kA/m at the force of 1.2 to 1.7 kN, and then reduced. The simulation results showed that because magnetisation at SCZs varies differently when compared to that of the surrounding area, it may produce a magnetic anomaly in the distribution of magnetisation.

Distribution of magnetisation with stress

Fig. 4.11 shows how the magnetisation of the samples varied with stress. Initially, the sample had a magnetic anomaly at the defect area before subjected to stress. This anomaly was resulted from the discontinuity of the material. By varying stress the anomaly could be enhanced or diminished. The reason for this is M at the defect area varied differently compared to that of the surrounding area under the same applied force. The magnetic anomaly was likely enhanced at 1 and 2 kN, however, it became weaker at 3 kN, see Fig. 4.11h. So, it is possible to state that in addition to the magnetic anomaly caused by discontinuity of ferrous material, a magnetic anomaly may also be induced by a SCZ because of dissimilar variation of the magnetisation at the SCZ compared to the surrounding area. The latter is unique as it allows the assessment of stress conditions of the material without a geometric discontinuity.

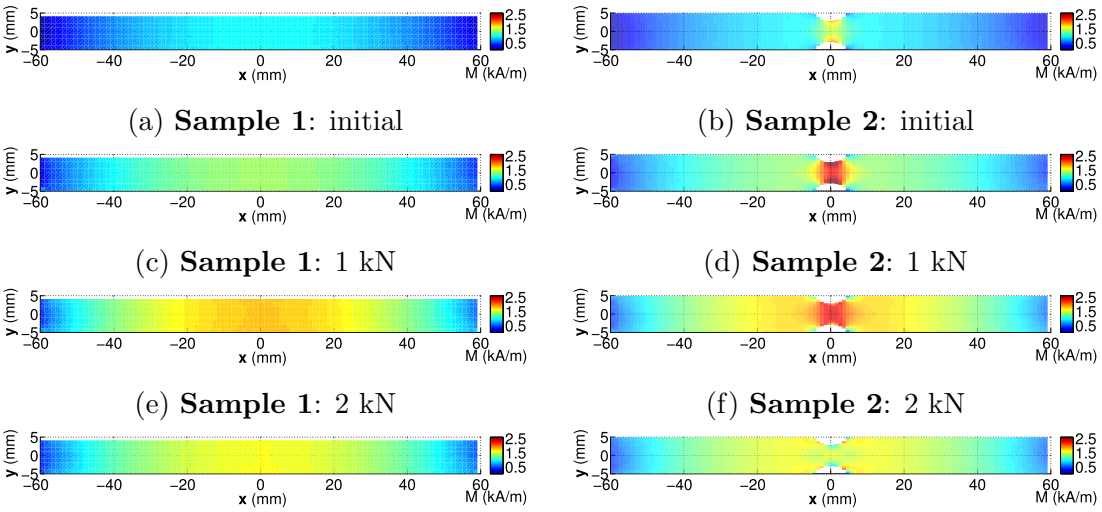

(a) **Sample 1**: initial

(b) **Sample 2**: initial

(c) **Sample 1**: 1 kN

(d) **Sample 2**: 1 kN

(e) **Sample 1**: 2 kN

(f) **Sample 2**: 2 kN

(g) **Sample 1**: 3 kN

(h) **Sample 2**: 3 kN

Figure 4.11: Simulation of distribution of the magnetisation M with the applied force. M at the defect varied differently compared to the surrounding area.

4.4.3 Effects of stress on the remote-sensing magnetic field and magnetic indication of stress concentration zone

As presented above, a magnetic anomaly in distribution of magnetisation may indicate a SCZ. Therefore, the surface magnetic field, which often reflects this distribution, can be used for inspection. However, because the aim is to study magnetic indication of SCZ when measured at a distance, the remote-sensing magnetic field must be used instead of the surface field.

Fig. 4.12 and Fig. 4.13 respectively show the experimental and simulation results of the magnetic field measured before and after subjecting the samples to the force of 3 kN. The measurement height d, which is the distance between the sample to the measurement plane P, was at 22 mm, about 1/5 of the length $L = 120$ mm of the sample.

Unlike the samples in the simulation, which were initially magnetised in the earth's field, the experimental samples were not demagnetised in advance. This explained the difference in the initial magnetic field between the experiment and the simulation. The initial magnetic condition plays a role in determining magnitude of the stress-induced magnetic field and will be studied further in Sec-

tion 4.4.4.

In the experimental results, although the initial field of two samples was different, their stress-induced field had a similar shape but with different magnitudes. It is possibly because the initial field of sample 1 was stronger than that of sample 2, more stress energy would be required to overwrite the initial condition. Therefore, the stress-induced field of sample 1 was weaker than sample 2.

Both of the experimental and simulation results agreed with the findings presented in the previous work [59]. After the sample had been stressed, the remote-sensing stress-induced magnetic field was similar to that of a magnetic dipole, in which B_x had a peak around the centre of the sample and B_z crossed a mean level with two opposite peaks. The above feature of B_x and B_z is used as the magnetic indication of a stress concentration zone (SCZ).

The magnetic indication of a local SCZ appears to be dominated by the bulk field of the surrounding material because of using the remote-sensing magnetic field. In the experiment, sample 2 had a defect which caused a local SCZ. However, in both of the experiment and simulation, as shown in Fig. 4.12d and Fig. 4.13d, the expected magnetic indication of this defect was unable to distinguish itself from the bulk field when measured at the height of $L/5$, i.e. 22 mm. A closer measurement at the height of $L/40$, 3 mm from the surface of the sample, revealed this magnetic indication as shown in Fig. 4.14b. At this height, the magnetic indication of the local SCZ appeared as a small peak in B_x right on top of the defect. The bulk effect will be discussed further in Section 4.4.5.

However, as can be seen in Fig. 4.12 and Fig. 4.13, because of using the parameters obtained from the Jiles-Atherton model, the simulation model was only able to qualitatively predict the shape and trend of the stress-induced magnetic field but not the magnitude of the magnetic features. For example, the stress-induced magnetic field was between -50 μT and +100 μT in the experiment but only $\pm$10 μT in the simulation result, which resulted in a factor of 10 difference.

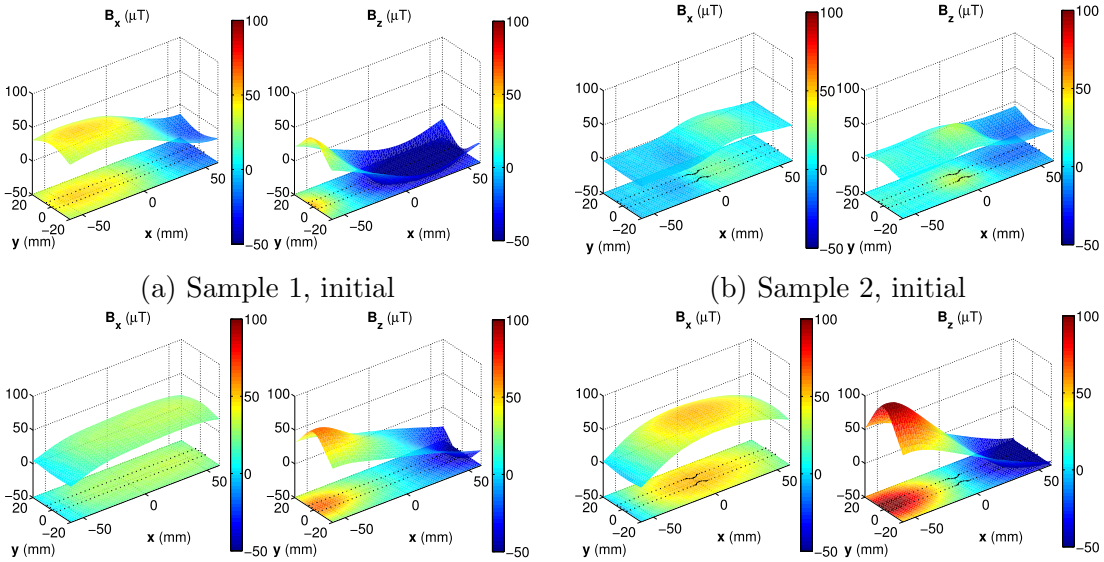

(a) Sample 1, initial

(b) Sample 2, initial

(c) Sample 1 at 3 kN

(d) Sample 2 at 3 kN

Figure 4.12: Experimental results of the magnetic field measured at the height of 22 mm, about $L/5$, before and after subjecting the sample to the force of 3 kN. The magnetic field after the sample being stressed was similar to that of a magnetic dipole. The dotted lines outline the underlying samples.

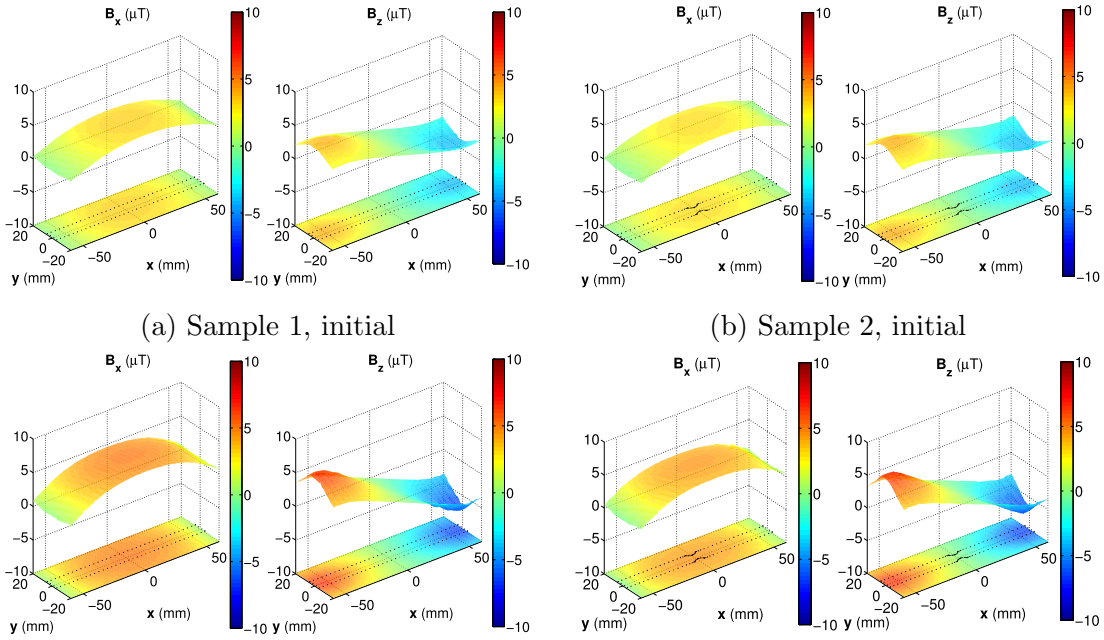

(a) Sample 1, initial

(b) Sample 2, initial

(c) Sample 1 after 3 kN

(d) Sample 2 after 3 kN

Figure 4.13: Simulation of the magnetic field measured at the height of 22 mm, $L/5$, before and after subjecting the sample to the force of 3 kN; The applied field $\mathbf{B_{bkg}} = (8, -7, -46)$ μT. At 3 kN, the shape of the simulated magnetic field was agreed with the experimental result.

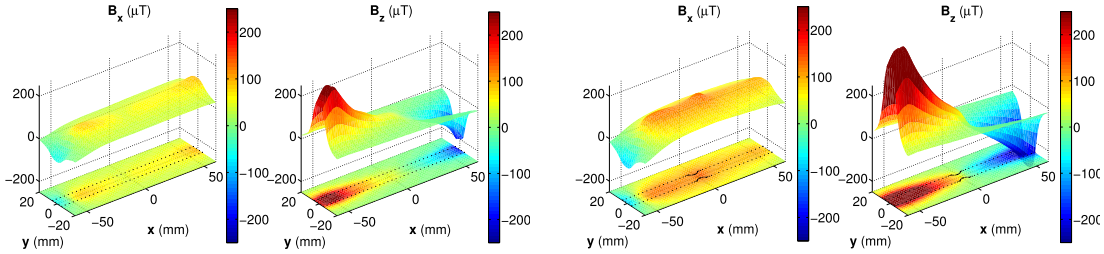

(a) Sample 1

(b) Sample 2

Figure 4.14: Experimental results of the surface magnetic field measured at the height of 3 mm, i.e. $L/40$, after subjecting the sample to the force of 3 kN; An indication of SCZ appeared on top of the defect in sample 2.

4.4.4 Strength of magnetic indication of stress concentration

Study on the stress level

In order to study the effect of stress on the strength of a magnetic indication, the plain bar, i.e. sample 1, was used because there was no additional defect interfering with the induced magnetic indication.

Fig. 4.15 simulates the magnetic field of the plain bar when measured on the centre line, $y = 0$, along the length of the sample, -60 mm $\leq x \leq +60$ mm, at the height of 22 mm, i.e. $L/5$. In this figure, there was a peak in B_x and a zero crossing in B_z indicating a stress concentration zone, which was the whole steel bar in this case. The peak of B_x and the slope of B_z was varied with the applied force because of the variation of magnetisation with stress, as presented in Section 4.4.2.

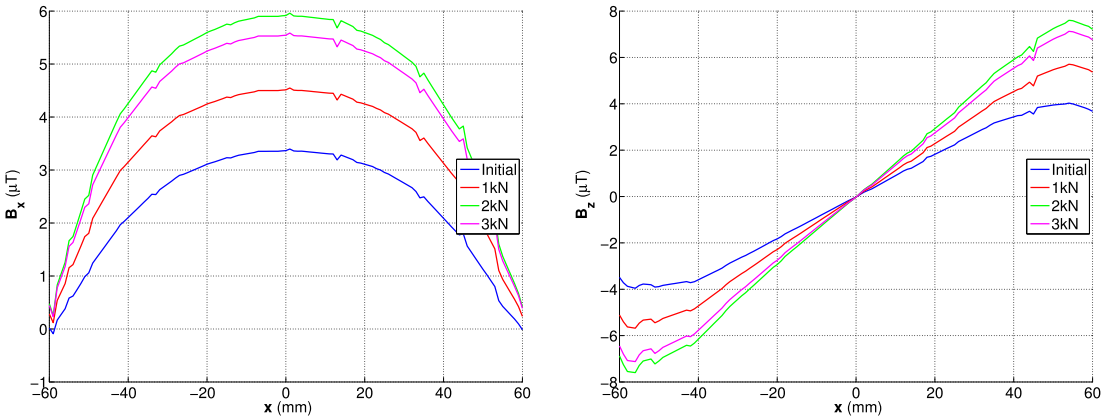

(a) Axial field B_x (b) Normal field B_z

Figure 4.15: Simulation of variation of the magnetic field with the applied force when measured on the centre line $y = 0$ along the length of the plain bar and at the height of $L/5$; The applied field $\mathbf{B_{bkg}} = (8, -7, -46)$ μT.

This study suggests using the gradient $K = \partial B_z/\partial x$ representing the slope of B_z as a basic diagnostic parameter for inspection. Fig. 4.16 shows the variation of K with stress after subjecting the plain bar to three force cycles of 1, 2 and 3 kN in the background field $B_{x_{bkg}} = 8$ μT applied along the length of the sample.

The strength of the magnetic indication K followed the stress-magnetisation relationship used in the simulation model. It predicted a stress threshold at which K became weaker, about 80 MPa in Fig. 4.16. In fact, this stress threshold may differ between materials, and may be predicted using the simulation model by replacing the actual stress-magnetisation relationship of that material into the model.

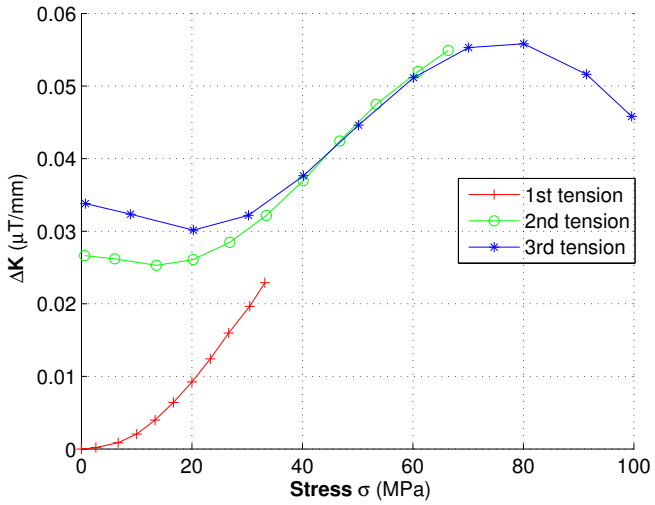

Figure 4.16: Variation of K with tensile stress when measured at the height of $L/5$ (22 mm), while applying three force cycles of 1, 2 and 3 kN, $B_{x_{bkg}} = 8$ μT. K followed the stress-magnetisation relationship used in the simulation model.

Study on the initial magnetic condition before applied stress

The initial magnetisation before applying stress plays an important role in determining variation of K with stress. In the simulation, this initial condition was determined by the background field. Fig. 4.17 and Fig. 4.18 shows the variation of K with both of the stress level and the background field applied.

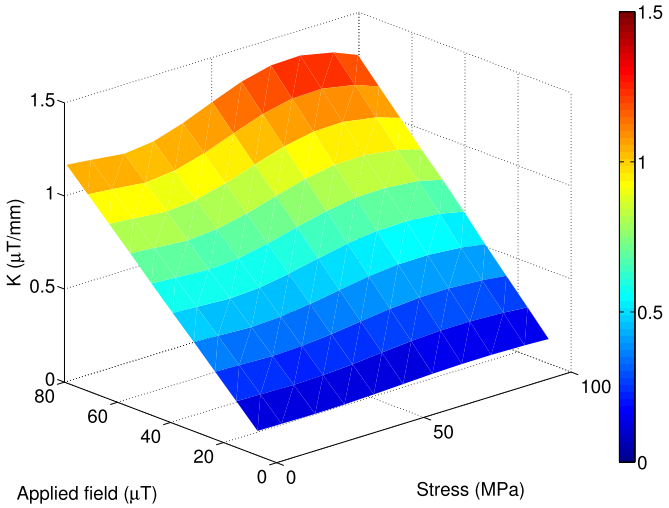

Figure 4.17: Simulation of variation of K with both of stress and the applied field. K is linear with the applied field. At stronger fields, K is more sensitive with stress.

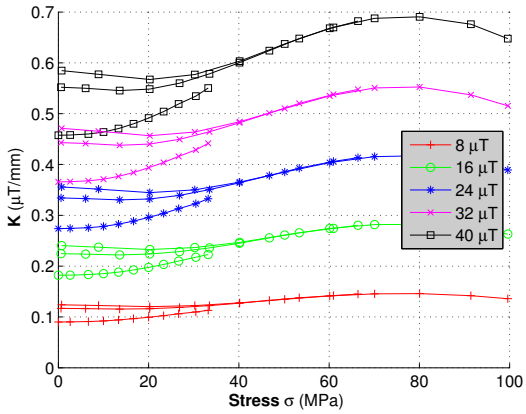

(a) Variation of K with stress in a given applied field.

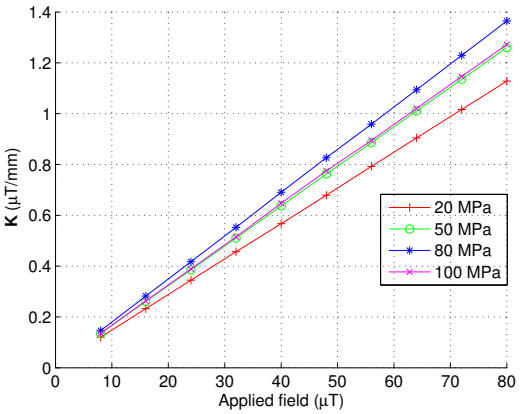

(b) Variation of K with $B_{x_{bkg}}$ at a given stress.

Figure 4.18: Simulation of variation of K with stress and the applied field. At a given applied field, $K(\sigma)$ follows the stress-magnetisation relationship. K is linear with the low applied field at a given stress.

In Fig. 4.18a, at a given applied field, the variation of K with stress was similar to that shown in Fig. 4.16 but its magnitude was gradually increased with increasing of the applied field. Inversely, Fig. 4.18b presents the variation of K with the applied field at a given stress. K is linear with the applied field at a given stress level, and as the applied field is higher, K is more sensitive with stress.

The relationship of K with the stress level and the applied field, which determines the initial magnetic condition, can be represented as

$$K = a(\sigma)B_{applied}, \tag{4.8}$$

in which a is a version of the stress-magnetisation curve of the material depending on the initial condition, and $B_{applied}$ is the external magnetic field applied in the same direction of the stress.

The above equation suggests that it is possible to solve the inverse problem in which the stress condition of the material is determined through the induced magnetic field, in particular, the strength of the magnetic indication K provided that the stress-magnetisation relationship representing $a(\sigma)$ and the applied field (or the initial magnetic condition of the material) must be known.

It should be noted that, in the simulation, the initial magnetisation was predictable as it was induced by the earth's field only. However, in practice, this initial condition may include magnetic history due to manufacturing, construction or previous magnetic inspections, which, therefore, is usually unpredictable.

Quantitative study on the measurement height

Because of using the remote-sensing magnetic field, it is required to study the variation of K with the measurement height d. Fig. 4.19a simulates the variation of K with both of the stress level and the ratio $r = d/L$, where L is the length of the SCZ; and Fig. 4.19b simulates $K(r)$ at given stresses.

The results in Fig. 4.19b shows that, at a given stress, K exponentially decays with r and can be represented using one of the following equations:

$$K_1(\sigma, r) = a_0 \exp(b_0 r), \tag{4.9a}$$

$$K_2(\sigma, r) = a_1 \exp(b_1 r) + a_2 \exp(b_2 r), \tag{4.9b}$$

where $r = d/L$; a_i is the stress-dependent coefficient, and b_i is the decaying rate.

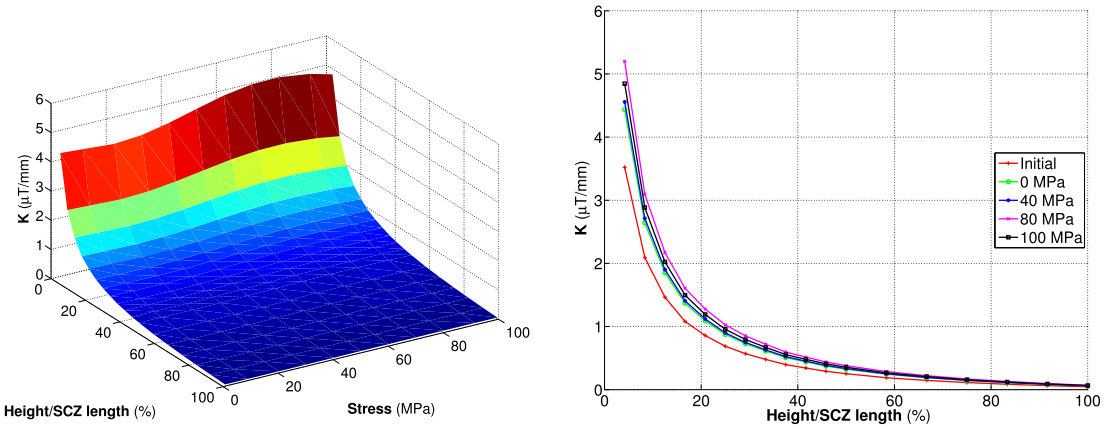

(a) In 3D

(b) At given stresses.

Figure 4.19: Simulation of variation of K with stress and the ratio r between the measurement height d and the length L of the SCZ in the applied field of 80 μT.

Fig. 4.20 shows the variation of a_i, b_i with stress which obtained from the simulation results. It can be seen that the variation of a_i with stress was identical with that of K, although that of a_2 was smaller than a_0 and a_1, meanwhile, b_i was independent with stress. In other words, the decaying rate of K with the measurement height d was a constant.

A comparison of the variation of K with $r = d/L$ between the experiment, the simulation, and the analytical equations is shown in Fig. 4.21. In the figure, the simulation result agreed with the experimental result, and so was K_2.

Although the equation of K_1 predicted a quicker decay than the others, it obviously provided a physical relationship between the remote-sensing magnetic field and the stress level, which therefore enables solving the inverse problem. In particular, when using K_1 the dependence of K with the measurement height d can be written as

$$K(\sigma, d) = a(\sigma) \exp(bd/L), \tag{4.10}$$

in which $a(\sigma) = K(d \to 0)$, in fact, represents the variation of the surface magnetic field B_z along the length of the SCZ. This provides evidence that it is theoretically possible to estimate stress from the remote-sensing magnetic field as long as the stress-magnetisation relationship of that material is known.

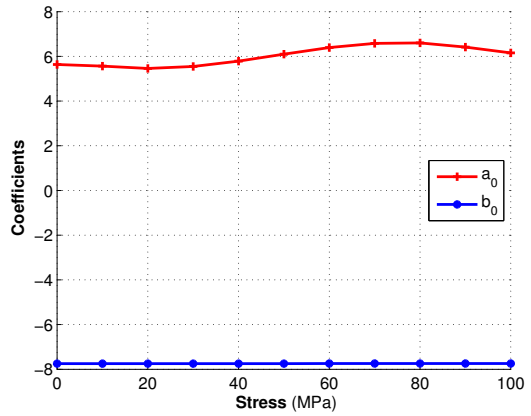

(a) $K_1 = a_0 \exp(b_0 r)$.

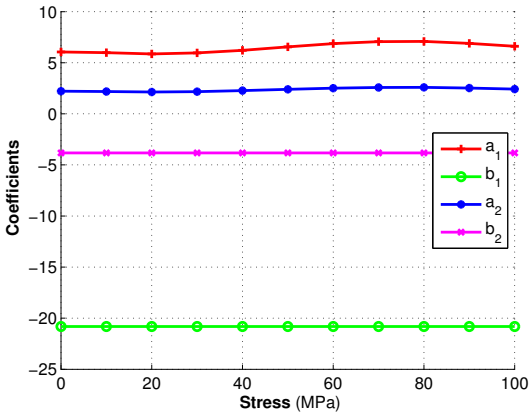

(b) $K_2 = a_1 \exp(b_1 r) + a_2 \exp(b_2 r)$.

Figure 4.20: Variation of coefficients of K_1, K_2 with stress. a_i follows the stress-magnetisation relationship in the simulation model, meanwhile $b_0 = -7.746, b_1 = -20.81, b_2 = -3.82$.

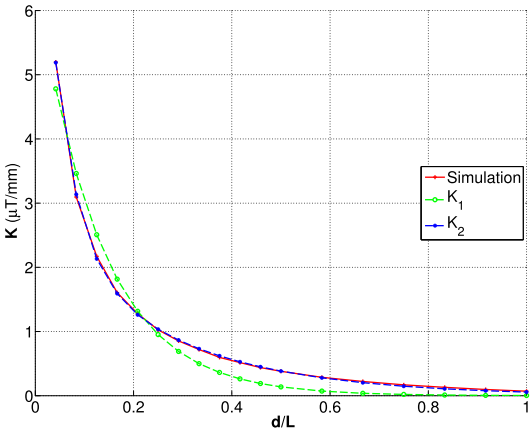

(a) Variation of K

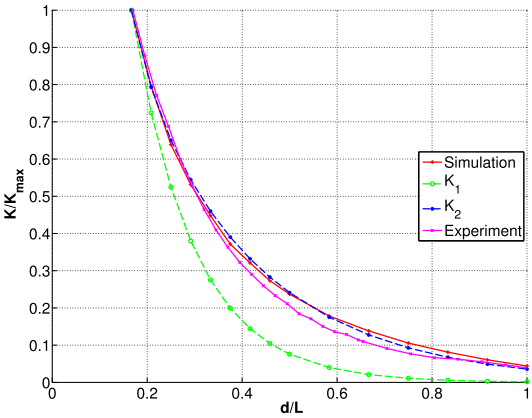

(b) Variation of the normalised K

Figure 4.21: A comparison of variation of K with the measurement height d and the length L of the SCZ between the experiment, the simulation, and the exponential equations at 80 MPa in the field of 80 μT. The simulation and the equation K_2 agreed with the experiment.

A proposed technique to solve the inverse problem

From the above discussion, it is possible to characterise a stress concentration zone (SCZ) using the remote-sensing magnetic field. This makes use of the equation of K_1 shown in Equ. 4.9.

Using this equation, given K_{11}, K_{12} derived from the magnetic field measured at two different heights d_1, d_2, the variation of the stress-dependent surface magnetic field a and the SCZ length L can be estimated using the following equations:

$$\begin{aligned} L &= b(d_2 - d_1)/\ln(K_{12}/K_{11}), \\ a &= K_{11}\exp(-b(d_1/L)). \end{aligned} \tag{4.11}$$

Equ. 4.11 plays an important role because it evidently shows that it is possible to characterise the length and the surface field of a SCZ by remotely measuring magnetic field at two different heights. In practice, there will be an upper limit for the measurement height because K exponentially decays with it.

4.4.5 Study on the bulk effect

As discussed in Section 4.4.3 and shown in Fig. 4.12d and Fig. 4.13d, in the experiment, the magnetic indication of the local SCZ caused by the defect in sample 2 was dominated by the magnetic field of the bulk material when measured at the height of $L/5$ (22 mm). However, this magnetic indication could be detected when measured closer to the surface of the bar, for example at $L/40$ (3 mm), see Fig. 4.14.

Fig. 4.22 compares the experimental and simulation results of the magnetic field of sample 2 when measured at the height of $L/40$ (3 mm). At this measurement height, there was a small magnetic indication appeared on top of the defect in addition to the magnetic indication of the bulk material.

At the height of $L/5$ (22 mm), in order to confirm the existence of the magnetic indication of the local SCZ in the bulk field, the magnetic field of sample 1, i.e. the plain bar, was subtracted from that of sample 2, i.e. the defective bar. The result was the magnetic field caused by the defect only, see Fig. 4.23. In the figure, the local SCZ caused by the defect, in fact, produced a magnetic indication of about 2 μT.

Fig. 4.24 shows B_z of the defective bar at given stresses when measured at three measurement heights; and Fig. 4.25 shows the magnetic field induced by the defect only, calculated by taking the difference between the magnetic field of the plain bar and the defective bar.

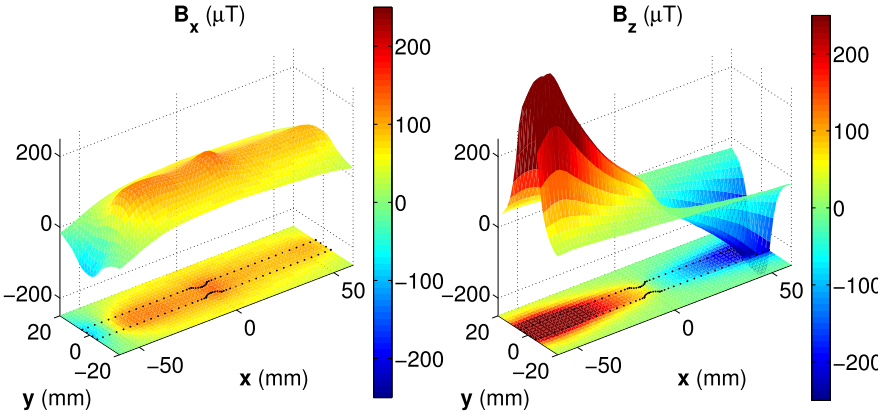

(a) Experiment

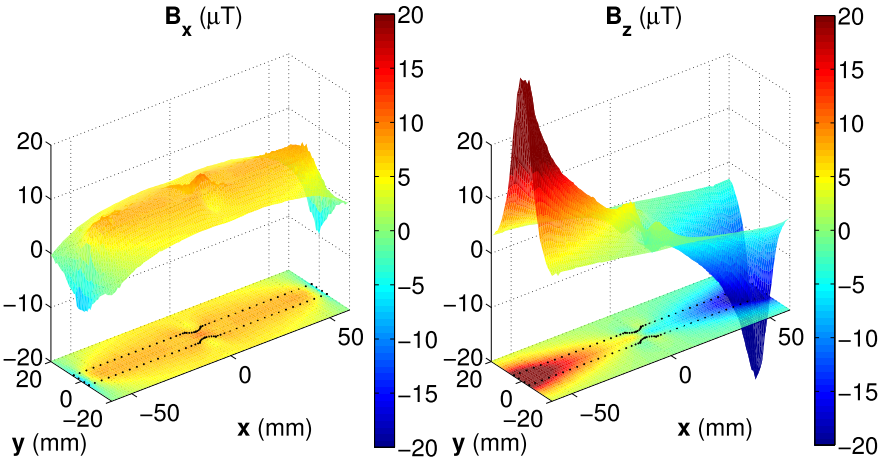

(b) Simulation

Figure 4.22: A comparison between the experimental and simulation results of the magnetic field of sample 2 when measured at the height of $L/40$ (3 mm) after applying the force of 3 kN. A magnetic indication of SCZ appeared on top of the defect.

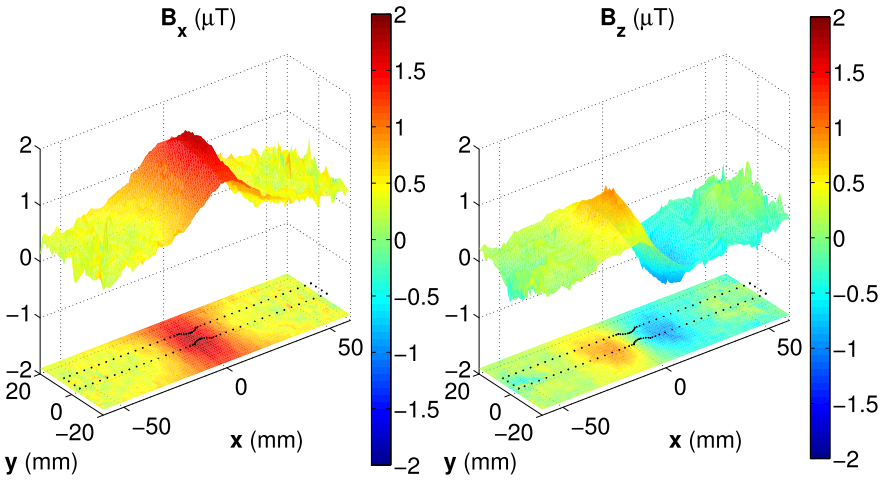

Figure 4.23: At $L/5$ (22 mm), the magnetic indication of the local SCZ can be detected when using the difference between the magnetic field of the plain bar and the defective bar. The bulk field was removed and the magnetic indication of the local SCZ clearly appeared.

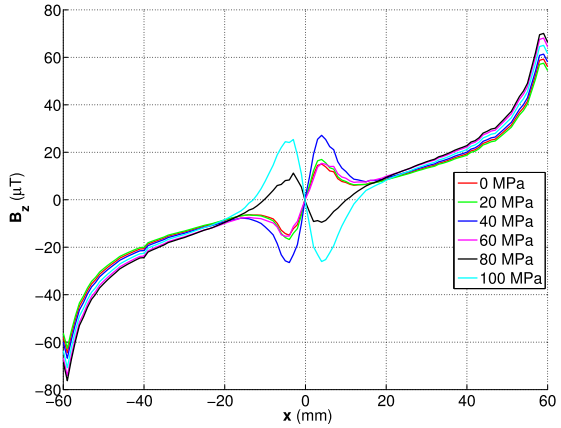

(a) B_z at $L/24$ (5 mm)

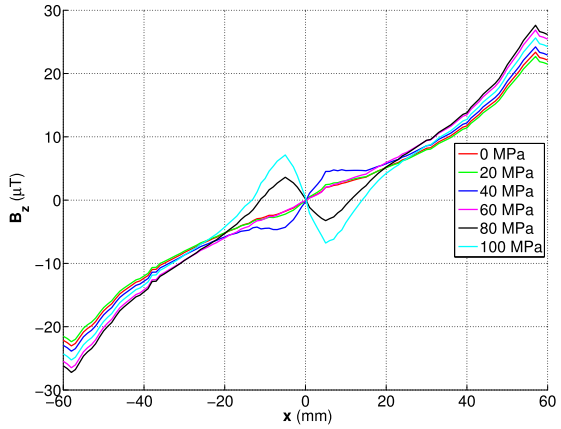

(b) B_z at $L/12$ (10 mm)

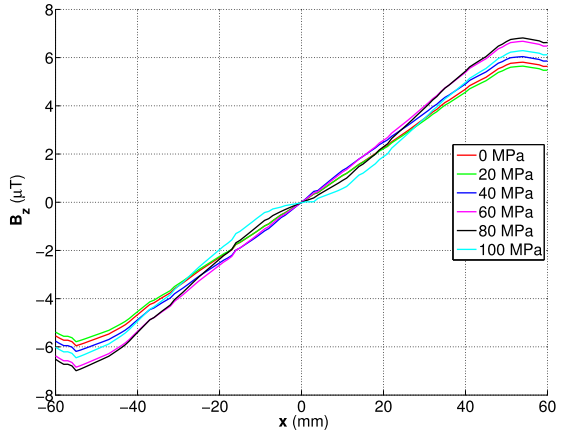

(c) B_z at $L/5$ (22 mm)

Figure 4.24: Simulation of the normal component B_z of sample 2 at given stresses when measured at three different heights. The magnetic indication of the local SCZ was dominated by the bulk field and decayed with the measurement distance.

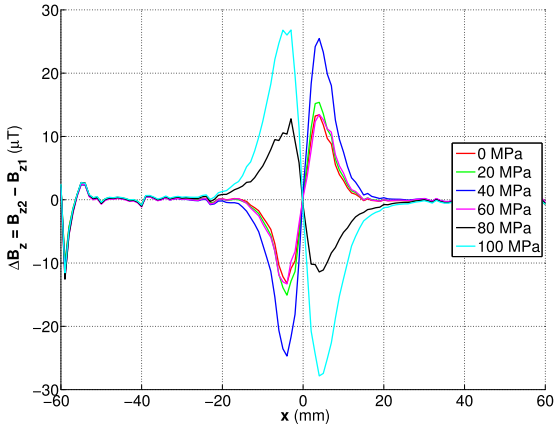

(a) ΔB_z at $L/24$ (5 mm)

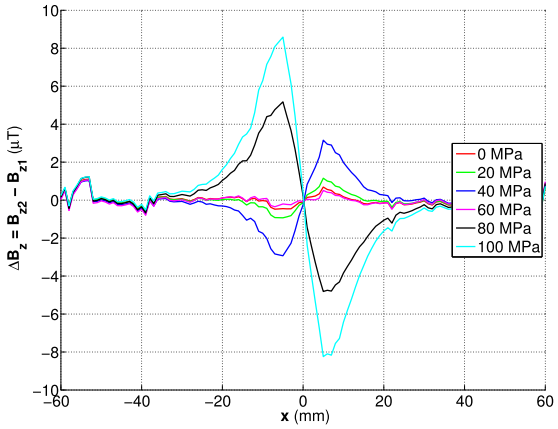

(b) ΔB_z at $L/12$ (10 mm)

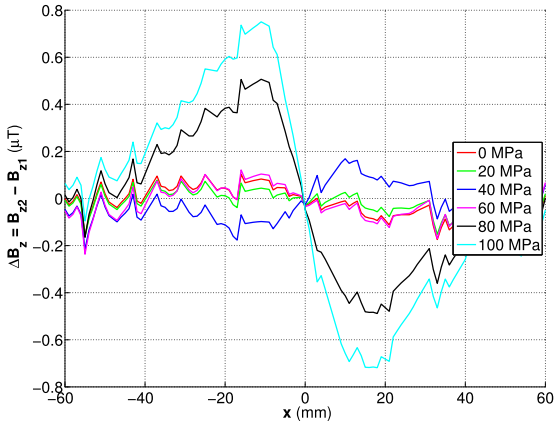

(c) ΔB_z at $L/5$ (22 mm)

Figure 4.25: Simulation of the difference between B_z of the plain bar and the defective bar, $\Delta B_z = B_{z_2} - B_{z_1}$, which represents the magnetic field induced by the local SCZ only, at given stresses when measured at three different heights. The bulk field was reduced.

Given K_L representing the strength of the magnetic indication of the bulk material with the length L, and K_{L_2} representing that of the local SCZ with the length L_2, both of them varied with stress. However, the variation was unique for K_{L_2} as it switched its sign with the variation of stress, meanwhile K_L was similarly varied as discussed in the previous sections. This can be clearly seen in Fig. 4.24a and Fig. 4.25a. At stresses less than 80 MPa, K_L and K_{L_2} had the same sign. But at 80 and 100 MPa, K_{L_2} reversed its sign. This also suggests there could be a stress level, at which $K_{L_2} = K_L$, which means it would be impossible to distinguish the magnetic indication of the local SCZ from the bulk material.

Both of the magnetic indication K_L and K_{L_2} varied with the measurement height. However, K_{L_2} decayed quicker than K_L at a given measurement height as it was much smaller. For example in Fig. 4.24c, while K_L was still detectable when measured at $L/5$, K_{L_2} was nearly diminished except for a small indication at 100 MPa. This suggests a lower limit on dimensions of a local SCZ associated with each measurement height at which its magnetic indication could still be differentiated from the bulk field.

A comparison between B_z and ΔB_z, Fig. 4.24 and Fig. 4.25, about the magnetic indication caused by the defect also showed that it is easier to detect the magnetic indication of the local SCZ using ΔB_z than using B_z. However, unless there is permanent monitoring, it would be impossible to obtain ΔB_z in practice.

Schema of the bulk effect

Fig. 4.26 presents a simple schema of the bulk effect. The normal-stressed area L induces a magnetic indication K_1 resulted from B_{z1}, and the local SCZ L_2 produces an additional magnetic indication K_2 calculated from B_{z2}. The measured magnetic field is the sum of both B_{z1} and B_{z2}.

Fig. 4.27 shows four types of magnetic indication which may appear in the total field. It is categorised based on the sign and the magnitude of K of the local-SCZ field and the bulk field. A comparison with the simulation results shown in Fig. 4.24 confirmed that when increasing stress, the magnetic indication of the defect in the simulation gradually shifted from type 4 to type 1 of the schema.

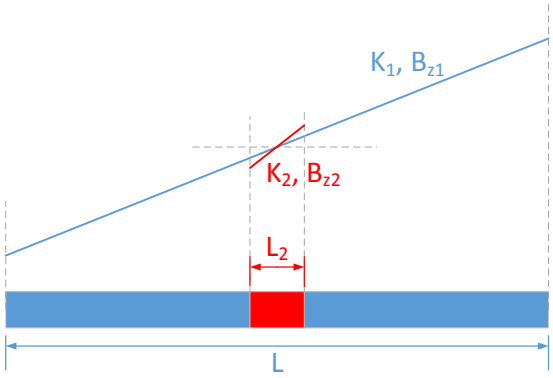

Figure 4.26: Schema of the bulk effect.

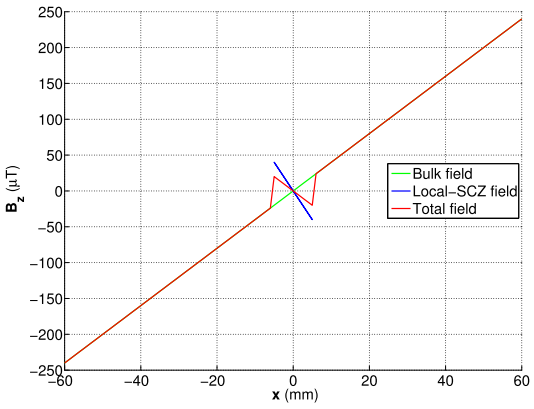

(a) Type 1: $K_1K_2 < 0$ and $K_2 \approx -2K_1$

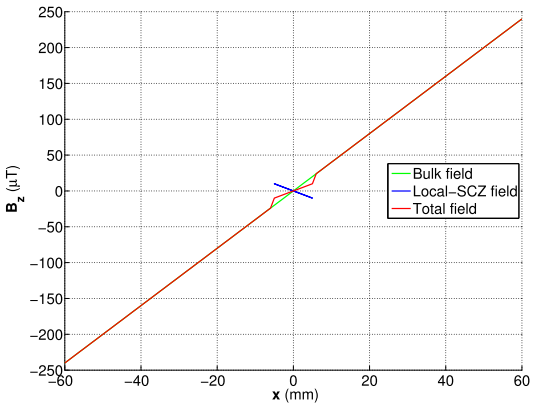

(b) Type 2: $K_1K_2 < 0$ and $|K_2| \to 0$

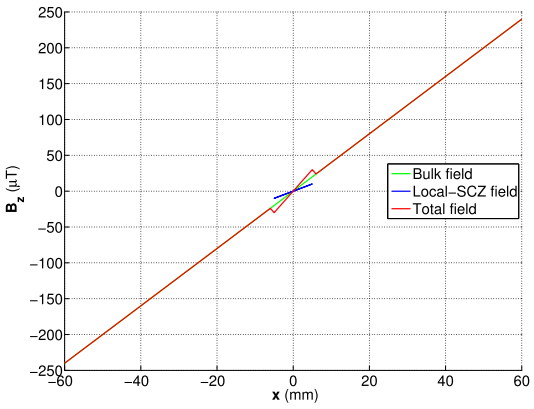

(c) Type 3: $K_1K_2 > 0$ and $|K_2| \to 0$

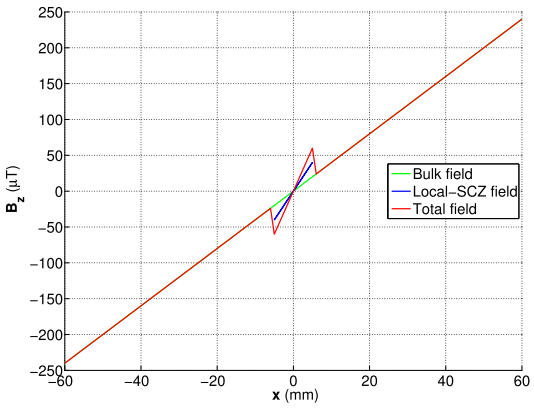

(d) Type 4: $K_1K_2 > 0$ and $K_2 \approx 2K_1$

Figure 4.27: Simulation of the total field and types of magnetic indication of a local SCZ when affected by the bulk field.

4.5 Conclusions

This chapter studied the stress-induced magnetic field of the steel bars and magnetic features of a stress concentration zone (SCZ) using the laboratory experiments and the finite element model.

A model of the magnetomechanical effect was implemented in the finite element model. Dependent variables including the stress-induced magnetisation were defined for each element of the model, so that it is ready to simulate the magnetisation induced by local stress areas. Another advantage is that it is able to simulate both of the application and relaxation of stress. Although the finite element model has shown a general agreement in the trend with the experimental results, it has limited use on predicting the magnitude of the stress-induced magnetic field as there was a factor of 10 difference between the simulation and the experimental results.

This study has shown that, when a force applying to a ferrous material is varied, magnetisation of the material areas under the same stress condition will vary in a similar way. Depending on the initial magnetic condition of the areas, the stress-induced magnetisation may have different magnitudes. A local SCZ may produce a magnetic anomaly as its stress-induced magnetisation dissimilarly varies with stress compared to that of the surrounding area. Because the stress-magnetisation relationship is non-monotonic, the stress-induced magnetisation of the local SCZ may be stronger or weaker than that of the surrounding area. This condition of observing a magnetic anomaly implies that there may be a stress level at which the magnetic anomaly of the SCZ diminished which may result in a miss in terms of detection of SCZ.

The study suggests using a peak in B_x and a mean-level crossing in B_z of the remote-sensing magnetic field as a magnetic indication of a SCZ, and an associated parameter K as a diagnostic parameter for inspection. It has shown that variation of K with stress follows the stress-magnetisation relationship of the material. And for a specific material, K depends on the stress level, the initial magnetic condition, the measurement distance and the bulk field.

The study has established the equation $K = a(\sigma)B_{applied}$, which implies that K is more sensitive with stress if the material area is in a stronger applied field,

and at a given stress level, K is linear with the strength of the initial magnetic condition induced by a low applied field. The coefficient a is a version of the stress-magnetisation relationship of the material which can be experimentally determined. The equation implies that it is possible to characterise the stress condition of the material from the remote-sensing magnetic field. However, the method is not suitable for the SCT technology as it requires knowing the initial condition B_i before applied stress which is impossible in practice.

The study has found that the strength of a magnetic indication K is approximately exponentially decayed with the measurement distance. It implies a method to characterise the surface field and stress condition through the remote-sensing magnetic field as long as the measurement distance is known. This also gives evidence to support the idea of rearranging magnetometers on the array of the UNISCAN instrument.

For the bulk effect, the results of this study have shown that because of not using the surface magnetic field, if the SCZ appears as a local area, the bulk field of the surrounding material may affect the magnetic indication of the local SCZ. A schema of the bulk effect has been proposed, based on this K of the local SCZ may be extracted from the measured magnetic field. The effect of the bulk field can be reduced by using the difference of the induced magnetic field between two stress levels, $\Delta B = B_{\sigma_2} - B_{\sigma_1}$, so K of the local SCZ can be improved. Moreover, the study has found that when stress is varied, K of the local SCZ may inverse its sign in the bulk field. That means it is possible to detect a local defect by measuring the remote magnetic field of the material at two different stress levels, or to detect a change of stress at an area by a permanent monitoring of magnetic condition of the material. However, it is not suitable for the SCT technology because the pressure cannot be changed and permanent monitoring is impossible.

The study enhances the understanding about detection of SCZ in underground pipelines. It provides evidence that it is possible to detect and characterise stress condition of a material using the remote sensing magnetic field and suggests the criteria of detection which should be used by the SCT technology. However, there will be a lower limit on dimensions of a detectable SCZ which depends on the measurement distance and the bulk material. Additionally, it may require

an upgrade of the instrument in order to collect enough data for characterising features of the SCZ.

4. STRESS-INDUCED MAGNETIC FIELD OF STEEL BARS IN THE EARTH'S FIELD

Chapter 5

Stress-Induced Magnetic Field of Thin-Wall Pressure Vessels in the Earth's Field

5.1 Introduction

This chapter studies the stress-induced magnetic field of steel pipes with and without a circumferential welded joint. This is to enhance the practical understanding of using the remote magnetic field as the magnetic field of individual pipe sections and welded joints contributes towards the total field of the pipeline. The experiments were performed on steel pipes in the laboratory, together with the field observations on the above-ground live pipelines at Pannal, UK. A finite element model has been developed and verified in order to support the analysis.

The simulation model of steel pipes is implemented in the COMSOL multiphysics modelling software. Similar to the bar model, the pipe model also requires three modules including the structural mechanics, the AC/DC and the non-linear magnetic material modules.

In the chapter, Section 5.2 proposes a hypothesis of magnetic features of a circumferential welded joint, which will be used to simulate the initial magnetic condition of the weld area. The experimental method was described in Section 3.5 and 3.6, and is summarised in Section 5.3. Section 5.4 describes the model development including implementation of the stress-magnetisation relationship. Sec-

tion 5.5 discusses the findings using the experimental and simulation results. In particular, variation of magnetisation with stress in pipelines is presented in Section 5.5.1. The resultant magnetic field and magnetic indication of stress on individual pipe sections are presented in Section 5.5.2 and 5.5.3. Its variation with the initial magnetic condition and the measurement height are analysed after that. Finally, the effect of welded joints is discussed in Section 5.5.4.

5.2 Hypothesis of magnetic features of a circumferential welded joint in pipeline

It is known that as a result of fabrication, each steel pipe section has a residual magnetisation which may produce fluctuations in magnetic field measured along the pipeline [43, 60]. Because it contributes towards the total field measured by the above-ground surveys as used in the SCT technology, the residual magnetisation needs to be included in the model.

This study proposes two possible types of magnetic orientation of a welded joint in pipeline as shown in Fig. 5.1. In fact, it is categorised based on the orientation of the residual magnetisation M_r of two pipe sections of the weld, which includes the magnetic history of the material before welding.

Type 1 is shown in Fig. 5.1a, where M_{r_1} and M_{r_2} are in the same orientation. The resultant magnetic feature may include a peak in B_x and a mean-level crossing in B_z. Location of the peak in B_x may be shifted toward left or right because it depends on the difference between M_{r_1} and M_{r_2}.

Type 2 is shown in Fig. 5.1b, where M_{r_1} and M_{r_2} are in the opposite orientation. Inversely, the resultant magnetic feature may include a peak in B_z and a mean-level crossing in B_x. In addition, its magnitude may be much stronger than type 1 because it is the sum of the magnetic field of two pipe sections.

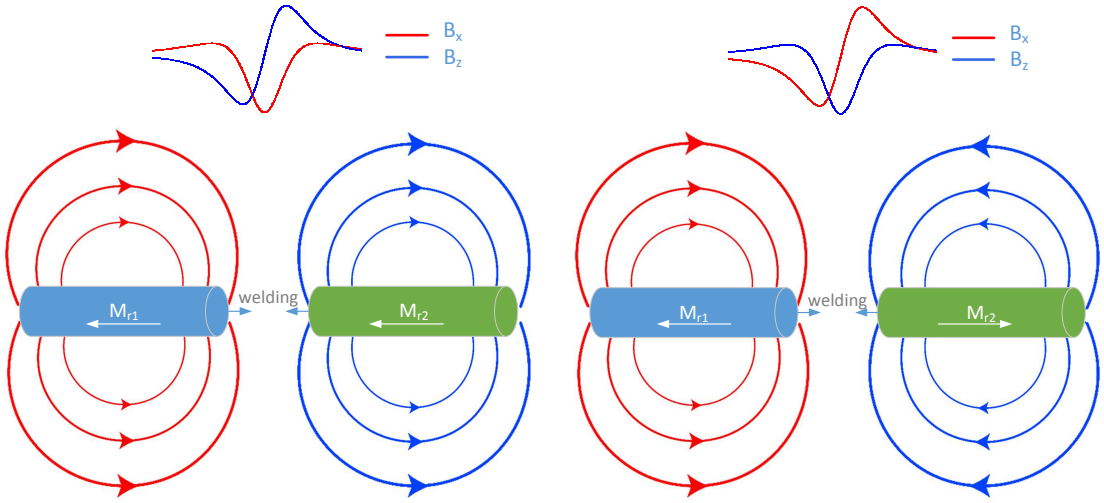

(a) Type 1: same orientation.

(b) Type 2: opposite orientation.

Figure 5.1: Two types of magnetic orientation of welded joint in pipeline. It is categorised based on the orientation of the residual magnetisation of two pipe sections of the weld.

In order to simplify the simulation model, it was assumed that M_r has only one component, which is along the length of the pipe. When pressure is applied, the weld acts as a discontinuity of magnetic properties between two pipe sections, and stress enhances the existing magnetic pattern of each pipe section. For this reason, magnetic features of a welded joint may be enhanced as well. This has not considered the effect of stress on the weld area itself yet.

5.3 Experimental method

The laboratory experiments and the field observations were performed, and the results were used to verify the pipe model. These were described in details in Chapter 3 and are summarised here.

In the laboratory, four of 1.8 m, 6-inch pipes were professionally manufactured and tested at 90 bar by the project partner DNV/GL. Two were plain pipes and the other two were made with a circumferential welded joint. The pressure of up to 60 bar was applied to the pipe and the magnetic field was measured on horizontal planes P_d above the pipe at different heights as shown in Fig. 5.2a. Details

of the laboratory experiment on steel pipes can be referenced to Section 3.5.

In addition to the experiments in the laboratory, field observations were performed on above-ground live pipelines at Pannal AGI site, where it allowed controlling the measurement height and visually checking pipeline features such as bends and welds. The observations were performed on the 18-inch and 30-inch pipelines. Details about the measurements using the mobile measurement system are shown in Fig. 5.2b. References should be made to Section 3.6 for the method of the field observations.

5.4 Model development

This section describes the pipe model to simulate the effect of stress to the magnetisation and magnetic field of the steel pipes with and without a welded joint.

As shown Fig. 5.3, the pipe model included three coupled models: the solid mechanics model, the magnetic model and the material model. The solid mechanics model solved for the displacement $\mathbf{u}$ of the pipe material. Its first principal stress σ was used as an input of the material model, which solved for the effect of stress to the magnetic property of the pipe material. The magnetic model then used this variation of magnetic property to solve for the induced magnetic field through the dependent variable V_m representing magnetic scalar potential of the pipe.

An addition parameter M_r was introduced in the model in order to simulate the residual magnetisation of individual pipe sections before welding, as presented in the hypothesis above. It required solving the initial magnetic condition of pipe sections in the earth's field before the pipe was pressurised.

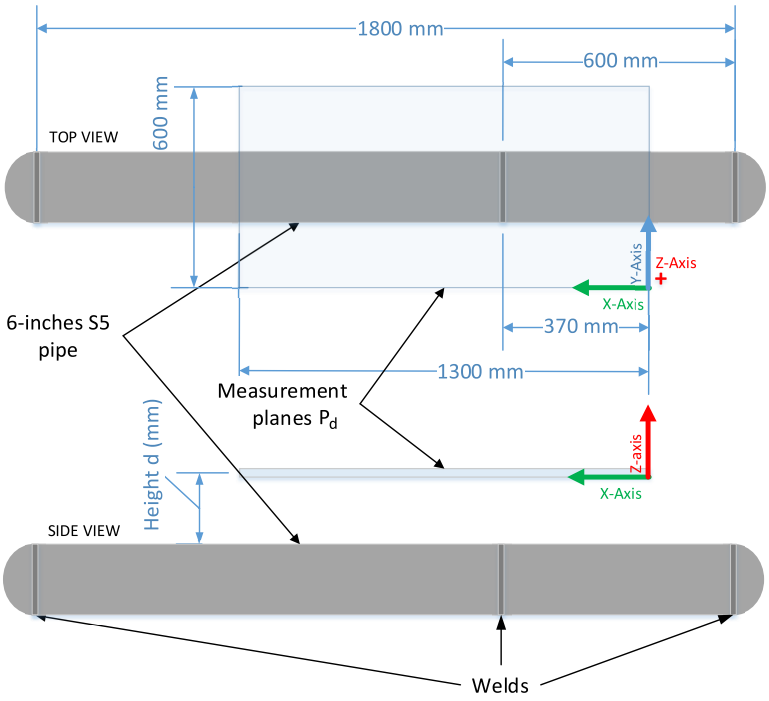

(a) A 6-inch pipe and its measurement planes.

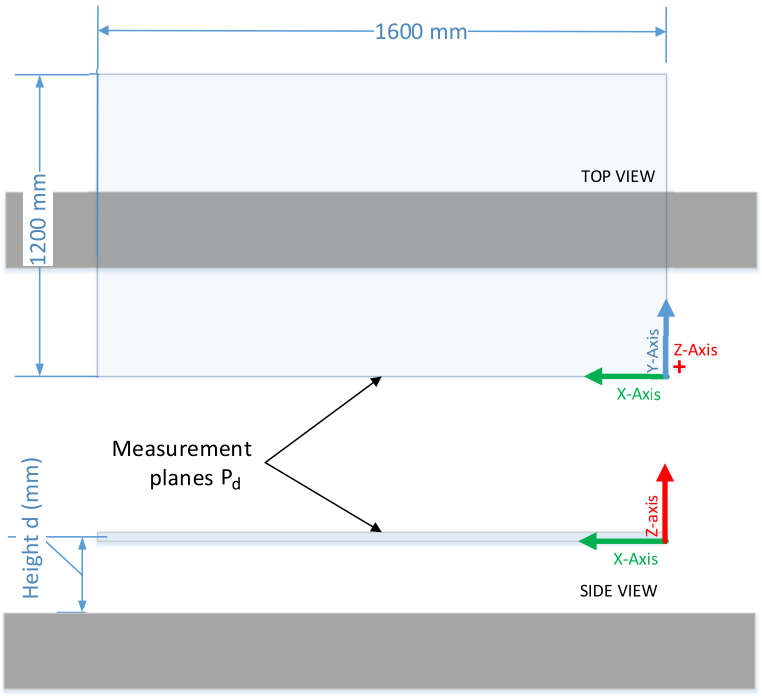

(b) Above-ground pipeline and its measurement planes.

Figure 5.2: Steel pipes and the measurement plane in the laboratory experiment and field observations.

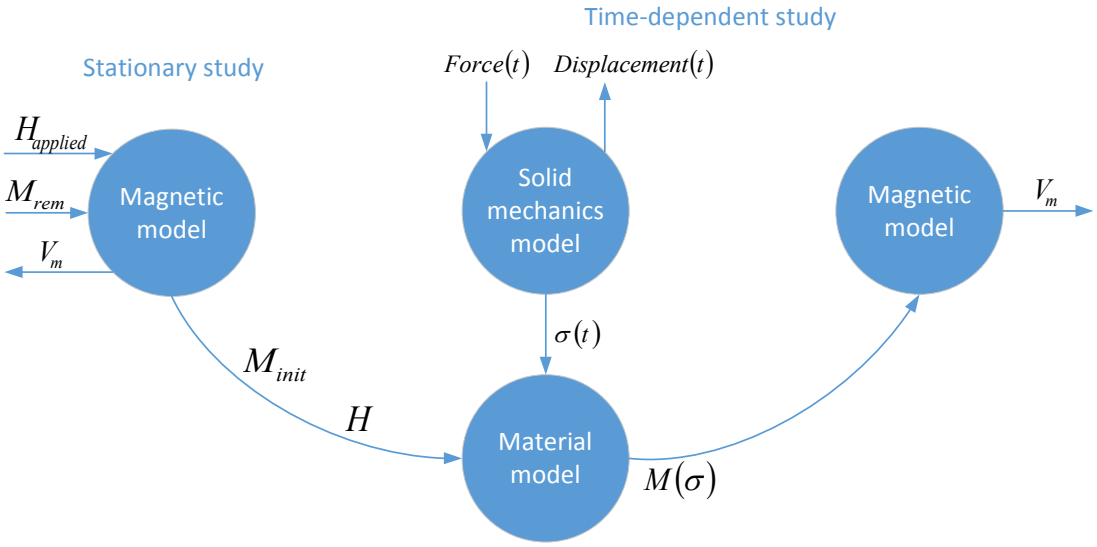

Figure 5.3: Method of coupling constitutive relations.

5.4.1 Geometry

Fig. 5.4a shows the geometry of the pipe, which was similar to the pipes used in the laboratory. It was a 6-inch pipe, 1.8 m length and 5.4 mm wall thickness. The pipe was supported by two wooden blocks positioned at ±500 mm. Actually, these wooden blocks caused no effect on the induced magnetic field, but using it helped the convergence of the solid mechanics model. A 20 mm width area simulating the welded joint was introduced at 300 mm offset from centre of the pipe. The weld position was chosen in order to avoid interference of magnetic features produced by the bulk material of the pipe itself.

Generally, the model consisted of six domains. Domain 1 was the surrounding air; domain 3 was the water inside the pipe; domains 2, 4 and 5 were three sections of the pipe in which domain 4 was to simulate the weld; and domain 6 was the wooden support. In case of modelling a plain pipe, i.e. pipe without the welded joint, domain 4 was merged with domain 2 and 5.

5.4.2 Boundary conditions

For the solid mechanics interface, the pressure was applied onto the inner wall of the pipe, meanwhile the wooden support was assumed to be fixed. Cycles of the applied pressure is shown in Fig. 5.4b.

For the magnetic interface, the pipe was assumed to be in the earth's field, $\mathbf{B_{bkg}} = (-10, -10, -35)$ μT, so six outer boundaries of the air domain were constrained to be the earth's field using the External Magnetic Field Interface in COMSOL.

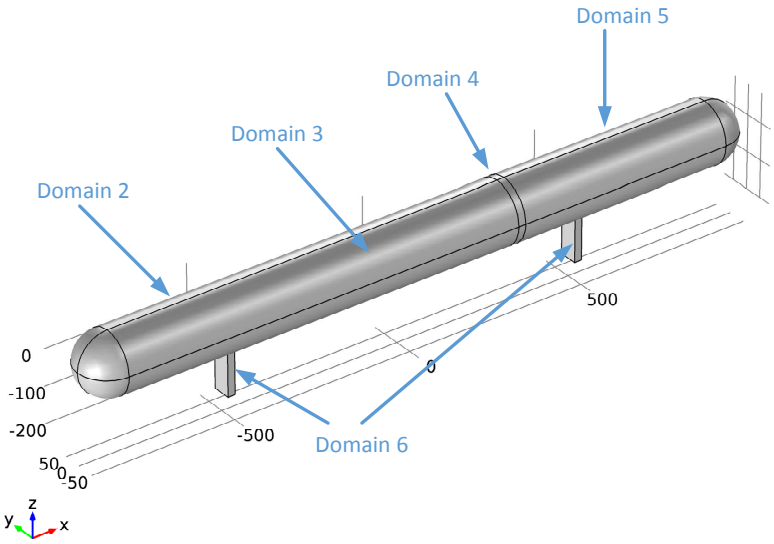

(a) Geometry of the model

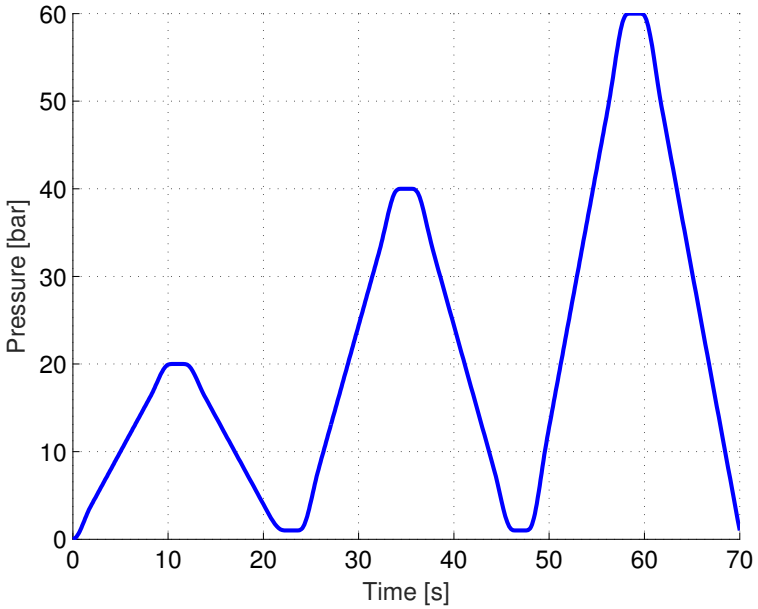

(b) Cycles of the applied pressure

Figure 5.4: Geometry and the applied pressure of the model.

5.4.3 Materials

In the model, air and wood were assigned to the surrounding air block and the supports, respectively; their relative magnetic permeability μ_r was set to 1.

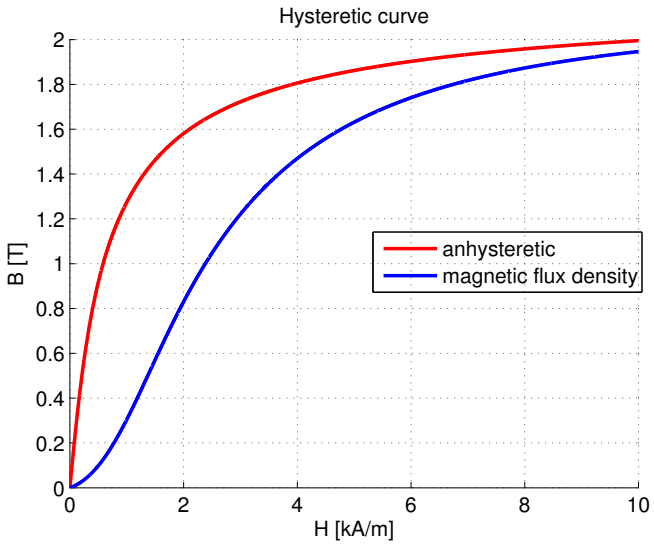

Figure 5.5: The hysteresis curve used to solve for the initial conditions.

The material of the pipe in the model was assigned as steel, see Table. 4.1 for its mechanical properties. The hysteresis curve of the material presented in Section 2.1 was separately solved in Matlab and imported into COMSOL, see Fig. 5.5. It was used to solve for the initial magnetic condition of the pipe in the earth's field, and to determine the relative permeability of the material. It should be noted that although the BH curve used in the model might not represent the actual curve of the material in the laboratory, this curve was defined as a model parameter, so it was ready to be replaced with the actual parameters. Determining magnetic properties of the material used in the laboratory was out of the scope of this study.

5.4.4 Meshing

There was no special requirement for meshing the model. The domains of the support blocks and the water were meshed with less elements when compared

to the domains representing the pipe and the surrounding air block to reduce simulation time.

Generally, the model consisted of more than 45000 domain elements and it was required to solve for more than 220000 degrees of freedom.

5.4.5 Model parameters

In addition to parameters explained in Chap. 4, additional parameters M_r were defined for individual sections of the pipe, see Table. C.2 in Appendix C. Using M_r allowed simulating the residual magnetisation of individual sections of the pipe before pressurised as explained in the proposed hypothesis.

5.4.6 Model studies

The model of steel pipes was solved by two studies. The first study was a stationary step, which solved for the initial magnetic condition of the plain pipe or individual pipe sections of the welded pipe in the earth's field. In this study, $\mathbf{H}_{bkg}$, M_r and the BH curve were used to determine the initial distribution of the magnetisation M_i and the quiescent working point on the BH curve.

The second study was a time-dependent step, in which the applied pressure was varied with time, see Fig. 5.4b. The study determined the stress σ and the corresponding stress-induced magnetisation $M(\sigma)$ for each element of the pipe using the Jiles-Atherton model. This was where the initial magnetic condition employed, by which varying the initial condition would produce a different resultant distribution of magnetisation in the pipe wall, and so was the induced magnetic field.

5.4.7 Implementation of the constitutive relations

Solving of the solid mechanics model and the magnetic model were supported in COMSOL. Given $\mathbf{u}(u, v, w)$ is a dependent variable representing the displacement of the solid material,

$$\mathbf{u} = \mathbf{0} \tag{5.1}$$

on the fixed boundaries of the support blocks.

Stress σ on the inner pipe wall was determined by the applied pressure P as follows:

$$\sigma \cdot \mathbf{n} = -P\mathbf{n}, \tag{5.2}$$

where $\mathbf{n}$ is the normal vector of the loaded boundary.

The displacement of the solid material was then solved with time t by:

$$\rho \frac{\partial^2 \mathbf{u}}{\partial^2 t} = \mathbf{f}_V - \nabla \cdot \sigma, \tag{5.3}$$

in which $\mathbf{f}_V$ is the volume force vector, and ρ is the material density.

The initial magnetic condition of pipe sections with the corresponding residual magnetisation M_r while the pipe was in the earth's field $\mathbf{H}_b$ was solved by:

$$\nabla \cdot \mathbf{B} = \nabla \cdot (\mu_0 \mu_r \mathbf{H}) = 0, \tag{5.4}$$

$$\mathbf{H} = -\nabla V_m + \mathbf{H}_b, \tag{5.5}$$

$$\mathbf{B} = \mu_0 \mu_r \mathbf{H} + \mathbf{B}_r, \tag{5.6}$$

where the residual field $B_r \approx \mu_0 M_r$; and the magnetic property of the pipe material μ_r was determined from the BH curve shown in Fig. 5.5.

In the time-dependent study, in order to solve for the stress-induced magnetic field, Equ. 5.6 was replaced by:

$$\mathbf{B} = \mu_0(\mathbf{H} + \mathbf{M}), \tag{5.7}$$

where M was stress-dependent and was determined as follows:

$$\frac{dM}{d\sigma} = \frac{1}{\epsilon^2}\sigma(M_{an} - M) + c\frac{dM_{an}}{d\sigma}. \tag{5.8}$$

5.5 Results and Discussions

5.5.1 Effects of stress on magnetisation

Because of using the Jiles-Atherton model for the magnetomechanical effect, the variation of magnetisation of the material with stress can be represented through the effective magnetic field H_{eff}. Fig. 5.6 shows variation of this effective field when the applied pressure was increased from 0 to 60 bar in the model. Before applying the pressure to the pipe, the effective field was approximately the applied field, $H_{eff} = 8$ A/m. It was increased to the maximum value of 35 A/m at 50 bar and then reduced after that. The shape of this curve followed the stress-magnetisation relationship used in the pipe model, which was the same relationship implemented in the bar model. The parameters of this relationship are shown in Table. C.2.

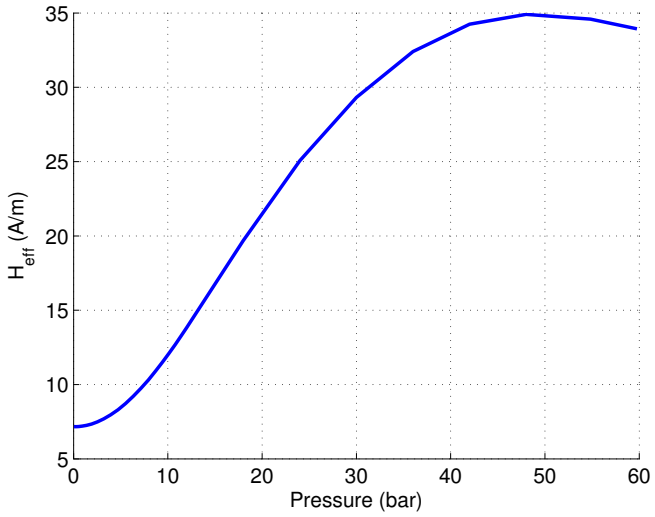

Figure 5.6: Variation of the effective magnetic field with the applied pressure.

Simulation of the magnetisation M of the pipe with stress is shown in Fig. 5.7. Because the pipe was placed in the earth's magnetic field, $\mathbf{B_{bkg}} = (-10, -10, -35)\ \mu$T, its magnetisation was about 2 kA/m and was distributed as shown in Fig. 5.7a. Under a pressure of 40 bar applied onto the inner wall of the pipe, M was increased to about 4 kA/m, see Fig. 5.7b.

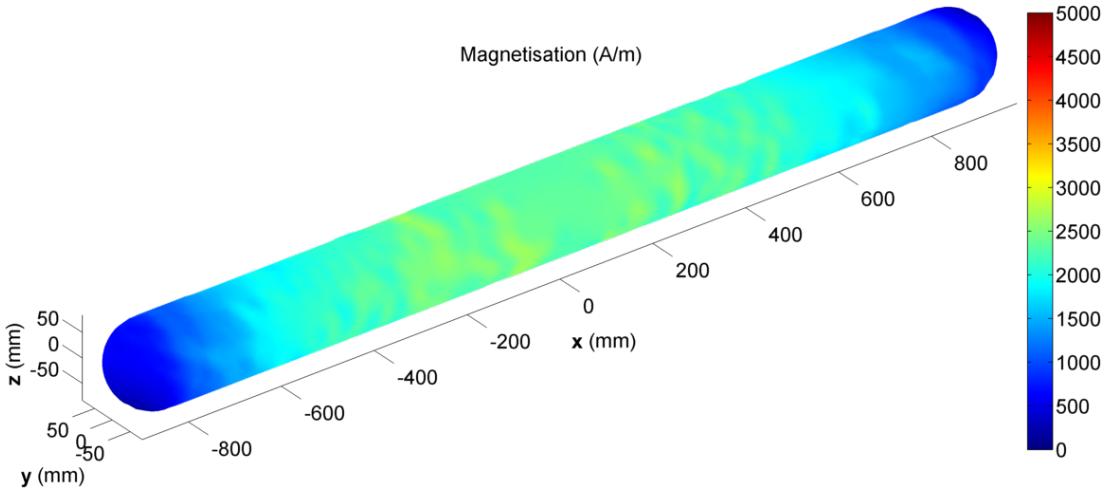

(a) Before applying the pressure.

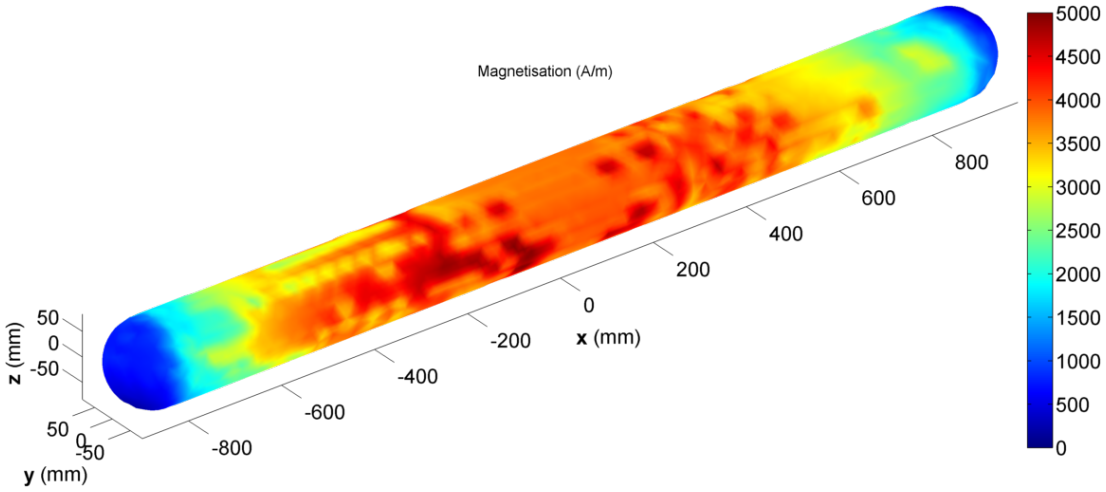

(b) At the pressure of 40 bar.

Figure 5.7: Simulation of magnetisation M of the plain pipe in the earth's field before and while being applied the pressure. M at the pressure of 40 bar was increased from the initial magnetic condition.

Fig. 5.8 shows the variation of the average magnetisation of the pipe with three cycles of the applied pressure from 20 bar to 60 bar. The average magnetisation M of the pipe increased and tended to approach the anhysteretic magnetisation M_{an}, so it complied with the Jiles-Atherton model. It should be noted that with this stress-magnetisation relationship, M was increased with increasing of the applied pressure, and then decreased when the pressure reached 50 bar, which was similar to the curve of $H_{eff}(\sigma)$.

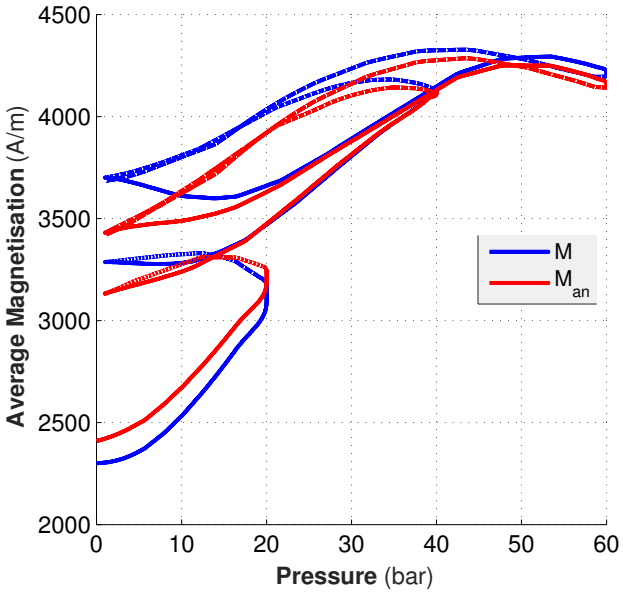

Figure 5.8: Variation of the average magnetisation of the plain pipe with three cycles of pressure. This followed the $M(\sigma)$ curve of the material used in the simulation model.

5.5.2 Effects of stress on the remote magnetic field and magnetic indication of stress concentration

Fig. 5.9 shows the background field $\mathbf{B_{bkg}}$ measured in the laboratory. Removal of this background field from the magnetic field measured above the pipe $\mathbf{B_{meas}}$ would result in the magnetic field of the pipe only $\mathbf{B_p}$:

$$\mathbf{B_p} = \mathbf{B_{meas}} - \mathbf{B_{bkg}}. \tag{5.9}$$

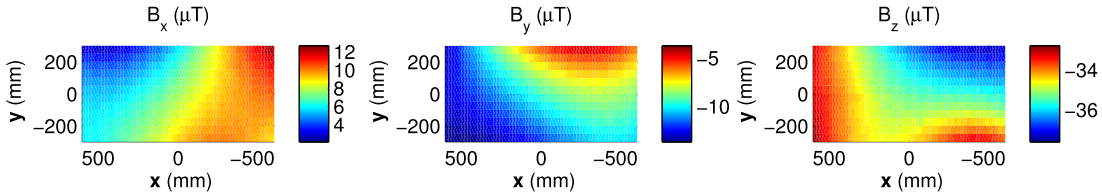

Figure 5.9: The background field $\mathbf{B_{bkg}}$ in the laboratory measured without the pipe.

Fig. 5.10 compares the magnetic field $\mathbf{B_p}$ of the plain pipe between the experiment and the simulation before and while being applied the pressure. The simulation predicted a similar field to the experiment, in particular, a peak appeared in B_x, and B_z gradually crossed a mean level.

The simulation also successfully predicted the effect of stress to the magnetic field when compared between Fig. 5.10c and Fig. 5.10d. Under stress, the shape of the magnetic features was kept with an increasing in its magnitude. There was a small difference in magnitude of $\mathbf{B_p}$ between the experiment and the simulation. It was because of not using the actual magnetic properties of the pipe material, instead, the simulation model used the BH curve shown in Fig. 5.5, and the stress-magnetisation relationship with parameters shown in Table. C.2. However, this does not affect qualitative studies on the stress-induced magnetic field of the pipe.

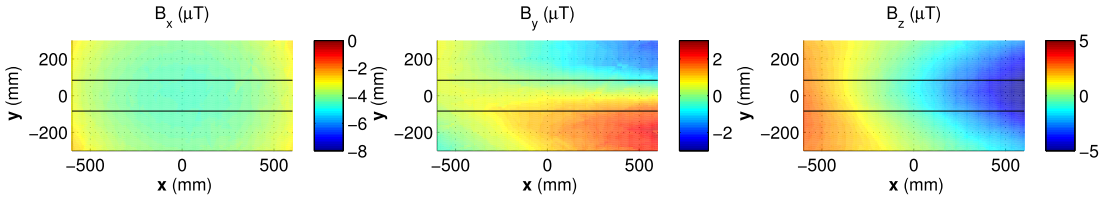

(a) **Simulation**: before the pressure was applied.

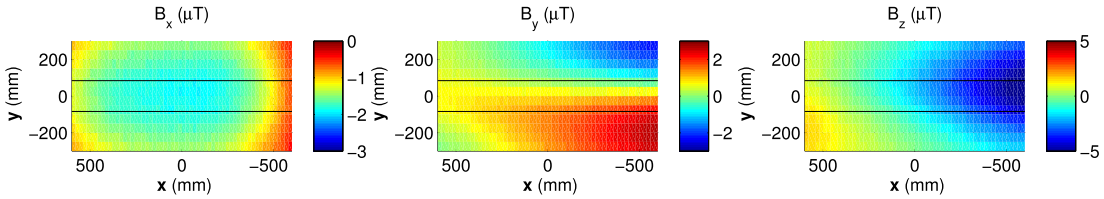

(b) **Experiment**: before the pressure was applied.

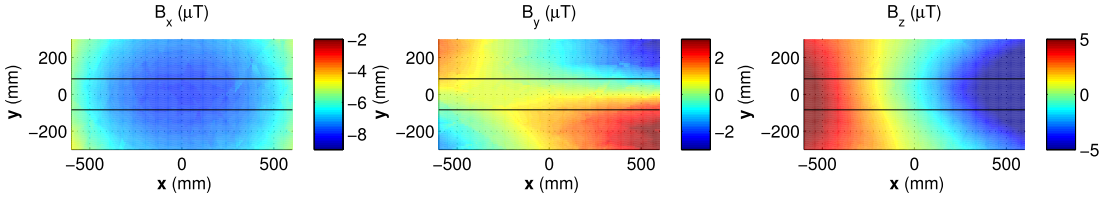

(c) **Simulation**: at the pressure of 40 bar.

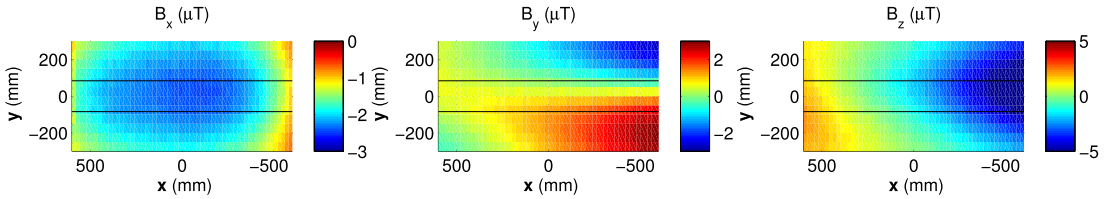

(d) **Experiment**: at the pressure of 40 bar.

Figure 5.10: Comparison of magnetic field $\mathbf{B_p}$ of the plain pipe between the experiment and the simulation before and while the pipe was being pressurised. The field was measured on a horizontal plane at the height of 300 mm above the pipe. The underlying pipe was represented as two solid black lines.

Magnetic indication of stress concentration of individual pipe sections

Fig. 5.11 shows B_x and B_z when measured along the centre line, at the height of 100 mm on top of the pipe. In the figure, the applied pressure varied the magnitude of B_x and the slope of B_z. In the experiment, after the pressure threshold of 20 bar, B_x was approximately increased 0.4 μT for every 10 bar, together with a steeper slope in B_z. In the simulation, the magnitude of B_x and the slope of B_z were also increased with the applied pressure from 10 bar to 50 bar, but then decreased at 60 bar. Although the simulation result was not completely agreed with the experimental result, it agreed with the $M(\sigma)$ relationship used in the simulation model as the curve predicted a decrease of magnetisation at around 50 bar to 60 bar, see Fig. 5.8.

The above disagreement of the variation of the magnetic field with stress between the experiment and the simulation was because the simulation used the stress-magnetisation relationship with the parameters shown in Table C.2 instead of the actual relationship of the material used in the experiment. But nonetheless, they both suggested that it may be possible to determine stress condition of the pipe through the magnetic field provided that the stress-magnetisation relationship $M(\sigma)$ of the material is known.

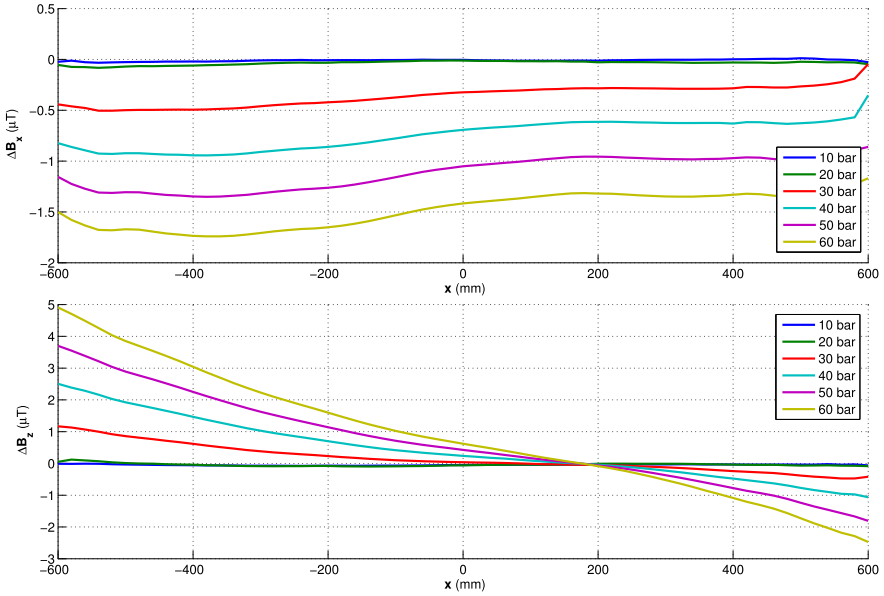

(a) Experiment

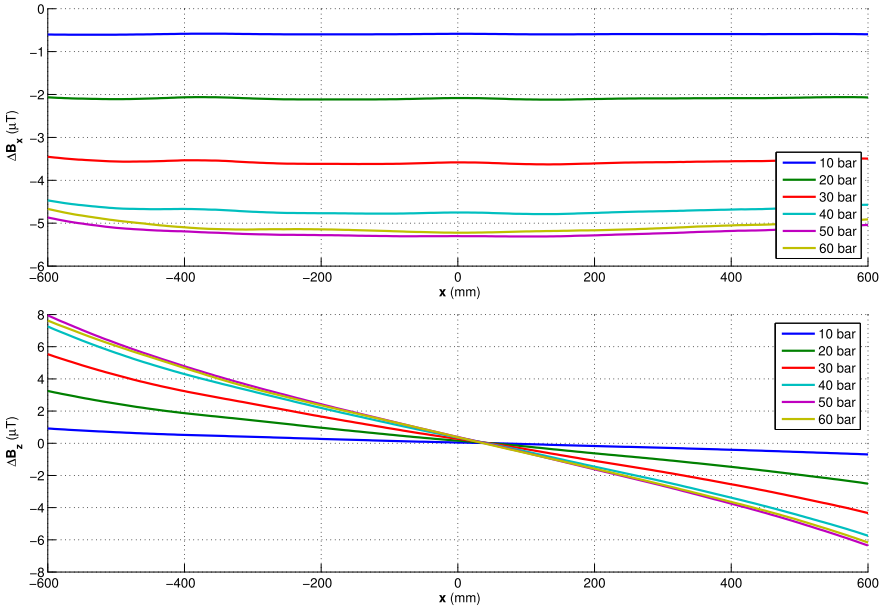

(b) Simulation

Figure 5.11: Variation of B_x and B_z with the applied pressure when measured along the centre line at 100 mm height right on top of the pipe. The variation depended on the stress-magnetisation relationship of the material.

5.5.3 Strength of magnetic indication of stress concentration

Study on the pressure level

Similar to the magnetic indication used in Chapter 4, given $K = \partial B_z/\partial x$ representing the slope of B_z, the variation of K with stress was determined by the stress-magnetisation relationship $M(\sigma)$ of the material. It suggested that K could be used as a basic diagnostic parameter for pipeline inspection.

Fig. 5.12 shows how K varied with the applied pressure in the experiment and the simulation when the field was measured at 100 mm height along the centre line of the pipe. In the experiment, a higher stress resulted in a stronger K. It was similar to the simulation except for the pressure of 50 bar to 60 bar. Again, this is explained by the fact that the $M(\sigma)$ curve used in the simulation model was probably not the $M(\sigma)$ curve of the pipe material in the laboratory.

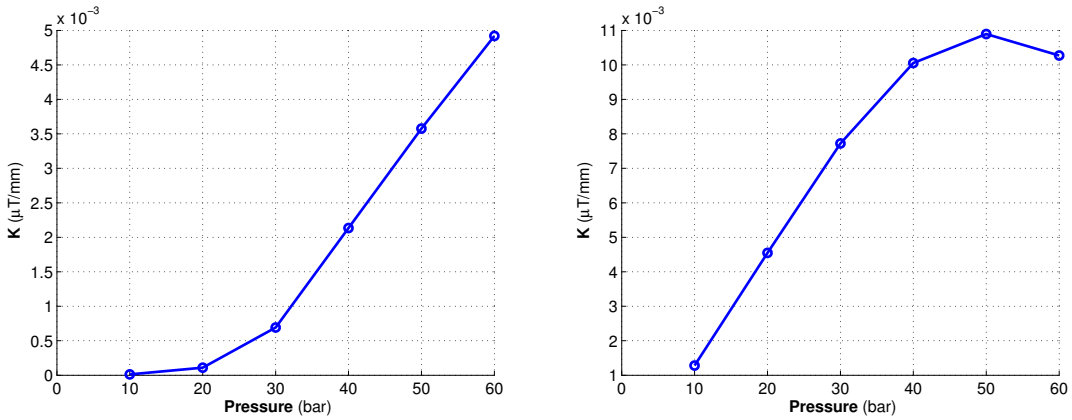

(a) Experiment (b) Simulation

Figure 5.12: A comparison of variation of K with the applied pressure between the experiment and the simulation. The magnetic field was measured at 100 mm height along the centre line of the pipe with the applied pressure of 10 bar to 60 bar.

Study on the initial magnetic condition before pressurisation

The initial magnetic condition before the pipe is pressurised plays an important role in determining strength of the magnetic indication because it affects the distribution and magnitude of the stress-induced magnetisation, so the induced magnetic field is also affected. In the plain pipe model, the initial magnetic condition of the pipe was determined while the pipe was placed in the earth's field only, no residual magnetisation was involved.

Fig. 5.13 shows the variation of K when the x component of the background field, which was parallel to the axial direction of the pipe, was increased from 10 μT to 100 μT at four pressures.

In the figure, K was linear with the applied field at the given pressures. Increasing the applied field resulted in an increase of K. This relationship was dependent on the applied pressure. In particular, the higher the applied pressure was, the more sensitive K was with varying of the applied field.

Inversely, K was more sensitive with stress at higher applied fields. For example, the variation of K with stress at the applied field of 10 A/m was much smaller than that at 100 A/m. In terms of pipeline inspection, it means there may be a higher probability of detecting the magnetic indication and estimating the strength K of a stress concentration if the pipe is in a higher applied field because K will be more sensitive with stress.

This behaviour of K with the initial magnetic condition was very similar to what has been found using the bar model. Therefore, the relationship of K with the applied field and stress can be represented as in the following equation:

$$K = a(\sigma)H_{applied}, \tag{5.10}$$

in which a is a version of the stress-magnetisation relationship, and $H_{applied}$ is the field applied along the axial direction of the pipe.

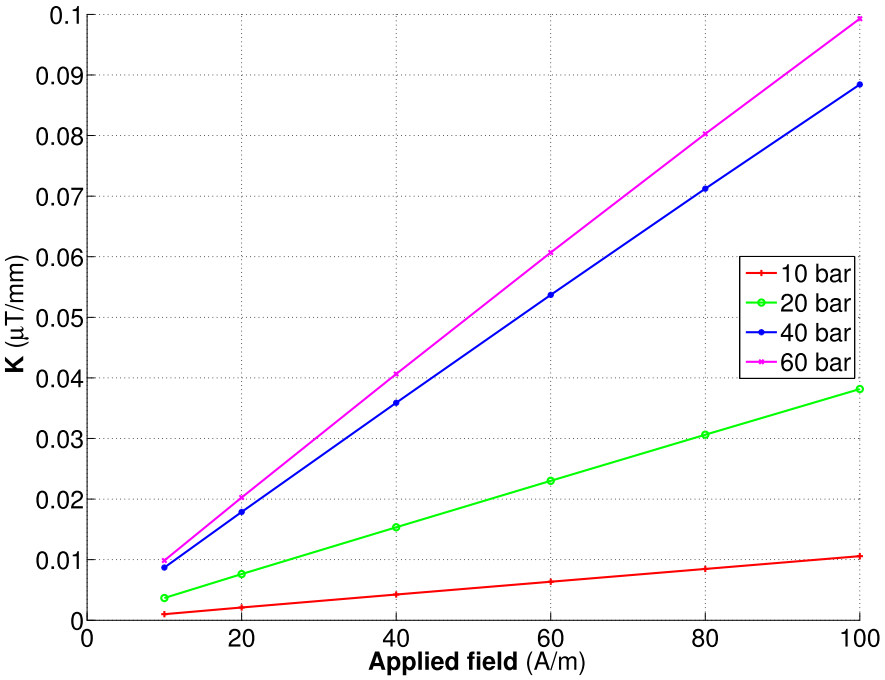

Figure 5.13: Simulation of variation of K with the applied field at the given pressure of 10 bar to 60 bar.

Quantitative study on the measurement height

This study focuses on using the remote-sensing magnetic field, which is the magnetic field measured at a distance from the material, to infer stress conditions of the pipeline, so the measurement height affects the strength of the magnetic indication K. In case of underground pipeline inspection, this measurement height is the depth of cover plus the height of the magnetometer array above the ground, which is usually between 2.5 m to 3.5 m.

Fig. 5.14 shows B_x and B_z measured along the centre line on top of the pipe at the height of 100 mm to 1100 mm and the pressure of 60 bar. In the figure, when moving away from the pipe, together with a decrease in magnitude of B_x, the slope of B_z was also decreased. It is expected that this relationship between K and the measurement distance will be similar to that obtained from the bar model, in which K exponential decays with the ratio of the measurement height d and the length of the pipe L.

Given a function $K(r)$ represented in one of the two following forms:

$$K_1(\sigma, r) = a_0 \exp(b_0 r), \tag{5.11a}$$

$$K_2(\sigma, r) = a_1 \exp(b_1 r) + a_2 \exp(b_2 r), \tag{5.11b}$$

in which $r = d/L$; a_i was stress-dependent and b_i was the same constants representing the decaying rate obtained from the bar model.

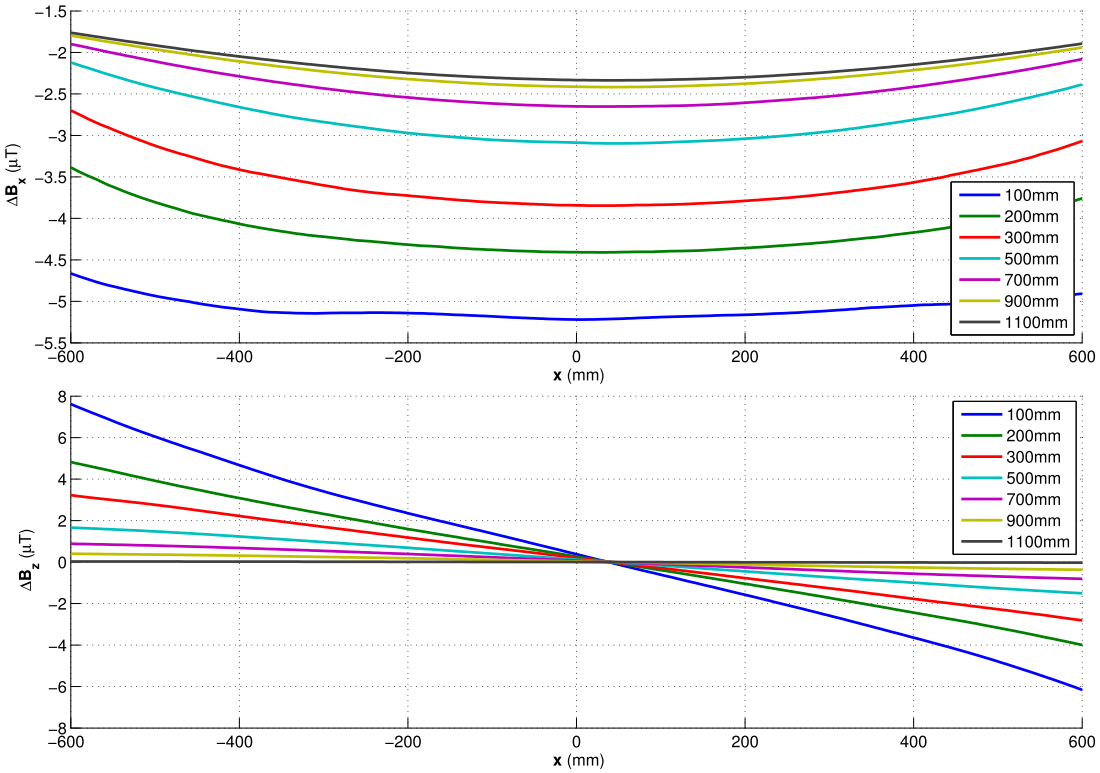

Figure 5.14: Simulation of B_x and B_z measured along the centre line right on top of the pipe with the measurement height. The magnetic field was measured at the heigh of 100 mm to 1100 mm while the pipe was pressurised at 60 bar in the background field $\mathbf{B_{bkg}} = (-10, -10, -35)\ \mu$T.

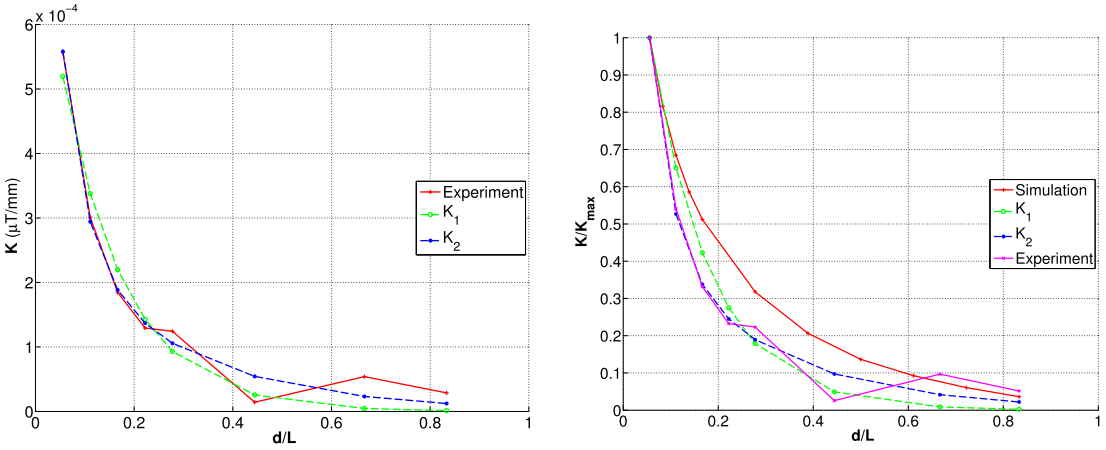

(a) K_1, K_2 and the experimental result.

(b) Variation of normalised K

Figure 5.15: A comparison of variation of K with $r = d/L$ between the experiment, the exponential equations and the simulation when the pipe was pressurised at 60 bar in the background field of $B_{bkg_x} = -10$ μT. $a_0 = 0.0008, b_0 = -7.746$; $a_1 = 0.001, b_1 = -20.81, a_2 = 0.00029, b_2 = -3.822$

Fig. 5.15 compares the experimental results with K_1 and K_2 and the simulation results. In Fig. 5.15a, K_1 and K_2 functions appeared to agree with the experimental result. Statistically, the root mean squared errors (RMSE) were $3.475e-5$ and $2.026e-5$, respectively.

However, as shown in Fig. 5.15b, although K_1 and K_2 still provided a good prediction, the simulation did not completely follow the experimental result. This behaviour of the simulation result is probably due to the fact that the model only took into account the x component of magnetisation, which is along the length of the pipe. Considering the other two components of the stress-induced magnetisation may help to improve the prediction of $K(r)$.

Nonetheless, the agreement between the experiment and the exponential functions of $K(d/L)$ is an important result because it confirms the possibility to solve for stress condition through the remote-sensing magnetic field using the technique presented in Sec. 4.4.4.

5.5.4 Effects of circumferential welded joints in pipeline on the remote magnetic field

Because pipeline consists of many pipe sections, in addition to studying the stress-induced magnetic field of a plain pipe section, it is also required to study the field caused by welding pipe sections together. In the laboratory experiment, a welded pipe was manufactured by cutting the pipe into halves and welding them together. The weld was located at 300 mm offset from the centre of the pipe.

The experimental procedure on the welded pipe was similar to what was performed on the plain pipe. In particular, the magnetic field was measured on horizontal planes above the pipe at the measurement height d before and while it was pressurised, denoted as $B_{\sigma=0}$ and B_σ respectively. The difference $\Delta B = B_\sigma - B_{\sigma=0}$ would show the effect of stress on the magnetic field of the pipe.

Fig. 5.16 shows three components of the stress-induced magnetic field of the welded pipe at three pressure levels. Although the welded pipe was very similar in shape to the plain pipe, the induced magnetic field was different and appeared to distinguish the weld. While applying the pressure on the plain pipe produced a peak in B_x and a mean-level crossing in B_z, for the welded pipe, B_x crossed a mean level, meanwhile, a peak appeared in B_z at the weld area. Moreover, the magnetic anomaly appearing at the weld area was enhanced with increasing of the applied pressure.

This behaviour may be explained using the hypothesis presented in Sec. 5.2. The weld acts as an area of discontinuity of magnetic property, so stress tends to enhance the existing domain structure on two sides of the weld. Therefore, the residual magnetisation M_r of pipe sections before applying the pressure plays an important role in determining magnetic features at the weld area.

Based on this hypothesis, the simulation model of a welded pipe was built, in which M_r of two pipe sections was -1.5 kA/m and 6 kA/m, respectively. This orientation of the residual magnetisation can be categorised as Type 2 in the hypothesis. The background field was set to $B_{bkg_x} = -10$ μT in the simulation.

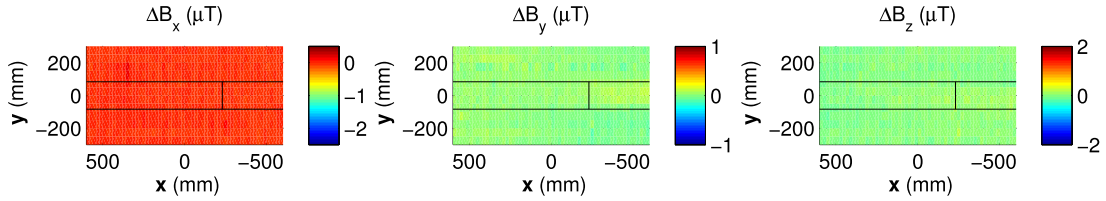

(a) 5 bar

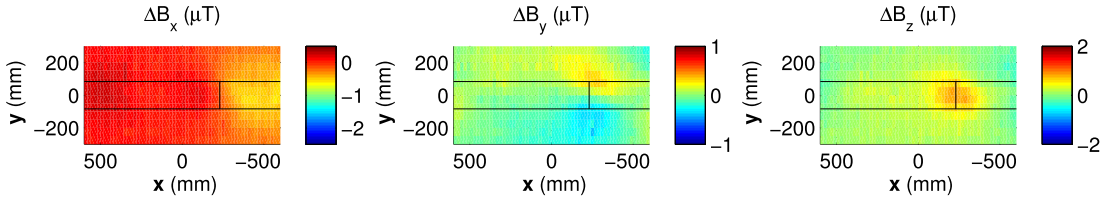

(b) 20 bar

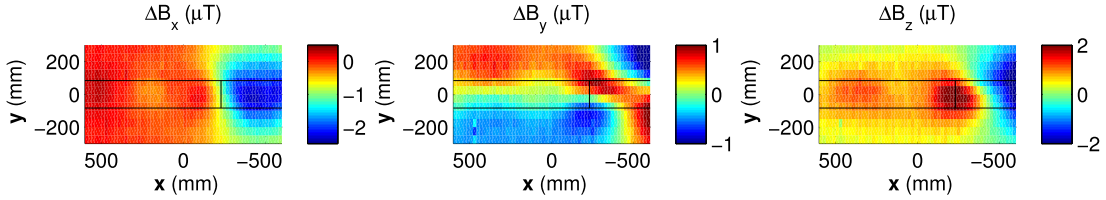

(c) 60 bar

Figure 5.16: Effects of stress on the magnetic field of the welded pipe in the experiment. The stress-induced magnetic field $\Delta B = B_\sigma - B_{\sigma=0}$ was measured at the height of 100 mm. The underlying pipe and the weld were represented as the black solid lines.

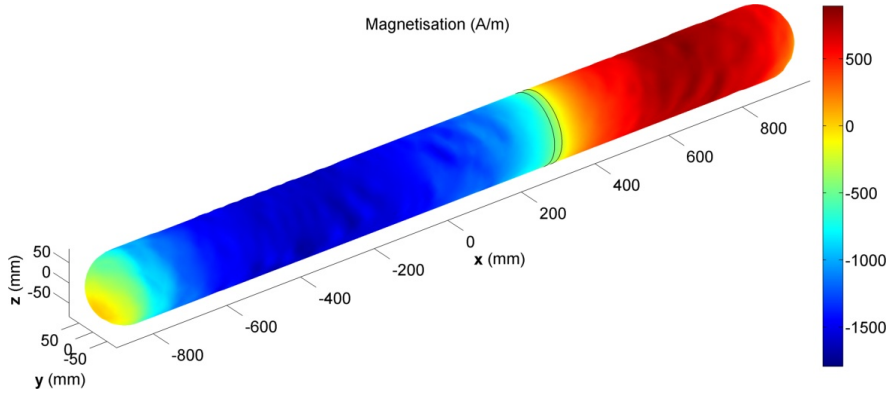

Figure 5.17: Simulation of magnetisation of the welded pipe in the earth's field, $B_{bkg_x} = -10$ μT, before applying the pressure. The remnant magnetisation of pipe sections $M_{r_1} = -1.5$ kA/m and $M_{r_2} = 6$ kA/m.

Fig. 5.17 shows the initial magnetisation of the welded pipe before pressurisation. M_i was negative on section 1, i.e. the left-hand pipe section, and was positive on section 2, i.e. the right-hand section.

With the initial magnetic condition presented above, Fig. 5.18 shows the simulation of the stress-induced magnetic field when measured on a horizontal plane at 100 mm height above the pipe. Stress enhanced the initial magnetic condition of individual pipe sections, which made a peak gradually appeared in B_z and a zero crossing appeared in B_x on top of the weld area. This magnetic indication became stronger with increasing of the applied pressure. Comparing with the experimental result shown in Fig. 5.16, the simulation and the experiment were agreed on the effect of stress to the magnetic indication of the weld. However, there was still a small difference in magnitude between the simulation and the experiment. And the values of M_r used in the simulation was established empirically.

Field observation of magnetic features caused by welding pipe sections

As summarised in Sec. 5.3, in addition to the simulation and the experiment with the small-scale pipes in the laboratory, field observations were performed on above-ground live pipelines at Pannal, where the pipeline and its welds were positioned using high accuracy GNSS receivers, and magnetic field was measured above the pipe using the mobile CNC-based measurement system, see Chap. 3.

Fig. 5.19a shows magnetic field measured on 4.8 m length of the 18-inch pipeline at Pannal. The magnetometer array was raised to 2 m above the pipeline. It should also be noted that, this magnetic field was measured by taking three consecutive 1.6 m-length measurements and stitched them together using the GNSS coordinates. This explained the artifact which appeared in the data.

When compared to the experiment and the simulation, the field observation confirmed that a peak in B_z and a mean-level crossing in B_x appeared on top of the weld area. Interestingly, because of measuring at a higher height, 2 m compared to 0.1 m, the magnetic features of the weld in the field observation were expanded. In fact, in Fig. 5.19a, only a half of the expected feature in B_z can be observed because it was impossible to locate the measurement system to measure the other half.

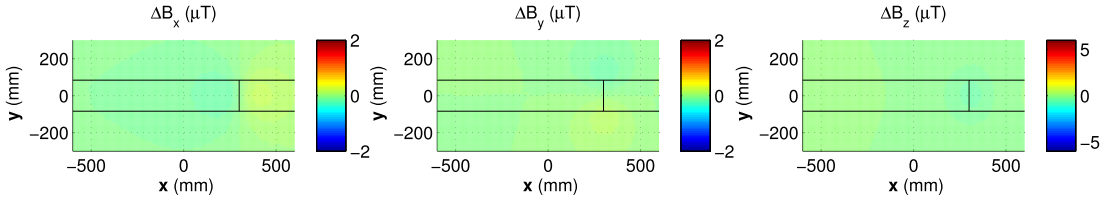

(a) 5 bar

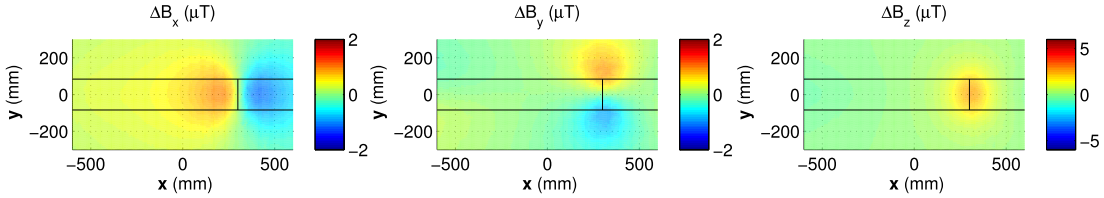

(b) 20 bar

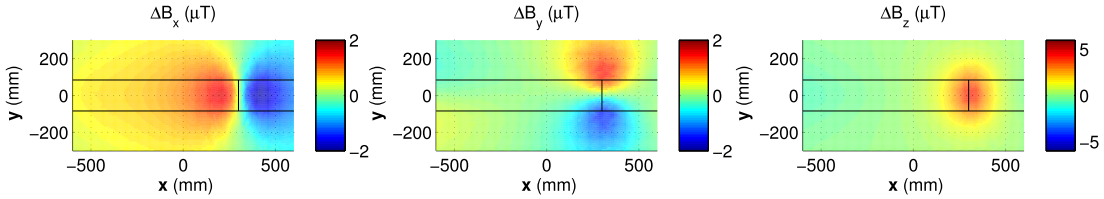

(c) 60 bar

Figure 5.18: Simulation of the stress-induced magnetic field of the welded pipe, in which $M_{rem_1} = -1.5$ kA/m and $M_{rem_2} = 6$ kA/m. The stress-induced magnetic field $\Delta B = B_\sigma - B_{\sigma=0}$ was measured at the height of 100 mm. The underlying pipe and the weld were represented as black solid lines.

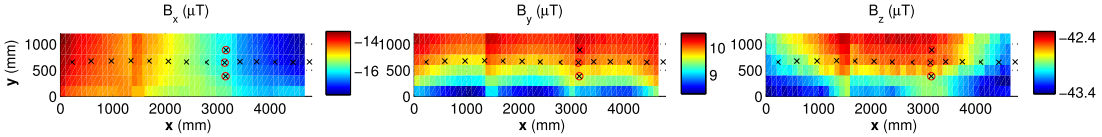

(a) **Field observation at Pannal**: Magnetic field was measured on 4.8 m length of the 18-inch pipeline at 2 m height. The centre of the pipe, marked as black crosses, and the location of the weld, marked as black crosses in red circles.

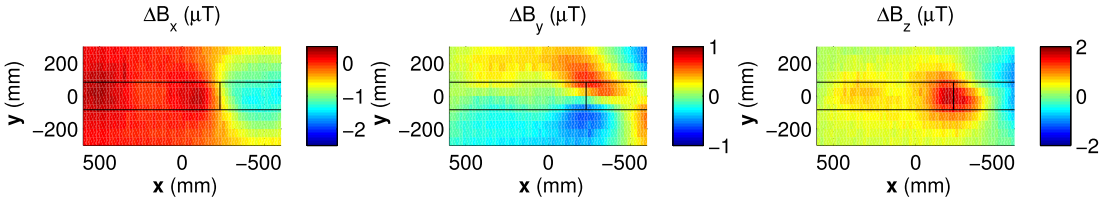

(b) **Experiment**: Magnetic field was measured at 100 mm height.

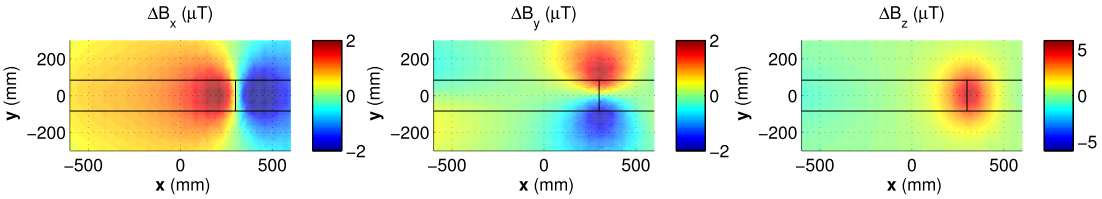

(c) **Simulation**: Magnetic field was measured at 100 mm height.

Figure 5.19: A comparison of magnetic features of welding pipe sections between the 18-inch live above-ground gas pipeline, the experiment in the laboratory and the simulation in COMSOL.

Effects of the residual magnetisation on magnetic features of a circumferential welded joint in pipeline

As suggested by the hypothesis presented in Section 5.2, magnetic features of a welded joint depend on the orientation of the residual magnetisation M_{r_1} and M_{r_2} of two pipe sections on two sides of the weld. In order to predict those magnetic features, a simulation was performed for the welded pipe, in which the residual magnetisation was varied both in the orientation and the magnitude.

Fig. 5.20 and Fig. 5.21 show the magnetic field measured on a horizontal plane at 100 mm height above the welded pipe pressurised at 60 bar, in which the residual magnetisation of individual pipe sections belonged to Types 1 and 2 in the hypothesis.

In the figure, a clear magnetic indication appeared around the weld area in all cases of Type 2, where M_{r_1} and M_{r_2} had opposite orientation. In 3 out of 4 cases, the magnetic features included a peak in B_z and a mean-level crossing in B_x. In cases of Type 1, where M_{r_1} and M_{r_2} had the same orientation, the magnetic indication only appeared when there was a considerable difference between M_{r_1} and M_{r_2}, see Figs. 5.20c, 5.20a. Otherwise, the magnetic indication of the weld was disappeared, as in Fig. 5.20d, or was very weak to detect compared to the others as in Fig. 5.20b. This means it is possible to locate welded joints of underground pipelines using the remote-sensing magnetic field. However, there would be a probability of missed detection, for example where two pipe sections have similar magnetisation in the same direction. Additionally, location of the weld may not be exactly at the location of the magnetic feature as this depends on the difference of magnetisation between two pipe sections.

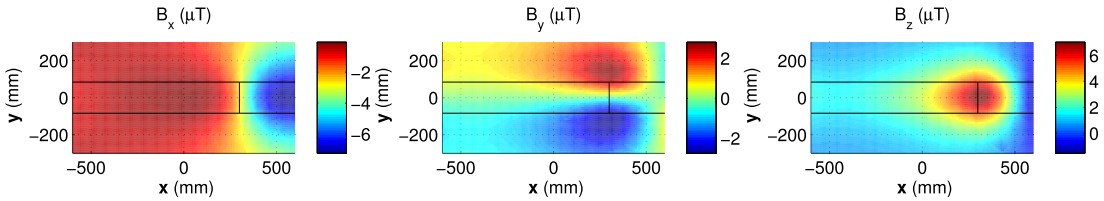

(a) $M_{r_1} = -1.5$ kA/m, $M_{r_2} = -6$ kA/m.

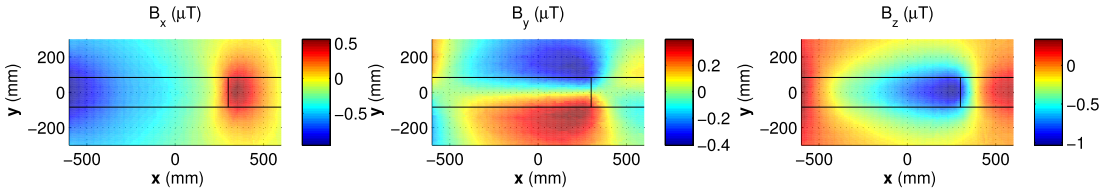

(b) $M_{r_1} = -1.5$ kA/m, $M_{r_2} = -1$ kA/m.

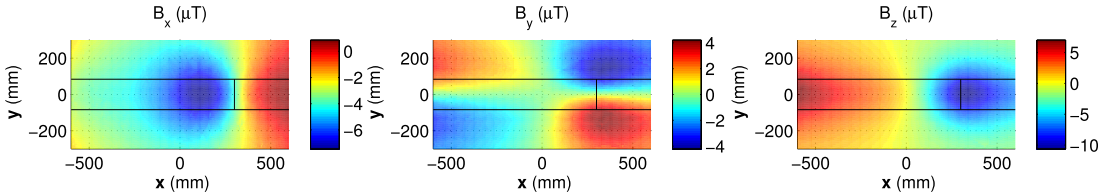

(c) $M_{r_1} = 1.5$ kA/m, $M_{r_2} = 6$ kA/m.

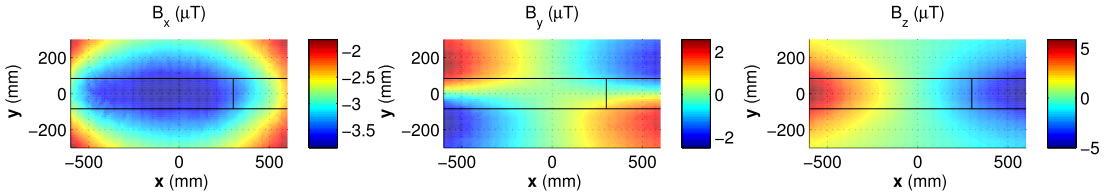

(d) $M_{r_1} = 1.5$ kA/m, $M_{r_2} = 1.0$ kA/m.

Figure 5.20: Simulation of typical magnetic features of a weld for Type 1 in the hypothesis. The field was measured on a horizontal plane at 100 mm height when the pipe was pressurised at 60 bar. The magnetic indication appeared when there was a considerable difference between M_{r_1} and M_{r_2}.

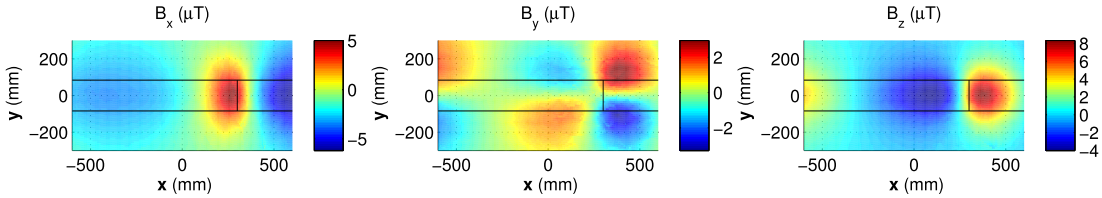

(a) $M_{r_1} = 1.5$ kA/m, $M_{r_2} = -6$ kA/m.

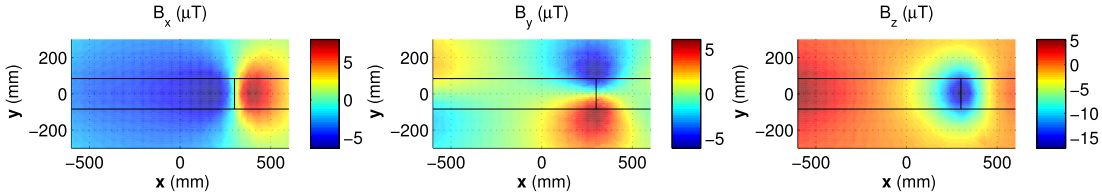

(b) $M_{r_1} = 1.5$ kA/m, $M_{r_2} = -1$ kA/m.

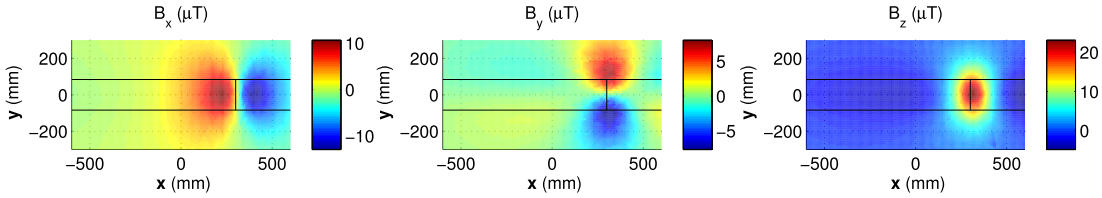

(c) $M_{r_1} = -1.5$ kA/m, $M_{r_2} = 6$ kA/m.

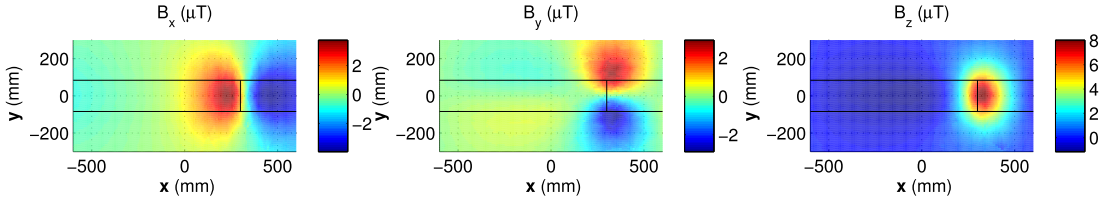

(d) $M_{r_1} = -1.5$ kA/m, $M_{r_2} = 1.0$ kA/m.

Figure 5.21: Simulation of typical magnetic features of a weld for Type 2 in the hypothesis. The field was measured on a horizontal plane at 100 mm height when the pipe was pressurised at 60 bar. The magnetic indication similarly appeared in 3 cases.

5.5.5 Magnetic indication of a circumferential welded joint using the spatial gradient magnetic field

Although magnetic features of individual pipe sections and that caused by a circumferential welded joint may appear in similar shapes, which includes a peak and a mean-level crossing in B_x and B_z, the magnetic indication of a section of the pipe extends on a longer length than that of a weld when measured at a given distance. Therefore, taking the gradient of magnetic field with respect to the axial direction could reveal the local magnetic indication of the weld.

Fig. 5.22 compares $\partial\mathbf{B}/\partial x$ measured above the welded pipe between the experiment and the simulation. The field was measured on a horizontal plane at 100 mm height on top of the pipe while it was pressurised at 60 bar. Clearly, the spatial gradient magnetic field enhanced the magnetic indication of the weld and diminished that of the bulk material.

Fig. 5.23 shows $\partial\mathbf{B}/\partial x$ on the centre line of the above measurement plane, i.e. $y = 0$. This was to simulate the magnetic field measured using only one magnetometer moving along the length of the pipe. It can be seen that, with just one magnetometer, the magnetic indication of the weld can be clearly distinguished from the surrounding material.

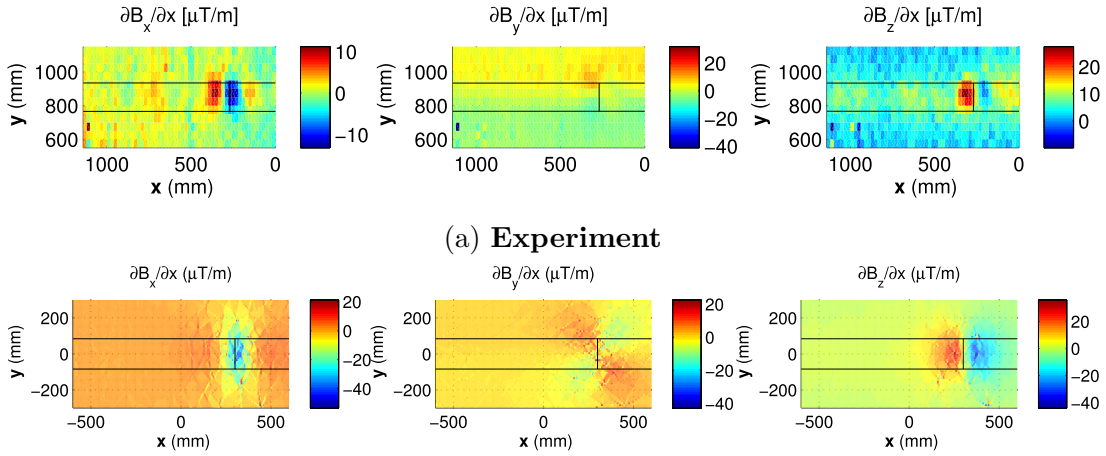

(a) **Experiment**

(b) **Simulation**: $M_{r_1} = -1.5$ kA/m, $M_{r_2} = 6.0$ kA/m.

Figure 5.22: Magnetic indication of the weld was improved when using $\partial\mathbf{B}/\partial x$ in both the experiment and simulation. The field was measured on a horizontal plane at 100 mm height above the welded pipe while pressurised at 60 bar.

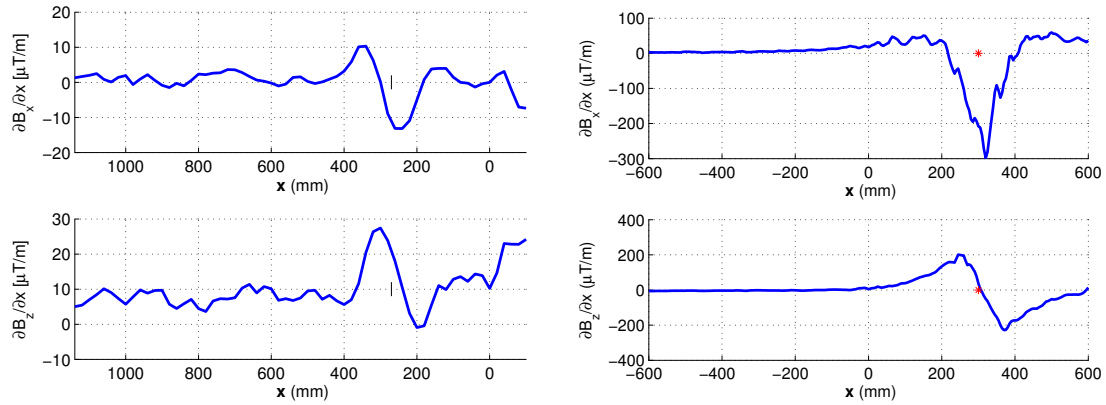

(a) Experiment

(b) Simulation

Figure 5.23: The magnetic indication of the weld using $\partial\mathbf{B}/\partial x$. The magnetic field was measured on the centre line at 100 mm height right on top of the welded pipe while pressurised at 60 bar. The result was similar between the experiment and the simulation.

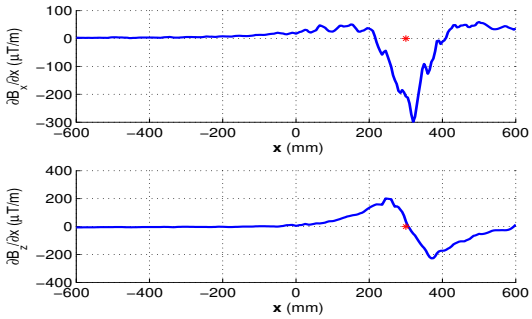

(a) $M_{r_1} = -1.5$ kA/m, $M_{r_2} = 6$ kA/m.

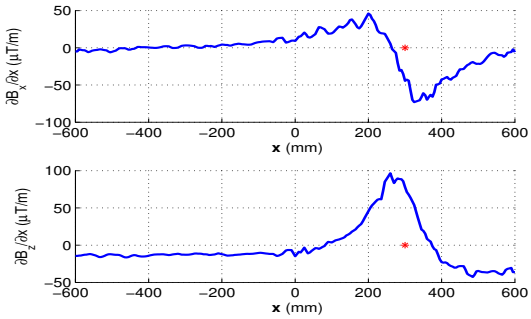

(b) $M_{r_1} = 1.5$ kA/m, $M_{r_2} = -6$ kA/m.

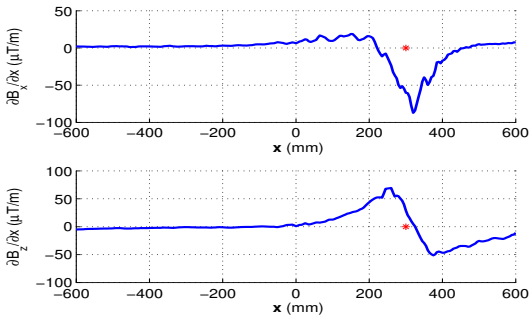

(c) $M_{r_1} = -1.5$ kA/m, $M_{r_2} = 1$ kA/m.

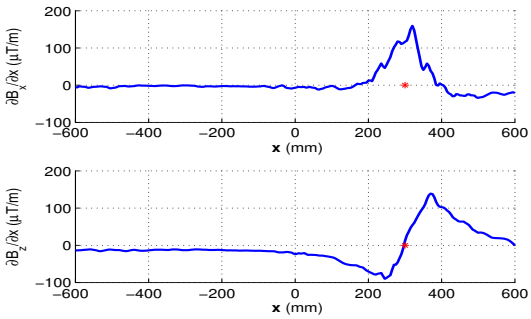

(d) $M_{r_1} = 1.5$ kA/m, $M_{r_2} = -1$ kA/m.

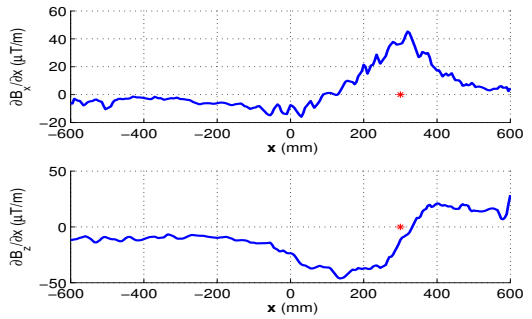

(e) $M_{r_1} = 1.5$ kA/m, $M_{r_2} = 6$ kA/m.

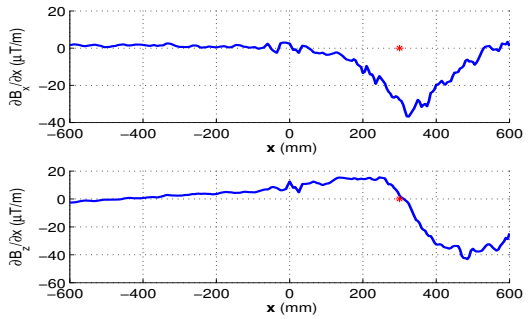

(f) $M_{r_1} = -1.5$ kA/m, $M_{r_2} = -6$ kA/m.

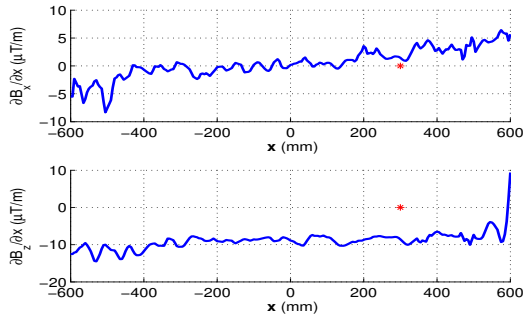

(g) $M_{r_1} = 1.5$ kA/m, $M_{r_2} = 1$ kA/m.

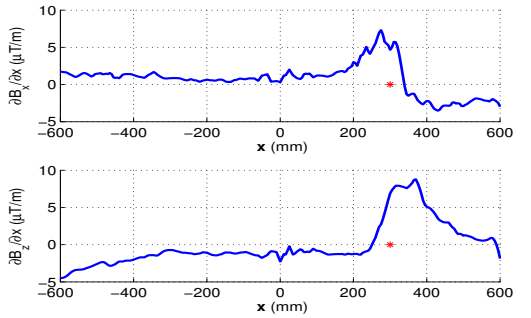

(h) $M_{r_1} = -1.5$ kA/m, $M_{r_2} = -1$ kA/m.

Figure 5.24: Simulation of $\partial\mathbf{B}/\partial x$ on the centre line, i.e. $y = 0$, for the field $\mathbf{B}$ shown in Figs. 5.20 and 5.21. The weld was represented as a red star at $x = 300$ mm. The magnetic indication can be clearly seen in cases of Type 2, or Type 1 with a considerable difference of M_r.

Prediction of the magnetic features of a weld when using only one magnetometer measuring along the centre line of the pipe is shown in Fig. 5.24. The residual magnetisation parameters were similarly varied both in the orientation and the magnitude as shown in Figs. 5.20 and Fig. 5.21. Using the spatial gradient magnetic field, the magnetic indication clearly appeared at the weld, marked as a red star at $x = 300\ mm$, in 3 cases of Type 2 or Type 1 with a considerable difference of M_r. However, this magnetic indication of the weld was disappeared, see Figs. 5.24g, or became weaker, see 5.24h, when M_{r_1} and M_{r_1} were the same orientation and had similar magnitudes. The results suggest using the gradient field instead of the magnetic field itself to locate circumferential welded joints in underground pipelines as it improves the magnetic indication of the weld. However, as discussed above, there are possibly a probability of missed detection and an offset between the actual location of a weld and that predicted using the magnetic indication.

Characterising the magnetic indication of a weld using a magnetic dipole model

In Fig. 5.25a, a magnetic dipole represents the circumferential welded joint sitting on the surface of the pipe at the weld area. Its magnetic features were plotted on the same figure with the gradient of the magnetic field in the experiment, see Fig. 5.25b. It can be seen that the dipole field fitted with the magnetic indication of the weld. This suggested using a dipole to characterise a circumferential welded joint in pipeline.

The magnetic moment of the dipole was determined from the magnetic indication of the weld. In particular, at 100 mm height, a dipole $\mathbf{m} = 0.001$ Am^2 produced a peak of 4 μT in $\partial B_x/\partial x$ and a peak-to-peak magnitude of 5.6 μT in $\partial B_z/\partial x$. Therefore, a dipole of $\mathbf{m} = 0.00425$ Am^2 would characterise the magnetic indication of the weld. It should be noted that strength of the magnetic indication is decayed by $1/z^3$, in which z represents the measurement height. However, further work is required to verify this variation.

(a) A magnetic dipole representing the weld.

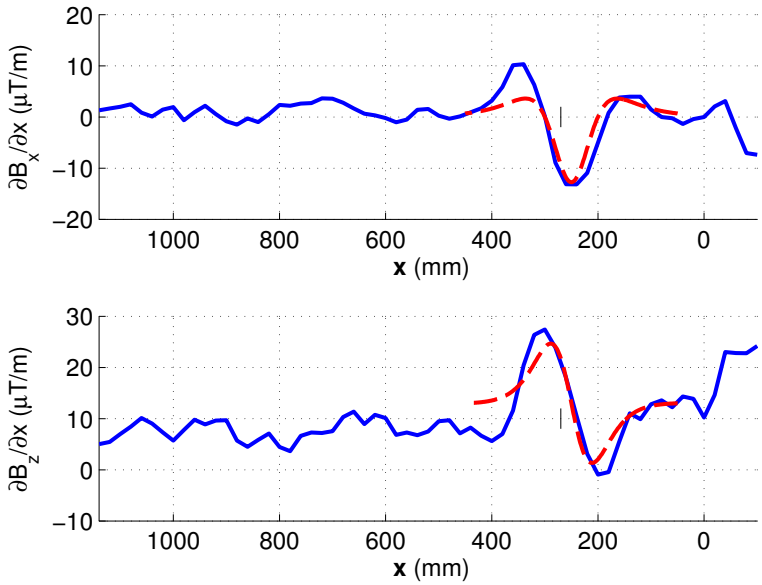

(b) Fit of a dipole field to the experimental magnetic indication of the weld.

Figure 5.25: A magnetic dipole represents the weld and its magnetic field compared to the gradient field of the welded pipe in the experiment. The field was measured at 100 mm height when the pipe was pressurised at 60 bar.

5.6 Conclusions

This chapter studied the stress-induced magnetic field of steel pipes in the earth's field using the laboratory experiments, the field observations on live pipelines and the finite element model.

The finite element model of steel pipes has been developed in COMSOL to simulate the effect of stress to the remote-sensing magnetic field while the pipe is being pressurised. A model of the magnetomechanical effect based on the Jiles-Atherton model has been implemented in the COMSOL model using the equations presented in Chapter 2. It is also capable of simulating the effect of a circumferential welded joint based on using the residual magnetisation of individual pipe sections. The simulation model has generally agreed with the laboratory experiments and the field observations. However, similar to the bar model, this pipe model is limited when used for predicting the magnitude of the stress-induced magnetic field because it hasn't considered the magnetomechanical effect at microscopic level. Another factor the simulation model needs to take into account is the effect of the pipeline length, which is usually very long in practice, as it will certainly enhance the magnetic flux density in the pipe wall.

The results of this study have shown that the magnetic indication induced by stress on individual pipe sections is similar to that of a steel bar, in particular, it includes a peak in B_x and a mean-level crossing in B_z. And the parameter K representing the strength of the magnetic indication can be used as a diagnostic parameter. Again, the stress-magnetisation relationship of the material determines variation of K with the applied pressure. For a specific material, with a known relationship, K varies with the applied pressure, the initial magnetic condition of pipe sections, and the measurement distance. In addition to that, welding pipe sections together produces a similar magnetic indication, but on a shorter length.

The study has found that the variation of K of pipe sections with the applied pressure and the initial magnetic condition has agreed with the findings presented in Chapter 4, in which K is linear with the initial condition at a given stress. The variation of K with stress is a version of the stress-magnetisation relationship

depending on the given applied field. K is more sensitive with stress at a higher applied magnetic field.

The exponential variation of K with the measurement distance has been clearly supported by the results of this study. The agreement between the exponential equations with the experimental results implies that the technique to estimate stress condition using the magnetic field measured at two different distances proposed in Section 4.4.4 can be applied to the pipeline as well, which also supports the idea of rearranging the magnetometer array of the UNISCAN instrument.

The study suggests a hypothesis of magnetic features of welding pipe sections together. It has found that the weld produces a distinguishable magnetic indication in most cases. This is also part of the bulk effect, together with the magnetic field of individual pipe sections. In the study, using the gradient field has improved the magnetic indication of a weld, so it provides evidence of a practical technique to locate circumferential welded joints of underground pipelines. The study also found that a magnetic dipole can be used as a model of a welded joint, which implies a possibility to characterise magnetic property of the weld using the remote-sensing magnetic field.

Although a study on the effect of the bulk field to magnetic indication of a local SCZ caused by a defect has not been performed, the results of this study has suggested that the magnetic indication of the local SCZ will be dominated by not only the magnetic field of individual pipe sections but also that of welding them together. A technique to detect local SCZs may need to be designed so that it looks for a local magnetic indication in the effect of the bulk field and may be based on the schema of the bulk effect presented.

Generally, the study has extended the understanding of magnetic field of pipelines. It confirms the possibility of detection of SCZ using the remote-sensing magnetic field. The gradient field can be used to improve the magnetic indication of a local SCZ and evaluate its strength at the same time. The study also confirms the idea of rearranging the magnetometers so that more data could be collected in order to characterise the SCZ from the remote magnetic field. The simulation model may be improved as it has only considered the axial component of magnetisation to be changed with stress. Although the effect of stress on the

magnetic field of the weld itself may be small when observed at a distance, it may need to take into account.

5. STRESS-INDUCED MAGNETIC FIELD OF THIN-WALL PRESSURE VESSELS IN THE EARTH'S FIELD

Chapter 6

Characterising Features of Underground Pipelines using Aboveground Magnetic Surveys

6.1 Introduction

This chapter presents practical techniques to estimate the depth of cover, locate circumferential welded joints and calculate an indication of SCZs of underground pipelines using the passive magnetic field measured by above-ground surveys. The results obtained from the current standard methods will be used to evaluate the performance of the presented techniques.

A technique to estimate the depth of cover of underground pipelines from the remote-sensing magnetic field contributes to the development of SCT. Moreover, it provides additional data for inspecting the integrity of the pipeline as the depth of cover is a safety factor of underground pipelines. For SCT, because it utilises above-ground surveys, information about the buried depth of the underground pipeline is required to be able to characterise stress conditions of the pipeline. In terms of pipeline integrity, according to a report produced by the European Gas Pipeline Incident Data Group in Feb 2015 [61], the failure frequency per 1000 km of pipelines with the depth of less than 80 cm was 5 times higher compared to pipelines buried deeper than 100 cm. In the UK, a depth of cover of at least

2 m is recommended by National Grid. Therefore, a technique that is possible to quickly estimate the depth would save the cost of separate depth surveys.

Information about the location of welded joints of underground pipelines is useful for both SCT and the In-Line Inspection method (ILI). For SCT, because magnetic indication of a local stress concentration zone (SCZ) is embedded in the bulk field induced by individual pipe sections and welded joints, a technique to locate these joints certainly reduces the number of magnetic indications, therefore, increases the probability of detection of SCZ. In addition, this information possibly complements to the ILI method as using high accuracy GNSS receivers for above-ground surveys means a welded joint can be accurately located by its GNSS coordinate, so an anomaly reported by ILI can be easily tracked back as it is usually reported as a distance to the upstream welded joint.

Importantly, a preliminary study to show the possibility of detection of stress concentration zones in underground pipelines through the remote magnetic field is also presented in this chapter.

Data from the experiments, simulation and field surveys supports developing the techniques. Their performance will be evaluated using the survey data and the latest ILI reports obtained from National Grid. Section 6.2 describes the survey method. Processing the survey data is shown in Section 6.3. The depth estimation technique is presented in Section 6.4, and Section 6.5 explains the technique to predict location of circumferential welded joints in underground pipelines. Finally, a technique to calculate magnetic indication of stress concentration zones is presented in Section 6.6, together with evaluating its performance on the field survey data.

6.2 The survey method

The design of the UNISCAN instrument used for the surveys was shown in Section 3.3.3, and the field survey method of SCT was explained in Section 3.7. It will be discussed further in this section.

Field surveys were performed on the underground high-pressure gas pipelines around the Pannal AGI site. During a survey, one GR-5 receiver (Topcon) was set up as the base station. The second GR-5 receiver was configured as the rover

that communicates with the base to achieve the accuracy of up to 15 mm. The system was configured in Real Time Kinematic mode (RTK). Then, the pipeline was tracked using an industrial pipeline locator, the RD8000 instrument made by SPX. The pipeline route was marked with flags where the depth was measured by the RD8000 together with their GNSS coordinate recorded by the rover. Finally, the SCT survey was performed to measure the magnetic field of the pipeline using the UNISCAN instrument.

6.2.1 Data from ILI surveys

In-Line Inspection (ILI) surveys were in fact not part of the surveys performed in this study. The ILI surveys were previously performed before the SCT surveys and the ILI reports were obtained from National Grid as a spreadsheet of GNSS coordinates of welded joints and other features of the pipeline for example bends or defects.

The SCT surveys were performed on two 48-inch pipelines from Pannal to Nether Kellet (PANE29) and from Asselby to Pannal (ASPA29), see Fig. 6.1, where the ILI data was available. The welded joints reported by ILI were marked as yellow dots in the figure. Although there was a level of uncertainty with the ILI data expressed in terms of probability of detection and accuracy of locating pipeline features, in practice, this inspection method is the current gold standard for pipeline inspection. Therefore, this data was used as the standard to evaluate the performance of the SCT techniques developed in this chapter.

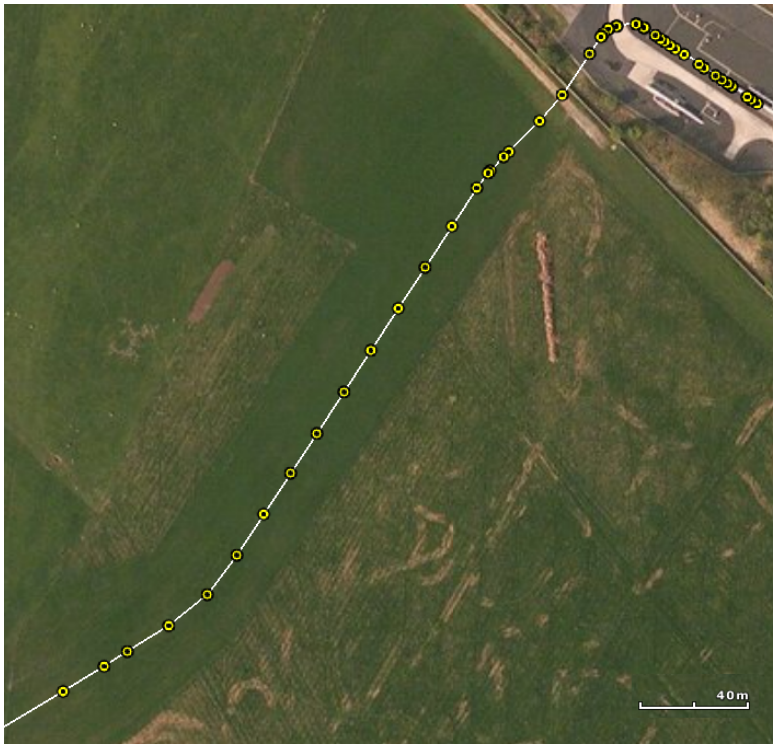

(a) 48-inch pipeline from Pannal to Nether Kellet (PANE29).

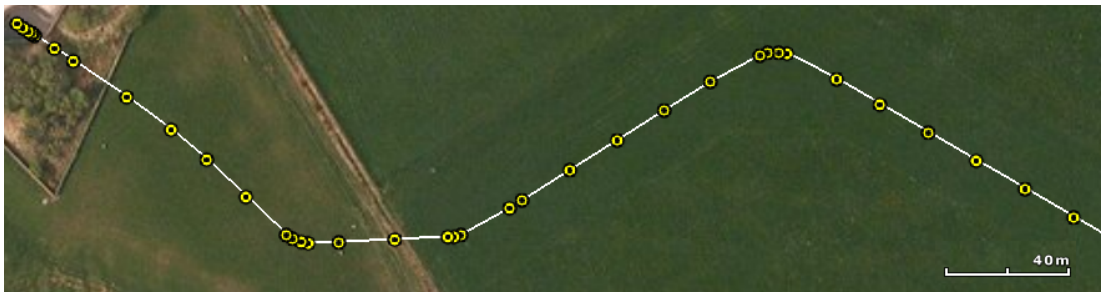

(b) 48-inch pipeline from Asselby to Pannal (ASPA29).

Figure 6.1: The surveyed pipelines and the features reported by the ILI surveys (In-line Inspection) using the MFL method (Magnetic Flux Leakage). **Yellow dot**: Welded joints reported by ILI.

6.2.2 The UNISCAN instrument

Fig. 6.2 shows the assembled prototype of the UNISCAN instrument used to measure magnetic field in the field surveys. The details of this instrument and the survey method were presented in Section 3.3.3 and Section 3.7 and will be summarised here.

Figure 6.2: The assembled UNISCAN instrument.

The surveyor wearing the harness holds the instrument and walks along the survey route. The instrument includes an array of three 3-axis magnetometers horizontally arranged at 0.5 m separation. The GNSS positioning system including two GR-5 receivers is configured in Real Time Kinematic mode (RTK). These receivers are used as the base station and the rover. The rover is attached to the back of the UNISCAN instrument. This system allows recording the GNSS coordinate associated with the samples of the measured magnetic field.

6.2.3 Measurement of depth of cover

For these surveys, the depth to the centre of the pipeline was measured along the pipeline using an RD8000 instrument made by SPX. The RD8000 is an industrial pipeline locator which includes a transmitter emitting a radio signal of 33 kHz into the pipe and a hand-held receiver picking up that signal using the antennas. The depth can then be calculated from the magnitude of the signals received by the antennas and the known distance between the antennas. Pipe location and the depth to the centre of the pipe can be read on the LCD of the receiver. Although the depth measured by the RD8000 specifically has the tolerance of $\pm 5\%$ with respect to the depth between 0.1 m to 3 m [62, 63], in practice, during the surveys, the depth displaying on the LCD screen was not a constant but continuously changed within a range which was even larger than the tolerance itself. In order to resolve the issue, the depth recorded was the average number within that range. It should be noted that all the surveys were performed on the field where the condition of the ground was rough, this would be another factor in the tolerance of the measured depth. Additionally, the GNSS coordinate of the locations where the depth measurement was performed was also recorded using the rover.

Fig. 6.3 shows the mapping and the depth of the pipeline (from the ground to the centre of the pipe) for the surveyed section of the PANE29 pipeline. White dots marks the locations where the depth was measured using the RD8000. In the figure, the depth was varied between 2 m to 4.5 m. The pipeline had side bends, and appeared to go deeper near to the end of the section. This gentle bend of the pipeline was not included in the ILI report, but inferred from the depth of cover as the ground was generally flat for the surveyed section.

(a) Mapping of locations where the depth was measured.

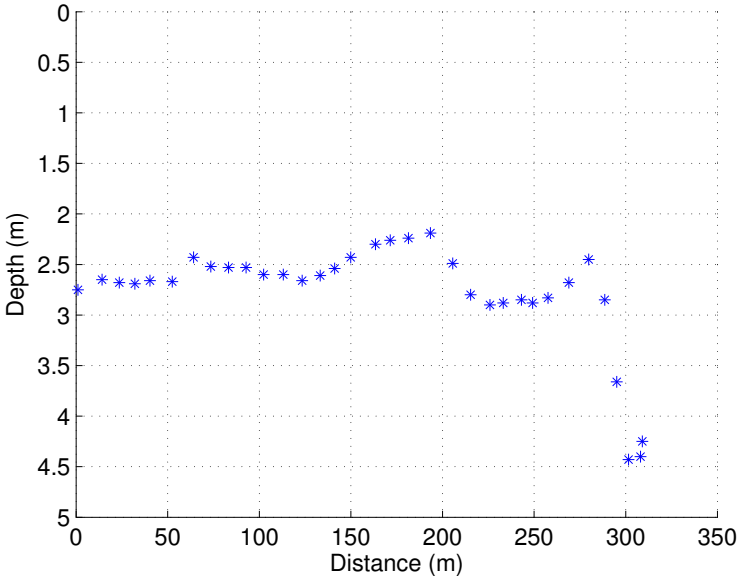

(b) The depth measured using the RD8000.

Figure 6.3: Mapping of the PANE29 pipeline and the depth to the centre of the pipe measured by the RD8000. **White dots**: locations where the depth was measured.

6.2.4 Localisation of pipeline features

Traditionally, for the ILI method, location of pipeline features is usually reported in the travel distance of the pig (the instrument used in ILI surveys). For these surveyed pipelines, in addition to the travel distance, the ILI method also reported the GNSS coordinate of the pipeline features in the Ordnance Survey (OS) National Grid reference system, which is based on the OSGB36 datum (Ordnance Survey Great Britan 1936). The detail of the technique to calculate those coordinates was not available, because the data was obtained from National Grid as a spreadsheet reported by a pipeline inspection service company. Nonetheless, it was known that the positional data was calculated from the pig speed (measured by on-board accelerometers and gyroscopes) and a number of reference points on the pipeline where DGPS measurements (Differential Global Positioning System) were conducted. So the positional accuracy was a function of the pig speed and the distance between reference points. This method uses the World Geodetic System (WGS84) reference system which includes a standard coordinate system for the Earth. Therefore, the coordinates in the ILI reports were probably converted from WGS84 to OSGB36.

In practice, because of using two different techniques to map the pipeline, and moreover, the UNISCAN instrument reported the coordinates in WGS84 (World Geodetic System), meanwhile the ILI method reported them in OSGB36, a conversion was required which resulted in further error. It turned out that there might be an offset of about 3 m between the pipeline mapping by the ILI method and the SCT method, see Fig. 6.4, which obviously would affect the evaluation of the SCT techniques.

In order to resolve that issue, because the two mapping lines were nearly running in parallel, so the features predicted by ILI and SCT were compared using the following steps:

- The SCT survey route and the SCT survey distance were calculated using the GNSS coordinates recorded by the UNISCAN instrument.

- The features reported by ILI were projected onto the SCT survey route.

- The distance offset between the ILI and SCT features on the SCT survey route was used in order to evaluate the performance.
- On the SCT survey route, an ILI feature and a SCT feature could be used as reference points and would be aligned together by offsetting the ILI feature. These were usually the first feature predicted by SCT and the closet ILI feature. Other ILI features would also be shifted with the same offset.

Figure 6.4: A comparison between the ILI and the SCT mapping data of the PANE29 pipeline. **White**: the ILI mapping data; **Red**: the SCT mapping data. Because of different positioning methods the conversions between OSGB36 and WGS84, the distance between two lines was approximately 3 m.

6.3 Processing the SCT survey data

For the survey data, the reference frame of the magnetometer array was as followed, see Fig. 6.5:

- In the survey direction, magnetometer No. 1 was on the left-hand side, magnetometer No. 2 was at the centre and magnetometer No. 3 was on the right-hand side.
- For each magnetometer, x was in the survey direction, y was perpendicular to x and parallel to the ground plane and z was in the vertical direction.
- During a survey, the operator put effort into keeping magnetometer No. 2 on top of the pipeline.

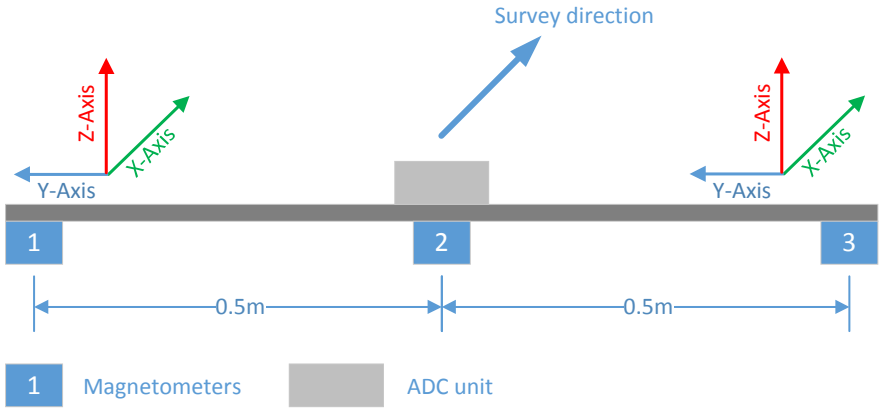

Figure 6.5: The magnetometer array.

Fig. 6.6 shows three components of the magnetic field B_x, B_y, B_z and the magnitude B measured by three magnetometers of the UNISCAN instrument along the PANE29 pipeline,

$$B = \sqrt{B_x^2 + B_y^2 + B_z^2}. \tag{6.1}$$

The surveyed section was about 300 m in length. Magnitude of B_x was between -40 μT to 10 μT; B_z was between -90 μT to 0 μT; and B_y was between -20 μT to 0 μT. Meanwhile, the magnitude B was varied between 10 μT to 100 μT. The

signals were quite noisy because of motion of the operator, especially in B_y. The measured magnetic field included the background field which was dependent on the orientation of the pipeline in the earth's field, so it might be different between sections of the surveyed pipeline.

6.3.1 Removing the mean field

Because a SCT survey was performed by a surveyor holding the UNISCAN instrument and walking along the pipeline, one of the issue of the SCT data was the magnetic field of the pipeline was distorted by the movement of the magnetometer array. In practice, the array moved up and down in sync with steps of the surveyor. It caused unwanted fluctuations which reduced the signal-to-noise ratio of the signal (SNR), especially with B_y, see Fig. 6.7a.

Since the background field is identical between three magnetometers, and from the previous chapters, it can be assumed that the magnetic field should be symmetrical on two sides of the pipe, the mean field of B_y can be approximately removed using the following equations:

$$\begin{aligned} Y_m &= (Y_1 + Y_2 + Y_3)/3, \\ Y_{1N} &= Y_1 - Y_m, \\ Y_{2N} &= Y_2 - Y_m, \\ Y_{3N} &= Y_3 - Y_m, \end{aligned} \tag{6.2}$$

in which, Y_m is the mean field of three magnetometers in y axis.

B_y after removing the mean field is shown in Fig. 6.7b. It can be seen that the unwanted fluctuations were removed, Y_1 and Y_3 were nearly symmetrical as predicted in the simulation, but Y_2 was not completely zero. This information could be used to predict the depth and the lateral offset between the survey route and the centre line of the pipeline during the survey, see Section 6.4.

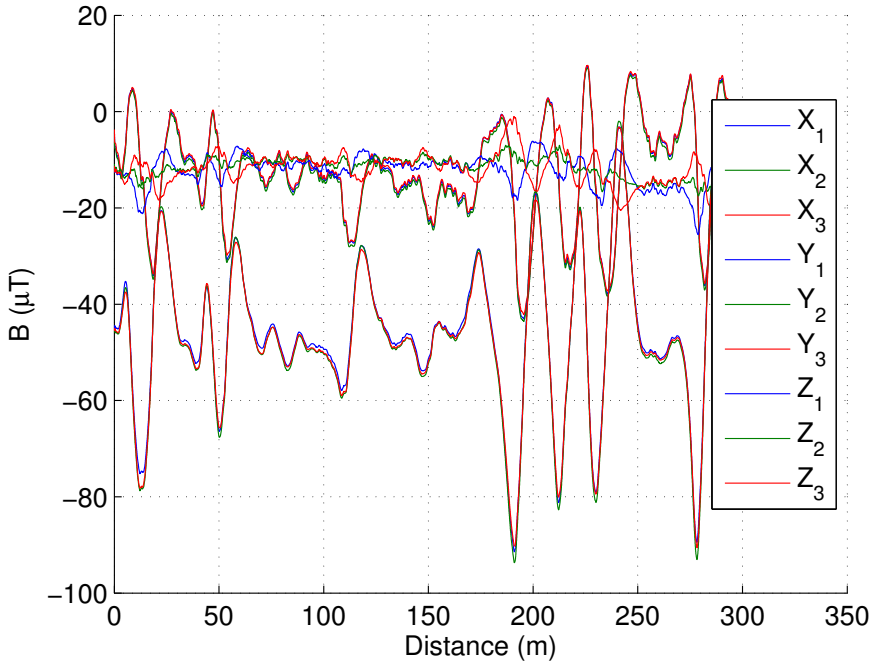

(a) B_x, B_y and B_z of three magnetometers.

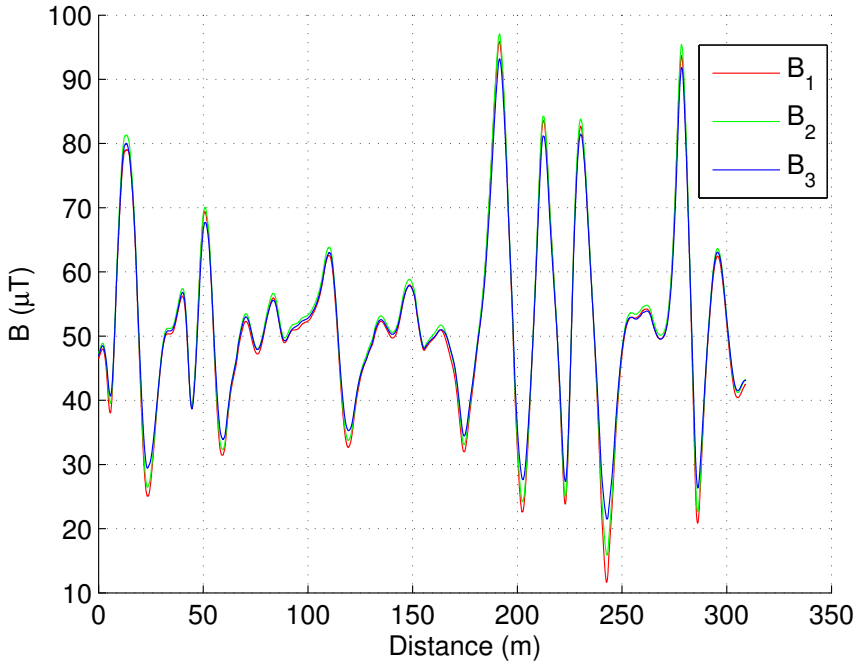

(b) B

Figure 6.6: Three components B_x, B_y and B_z and the norm B of the magnetic field measured by three magnetometers of the UNISCAN instrument along the PANE29 pipeline.

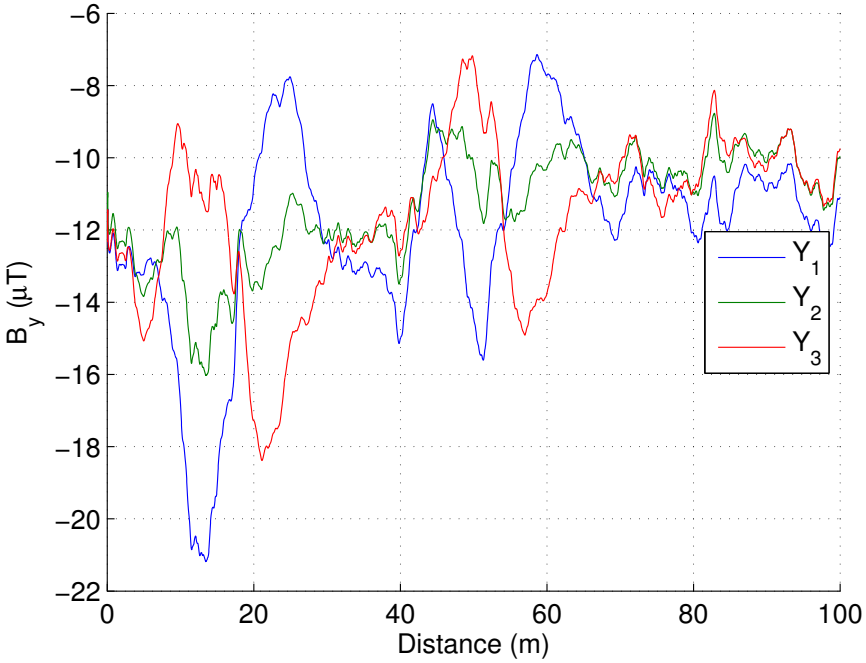

(a) B_y before removing Y_m.

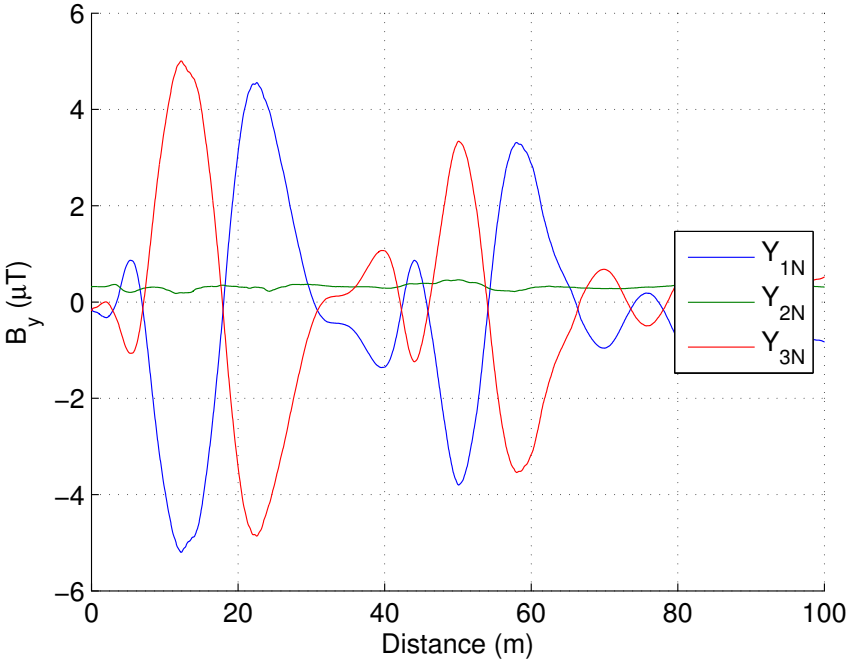

(b) B_{yN}: B_y after removing Y_m. The effect of motion was reduced.

Figure 6.7: B_y of three magnetometers before and after removing the mean field. Y_{1N} and Y_{3N} became symmetrical and the effect of motion was significantly reduced.

6.3.2 Gradient field

As presented in Chapter 5, the gradient of the magnetic field with respect to the axial direction of the pipeline should be used to predict pipeline features. For the field survey data, because of noise due to magnetometer movements, the signal was firstly filtered using a moving average filter. The length of the filter was 40 samples, which was about 0.8 m in terms of the survey distance at typical walking speed. Then, the gradient with respect to the pipeline distance was calculated for all three components of three magnetometers of the UNISCAN instrument.

Fig. 6.8 shows the gradient field of the PANE29 pipeline. In the figure, the mean value of the magnetic components became zero regardless the orientation of the pipeline. This is another advantage of using the gradient field. In addition, $\partial B_x/\partial x$ and $\partial B_z/\partial x$ of three magnetometers were very similar. So it is possible to use $\partial B_x \partial x$ and $\partial B_z/\partial x$ of magnetometer 2 in the analysis instead of the data from all three magnetometers. $\partial B_y/\partial x$ of magnetometer 1 and 3 was symmetrical and that of magnetometer 2 was nearly zero as it was on top of the pipeline. This was plotted in Fig. 6.8b for a comparison.

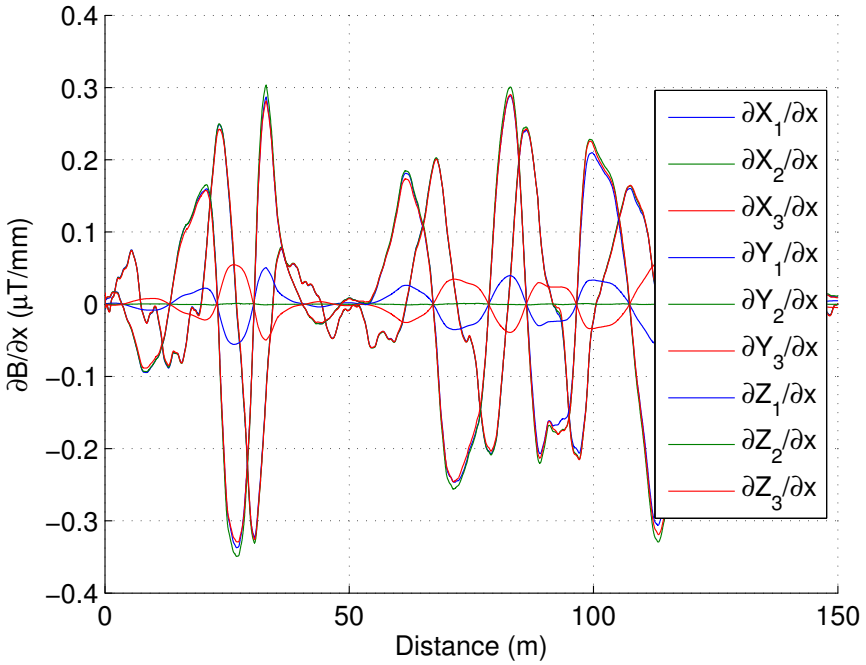

(a) The gradient of three magnetic field components of three magnetometers.

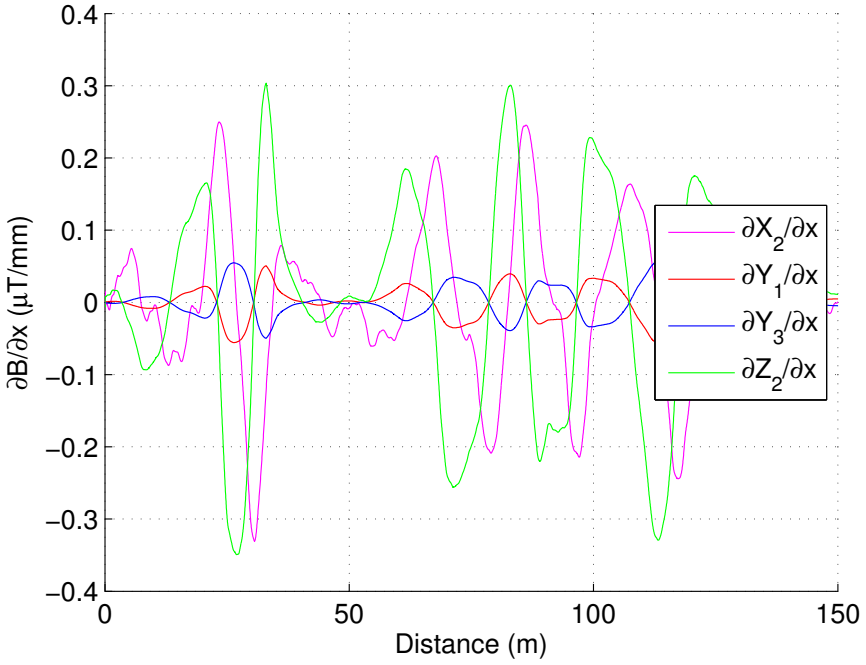

(b) $\partial B_x/\partial x$ and $\partial B_z/\partial x$ of sensor 2 and $\partial B_y/\partial x$ of sensor 1 and 3.

Figure 6.8: The gradient of three magnetic field components of three magnetometers with respect to the pipeline distance.

6.4 Estimate the depth of cover of underground pipelines

This study proposes a technique to estimate the depth of cover of underground pipelines from the passive magnetic field measured using the UNISCAN instrument. An advantage of such a technique is SCT now can provide information about not only stress condition but also the depth of cover of the pipeline, so saving costs of separate depth surveys. Knowledge of the pipeline depth also improves characterising SCZs as SCT aims to use the remote-sensing magnetic field to inspect the pipeline.

Fig. 6.9 shows variations of B_z with B_y when measured along the 6-inch steel pipe at different measurement heights in the experiment and the simulation. In both cases, changing the measurement height, which is equivalent to the depth in case of underground pipelines, also changed the angle of the vector B_{yz}. Lower measurement height results in wider angle.

Fig. 6.10a shows variations of both B_{yN} and B_z of three magnetometers of the UNISCAN instrument along 100 m of the PANE29 pipeline, and Fig. 6.10b shows this variation when viewed in the cross-sectional yz plane. It should be noted that the figure used B_{yN}, which was B_y after removing the mean field, otherwise, the signal was very noisy. Another issues were B_{yz} of three magnetometers was not crossed at the same position, and there was still a DC offset in B_z. This resulted from the survey method and the fact that the background field was not a constant along the surveyed section. An algorithm was developed in this study in order to minimise the mean field, see Section 6.4.2. Nonetheless, in the figure, the magnetic field of the PANE29 pipeline shows similar characteristics to those observed from the experiment and the simulation, so B_{yz} might reflect the depth of the pipeline.

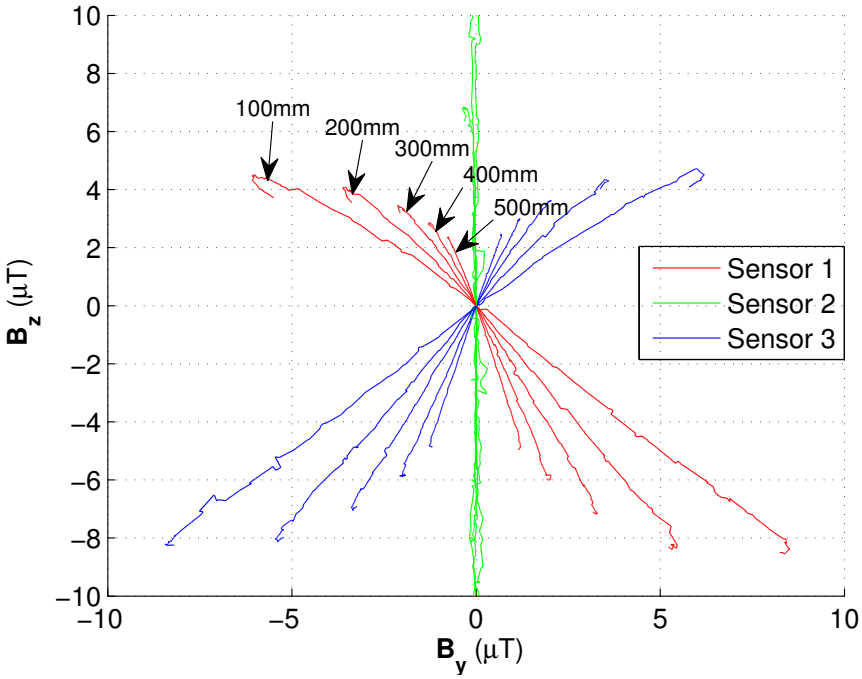

(a) Simulation

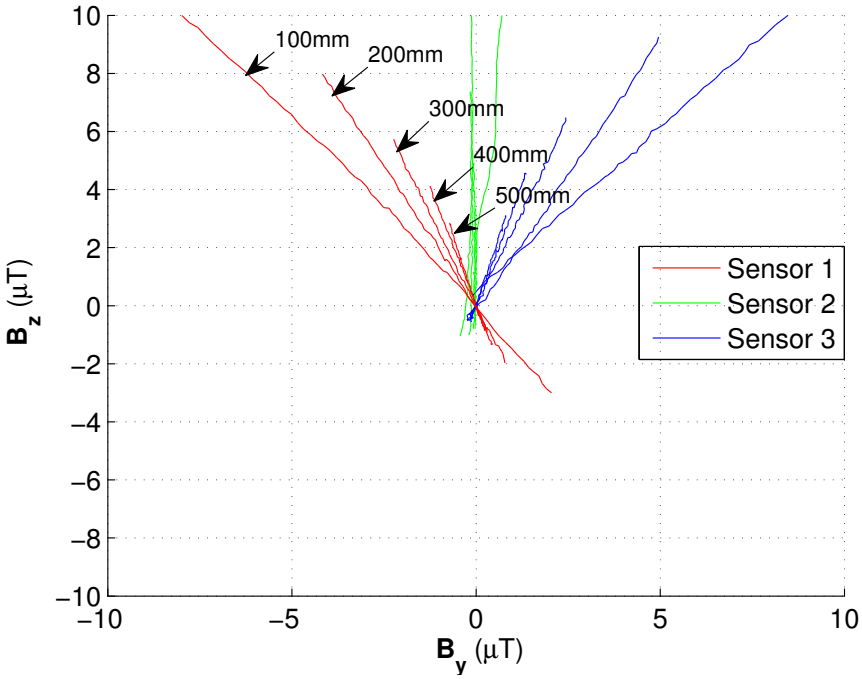

(b) Experiment

Figure 6.9: Variation of vector B_{yz} of three sensors along the length of the 6-inch pipe with the measurement height in the simulation and experiment. The angle of vector B_{yz} changed with the measurement height.

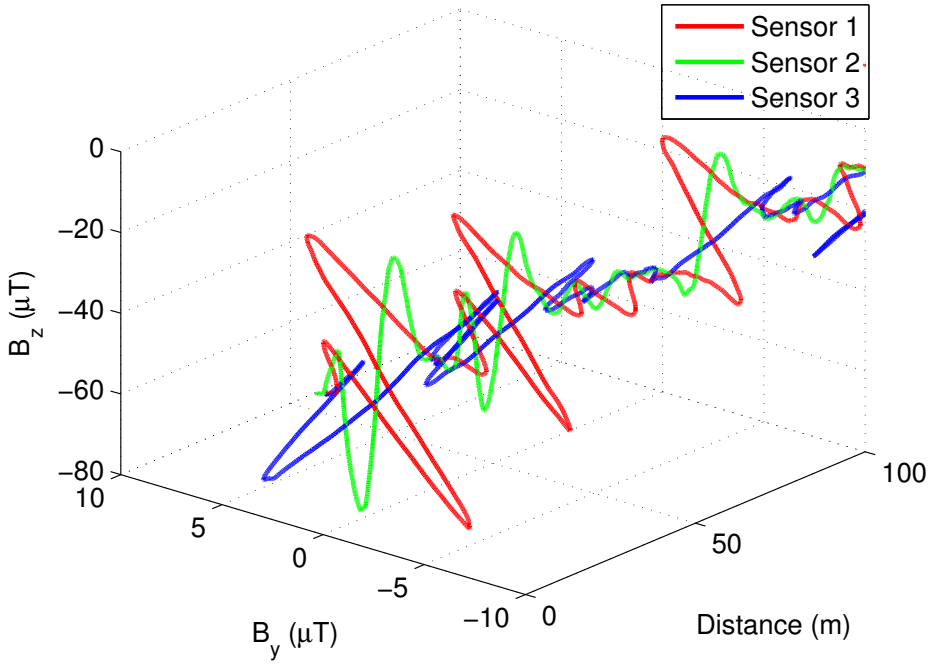

(a) With distance.

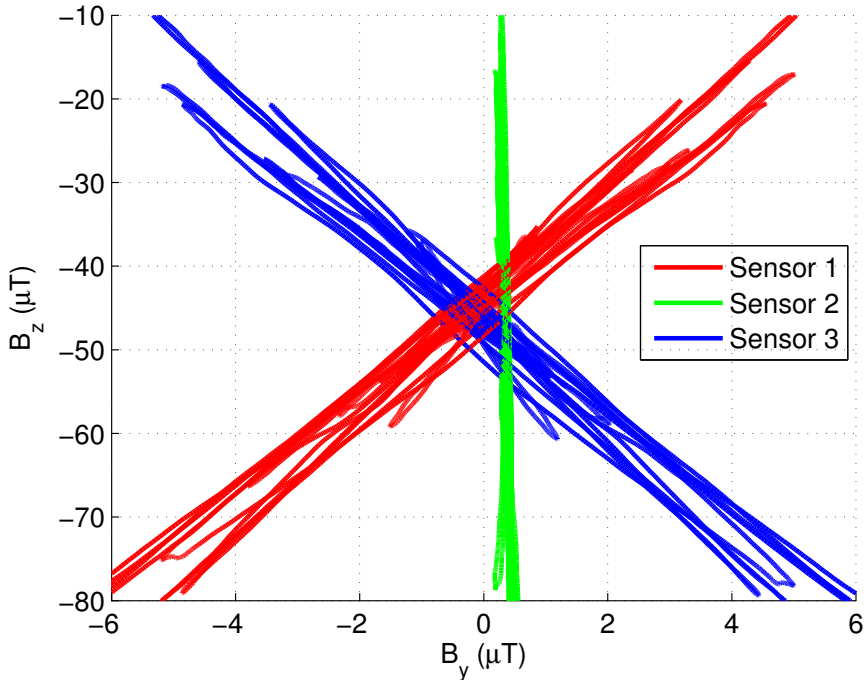

(b) Viewed in the cross sectional yz plane.

Figure 6.10: Variation of B_z with B_{yN} of three magnetometers along 100 m of the PANE29 pipeline. This variation was similar to the experiment and simulation.

6.4.1 Principle of the depth estimation technique

Fig. 6.11 explains the relationship between the magnetic field measured by three magnetometers of the UNISCAN instrument and the depth to the centre of the pipeline when viewing in the cross-sectional yz plane. In the figure, the magnetometers on the magnetometer array of the UNISCAN instrument are represented as three blue circles labelled 1, 2 and 3. The separation between them is 0.5 m. d_s is the distance between a magnetometer to the centre of the pipe. The pipeline is at the depth d_m to the magnetometer array, in which, d is the depth of cover of the pipeline and h_m is the height of the magnetometer array above the ground, $d_m = d + h_m$.

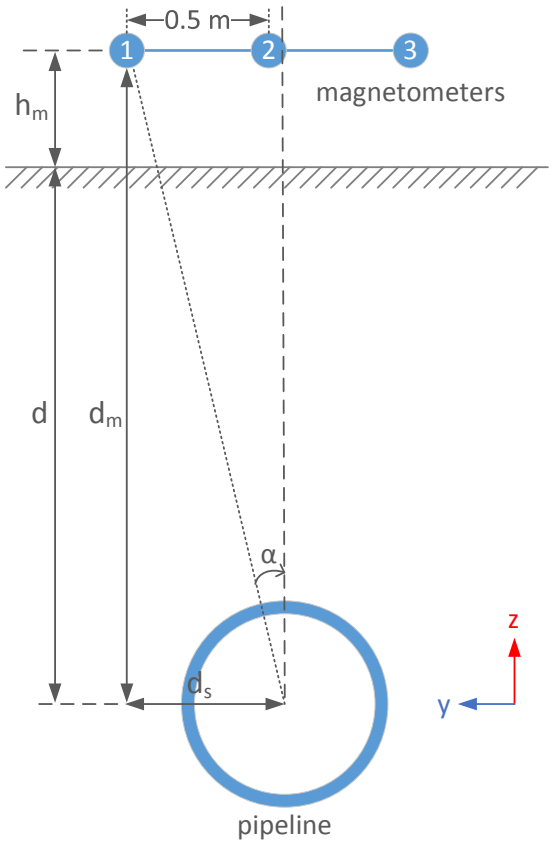

Figure 6.11: Schematic of the relationship between the magnetic field of three magnetometers measured along the pipeline and the depth of cover.

Because the magnetic field is induced from the pipeline, B_{yz} picked up by a

magnetometer will be at an angle α, which can be calculated as:

$$\tan(\alpha) = \frac{B_y}{B_z}. \tag{6.3}$$

In terms of depth, the angle α can also be represented as:

$$\tan(\alpha) = \frac{d_s}{d_m}, \tag{6.4}$$

so

$$d_m = (B_z/B_y)d_s. \tag{6.5}$$

In practice, because of the survey method, d_s is usually unknown. However, the above equations can be applied for any of the three magnetometers:

$$\begin{aligned} d_m &= (B_{z_1}/B_{y_1})d_{s_1}, \\ d_m &= (B_{z_2}/B_{y_2})d_{s_2}, \\ d_m &= (B_{z_3}/B_{y_3})d_{s_3}, \end{aligned} \tag{6.6}$$

and because the distance between the magnetometers 1 and 3 is 1m: $d_{s_1} + d_{s_3} = 1$, the depth d_m can be calculated as:

$$d_m = 1/(\frac{B_{y_1}}{B_{z_1}} - \frac{B_{y_3}}{B_{z_3}}). \tag{6.7}$$

The offset between the magnetometer 2 and the centre of the pipe is:

$$d_{s_2} = \frac{B_{y_2}}{B_{z_2}} d_m. \tag{6.8}$$

Because the height of the magnetometer array above the ground h_m can be measured before every survey, the depth of cover of the pipeline d can be calculated as $d = d_m - h_m$ (to the centre of the pipe). In practice, h_m is usually dependent on the surveyor, and also not a constant during the survey. In fact, an approximate value of h_m can be used, for example, for the PANE29 and ASPA29 pipelines, $h_m \approx 65$ cm with a tolerance of ± 5 mm. The above calculation of depth is eligible as long as the magnetometers 1 and 3 are on two sides of the pipeline.

It can be seen that the UNISCAN instrument is potentially operated as a pipeline locator, where it can locate the centre of the pipeline by calculating d_{s_2} and estimate the depth of cover d at the same time. The advantage of this technique is it works with the passive magnetic field, without actively putting any energy into the pipeline. However, its performance needs to be evaluated with the field survey data.

6.4.2 Evaluate the depth estimation technique with field survey data

In practice, applying the depth estimation technique to the field survey data has some limitations. First, the magnetic field has to be measured on a section of the pipeline that long enough to be able to observe the crossing of B_{yz} of the magnetometer 1 and 3, see Fig. 6.10b.

Second, a correct removal of the mean level of B_y and B_z may be required, so that, the crossing appears at 0 μT. As the experiment and the simulation were in control, this mean level was removed by a background measurement, see Fig. 6.9. However, for the field survey data, the mean level was just removed from B_y only, but not B_z, see Fig. 6.10b. The issue was because of the survey method and the orientation of the pipeline, the mean level was not a constant but continuously varied along the pipeline, which made it difficult to remove.

Third, because the depth estimation technique is based on division, near-zero magnetic field will result in infinite depth. Setting a threshold may avoid the issue.

This section aims to evaluate the depth estimation technique using the depth measured by the RD8000 instrument, through that the performance and confidence level of the technique can be assessed.

Fig. 6.12a compares the depth measured by two different RD8000 instruments and the associated deviation representing the confidence level of 99.7%, the depth estimated by the technique using the magnetic field shown in Fig. 6.12b, and the smooth version of the estimated depth, in which:

- The mean field Y_m of B_y was calculated using Equ. 6.2 and was removed from B_y.
- The mean field Z_m of B_z was determined as the mean value of B_z at locations where B_{y_1} crosses B_{y_3}. It was then removed from B_z.
- A threshold of 1 μT was set for both B_y and B_z, so that the depth was only calculated from the magnetic field above the threshold.
- The magnetometer array height above the ground was 0.6 m.

- The estimated depth was smoothed using a moving average filter of 50 m length.

Although there were locations where the estimated depth suddenly changed from over 3 m to less than 2 m and vice versa, the smooth version of the estimated depth followed the trend of the pipeline depth. In the figure, the mean field appeared to be removed as both B_{yN} and B_{zN} fluctuated around zero. However, because the original calculation was heavily dependent on correctly determining the magnitude of the mean field, sharp changes in the estimated depth probably resulted from not removing the correct mean field at that particular locations. In the calculation, Z_m was assumed to be constant, but, in fact, this mean field could be affected by the array movement during the survey as explained above.

A closer look on the magnetic data indicated that there was still a small offset in B_{yN} and B_{zN} when Z_m was assumed as a constant for the whole survey route. In order to resolve the issue, B_{yN} and B_{zN} of the magnetometers 1 and 3 were assumed to cross zero at the same location, and the mean field was only constant within a short section of the pipeline, so the pipeline was divided into several sections for which the mean field was manually determined. The depth was not calculated for every point any more, instead, it was calculated at locations where B_{yN} crossed B_{zN} and could be interpreted as the average depth of that section.

Fig. 6.13 shows the resultant depth estimated using this technique. Obviously, removing the correct mean field played an important role in estimating the depth of the pipeline. For example, the depth was estimated as 2.55 m for the first section, which was acceptable compared to the RD8000. It also followed the trend of the depth quite well.

Rather than manually remove the correct mean field, an algorithm was developed and then tested with the PANE29 and ASPA29 pipelines. The result is shown in Fig. 6.14. Generally, the estimated depth followed the trend of the pipeline depth, especially at the distance of 300 m in PANE29 and 120 m in ASPA29, where the pipeline went deeper through a ditch. Strictly speaking. there were locations, 3 out of 26 in PANE29 and 9 out of 28 in ASPA29, where the depth estimated using the algorithm was outside of the closet error bar of the second RD8000 instrument. However, as can be seen in Fig. 6.14b, there were

6 locations where the depth measured by the first RD8000 instrument was also outside of the error bar of the second RD8000. If it is assumed that the depth measured by the second RD8000 instrument is the actual depth, a tolerance of 8% of the measurement depth would cover all the depth estimated by SCT.

During the course of this research, two areas were excavated by National Grid, which allowed physical verification of the depth of cover. Before the excavation, the depth estimated using the SCT technique was 2.07 m and 1.668 m, meanwhile, it was 2.14 m and 1.93 m, respectively, when measured using the RD8000. The physical checks later confirmed the depth of 1.82 m and 1.62 m, which was actually close to the estimation of the SCT technique than the RD8000 measurement. It is noted that the pipe diameter was removed so that the depth presented here was from the ground surface to the top of the pipe.

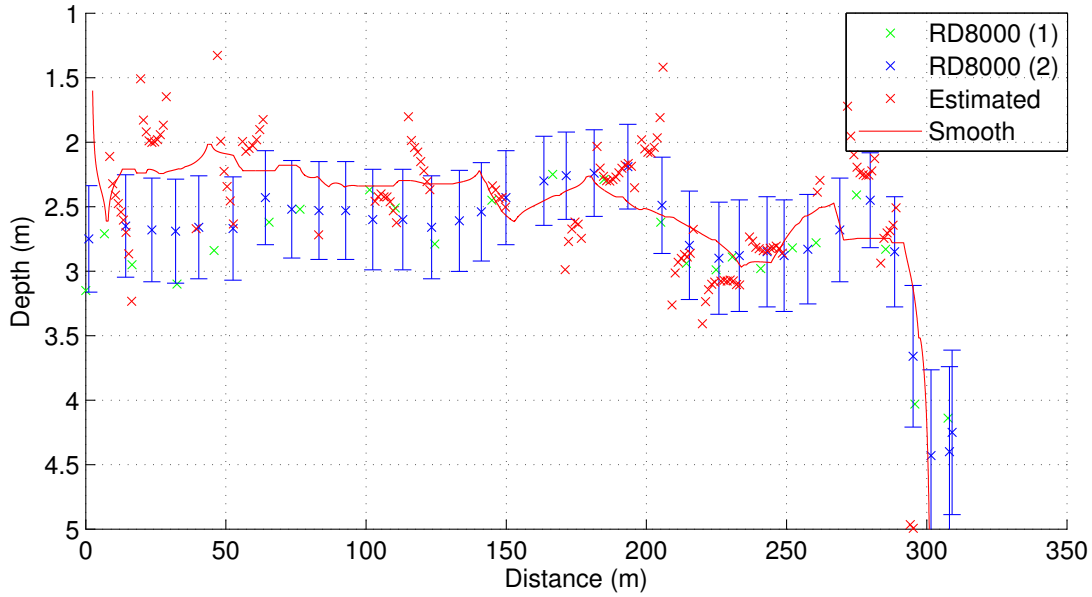

(a) A comparison between the depth estimated by SCT and that measured by two different RD8000 instruments.

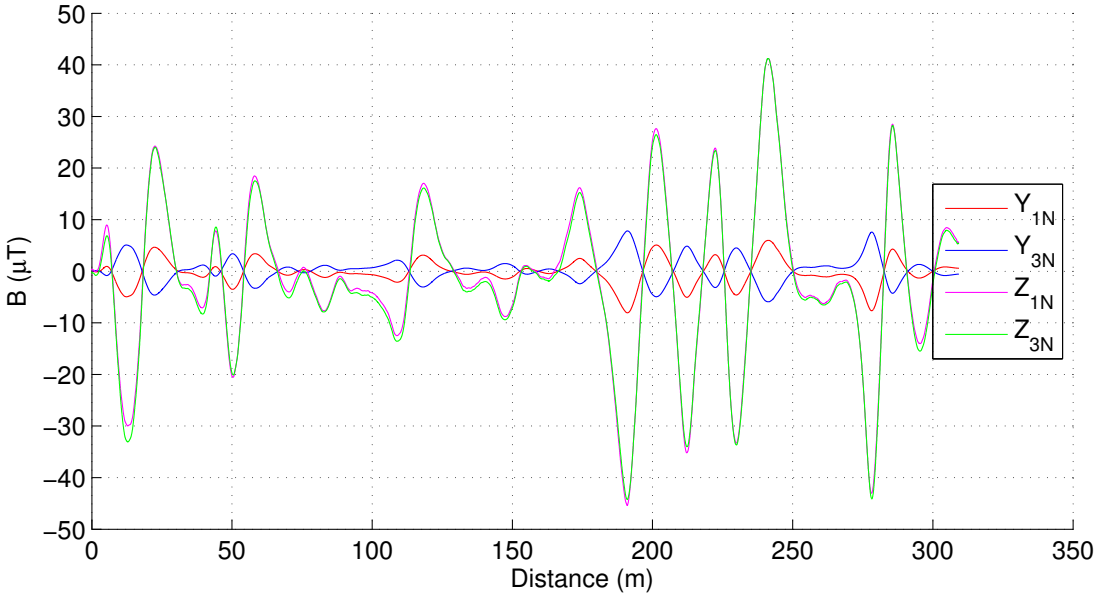

(b) B_y and B_z of the magnetometers 1 and 3 after the mean magnetic field was removed.

Figure 6.12: The magnetic field, the measured depth and the estimated depth of the PANE29 pipeline when a threshold of 1 μT was used. One value of the mean field was used for the whole surveyed section.

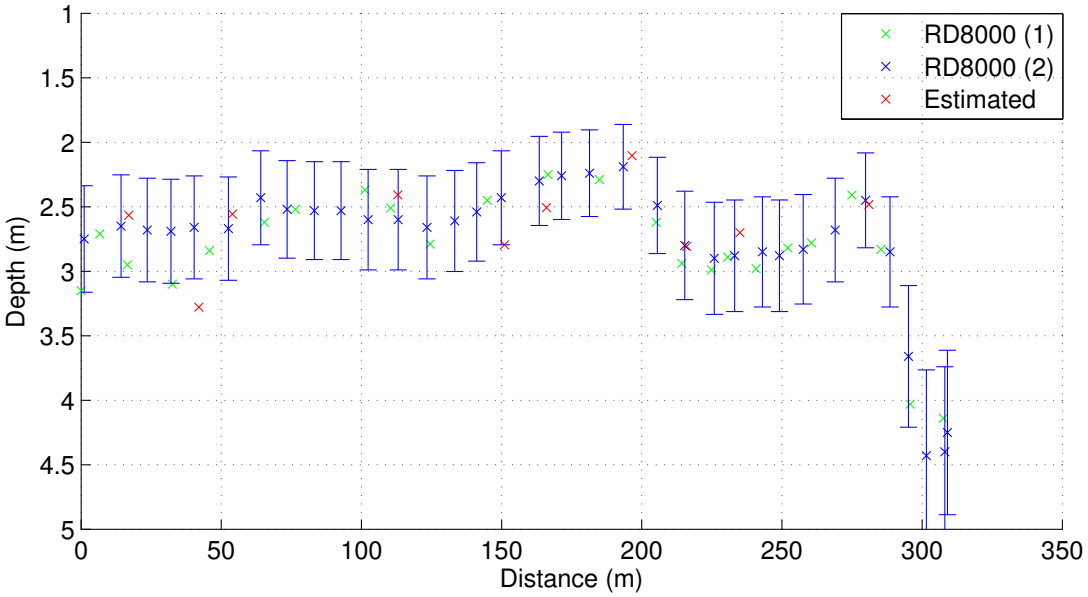

Figure 6.13: A comparison of depth measured by two different RD8000 instruments and estimated after different values of the mean field were used for individual sections.

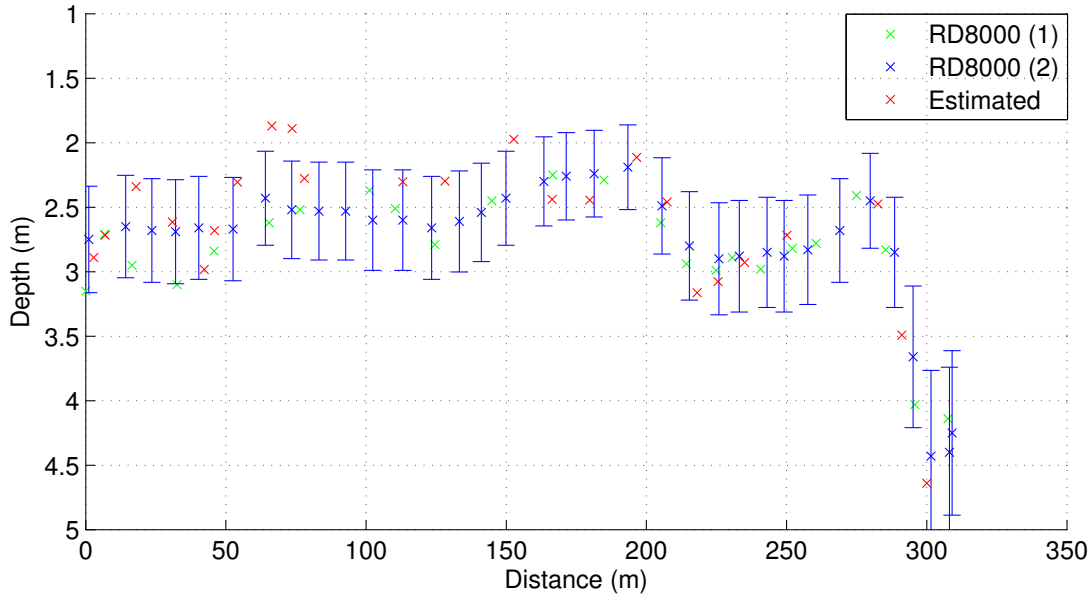

(a) The PANE29 pipeline

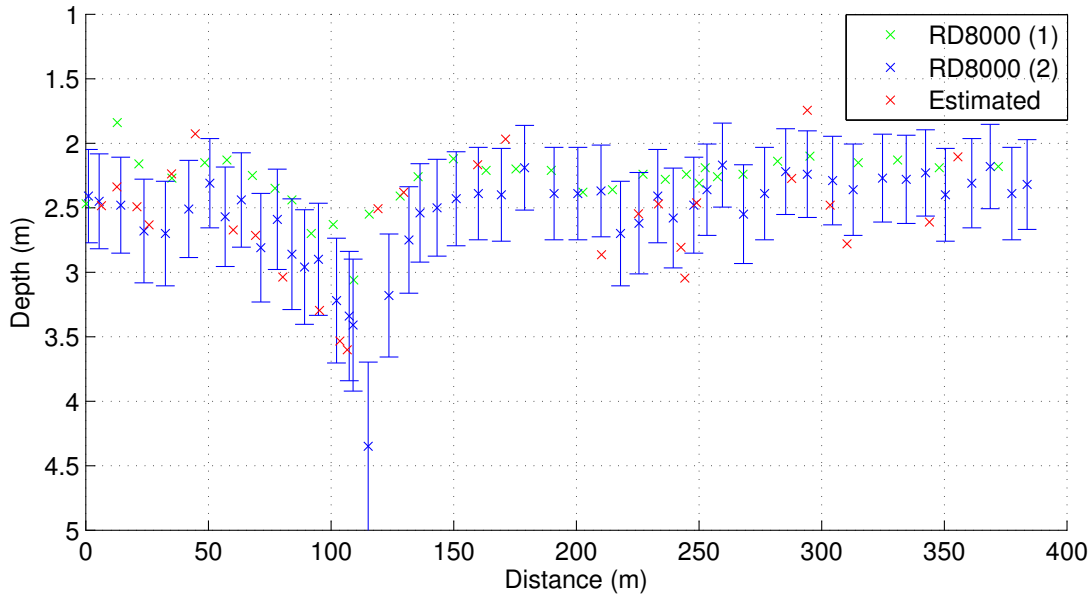

(b) The ASPA29 pipeline

Figure 6.14: A comparison of depth measured by two different RD8000 instruments and estimated using the depth algorithm. The mean field was automatically determined for individual sections of the pipeline. The estimation of the depth was better compared to using only one value of the mean field.

6.5 Locate welded joints in underground pipelines

As discussed in Section 5.5.5, a circumferential welded joint in underground pipeline may produce a magnetic indication which can be detected using the spatial gradient field. A technique to locate welds is developed in this section. Its performance will be evaluated using the field survey data and the ILI data.

Magnetic indication of a weld appears as a zero crossing in $\partial B_z/\partial x$ together with a peak in $\partial B_x/\partial x$. However, the simulation results in Section 5.5.4 shows that the exact location of the weld depends on the residual magnetisation of two pipe sections of the weld. For this reason, the weld location is not always coincident with the zero crossing or the peak location. In addition, other features of the pipelines, for example bends or stress concentration zones, could also affect the magnetic indication.

Fig. 6.15a compares $\partial B_{z_2}/\partial x$ to $\partial B_{y_{12}}/\partial x$ and $\partial B_{y_{32}}/\partial x$, in which, $\partial B_{z_2}/\partial x$ is the spatial gradient of the magnetic field measured by the magnetometer 2, $\partial B_{y_{12}}/\partial x$ and $\partial B_{y_{32}}/\partial x$ are the gradient of $Y_{12} = Y_1 - Y_2$ and $Y_{32} = Y_3 - Y_2$, respectively. The data was collected on a straight section of the underground pipeline from Pannal to Cawood (PACA07) near to the Pannal AGI site.

In the figure, where $\partial B_{z_2}/\partial x$ crossed zero, $\partial B_{y_{12}}/\partial x$ would cross $\partial B_{y_{32}}/\partial x$ as well. Therefore, intersection of $\partial B_{y_{12}}/\partial x$ and $\partial B_{y_{32}}/\partial x$ could be used as a magnetic indication of a weld instead of zero crossing of $\partial B_{z_2}/\partial x$. However, because every individual pipe section also produces a similar indication but on a longer distance, not all crossings shown in Fig. 6.15a were welded joints. The difference here is the magnetic indication of a welded joint occurs on a short distance, so it should result in a higher slope compared to that of a pipe section.

Fig. 6.15b shows the gradient field of the first 100 m of the survey route, together with the welds reported by ILI. As expected, the ILI welds, magenta dots, appeared very close to the locations where $\partial B_{y_{12}}/\partial x$ crossed $\partial B_{y_{32}}/\partial x$, except for the 470 one which would result in a miss of detection. The difference in the slope of the magnetic indication can be seen in case of the weld 468 or 471, at which the slope of $\partial B_{y_{12}}/\partial x$ and $\partial B_{y_{32}}/\partial x$ was very steep. These locations would be predicted as welds with more confidence than the others.

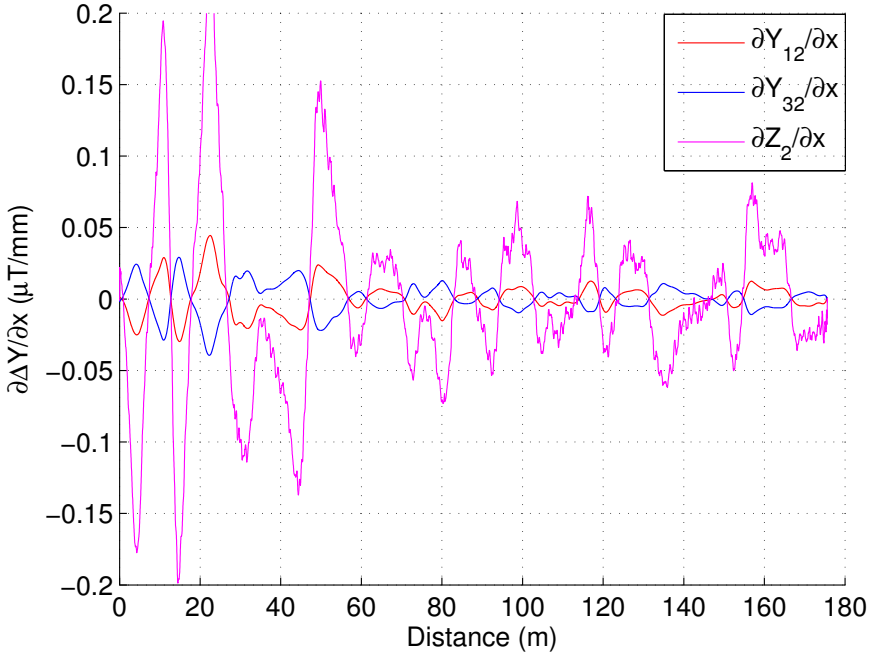

(a) A comparison between the crossings of $\partial B_{y_{12}}/\partial x$ and $\partial B_{y_{32}}/\partial x$ and the zero crossing of $\partial B_z/\partial x$.

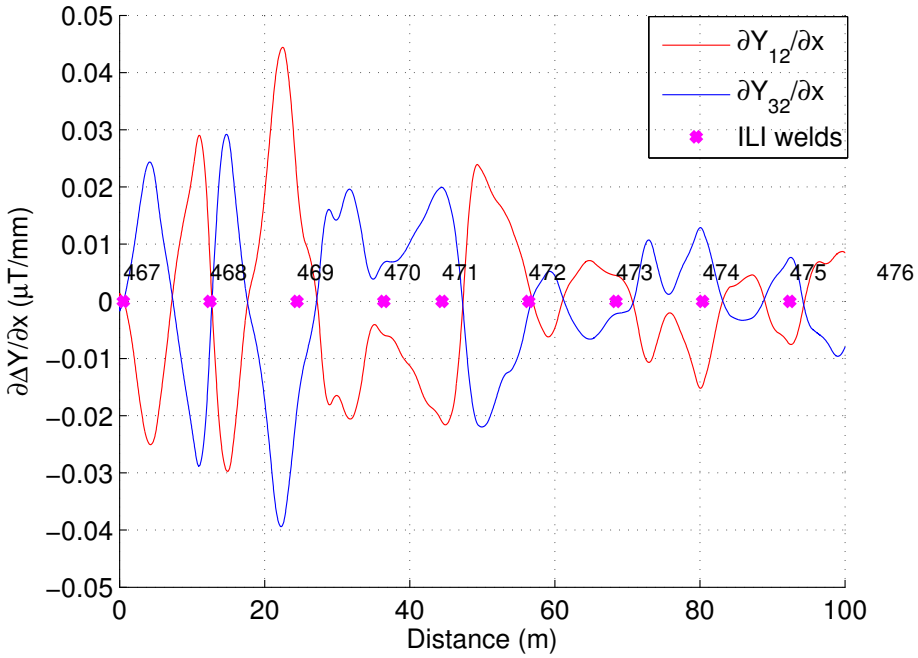

(b) Crossings of $\partial B_{y_{12}}/\partial x$ and $\partial B_{y_{32}}/\partial x$ as the magnetic indication of welded joints.

Figure 6.15: Gradient field of the first 100 m of the PACA07 pipeline and the welds reported by ILI. The indication was close the welds reported by ILI.

Using the above indication, Fig. 6.16 compares the welded joints predicted by SCT and those obtained from the ILI report. Only strong indications where $\partial B_{y_{12}}/\partial x$ crossed $\partial B_{y_{32}}/\partial x$ at a high slope were manually picked up during the analysis. Other crossings with lower slope, which actually caused by individual pipe sections, were manually ignored.

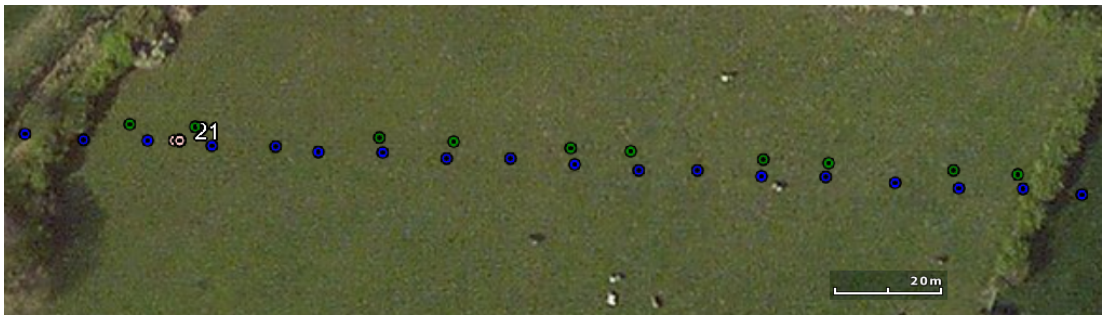

Figure 6.16: A comparison of welded joints predicted by SCT and ILI for the PACA07 pipeline. Their location was plotted using the corresponding GNSS coordinate. **Blue dot**: ILI welds; **Green dot**: SCT welds.

For this particular straight section, ILI reported 15 welded joints and an average pipe length of 12 m. Meanwhile, SCT predicted 10 welds with the same pipe length using the presented magnetic indication. Five of the ILI welds were missed because the magnetic indication was not clear. The maximum difference, in terms of survey distance, between the SCT and ILI welds was less than ± 2 m, except for the two welds on the left-hand side of the figure, where the error was about 3 m. It turned out that, based on the ILI report, there was a group of metal losses at this area, which could interfere with the survey magnetic field. The area will be excavated by National Grid later for repairing.

Because of using different positioning methods, there was a certain degree of error when comparing ILI and SCT using the GNSS coordinates. For example, the distance between the survey routes of the same pipeline reported by ILI and SCT was about 3 m. This caused an issue in assessing the SCT performance and was previously explained in Section 6.2.4. In fact, for this PACA07 pipeline, the location of the ILI welds were shifted 3.5 m along the SCT survey distance in order to align the first weld predicted by SCT and the closet ILI weld.

Fig. 6.17 shows the gradient field of the SCT survey and the location of the welds reported by ILI for the ASPA29 pipeline. Similarly, the ILI welds appeared very close to the magnetic indications, where $\partial B_{y_{12}}/\partial x$ crossed $\partial B_{y_{32}}/\partial x$ at a high slope. In this survey section, there was a bend at around 80 m, which consisted of 4 welded joints of approximate 3 m pipe sections. However, only one magnetic indication appeared, which meant three welds were missed. The reason for this is the survey was performed on the ground, more than 3 m away from the pipe, so the magnetic indication of these close welds was probably overlapped.

Fig. 6.18 shows the location of the welds predicted by SCT and ILI using their GNSS coordinates. In the figure, the welds predicted by SCT were lined up with the welds reported by ILI within a certain offset. However, at the bends, only one or two welds were located by SCT, some of them were missed. There were possible misses occurred on the straight section as well, for example at the SCT weld No. 10, there were actually two welds reported by ILI, but only one magnetic indication was picked up in SCT. For the ILI weld between the SCT weld No. 7 and 8, no magnetic data was collected for this section as it crossed a ditch and a fence here.

For this particular survey section, there were 30 welded joints reported by ILI with an average pipe length of 16.51 m compared to the constructed length of 17 m. This average length was calculated by ignoring three pipe bend sections because of shorter length. Meanwhile, SCT predicted 23 welds with an average pipe length of 16.54 m.

Because of the positioning methods, on the map, in order to align the welds predicted by ILI and SCT, the ILI welds were firstly projected onto the SCT survey route. These projected locations were then shifted forward 1.8 m in the survey distance to align with the first indication predicted by SCT with the closet ILI weld. The GNSS coordinate of these new locations were used to plot the ILI welds on the SCT survey route.

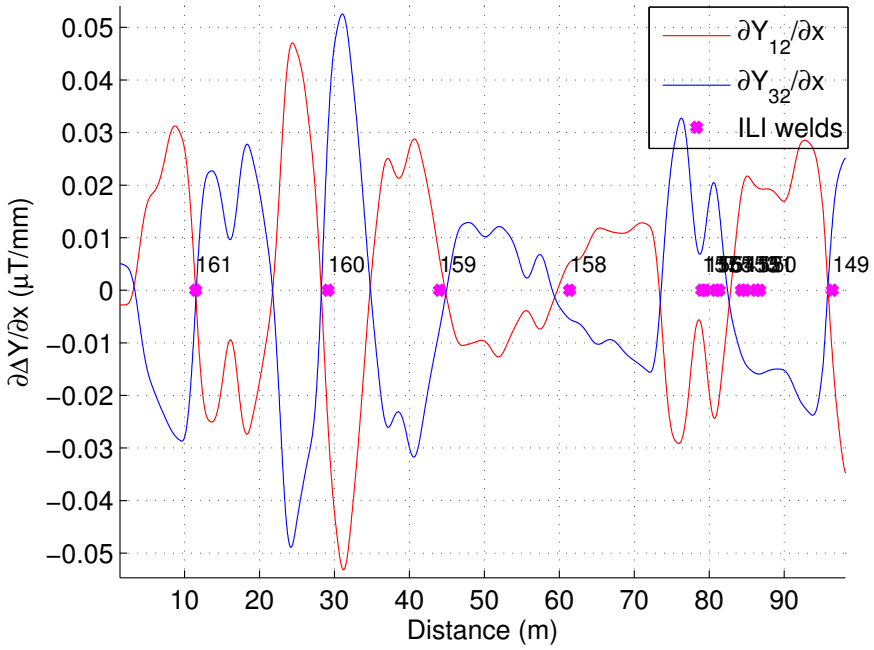

Figure 6.17: Gradient field of the first 100 m of the ASPA29 and the ILI welds. A horizontal bend with 4 welds reported by ILI was at around 80 m.

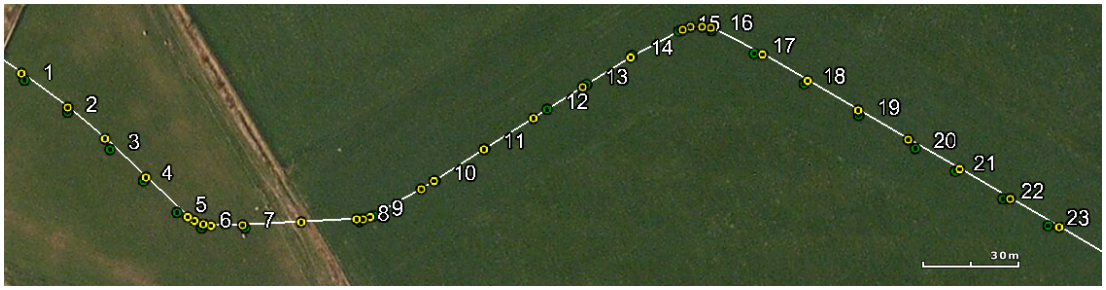

Figure 6.18: A comparison of welded joints located by SCT and ILI for the ASPA29 pipeline. The location was mapped using the corresponding GNSS coordinate. An offset of 1.8 m was added to the distance of the ILI welds after they were projected onto the SCT survey route. **Yellow dot**: ILI welds; **Green dot**: SCT welds. SCT predicted a weld close to an ILI weld within an offset.

Fig. 6.19a shows the histogram of the distance offset between a predicted SCT weld to the closet ILI weld. All the welds located by SCT stayed within ±5 m from an ILI weld. Practically, the maximum offset can be kept at around ±3 m, a weld predicted out of this range is considered as a false call.

Given the probability of detection (PoD), false detection (PoF) and missed detection (PoM) as follows:

$$\text{PoD} = \frac{\text{number of SCT welds matched with ILI welds}}{\text{total number of SCT welds}},$$
$$\text{PoF} = \frac{\text{number of SCT welds didn't match with ILI welds}}{\text{total number of SCT welds}},$$
$$\text{PoM} = \frac{\text{number of ILI welds not detected by SCT}}{\text{total number of ILI welds}},$$

Fig. 6.19b shows PoD, PoF and PoM with the maximum offset of 3 m. From the results, PoD = 87% (20/23) for the offset of 3 m. It means 20/23 of the welds predicted by SCT were within the range of 3 m compared to the ILI welds. 33.3% (10/30) of the ILI welds were missed including the one at the ditch where there was no magnetic data, 80% (8/10) of the missed welds were at the pipe bends. PoD was reduced to 65% and 52%, and PoM was increased to 50% and 60% for the offset of 2 m and 1 m respectively.

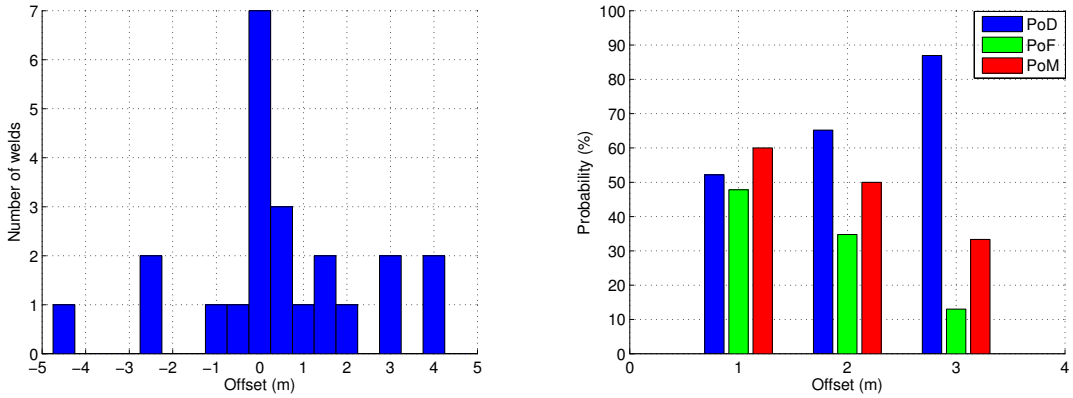

(a) Histogram with distance offset

(b) Probability

Figure 6.19: Results of the welds predicted by SCT on the ASPA29 pipeline.

The analysis was repeated for the PANE29 pipeline. Fig. 6.20 shows the gradient magnetic field together with the welds reported by ILI for the first 100 m of this surveyed section. Again, the magnetic indications resulted from the crossing of $\partial B_{y12}/\partial x$ and $\partial B_{y32}/\partial x$ appeared to be close to the ILI weld locations. However, there would be misses at around 30 m to 40 m, which was due to the pipe bend; or the ILI weld No. 51 as it was too far from a magnetic indication.

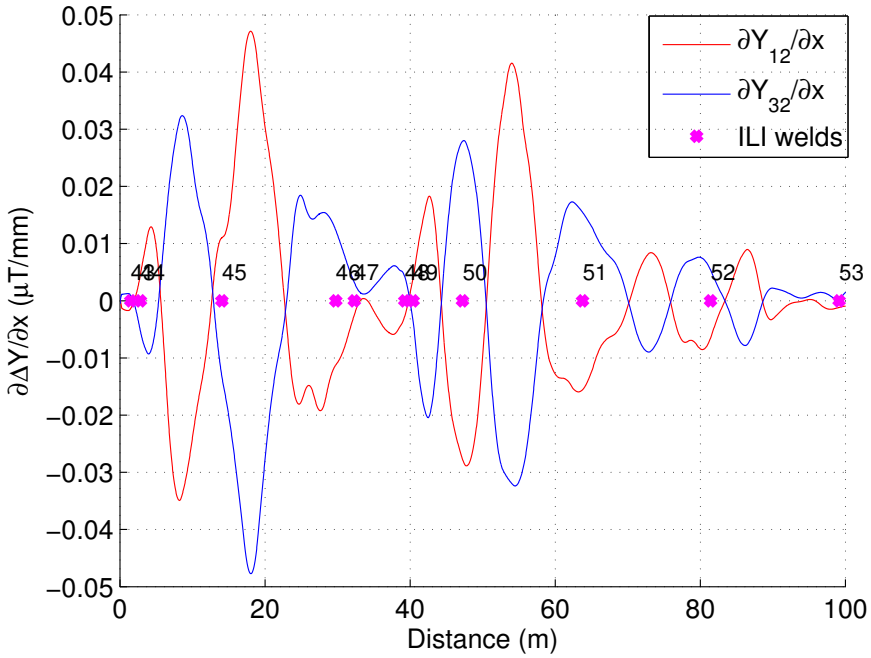

Figure 6.20: Gradient field of the first 100 m of the PANE29 and the ILI welds.

Fig. 6.21 shows the welds predicted by SCT using the crossing of $\partial B_{y12}/\partial x$ and $\partial B_{y32}/\partial x$ compared to that reported by ILI. For this surveyed section, the number of ILI welds was 21 with an average pipe length of 13.76 m. SCT predicted 17 welds with an average length of 17.75 m. It should be noted that the constructed length for this section was 17 m. In the figure, the ILI welds were aligned to the welds predicted by SCT by an offset of 1.3 m.

Fig. 6.22a shows the histogram of the distance offset between the welds predicted by SCT and their closet ILI welds. All the SCT indications were around ±5 m from an ILI weld. Using the maximum offset of 3 m, Fig. 6.22b shows the probabilities of the SCT prediction when compared to the ILI report. For this

particular section, PoD was 82% (14/17) for the offset of 3 m, and PoM was 33% (7/21), 40% (3/7) of the missed welds were at the bending section. PoD was reduced to 71% (12/17) and 41% (7/17), and PoM was increased to 43% (9/21) and 67% (14/21) for the offset of 2 m and 1 m respectively.

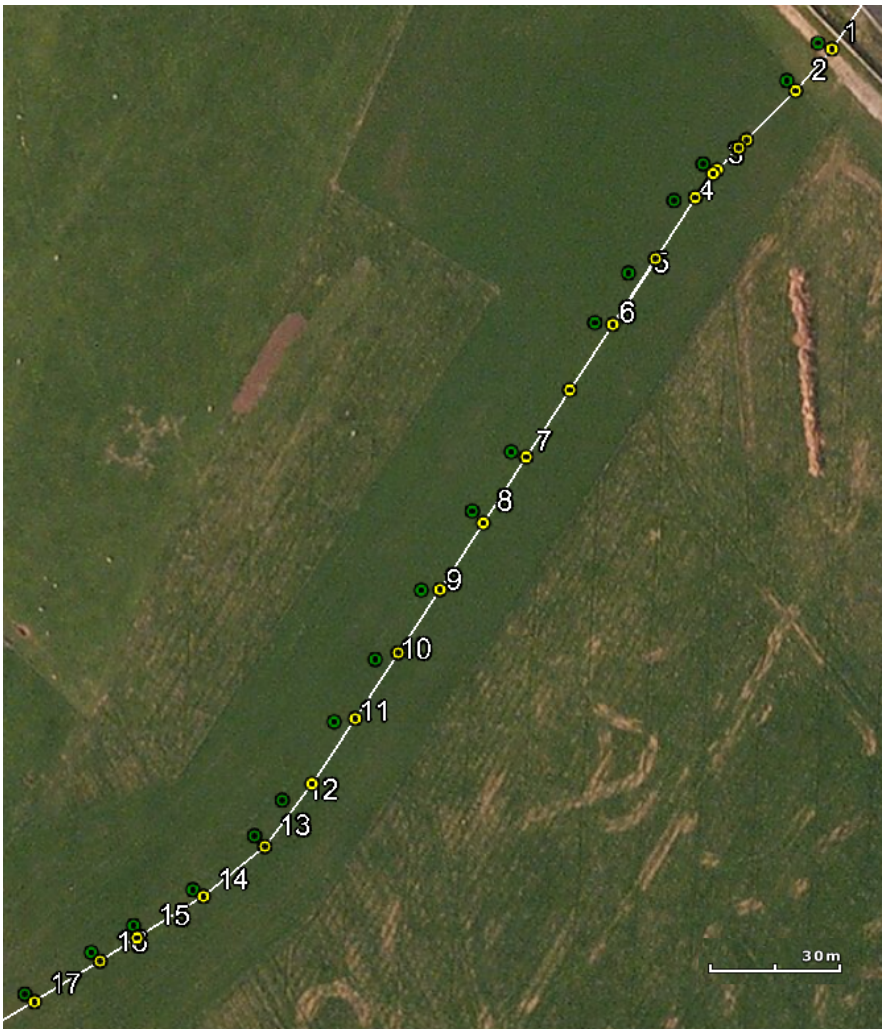

Figure 6.21: A comparison of welded joints located by SCT and ILI for the PANE29 pipeline. **Yellow dot**: ILI welds; **Green dot**: SCT welds.

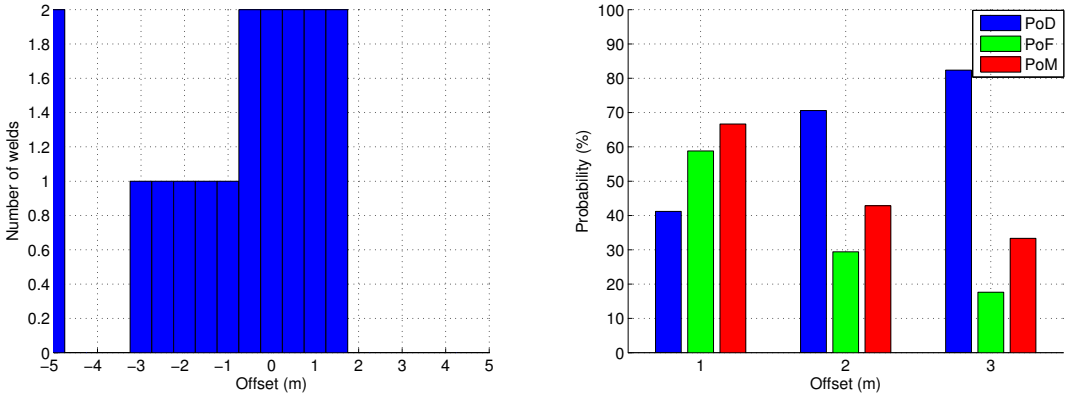

(a) Histogram with distance offset

(b) Probability

Figure 6.22: Results of the welds predicted by SCT on the PANE29 pipeline.

Offset (m)	**#3**	**#2**	**#1**
PoD (ASPA29) (%)	87	65	52
PoD (PANE29) (%)	82	71	41
PoM (ASPA29) (%)	33	50	60
PoM (PANE29) (%)	33	43	67

Table 6.1: Comparison of probability of the ASPA29 and PANE29 surveys.

Table. 6.1 compares the probabilities of the two surveys. Both PoD and PoM of the two surveys were similar. It can be said that, using the crossing of $\partial B_{y_{12}}/\partial x$ and $\partial B_{y_{32}}/\partial x$ as a magnetic indication, 80% of the welded joints of underground pipelines predicted by SCT stays within an offset of 3 m from an actual weld with a probability of missed detection of about 30%. The reason by which the weld predicted by using the crossing is not always coincident with the actual weld is it depends on magnetisation of two pipe sections of the welded joint as discussed in Section 5.5.4. Importantly, it should also be noted that the SCT performance was evaluated based on the ILI report, and used it as the gold standard. In practice, ILI has its own accuracy limitations.

The weld location technique can be improved further in association with knowledge of the constructed length of pipe sections of the pipeline. In practice, this length is usually known, for example, it was 12 m for the Pannal to

Cawood pipeline and was 17 m for the ASPA29 and PANE29 pipelines. The information of this constructed length can be used together with the location of the welds predicted by SCT in order to adjust their own locations, and more important, reduce the PoM by inserting theoretical predicted welds in the middle of the sections longer than the constructed length which indicate a missed detection.

6.6 Preliminary study on detecting stress concentration zones

From the above results, it can be stated that for magnetometer surveys of underground pipelines, the magnetic field induced by individual pipe sections and welding them together plays the role of the bulk field. Therefore, based on the understanding of the bulk effect, this study suggests that in order to extract magnetic indication of stress concentration zones (SCZs), one should look into the details of the measured magnetic field, which is the component superimposed by magnetic features of individual pipe sections and welded joints. In other words, techniques that are possible to represent the measured magnetic field by its approximation, which represents the magnetic field induced by pipe sections, and the detail signal, which possibly represent the field induced by SCZs, should be used.

Based on this idea, this study attempted to decompose the measured magnetic into approximation and detail coefficients using wavelets. The signal reconstructed from the approximation coefficients should be the magnetic field of individual pipe sections and the effect of welding, i.e. the bulk field, and the signal reconstructed using detail coefficients may reflect magnetic features of SCZs.

In fact, there are other techniques that could be used to decompose the measured magnetic field, for example Fourier methods. However, the wavelet technique appears to be more suitable for this application. The reasons for this are, firstly, the length of magnetic features of a SCZ is usually unknown as it depends on the dimensions and the depth of the SCZ. Secondly, the magnetic features may appear at any location along the pipeline. Therefore, the ability to independently scale and shift the wavelet is an advantage. Importantly, an approximate

version of the detected magnetic feature extracted from the bulk magnetic field can be reconstructed using the wavelet coefficients, which may allow a measure to evaluate the severity of the detected SCZ.

6.6.1 Signal decomposition using wavelets

Theoretically, a function $f(t)$ can be reconstructed from the weighted basis functions $\psi_{j,k}(t)$ as follows [64]

$$f(t) = \sum_{j,k} \gamma(j,k)\psi_{j,k}(t), \tag{6.9}$$

in which $\psi_{j,k}(t)$ is scaled and translated in discrete steps from the function $\psi(t)$

$$\psi_{j,k}(t) = \frac{1}{\sqrt{s_0}}\psi(\frac{t - k\tau_0 s_0^j}{s_0^j}), \tag{6.10}$$

where s_0 is the scaling factor, τ_0 is the translating factor. The function $\psi(t)$ is called the mother wavelet and $\gamma(j,k)$ are wavelet coefficients.

When looking the wavelet as a signal, it has a band-pass spectrum and a zero average value in the time domain. Compression the mother wavelet in the time domain reduces its spectrum and shifts it up in the frequency domain. Therefore, in order to reconstruct the signal spectrum to its zero frequency, an infinite number of wavelets is required. A scaling function $\varphi(t)$ which has a low-pass spectrum was introduced in order to reduce the number of wavelets [65]. This scaling function can also be represented using wavelets as follows

$$\varphi(t) = \sum_{j,k} \gamma(j,k)\psi_{j,k}(t). \tag{6.11}$$

A reconstructed signal spectrum is now covered by the spectrum of the scaling function and the wavelet functions. The wider the scaling function spectrum, the less wavelet coefficients. In terms of the discrete wavelet transform (DWT), the function $f(t)$ can be represented as

$$f(t) = \sum_k \lambda_{j-1}(k)\varphi(2^{j-1}t - k) + \sum_k \gamma_{j-1}(k)\psi(2^{j-1}t - k), \tag{6.12}$$

in which

$$\begin{aligned} \varphi(2^{j-1}t) &= \sum_k g_j(k)\varphi(2^j t - k), \\ \psi(2^{j-1}t) &= \sum_k h_j(k)\varphi(2^j t - k). \end{aligned} \tag{6.13}$$

$g(k)$ and $h(k)$ are usually referred as low-pass and high-pass filters since the wavelet transform of a signal is identical to pushing the signal through the low-pass filter with the coefficients $g(k)$ and the high-pass filter $h(k)$. This process can be iterated on the next level for the scaling function coefficients as shown in Fig. 6.23a. For every next level, the high-pass spectrum will be shifted down and half in the width. The signal reconstructed from the wavelet coefficients γ_j is called the detail signal as it has the high-pass spectrum, and that reconstructed from the coefficients of the scaling function λ_j is the approximation signal.

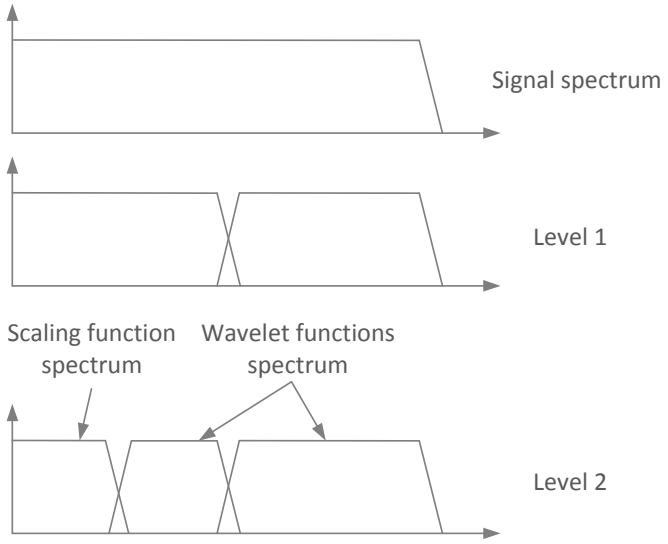

(a) Spectrum of the signal and wavelet transforms.

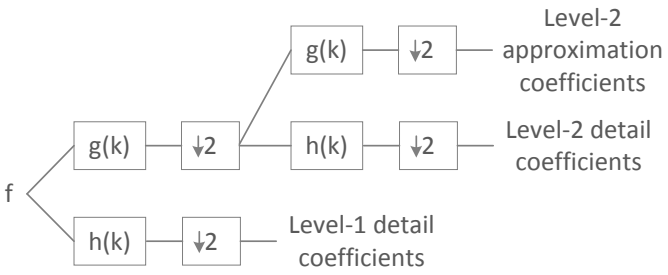

(b) Filter bank.

Figure 6.23: Signal spectrum with iterated filter bank.

6.6.2 Detection of stress concentration zone using wavelets

Fig. 6.25 shows the magnetic field of magnetometer 2 of the PACA07 pipeline, together with its approximation and the details. A discrete wavelet transform (DWT) was performed on the magnetic field using the biorthogonal 3.3 wavelet. This resulted in the detail coefficients and approximation coefficients of level 1. The decomposition was repeated for the approximation coefficients up to level 7 in order to increase the frequency resolution. These coefficients were then used to reconstruct the corresponding signals including the approximation of the magnetic field and the detail signals for each level as shown in the figure. This type of wavelet transform uses two different scaling and wavelet filters for decomposition and reconstruction of the signal, see Fig. 6.24.

At first, the detail signal at level 7 of B_z appeared to be coincident with the location of the stress concentration zone (SCZ) reported by ILI. In order to provide an indication, the envelope of this detail signal was calculated and is shown in Fig. 6.26 together with the location of the ILI defect. In the figure, a strong indication of 5 μT appeared at the defect location. An excavation was performed and the defect was confirmed, however, it was also found a sag bend of 22° within 1 m from the feature. This means it may be possible to detect a SCZ using this technique, however, in this case, it was unclear whether the indication was due to the defect or the pipe bend.

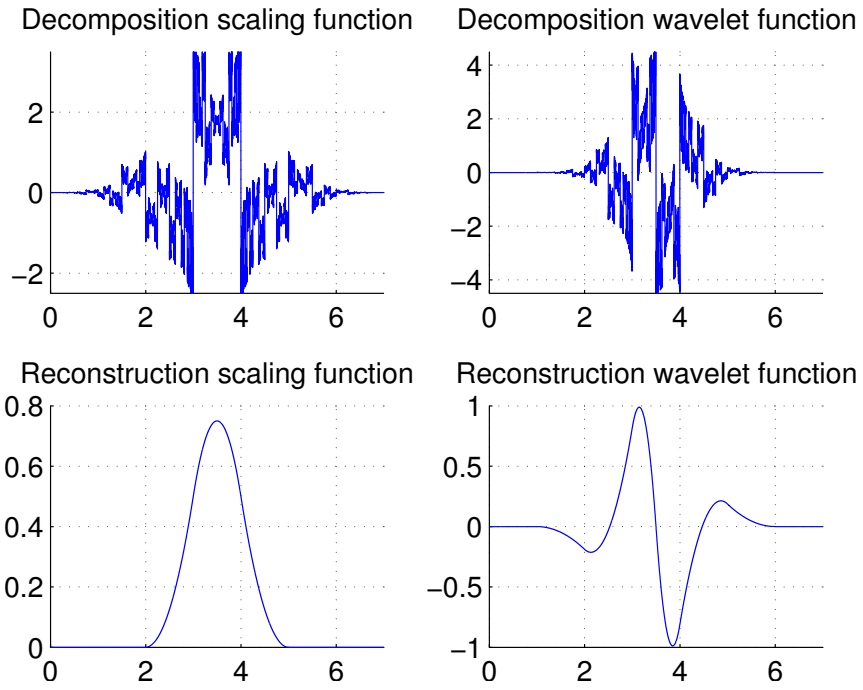

(a) Scaling and wavelet functions.

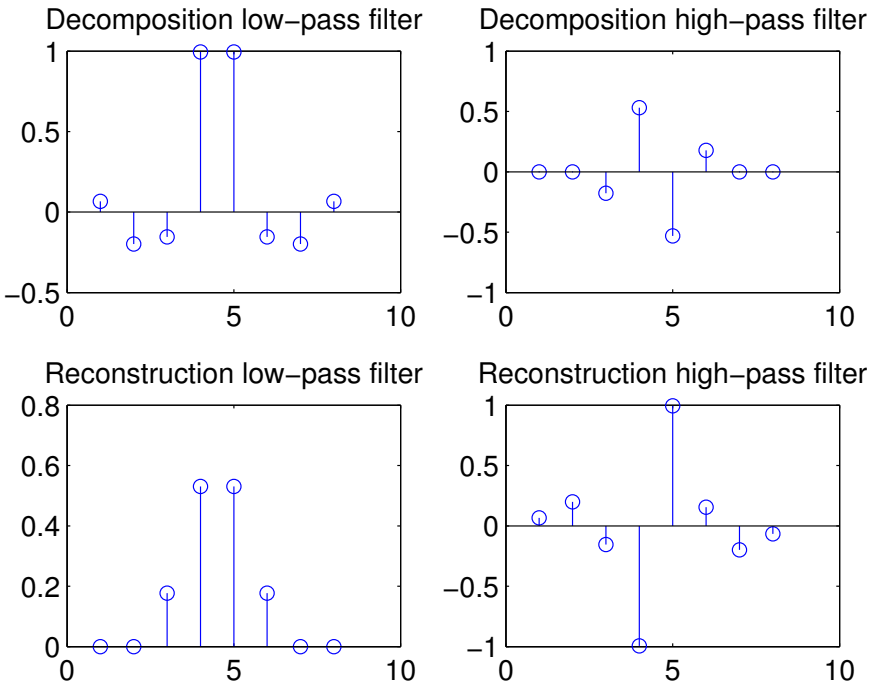

(b) The impulse response of the decomposition and reconstruction filters.

Figure 6.24: Filters and functions of the wavelet biorthogonal 3.3.

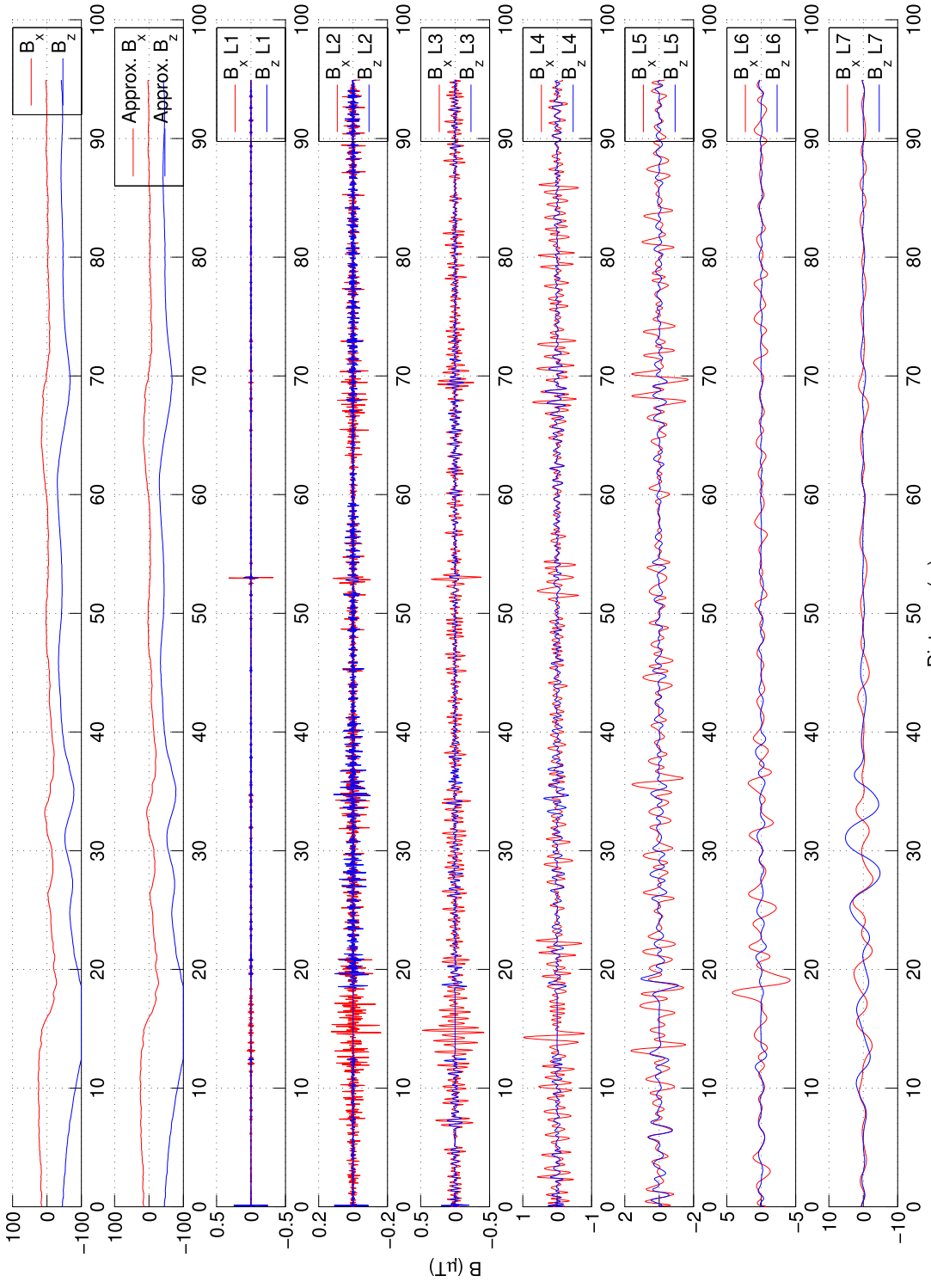

Figure 6.25: Magnetic field of the surveyed section of the PACA07 pipeline (feature No. 8) and its approximation and detail signals using wavelet decomposition.

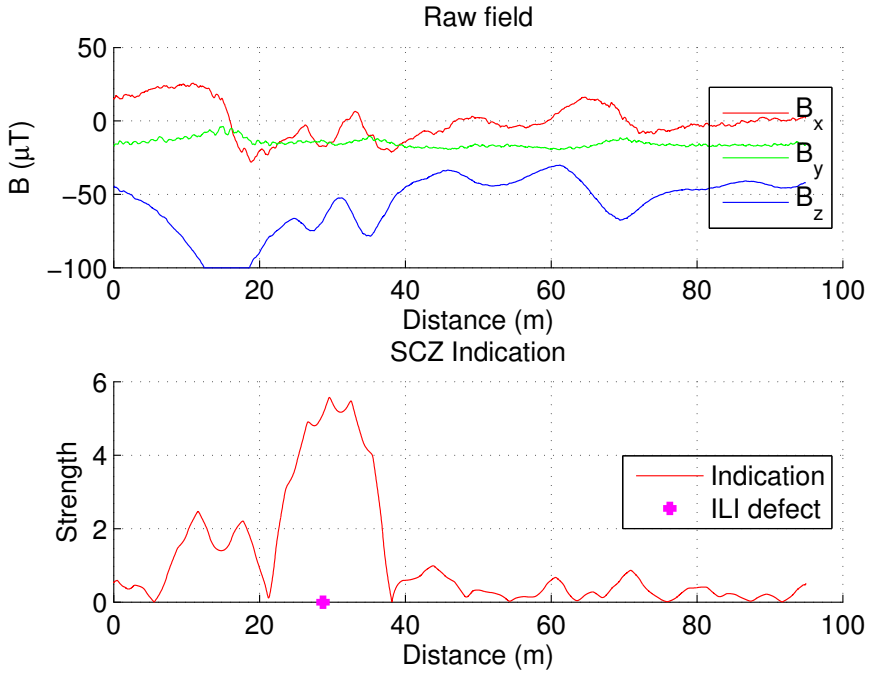

Figure 6.26: Magnetic field of the surveyed section of the Pannal to Cawood pipeline (PACA07), the calculated indication of SCZ and the location of the defect feature No. 8 reported by ILI.

The analysis was repeated for another section of the PACA07 pipeline, for which, ILI also reported a defect (feature No. 9). Fig. 6.27 shows the approximation and detail signals up to level 7 for the magnetic field of this surveyed section and Fig. 6.28 shows the magnetic field of magnetometer 2, the calculated indication and the location of the defect. Again, the indication appeared at the defect location, which was about 10 m from the start point. An excavation was also performed and confirmed the defect. Both the indications were stronger than 4 μT and stood out from the rest.

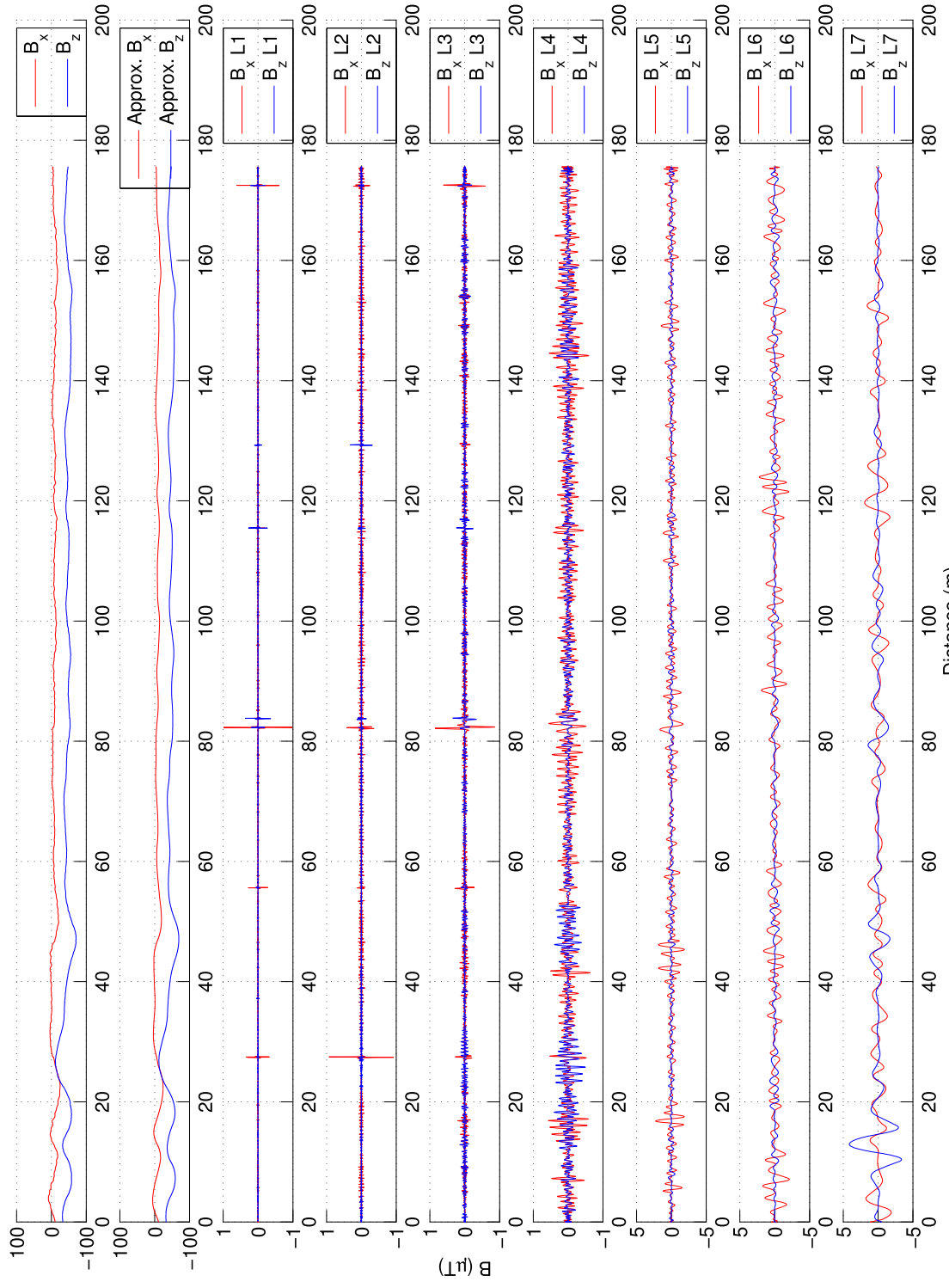

Figure 6.27: Magnetic field of another surveyed section of the PACA07 pipeline (feature No. 9) and its approximation and detail signals using wavelet decomposition.

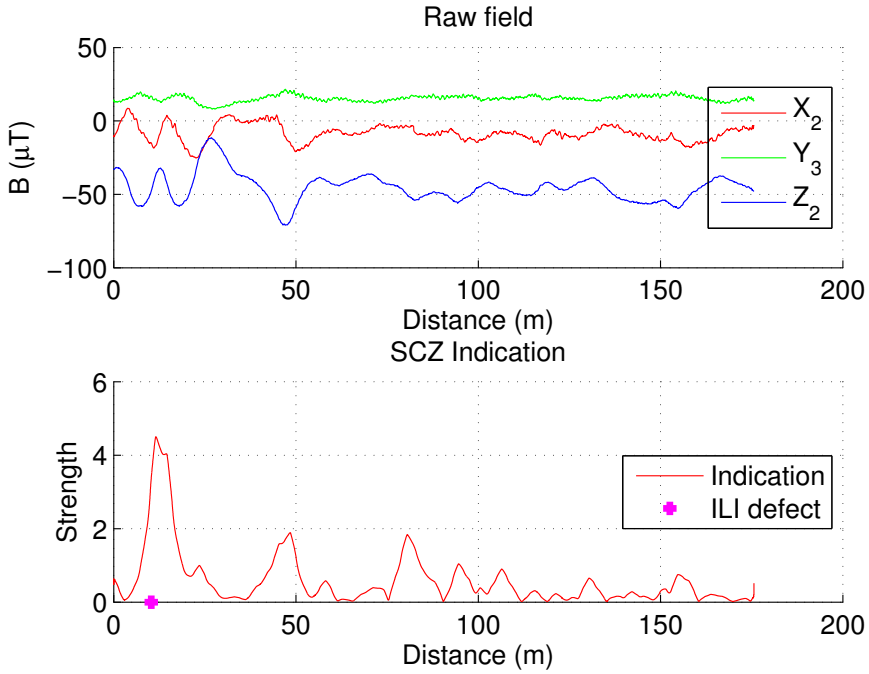

Figure 6.28: Magnetic field of another section of the Pannal to Cawood pipeline (PACA07), the calculated indication of SCZ and the location of the defect feature No. 9 reported by ILI.

The technique was also tested on the surveyed sections of the PANE29 and ASPA29 pipelines. No defect was reported by ILI for these two sections. Based on the positioning coordinates reported by ILI and SCT, there were side bends along the surveyed sections. Fig. 6.29a shows the ASPA29 pipeline together with its features, and Fig 6.29b shows the indication calculated using the wavelet decomposition. For this section, the coordinate of the side bends No. 1, 2 and 3 were reported by ILI. These were projected onto the SCT survey route together with the location of the ditch.

In Fig. 6.29b, there were strong indications coincident with the side bends. In particular, the ASPA29 surveyed section has three side bends. The first one at 75-83 m was associated with the indication of more than 5 μT. The indication of the second one at 128-133 m was smaller, only about 2.5 μT. The last one at around 250 m was a sharp bend, so the strength of its indication was about 8 μT compared to the other two. Interestingly, there were two similar indications

at around 100 m but without any side bend reported. It was found that there was a change in the depth of cover of the pipeline as it went under a ditch at this location, so there were possibly sag bends here, which resulted in two indications around the ditch location,see Fig. 6.14b. The depth of the pipeline at this location was changed from 2.5 m and 4.5 m and back to 2.5 m. Although all the indications appeared to be at the bends, the indication of the side bend No. 2 was only 2.5 μT. If a threshold of 4 μT was used to detect SCZs, this would result in a missed detection.

For the PANE29 pipeline, see Fig. 6.30 and Fig. 6.31, the result was very similar. For this surveyed section, because the start and end locations of the bends were not included in the ILI report, the bend locations were measured on the map, which were 15 m, 40 m and 227 m (including 1.8 m offset to align the SCT and ILI coordinates). In Fig. 6.31, the indication of the three side bends was smaller than 4 μT, probably because these were gentle bends. Although there were two strong indications at 277 m and 287 m, there was no side bends or defects reported at these locations. However, as shown in Fig. 6.32, there were probably sag bends between 268-300 m as the depth was changed from 3 m to 2.5 m and then back to 4.5 m.

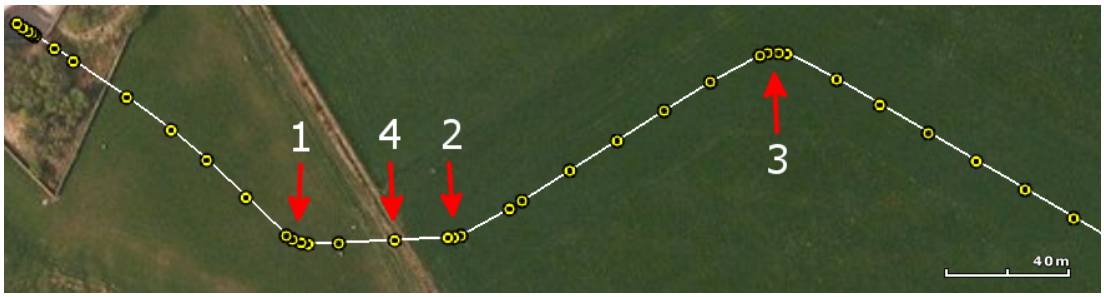

(a) The ASPA29 pipeline and its three side bends. **No. 1**: 76-83 m, **No. 2**: 128-133 m, **No. 3**: 246-254 m, **Ditch**: 110 m.

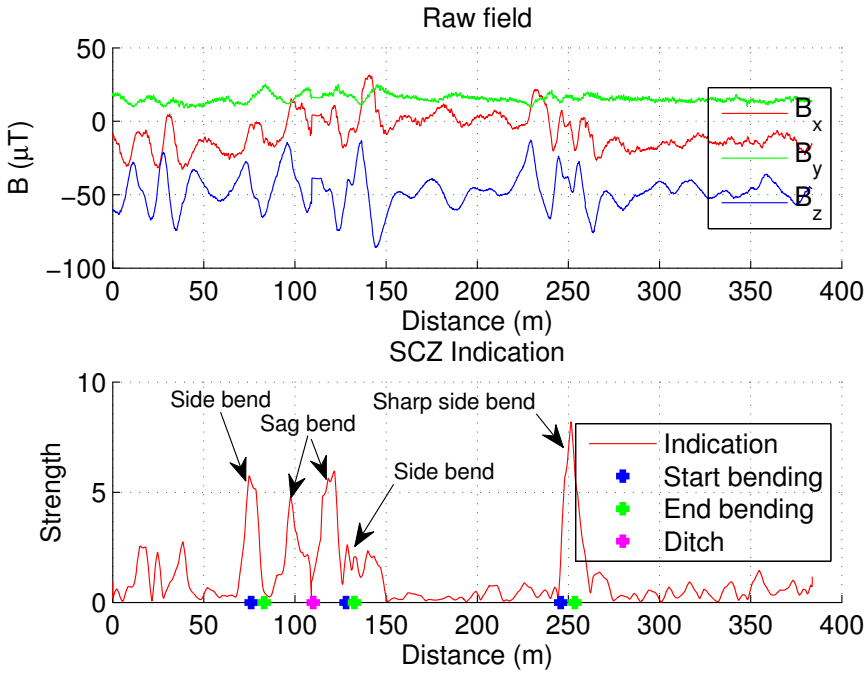

(b) Magnetic field of the ASPA29 pipeline and the calculated indication of SCZ.

Figure 6.29: The ASPA29 pipeline and its bends, together with the magnetic field and the calculated indication of SCZ. No defect was reported by ILI. There were strong indications at bends.

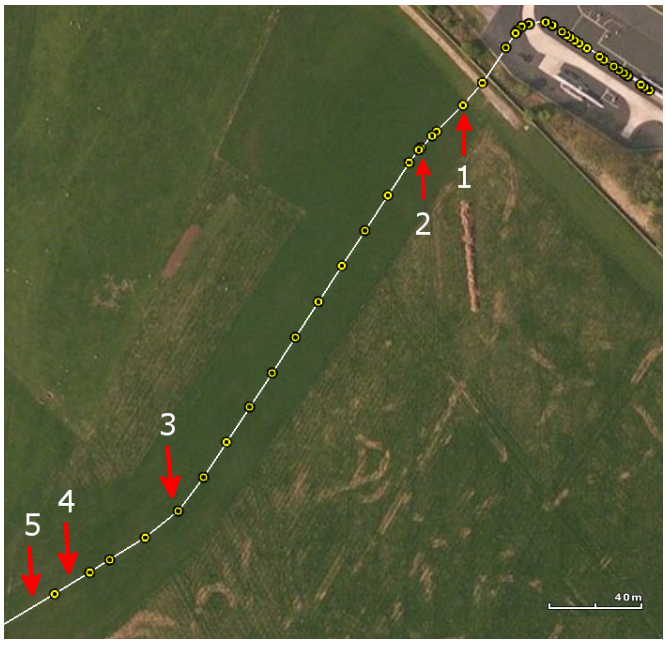

Figure 6.30: The PANE pipeline and its three side bends (1, 2, 3). **No. 1**: 15 m, **No. 2**: 40 m, **No. 3**: 227 m, **No. 4**: 278 m, **No. 5**: 288 m.

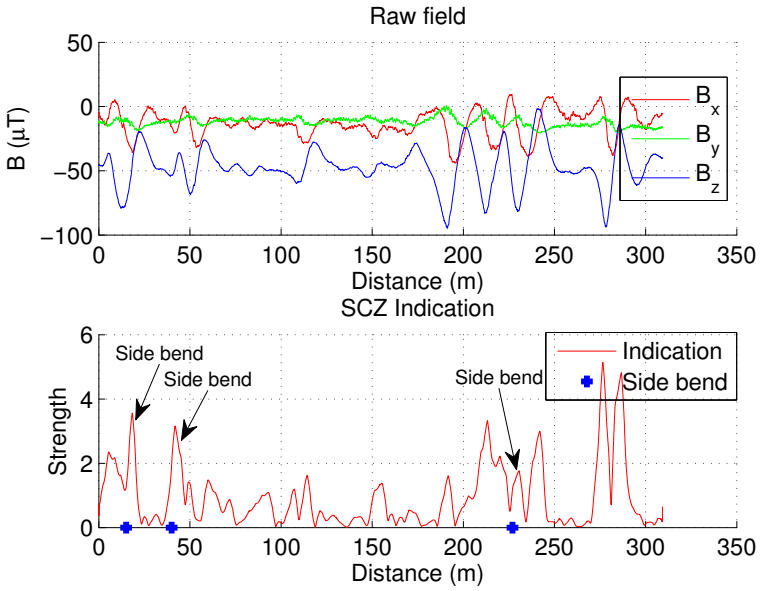

Figure 6.31: Magnetic field of the PANE29 pipeline and the calculated indication of SCZ. No defect was reported by ILI. There were indications at side bends, together with two strong indications between 268 m to 288 m probably due to changes in the depth.

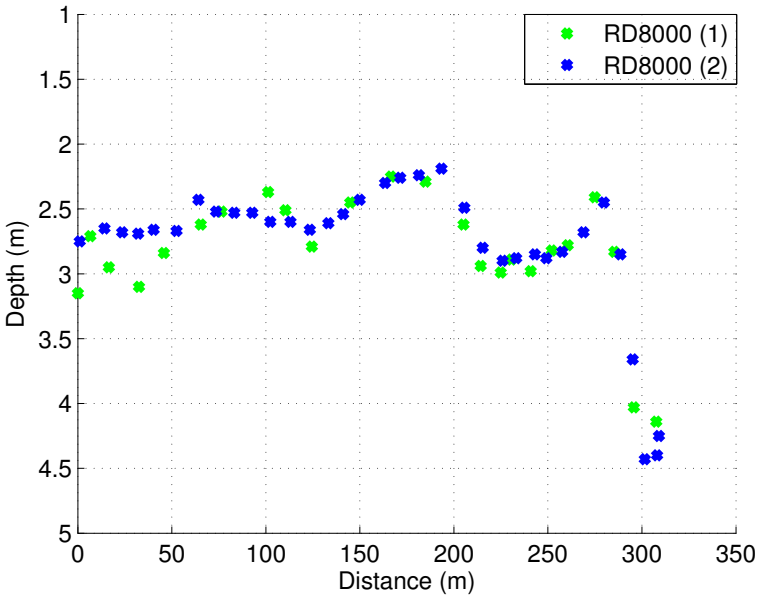

Figure 6.32: Depth of the PANE29 pipeline measured by two different RD8000 instruments was changed between 268-300 m.

It can be said that, for the first time, stress concentration zones of underground pipelines were detected through the remote magnetic field with clear indications and high confidence. In addition, there seemed to have a relationship between the stress level and the strength of the magnetic indication. Most of the predicted features were close to bends. There were two predictions close to the defects reported by ILI, but one of them was close to the sag bend too. Nonetheless, it may be possible that defects can be detected using this technique as well. Importantly, the technique appeared to be able to detect sag bends, which is, in practice, not included in the ILI reports. This means it is possible to use SCT as a complementary technique for ILI, for example to detect land subsidence, which may cause a serious hazard to pipeline. It should be noted that this information was inferred from the depth of the pipeline only, no physical verification of the sag bends was able to be performed during the course of this study.

6.7 Conclusions

Depth of cover is critical for the integrity of underground pipelines. With an industrial pipeline locator such as the RD8000 instrument, the surveyor has to stop and take the measurement at individual locations on the ground, therefore, it may be unsuitable to follow the depth for long sections, for example several kilometres. Besides that, location of welded joints of underground pipelines are useful complementary information. The reason is, using the ILI method, location of a defect is usually reported in distance to the upstream weld, therefore, correctly locating the weld may help to reduce the cost of excavation. The UNISCAN instrument featuring an array of three magnetometers and a high accuracy GNSS receiver is able to measure the magnetic field along the pipeline at a walking speed of about 3.6 km/h (1 m/s). Utilising the techniques presented in this chapter, it is possible to use it as a complementary tool for ILI.

The main advantage of using the passive magnetic field to estimate the depth and locate welded joints is time and cost reduction. In practice, it is possible for a team of two people to collect the data of about 6 km pipeline in a day, three to four days per week. The data includes magnetic field and geolocation mapping at the same time.

6. CHARACTERISING FEATURES OF UNDERGROUND PIPELINES USING ABOVEGROUND MAGNETIC SURVEYS

In this study, field surveys on underground pipelines have been performed using the UNISCAN instrument. About 1 km of data has been analysed and presented in this chapter. In order to evaluate the performance of the depth estimation technique, the depth of cover was measured by the RD8000 instrument at reference locations together with their geolocation. For verifying location of welded joints, data from the ILI report was used. The coordinates in the ILI report were in OSGB36 Easting/Northing, so a conversion to WGS84 Latitude/Longitude was required. It caused an issue when assessing the SCT performance, for example, the difference in the system of geographic grid reference used by ILI and SCT resulted in an offset of about 3 m between the pipelines mapped by ILI and SCT. Although ILI has its own accuracy, in this study, the ILI data has been treated as the gold standard for evaluate of SCT.

This study suggests using the remote-sensing passive magnetic field to estimate the depth of cover of underground pipelines. A technique to remove effects of the operator movement has been developed and shown to work. The results of this study show that the estimated depth has been able to follow the trend of the depth of cover. In terms of its own accuracy, the technique has a tolerance of 8% of the measurement depth.

The results of this study has also shown that the crossing of the horizontal component of two magnetometers can be used as a magnetic indication of a circumferential welded joint, in addition to using the vertical component of one magnetometer. However, this feature is required to distinguish from a similar feature produced by individual pipe sections. The slope of the gradient field of the magnetic indication has been chosen to determine whether it is created by a weld or pipe section. The reason for this is a weld is much shorter in length than one pipe section, several centimetres compared to over 10 m respectively. The higher slope, the higher probability to be an indication of a weld. Assumed that the ILI data is the gold standard, the study has shown that the weld detection technique is able to locate about 70% of the actual welded joints within ± 3 m with the probability of false call of 20%. The probability may increase for straight sections of underground pipelines. If there are bending sections, at least 50% of the welds SCT missed could be at the bends. The worst case is for the offset of ± 1 m, only 30-40% of the actual welds can be detected by SCT within this offset,

with a probability of false call of 50-60%. The reason for this is the magnetic indication depends on magnetisation of pipe sections on two sides of the weld and the depth of cover, therefore, it could shift the magnetic indication from the actual weld location.

Importantly, a practical technique to calculate the measure of stress concentration zone (SCZ) of underground pipelines has been proposed. The results were very consistent between different surveyed sections. This study has provided strong evidence that it is possible to observe the magnetic indication of a SCZ in underground pipelines using magnetometer surveys. More work is required to differentiate the indication due to bends and defects. In terms of a complementary tool, the technique presented in this study is capable of detecting sag bends.

The study has established promising techniques which can provide additional information for current inspection methods. It has certainly extended the understanding on the magnetic field of underground pipelines. Importantly, it provides evidence to support the idea of a method finding magnetic indication of SCZ by looking into the details of the measured magnetic field. However, more work needs to be done to improve the techniques. A better algorithm to accurately remove the mean field could improve the depth estimation technique. The current study has used only one component of the measured magnetic field to locate the weld; other components could be used as well. Also, evaluation on the performance of the techniques will certainly improve the confidence level.

6. CHARACTERISING FEATURES OF UNDERGROUND PIPELINES USING ABOVEGROUND MAGNETIC SURVEYS

Chapter 7

Conclusion and Future Work

7.1 Conclusion

Pipeline networks are a vital part of the energy infrastructure. Technologies have been developed for many years to proactively ensure their integrity. In recent years, a new magnetic technology has been applied to pipeline inspection, said to be able to detect stress concentration zones (SCZ) in pipelines using stand-off magnetometry. However, very little scientific evidence related to this technology can be found in literature, so there have been questions about its reliability.

This study provides scientific background to improves the reliability and confidence in the technology. A series of experiments on steel bars and small to large-scale steel pipes were performed. Finite element models have been built to support the study, especially on effects of the bulk field when measuring the remote magnetic field. Finally, practical techniques have been developed and tested with field surveys. Their performance has been evaluated against the current gold standard methods used by industry.

This study has modified the original Jiles-Atherton model of the magnetomechanical effect so that it is able to solve for effects of both tensile and compressive stress cycles on magnetisation of the material. The differential equations presented in Chapter 2 have supported building finite element models of steel bars and steel pipes, so the stress-induced magnetic field can be analysed. However, it is acknowledged that the stress-magnetisation model has limited used in predicting the magnitude of the stress-induced magnetic field.

The results shown in Chapter 4 have extended the understanding on magnetic indication of stress concentration zones (SCZ). For this initial study, introducing a geometry defect, on one hand, has produced a magnetic anomaly which is enhanced when stressed, as expected. On the other hand, the magnetic anomaly can be observed even without effects of stress. Therefore, one could possibly argue that the magnetic anomaly is due to the geometric defect rather than stress. Positively, the simulation results have shown the non-linear variation of magnetisation with stress cycles. It implies the possibility for a magnetic anomaly to appear without a geometric defect as long as there is a local SCZ. This effect is unique, which makes the technology promising. This study has suggested that a magnetic anomaly in this case is due to the difference in magnetisation of the local SCZ and the surrounding material rather than leakage of the magnetic flux as in the MFL technique. And because the stress-magnetisation relationship is non-linear, this difference of magnetisation can be positive or negative depending on the stress level. This is the reason of why the magnetic indication of the local SCZ may reverse its polarity with variation of stress. Based on this, although it is unsuitable for SCT, the study has suggested a possible technique to remotely detect changes of stress by permanently monitoring the magnetic field of the material.

This study has found that when using the remote-sensing magnetic field, magnetic indication of a local SCZ is superimposed by the magnetic field of the bulk material. Using the gradient magnetic field with respect to the axial direction may reduce the bulk effect and reveal the local magnetic indications, whose strength can be characterised by the value of the parameter K at the zero crossing of B_z.

The study has investigated the variation of K with stress, the initial magnetic condition of the material and the measurement distance. It has found that the variation of K with stress follows the stress-magnetisation relationship; and magnitude of this variation depends on the initial magnetic condition of the material. Inversely, K is linear with the initial magnetic condition at a given stress. The study has quantitatively established the exponential relationship between K and the measurement distance. The relationship is important as the aim of the study is to utilise the remote magnetic field. In this study, the experiments, the simulations and the analytical equations have shown similar results, in which, K

exponential decays with the measurement distance. However, it may be possible that the decay rate is not a constant but varied within a small range depending on the dimensions of the SCZ. Nonetheless, the analytical equations of K with the measurement distance implies that it is possible to estimate the surface magnetic field and dimensions of the SCZ from the remote magnetic field. Based on this, the study has provided evidence of solving the inverse problem, where stress condition is estimated from the remote magnetic field.

The extended study on pipelines has confirmed the findings of the initial study, see Chapter 5. Although the simulation model has only considered the effect of stress on one component of magnetisation, its results have generally agreed in the trend with the experiments and field observations except for the variation of K with the measurement distance, where the model has predicted a slightly slower rate.

The study has found that in addition to the magnetic features of individual pipe sections, that of welding pipe sections together may also be a part of the bulk field. Because the residual magnetisation of individual pipe sections and its orientation may be random, this further complicates detection of local SCZ in pipelines. It has suggested that a weld may produce distinguished features, which is observable using the gradient of the remote magnetic field. This implies a possibility of locating them. It also means in order to find the magnetic indication of a local SCZ, one should locally look into the details of the measured magnetic field.

Based on the understanding of the remote magnetic field, the study has presented three practical techniques to estimate the depth of cover, locate circumferential welded joints and especially detect SCZs of underground pipelines, see Chapter 6. These techniques have been tested with field survey data and the results have been compared with the current industrial methods. At this time, assume that the prediction of the current methods is the gold standard, the depth estimation technique can predict the depth of underground pipelines with a tolerance of 8% of the measurement depth. The weld detection technique can locate about 70% of the actual welded joints within an offset of 3 m, with a probability of false call of 20%. And it is possible to predict all the bends including down-

ward bends with a high confidence, and may be possible to detect SCZs caused by defects as well.

The study has extended the understanding and provided evidence of detecting and characterising SCZs using the remote magnetic field with a modification of the magnetometer array. However, the main issue will be the effect of the bulk field to the magnetic indication of a local SCZ, so there must be a lower limit for dimensions of a detectable SCZ at a given distance. The study has confirmed that at this stage, the technology can be used as a complementary tool for the standard methods such as ILI.

7.2 Future work

For the modelling, the stress-magnetisation relationship of steel pipes needs to be improved so that it considers the effects of stress on all three components of magnetisation. This will contribute not only to improving the relationship between K and the measurement distance but also to simulating the induced magnetic field of a defect such as metal loss in pipelines. In addition, a model of three pipe sections with the constructed length of 12 m will further support the development of the weld detection technique.

In the lab, demagnetising the steel pipes before pressurised would allow investigating the stress-magnetic field curves of the pipe material. This is very useful as it contribute to solving the inverse problem. Experiments may be performed on steel pipes with a defect. However, health and safety requirements must be taken very carefully as it could cause serious injury. A different mechanism to apply stress on a defect is desirable.

The relationship between the measurement distance and the dimensions of the SCZ also needs to be further investigated in order to determine its lower limit. It will also improve the exponential equations of K and the measurement distance.

For the weld detection technique, it may be possible to improve the accuracy using other components of magnetic field, for example by combining with the peak and the zero crossing in B_x and B_z respectively. Magnetisation of individual pipe sections can also be taken into account in order to adjust the weld location from the location of the magnetic indication.

For detecting SCZs, the proposed technique can be developed further as the result so far is very promising. However, other techniques that are capable of looking into details of the signal should also be tested. Characterising features of a local SCZ may also be achieved by re-arranging the magnetometer array combined with the relationship between the strength of the magnetic indication and the measurement distance. The idea can be firstly verified using the experimental data as there may be an issue in testing the technique with field survey data.

Appendix A

Magnetic Dipole Model

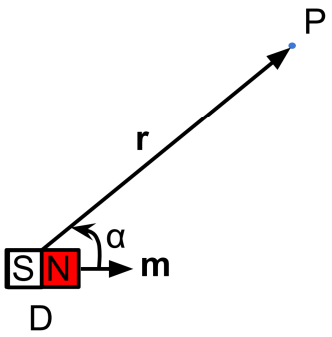

Figure A.1: Ideal magnetic dipole.

Consider a dipole D of magnetic moment $\mathbf{m}$ at the origin O of the polar coordinate system as shown in Fig. A.1, magnetic flux density $\mathbf{B}$ at a measurement point $P(r, \alpha)$ can be calculated as following

$$\begin{cases} \phi(\mathbf{r}) & = \frac{\mathbf{m}\cdot\mathbf{r}}{4\pi r^3} \\ \mathbf{A}(\mathbf{r}) & = \frac{\mu}{4\pi}\frac{\mathbf{m}\times\mathbf{r}}{r^3} \\ \mathbf{B}(\mathbf{r}) & = -\nabla\times\mathbf{A}(\mathbf{r}) = \frac{\mu}{4\pi}[\frac{3(\mathbf{m}\cdot\mathbf{r})\cdot\mathbf{r}}{r^5} - \frac{\mathbf{m}}{r^3}] \end{cases} \tag{A.1}$$

where $\phi(\mathbf{r})$ is magnetic scalar potential, $\mathbf{A}(\mathbf{r})$ is magnetic vector potential and $\mathbf{r}$ is $\overrightarrow{OP}$.

In the Cartesian coordinate system, if the dipole is at $D(x_d, y_d, z_d)$, whose magnetic moment $\mathbf{m} = m_x\hat{\mathbf{i}} + m_y\hat{\mathbf{j}} + m_z\hat{\mathbf{k}}$, $\mathbf{B}$ at $P(x, y, z)$ is presented as following

$$\begin{cases} B_x(x,y,z) & = \frac{\mu}{4\pi}[\frac{3mr_x\cos\alpha}{r^4} - \frac{m_x}{r^3}] \\ B_y(x,y,z) & = \frac{\mu}{4\pi}[\frac{3mr_y\cos\alpha}{r^4} - \frac{m_y}{r^3}] \\ B_z(x,y,z) & = \frac{\mu}{4\pi}[\frac{3mr_z\cos\alpha}{r^4} - \frac{m_z}{r^3}] \end{cases} \tag{A.2}$$

where $\mathbf{r} \equiv \overrightarrow{DP} = r_x\hat{\mathbf{i}} + r_y\hat{\mathbf{j}} + r_z\hat{\mathbf{k}}$ and α is the angle between $\mathbf{m}$ and $\mathbf{r}$.

Appendix B

Summary of stress cycles and measurements in the experiment on steel bars

B. SUMMARY OF STRESS CYCLES AND MEASUREMENTS IN THE EXPERIMENT ON STEEL BARS

Experiment	Applied force (kN)	Equivalent stress (MPa)	Measurements
1	Before stress	Before stress	Background field
2	1.8 kN	60 MPa	5 samples; from P_{3mm} to P_{34mm}
3	3 x 1.8 kN	3 x 60 MPa	5 samples; from P_{3mm} to P_{28mm}
4	3 x 1.8 kN	3 x 60 MPa	Sample 2, 3, 5; defect area at high resolution; PF_{3mm} to PF_{7mm} and PF_{20mm} to PF_{24mm}
5	3 kN	100 MPa	5 samples; from P_{3mm} to P_{28mm}
6	3 kN	100 MPa	Sample 2, 3, 5; defect area at high resolution; PF_{3mm} to PF_{7mm} and PF_{20mm} to PF_{24mm}
7	4.8 kN	160 MPa	5 samples; from P_{3mm} to P_{28mm}
8	4.8 kN	160 MPa	Sample 2, 3, 5; defect area at high resolution; PF_{3mm} to PF_{7mm} and PF_{20mm} to PF_{24mm}
9	3 kN	100 MPa	Sample 2, 5; defect side at high resolution; 3 mm and 5 mm depths
10	4.8 kN	160 MPa	Sample 2; defect area with distances, from 3 mm to 500 mm depth

Table B.1: Summary of stress cycles and the measurements performed in the experiments on steel bars.

Appendix C

Parameters in the Finite Element Model

C. PARAMETERS IN THE FINITE ELEMENT MODEL

Parameter	**Value**	**Description**
Length	120 mm	Length of the stressed section
Width	10 mm	Width of the bar
Thickness	3 mm	Thickness of the bar
Earth's field	$(8, -7, -46)$ μT	Components of the earth's field
M_s	1.71×10^6 A/m	Saturation magnetisation
ξ	605 Pa	JA model coefficient
E	205×10^9Pa	Elastic modulus
c	0.1	Flexibility of magnetic domain walls
a	900 A/m	Shape of the anhysteretic magnetisation
α	0.0011	Mean field parameter
K	2000 A/m	JA model coefficient
γ_{11}	$2 \times 10^{-18}\mathrm{m}^2/\mathrm{A}^2$	Magnetostriction coefficient
γ_{12}	$-1.5 \times 10^{-26}\mathrm{m}^2/(\mathrm{A}^2\mathrm{Pa})$	Magnetostriction coefficient
γ_{21}	$-2 \times 10^{-30}\mathrm{m}^4/\mathrm{A}^4$	Magnetostriction coefficient
γ_{22}	$5 \times 10^{-39}\mathrm{m}^4/(\mathrm{A}^4\mathrm{Pa})$	Magnetostriction coefficient
F	0 to 3 kN	The applied force

Table C.1: Parameters of the bar model.

Parameter	**Value**	**Description**
Length	1.8 m	Length of the pipe
Radius	84.15 mm	Radius of the pipe
Thickness	5.4 mm	Wall thickness of the pipe
Earth's field	$(-9, -10, -35)$ μT	Components of the earth's field
M_s	1.71×10^6 A/m	Saturation magnetisation
ξ	605 Pa	JA model coefficien
E	205×10^9Pa	Elastic modulus
c	0.1	Flexibility of magnetic domain walls
a	900 A/m	Shape of the anhysteretic magnetisation
α	0.0011	Mean field parameter
K	2000 A/m	JA model coefficien
γ_{11}	$2 \times 10^{-18}\text{m}^2/\text{A}^2$	Magnetostriction coefficient
γ_{12}	$-1.5 \times 10^{-26}\text{m}^2/(\text{A}^2\text{Pa})$	Magnetostriction coefficient
γ_{21}	$-2 \times 10^{-30}\text{m}^4/\text{A}^4$	Magnetostriction coefficient
γ_{22}	$5 \times 10^{-39}\text{m}^4/(\text{A}^4\text{Pa})$	Magnetostriction coefficient
P	0 to 60 bar	The applied pressure
M_r	in kA/m	The residual magnetisation

Table C.2: Parameters of the pipe model.

Appendix D

Field Survey Data

Latitude	**Longitude**	**Depth** (m)
53.950974	-1.617156	2.75
53.950882	-1.617285	2.65
53.950824	-1.617390	2.68
53.950780	-1.617480	2.69
53.950716	-1.617567	2.66
53.950630	-1.617680	2.67
53.950543	-1.617772	2.43
53.950469	-1.617850	2.52
53.950398	-1.617934	2.53
53.950326	-1.618014	2.53
53.950253	-1.618092	2.6
53.950171	-1.618179	2.6
53.950095	-1.618267	2.66
53.950021	-1.618350	2.61
53.949963	-1.618416	2.54
53.949895	-1.618488	2.43
53.949793	-1.618599	2.30

Latitude	**Longitude**	**Depth** (m)
53.949734	-1.618667	2.26
53.949659	-1.618752	2.24
53.949570	-1.618853	2.19
53.949478	-1.618954	2.49
53.949405	-1.619037	2.8
53.949333	-1.619142	2.9
53.949287	-1.619221	2.88
53.949236	-1.619339	2.85
53.949206	-1.619425	2.88
53.949166	-1.619533	2.83
53.949113	-1.619683	2.68
53.949060	-1.619823	2.45
53.949019	-1.619935	2.85
53.948985	-1.620017	3.66
53.948955	-1.620103	4.43
53.948925	-1.620187	4.40
53.948917	-1.620210	4.25

Table D.1: Depth measurement and the corresponding coordinate of the PANE29 pipeline.

Latitude	**Longitude**	**Depth** (m)
53.950567	-1.615633	2.41
53.950547	-1.615572	2.45
53.950501	-1.615464	2.48
53.950451	-1.615349	2.68
53.950404	-1.615241	2.7
53.950346	-1.615133	2.51
53.950291	-1.615040	2.31
53.950256	-1.614971	2.57
53.950212	-1.614898	2.44
53.950165	-1.614807	2.81
53.950123	-1.614733	2.59
53.950111	-1.614646	2.86
53.950113	-1.614569	2.96
53.950115	-1.614482	2.9
53.950121	-1.614369	3.22
53.950121	-1.614291	3.34
53.950123	-1.614251	3.41
53.950128	-1.614174	4.35
53.950130	-1.614043	3.18
53.950133	-1.613920	2.75
53.950152	-1.613864	2.54
53.950181	-1.613765	2.5
53.950218	-1.613666	2.43
53.950260	-1.613548	2.39
53.950307	-1.613427	2.4

Latitude	**Longitude**	**Depth** (m)
53.950352	-1.613305	2.19
53.950410	-1.613150	2.39
53.950457	-1.613024	2.39
53.950499	-1.612907	2.37
53.950541	-1.612803	2.7
53.950576	-1.612705	2.62
53.950613	-1.612604	2.41
53.950640	-1.612521	2.58
53.950667	-1.612398	2.48
53.950664	-1.612315	2.36
53.950638	-1.612220	2.17
53.950603	-1.612116	2.55
53.950562	-1.611999	2.39
53.950524	-1.611888	2.22
53.950482	-1.611772	2.24
53.950437	-1.611636	2.29
53.950398	-1.611524	2.36
53.950343	-1.611364	2.27
53.950300	-1.611240	2.28
53.950265	-1.611134	2.23
53.950229	-1.611027	2.4
53.950180	-1.610885	2.31
53.950145	-1.610787	2.18
53.950107	-1.610669	2.39
53.950075	-1.610583	2.32

Table D.2: Depth measurement and the corresponding coordinate of the ASPA29 pipeline.

ILI		SCT	
Latitude	Longitude	Latitude	Longitude
53.950115	-1.610664	53.950119	-1.610715
53.950193	-1.610893	53.950193	-1.610928
53.950275	-1.611131	53.950269	-1.611151
53.950356	-1.611371	53.950332	-1.611338
53.950437	-1.611606	53.950423	-1.611603
53.950518	-1.611842	53.950510	-1.611858
53.950591	-1.612054	53.950594	-1.612093
53.950664	-1.612296	53.950657	-1.612293
53.950667	-1.612337	53.950655	-1.612446
53.950667	-1.612391	53.950588	-1.612665
53.950659	-1.612429	53.950508	-1.612878
53.950583	-1.612672	53.950440	-1.613064
53.950501	-1.612897	53.950331	-1.613356
53.950415	-1.613128	53.950243	-1.613589
53.950329	-1.613360	53.950146	-1.613877
53.950242	-1.613593	53.950131	-1.613943
53.950220	-1.613653	53.950113	-1.614479
53.950143	-1.613892	53.950113	-1.614683
53.950137	-1.613927	53.950156	-1.614798
53.950137	-1.613956	53.950243	-1.614955
53.950129	-1.614216	53.950329	-1.615112
53.950121	-1.614490	53.950432	-1.615310
53.950119	-1.614638	53.950520	-1.615512
53.950123	-1.614674		
53.950132	-1.614717		
53.950143	-1.614747		
53.950252	-1.614943		
53.950359	-1.615136		
53.950445	-1.615310		
53.950539	-1.615527		

Table D.3: Coordinate of welded joints reported by ILI and predicted by SCT of the ASPA29 pipeline.

ILI		SCT	
Latitude	Longitude	Latitude	Longitude
53.950954	-1.617120	53.950972	-1.617160
53.950869	-1.617246	53.950895	-1.617268
53.950769	-1.617415	53.950726	-1.617558
53.950753	-1.617443	53.950652	-1.617658
53.950708	-1.617517	53.950504	-1.617816
53.950701	-1.617510	53.950404	-1.617933
53.950652	-1.617592	53.950141	-1.618219
53.950527	-1.617729	53.950020	-1.618354
53.950394	-1.617876	53.949864	-1.618526
53.950261	-1.618025	53.949719	-1.618690
53.950125	-1.618175	53.949593	-1.618832
53.949990	-1.618324	53.949432	-1.619010
53.949855	-1.618473	53.949359	-1.619104
53.949726	-1.618617	53.949248	-1.619318
53.949593	-1.618765	53.949175	-1.619519
53.949460	-1.618914	53.949121	-1.619665
53.949332	-1.619077	53.949037	-1.619894
53.949231	-1.619289		
53.949147	-1.619518		
53.949099	-1.619645		
53.949017	-1.619872		

Table D.4: Coordinate of welded joints reported by ILI and predicted by SCT of the PANE29 pipeline.

References

[1] I. Kolesnikov *et al.*, "Magnetic tomography method (mtm) &ndash a remote non-destructive inspection technology for buried and sub sea pipelines," in *OTC Arctic Technology Conference*. Offshore Technology Conference, 2014. 2, 7

[2] G. Hiltscher, W. Mühlthaler, and J. Smits, *Industrial pigging technology: fundamentals, components, applications*. John Wiley & Sons, 2006. 2

[3] D. Jiles, "Review of magnetic methods for nondestructive evaluation (part 2)," *NDT International*, vol. 23, no. 2, pp. 83–92, 1990. 3

[4] Z. Wang, Y. Gu, and Y. Wang, "A review of three magnetic ndt technologies," *Journal of Magnetism and Magnetic Materials*, vol. 324, no. 4, pp. 382–388, 2012. 3

[5] J. Tiratsoo, "The ultimate guide to unpiggable pipelines," *Pipelines International*, 2013. 3

[6] S. Freear, B. Varcoe, D. M. J. Cowell, S. G. H. Staples, and C. Vo, "Fault detection for pipelines," Mar. 5 2015, uS Patent 20,150,061,659. 3

[7] ——, "Fault detection for pipelines," Feb. 12 2015, uS Patent 20,150,042,323. 3

[8] J. Joule, "On a new class of magnetic forces," *Ann. Electr. Magn. Chem*, vol. 8, no. 1842, pp. 219–224, 1842. 4

[9] E. Villari, "Change of magnetization by tension and by electric current," *Ann. Phys. Chem*, vol. 126, pp. 87–122, 1865. 4

[10] P. Weiss, "Hypothesis of the molecular field and ferromagnetic properties," *J. phys*, vol. 6, no. 4, pp. 661–690, 1907. 4

[11] R. M. Bozorth, "Ferromagnetism, 1951," *New York*, p. 279, 1951. 4, 5, 6

[12] E. Lee, "Magnetostriction and magnetomechanical effects," *Reports on progress in physics*, vol. 18, p. 184, 1955. 4

[13] B. Cullity, "Introduction to magnetic materials," *Chapter*, vol. 6, p. 184, 1972. 4

[14] E. C. Stoner and E. Wohlfarth, "A mechanism of magnetic hysteresis in heterogeneous alloys," *Philosophical Transactions of the Royal Society of London. Series A. Mathematical and Physical Sciences*, pp. 599–642, 1948. 4

[15] E. C. Stoner, "Ferromagnetism: magnetization curves," *Reports on Progress in Physics*, vol. 13, no. 1, p. 83, 1950. 4

[16] ——, "Lxxxiv. magnetic energy and the thermodynamics of magnetization," *The London, Edinburgh, and Dublin Philosophical Magazine and Journal of Science*, vol. 23, no. 157, pp. 833–857, 1937. 4

[17] W. F. Brown Jr, "Domain theory of ferromagnetics under stress: Part i," *Physical Review*, vol. 52, no. 4, p. 325, 1937. 4

[18] W. Heisenberg, "Theory of magnetostriction and the magnetization curve," *Physik*, vol. 69, pp. 287–297, 1931. 4

[19] R. M. Bozorth, "The theory of the ferromagnetic anisotropy of single crystals," *Physical Review*, vol. 42, no. 6, p. 882, 1932. 4

[20] W. Brown Jr, "Irreversible magnetic effects of stress," *Physical Review*, vol. 75, no. 1, p. 147, 1949. 4, 6

[21] B. Cullity and C. Graham, *Introduction to magnetic materials*. Wiley-IEEE Press, 2011. 5

[22] D. Craik and M. Wood, "Magnetization changes induced by stress in a constant applied field," *Journal of Physics D: Applied Physics*, vol. 3, p. 1009, 1970. 5, 6

[23] R. Birss, C. Faunce, and E. Isaac, "Magnetomechanical effects in iron and iron-carbon alloys," *Journal of Physics D: Applied Physics*, vol. 4, no. 7, p. 1040, 1971. 5

[24] R. Birss, "Magnetomechanical effects in the rayleigh region," *Magnetics, IEEE Transactions on*, vol. 7, no. 1, pp. 113–133, 1971. 5, 6

[25] D. Jiles and D. Atherton, "Theory of the magnetisation process in ferromagnets and its application to the magnetomechanical effect," *Journal of Physics D: Applied Physics*, vol. 17, no. 6, p. 1265, 1984. 5

[26] ——, "Theory of ferromagnetic hysteresis," *Journal of magnetism and magnetic materials*, vol. 61, no. 1, pp. 48–60, 1986. 6, 13, 18

[27] K. Pitman, "The influence of stress on ferromagnetic hysteresis," *Magnetics, IEEE Transactions on*, vol. 26, no. 5, pp. 1978–1980, 1990. 6

[28] M. Sablik, H. Kwun, G. Burkhardt, and D. Jiles, "Model for the effect of tensile and compressive stress on ferromagnetic hysteresis," *Journal of applied physics*, vol. 61, no. 8, pp. 3799–3801, 1987. 6

[29] D. Jiles, "Theory of the magnetomechanical effect," *Journal of physics D: applied physics*, vol. 28, p. 1537, 1995. 6, 13, 15, 16, 18, 71

[30] D. Jiles and L. Li, "A new approach to modeling the magnetomechanical effect," *Journal of applied physics*, vol. 95, no. 11, pp. 7058–7060, 2004. 6

[31] L. Li and D. Jiles, "Modeling of the magnetomechanical effect: application of the rayleigh law to the stress domain," *Journal of applied physics*, vol. 93, p. 8480, 2003. 6

[32] J. Li and M. Xu, "Modified jiles-atherton-sablik model for asymmetry in magnetomechanical effect under tensile and compressive stress," *Journal of Applied Physics*, vol. 110, no. 6, pp. 063 918–063 918, 2011. 6

[33] J. Wilson, G. Tian, and S. Barrans, "Residual magnetic field sensing for stress measurement," *Sensors and Actuators A: Physical*, vol. 135, no. 2, pp. 381–387, 2007. 6

[34] D. Lihong, X. Binshi, D. Shiyun, C. Qunzhi, and W. Dan, "Variation of stress-induced magnetic signals during tensile testing of ferromagnetic steels," *NDT & E International*, vol. 41, no. 3, pp. 184–189, 2008. 6

[35] L. Dong, B. Xu, S. Dong, L. Song, Q. Chen, and D. Wang, "Stress dependence of the spontaneous stray field signals of ferromagnetic steel," *NDT & E International*, vol. 42, no. 4, pp. 323–327, 2009. 6

[36] C. Shi, S. Dong, B. Xu, and P. He, "Metal magnetic memory effect caused by static tension load in a case-hardened steel," *Journal of Magnetism and Magnetic Materials*, vol. 322, no. 4, pp. 413–416, 2010. 6

[37] G. Pengju, C. Xuedong, G. Weihe, C. Huayun, and J. Heng, "Effect of tensile stress on the variation of magnetic field of low-alloy steel," *Journal of Magnetism and Magnetic Materials*, vol. 323, no. 20, pp. 2474–2477, 2011. 6

[38] Y. En, C. Xing *et al.*, "Magnetic field aberration induced by cycle stress," *Journal of magnetism and magnetic materials*, vol. 312, no. 1, pp. 72–77, 2007. 6

[39] H. Huang, J. Yao, Z. Li, and Z. Liu, "Residual magnetic field variation induced by applied magnetic field and cyclic tensile stress," *NDT & E International*, 2014. 6

[40] J. Leng, M. Xu, G. Zhou, and Z. Wu, "Effect of initial remanent states on the variation of magnetic memory signals," *NDT & E International*, 2012. 6

[41] D. Atherton, L. Coathup, D. Jiles, L. Longo, C. Welbourn, and A. Teitsma, "Stress induced magnetization changes of steel pipes–laboratory tests," *Magnetics, IEEE Transactions on*, vol. 19, no. 4, pp. 1564–1568, 1983. 6

[42] D. Atherton, C. Welbourn, D. Jiles, L. Reynolds, and J. Scott-Thomas, "Stress-induced magnetization changes of steel pipes–laboratory tests, part ii," *Magnetics, IEEE Transactions on*, vol. 20, no. 6, pp. 2129–2136, 1984. 6

[43] D. Atherton and A. Teitsma, "Detection of anomalous stresses in gas pipelines by magnetometer survey," *Journal of Applied Physics*, vol. 53, no. 11, pp. 8130–8135, 1982. 7, 100

[44] D. Atherton and D. Jiles, "Effects of stress on magnetization," *NDT international*, vol. 19, no. 1, pp. 15–19, 1986. 7

[45] A. Viana, L.-L. Rouve, G. Cauffet, and J.-L. Coulomb, "Magneto-mechanical effects under low fields and high stresses-application to a ferromagnetic cylinder under pressure in a vertical field," *Magnetics, IEEE Transactions on*, vol. 46, no. 8, pp. 2872–2875, 2010. 7

[46] A. Viana, L. Rouve, G. Cauffet, and J.-L. Coulomb, "Analytical model for external induction variations of a ferromagnetic cylinder undergoing high mechanical stresses in a low magnetic field of any orientation," *Magnetics, IEEE Transactions on*, vol. 47, no. 5, pp. 1366–1369, 2011. 7

[47] A. Viana, L.-L. Rouve, O. Chadebec, G. Cauffet, and J.-L. Coulomb, "Inverse problem approach to characterize and model magnetization changes in a thin shell structure undergoing magneto-mechanical effects," *Magnetics, IEEE Transactions on*, vol. 47, no. 5, pp. 1450–1453, 2011. 7

[48] A. Dubov, "A study of metal properties using the method of magnetic memory," *Metal science and heat treatment*, vol. 39, no. 9, pp. 401–405, 1997. 7

[49] ——, "Principle features of metal magnetic memory method and inspection tools as compared to known magnetic ndt methods," *CINDE JOURNAL*, vol. 27, no. 3, p. 16, 2006. 7

[50] I. Standard, "24497: Non-destructive testing–metal magnetic memory," *Geneve, Switzerland: International Standard Organization*, 2007. 7

[51] M. J. Dapino, R. C. Smith, L. E. Faidley, and A. B. Flatau, "A coupled structural-magnetic strain and stress model for magnetostrictive transducers," *Journal of intelligent material systems and structures*, vol. 11, no. 2, pp. 135–152, 2000. 13

[52] B. Instruments, "Mag648 and mag649 low power three-axis magnetic field sensors," 2014. [Online]. Available: http://www.bartington.com/mag648-649-low-power-three-axis-magnetic-field-sensors.html 27

[53] Topcon, "Gr-5 with vanguard technology - advanced gnss receiver," 2014. [Online]. Available: https://www.topconpositioning.com/sites/default/files/product_files/gr-5_broch_7010_2071_reve_tf_sm.pdf 33

[54] S. M. Dutta, F. H. Ghorbel, and R. K. Stanley, "Simulation and analysis of 3-d magnetic flux leakage," *Magnetics, IEEE Transactions on*, vol. 45, no. 4, pp. 1966–1972, 2009. 63

[55] L. Zhong, L. Li, and X. Chen, "Simulation of magnetic field abnormalities caused by stress concentrations," *Magnetics, IEEE Transactions on*, vol. 49, no. 3, pp. 1128–1134, 2013. 63

[56] K. Yao, K. Shen, Z.-D. Wang, and Y.-S. Wang, "Three-dimensional finite element analysis of residual magnetic field for ferromagnets under early damage," *Journal of Magnetism and Magnetic Materials*, vol. 354, pp. 112–118, 2014. 63

[57] COMSOL, "Structural mechanics module for comsol 4.4," pp. 173–229, 2013. 70

[58] ——, "Ac/dc module for comsol 4.4," p. 267, 2013. 71

[59] S. Staples, C. Vo, D. Cowell, S. Freear, C. Ives, and B. Varcoe, "Solving the inverse problem of magnetisation–stress resolution," *Journal of Applied Physics*, vol. 113, no. 13, pp. 133 905–133 905, 2013. 79

[60] W. Sowerbutts, "The use of geophysical methods to locate joints in underground metal pipelines," *Quarterly Journal of Engineering Geology and Hydrogeology*, vol. 21, no. 3, pp. 273–281, 1988. 100

[61] M. Drge, "Gas pipeline incidents - 9th report of the european gas pipeline incident data group (period 1970 - 2013)," Feb 2015. [Online]. Available: http://www.egig.eu/uploads/bestanden/ba6dfd62-4044-4a4d-933c-07bf56b82383 139

[62] Radiodetection, "Rd8000 radiodetection's universal precision locator," Mar 2013. [Online]. Available: http://www.spx.com/en/assets/pdf/RD8K_OPMAN_ENG_02_en.pdf 144

[63] ——, "Rd8000 universal precision cable, pipe and rf marker locator range," 2014. [Online]. Available: http://www.spx.com/en/assets/pdf/RD8000brochureV10.pdf 144

[64] A. D. Poularikas, *Transforms and applications handbook*. CRC press, 2010. 175

[65] S. G. Mallat, "A theory for multiresolution signal decomposition: the wavelet representation," *Pattern Analysis and Machine Intelligence, IEEE Transactions on*, vol. 11, no. 7, pp. 674–693, 1989. 175